Three-Dimensional, Transient Temperature Analysis of Friction Welding of Cylindrical Bars

by

Shaik Ilias Ahamad

A Thesis Presented to the

FACULTY OF THE COLLEGE OF GRADUATE STUDIES

KING FAHD UNIVERSITY OF PETROLEUM & MINERALS

DHAHRAN, SAUDI ARABIA

In Partial Fulfillment of the
Requirements for the Degree of

MASTER OF SCIENCE

In

MECHANICAL ENGINEERING

April, 1996

INFORMATION TO USERS

This manuscript has been reproduced from the microfilm master. UMI films the text directly from the original or copy submitted. Thus, some thesis and dissertation copies are in typewriter face, while others may be from any type of computer printer.

The quality of this reproduction is dependent upon the quality of the copy submitted. Broken or indistinct print, colored or poor quality illustrations and photographs, print bleedthrough, substandard margins, and improper alignment can adversely affect reproduction.

In the unlikely event that the author did not send UMI a complete manuscript and there are missing pages, these will be noted. Also, if unauthorized copyright material had to be removed, a note will indicate the deletion.

Oversize materials (e.g., maps, drawings, charts) are reproduced by sectioning the original, beginning at the upper left-hand corner and continuing from left to right in equal sections with small overlaps. Each original is also photographed in one exposure and is included in reduced form at the back of the book.

Photographs included in the original manuscript have been reproduced xerographically in this copy. Higher quality 6" x 9" black and white photographic prints are available for any photographs or illustrations appearing in this copy for an additional charge. Contact UMI directly to order.

UMI

A Bell & Howell Information Company
300 North Zeeb Road, Ann Arbor MI 48106-1346 USA
313/761-4700 800/521-0600

Three-Dimensional, Transient Temperature Analysis of Friction Welding of Cylindrical Bars

Shaik Ilias Ahamad

Mechanical Engineering

Dhu-al-qa'dah, 1416H.

April, 1996G.

KING FAHD UNIVERSITY OF PETROLEUM AND MINERALS
DHAHRAN, SAUDI ARABIA

COLLEGE OF GRADUATE STUDIES

This thesis, written by

Shaik Ilias Ahamad

under the direction of his Thesis Advisor, and approved by his Thesis committee, has been presented to and accepted by the Dean, College of Graduate Studies, in partial fulfillment of the requirements for the degree of

MASTER OF SCIENCE
IN
MECHANICAL ENGINEERING

Thesis Committee:

Ahmet Sahin 2/7/96

Dr. Ahmet Z. Sahin (Chairman)

Dr. Bekir S. Yilbas (Co-Chairman)

Dr. Syed M. Zubair (Member)

Dr. Mohammed O. Budair
Department Chairman

Dr. Ala H. Al-Rabeh
Dean, College of Graduate Studies

Date: 22-7-96.

Dedicated to

My beloved

Parents,

Brothers and Sisters

whose love, sacrifice and perseverance

led to this accomplishment.

Acknowledgments

In the name of Allah, Most Beneficent and Most Merciful. Read, In the name of thy Lord and Cherisher, Who created. Created man from a [leech-like] clot. Read, and thy lord Is Most Bountiful, He Who taught [the use of] the pen. Taught man that Which he knew not. Nay, but man doth Transgress all bounds. In that he looketh Upon himself as self-sufficient. Verily, to thy Lord Is the return [of all]. (The Holy QURAN, Surah no. 96)

First and foremost, all praise and thanks to Allah *subhanahu-wa-ta'ala*, for his blessings, guidance, mercy and all that he has provided me with, and peace be upon his prophet Mohammed. This work is an attempt towards understanding more and using in the best possible way the fabulous world ALLAH has created. I seek ALLAH's mercy, favor and forgiveness, and peace and prayers be upon his Prophet.

Acknowledgements are due to King Fahd University of Petroleum and Minerals for having given an opportunity to pursue my graduate study here, for providing research facilities and financial assistance during the course of the study.

I am extremely thankful and deeply indebted to my thesis committee chairman, Dr. Ahmet Z. Sahin for his guidance and advice. I acknowledge him for his efforts, constant encouragement, support, concern, patience, guidance and valuable time during all stages of this work and above all for having complete faith in me.

I wish to express my sincere appreciation and gratitude to my thesis committee co-chairman Dr. Bekir S. Yilbas and committee member Dr. Syed M. Zubair for their interest, constructive criticism and personal understanding. I acknowledge them for their useful and valuable comments and suggestions in making this report a proffessional one.

I am also thankful to the department chairman, Dr. Mohammad O. Budair and other faculty members for their cooperation throughout the duration of my stay in KFUPM. I would also like to thank the secretaries of the department, Mr. Abdul Ghani Latif, Mr. Jameel and Mr. Thomas for their help during my stay. I am also thankful to the CCSE for providing the excellent, state-of-art computational facilities.

I also express thanks to my friends Yunus, Sadath, Abbas Qureshi, Asad, Abdul Waris, Akbar and Hadi for standing by me at all times and for making my stay at KFUPM a memorable one. A word of appreciation is also due to my friends and the Hyderabadi community whose moral support and patronage provided an impetus for the completion of this work. In short, I should say that they have made my work a joy, and my life worth living.

Finally, without the emotional and moral support, prayers, sacrifices, love, patience, encouragement and understanding of my parents, brothers and sisters and other family members the completion of this would not have been a possibility.

Contents

List of Tables

List of Figures

Abstract

Name: Shaik Ilias Ahamad

Title: Three-Dimensional Transient Temperature Analysis For Friction Welding of Cylindrical Bars

Major Field: Mechanical Engineering

Date of Degree: Dhu-al-qa'dah, 1416H. (April, 1996G.)

In this work, three-dimensional transient temperature distribution occuring during the friction welding process of two cylindrical bars is investigated. A finite difference scheme is used to solve the governing heat conduction equations for the two bars. The algorithm developed can be used for friction welding of similar as well as for dissimilar material combinations. The effect of variation of jet velocity and angular speed on the temperature is studied. Transient temperature profiles are obtained in axial, radial and circumferential directions for steel-steel, steel-copper and steel-aluminum combinations. The temperature gradients within the two bars increase with the increase in jet velocity and the duration of welding cycle reduces with increase in angular speed. To validate the results obtained a comparison is made with previous numerical studies.

Master of Science Degree
King Fahd University of Petroleum and Minerals
Dhahran, Saudi Arabia
Dhu-al-qa'dah, 1416H. (April, 1996G.)

ملخص

الإسم : شيخ الياس أحمد

العنوان : تحليل ثلاثي الأبعاد للحرارة المتغيرة للحام الاحتكاكي لقضيب اسطواني

التخصص : هندسة ميكانيكية

التاريخ : ذو القعدة ١٤١٦

في هذا العمل تم بحث التوزيع الحراري ثلاثي الأبعاد والذي يحدث خلال اللحام الاحتكاكي لقضبين اسطوانيين تم استخدام طريقة الفروق المحددة كل المعادلات المتحكمة في حرارة القضبين . النموذج المستخدم في هذا التحليل يمكن استخدامه للحام الاحتكاكي لاسطوانتين من نفس المادة او من مواد مختلفة . تم ايضا دراسة اثر تغير سرعة الضخ والسرعة الدورانية على الحرارة . تم استخراج توزيع الحرارة افقيا وقطريا ومحيطيا لمجموعات مكونة من حديد – حديد وحديد – نحاس وحديد – المنيوم لوحظ ان التوزيع الحراري يزداد بازدياد الضخ . كما لوحظ ايضا ان مدة دورة اللحام تقل بازياد السرعة الدورانية . ولاثبات صحة الدراسة تم مقارنتها مع دراسات رقمية سابقة .

درجة الماجستير في العلوم

جامعة الملك فهد للبترول والمعادن

الظهران – المملكة العربية السعودية

ذو القعدة ١٤١٦ ؛ الموافق ابريل ١٩٩٦ .

Nomenclature

B	Biot number
h	Heat transfer coefficient , $\frac{w}{m^2-K}$
k	Thermal conductivity, $\frac{w}{m-K}$
P	Pressure across the interface, Pa
R	Radius of the bar
r	Radius, m
r_k	Ratio of thermal conductivity
r_α	Ratio of thermal diffusivity
t	Time, s
z	length of the bar, m

Greek Symbols

α	Thermal diffusivity, $\frac{m^2}{s}$
ψ	Temperature in Domain I, $^\circ C$
ϕ	Temperature in Domain II, $^\circ C$
Φ	Angle, radians
μ	Coefficient of friction

ω	Speed of rotation, rpm
τ	Dimensionless time
ρ	Dimensionless radius
ξ	Dimensionless length
Θ	Temperature at the interface, $^{\circ}C$

Subscripts

1	For Domain I
2	For Domain II
i	No. of nodes in axial direction
j	No. of nodes in radial direction
k	No. of nodes in peripheral direction

Chapter 1

Introduction

Friction is an energy dissipative process in which a mechanical contact is subjected to relative motion and pressure. Heat generation is inseparable result of the friction phenomenon. The heat generation during any machining process is a consequence of the first law of thermodynamics which states that the quantity of heat generated is equivalent to the amount of work done when there is no change in the internal energy of the system.

1.1 Friction Welding

There are about 40 different welding processes. which can be broadly divided into two groups-*fusion welding*, which relies on the formation of a molten bridge, and *deformation welding*, relying on the flow of metal. Pressure welding is one of the oldest forms of joining. It is known that joints can be made in very ductile materials at room temperature using high pressure and appreciable deformation. In theory, all ductile metals could be prohibitive. Therefore materials were heated to improve

ductility, allowing pressure welds to be made with lower forces. Several heating methods are used commercially such as flame heating, induction, resistance, and more recently friction.

Apart from being a very efficient heat source, friction provides an effective cleaning action, removing the surface contamination which prevents metals from bonding together.

Friction welding is one of such machining processes where heat generation due to friction between the two parts which are being welded. This process is now being used throughout the world as a reliable and automated welding process in industries such as automotive industry.

"Friction welding is a solid-state joining process that produces coalescence of materials under compressive force contact of workpieces rotating or moving relative to one another to produce heat and plastically displace material from the rubbing surfaces. Under normal conditions, the rubbing surfaces do not melt. Filler metal and flux are not required with this process."

Thus the heat for welding in friction welding is produced by direct conversion of mechanical energy to thermal energy at the interface of the workpieces, without the application of electrical energy, or heat from other sources. Friction welds are generally made by holding a non-rotating workpiece in contact with a rotating work piece under a constant or gradually increasing axial pressure until the interface reaches welding temperature and then stopping the rotation to complete the weld.

The basic steps in friction welding are illustrated in Figure 1.1.

Advantages

Friction welding has numerous advantages over other welding processes. Some of them are

- Ecologically clean, no smoke, slag during the process,
- Consumables such as flux, filler material are not required,
- 100% butt joint weld is obtained throughout the contact area,
- No solidification defects occurs because of uniform heating across the interface,
- Economical advantages are: short time cycle, low loss of material and low reject rate.

Friction welding involves heat generation through friction and abrasion, heat dissipation, plastic deformation, and physical interdiffusion. The interrelationship among these factors during friction welding leads to complications when trying to develop predictive models of the friction welding process. However, from a qualitative standpoint, five qualitative factors influence the quality of a friction weld. They are

- Relative velocity of the surfaces,
- Applied pressure,

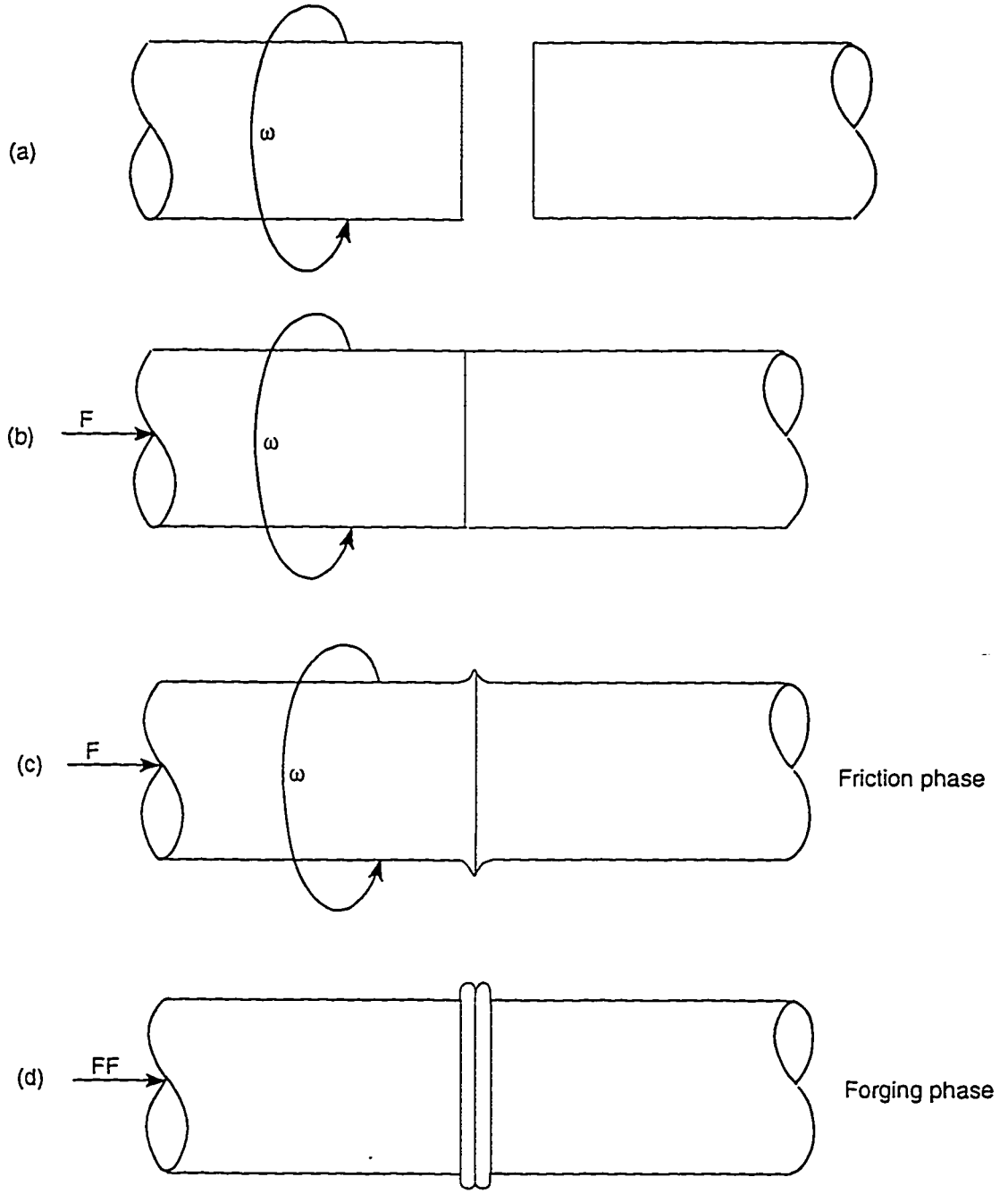

Figure 1.1: Fundamental Steps in the Friction Welding Process

- Surface temperature,
- Bulk material properties,
- Surface condition and presence of surface films.

The first three factors are related to friction welding process, while the last two are related to the properties of the materials being welded.

The frictional heat developed at the interface rapidly raised the temperature of the workpieces over a very short axial distance to a value approaching, but below the melting range; welding occurs under the influence of a pressure that is applied while the heated zone is in the plastic temperature range.

The rotational speed, the axial pressure, and the welding time are the principal variables that are controlled in order to provide the necessary combination of heat and pressure to form the weld.

The friction welding processes are divided and named by motion and drive(or energy source). One is direct-drive friction welding and the other is inertia friction welding.

1.1.1 Continuous Drive Friction Welding

In this type of welding, one of the workpieces is attached to a motor-driven unit, while the other is restrained from rotation. The motor-driven workpiece is rotated at a predetermined constant speed. The workpieces to be welded are brought to-

gether, and then a friction welding force is applied. Heat is generated as the rubbing surfaces (weld interface) rub together. This continues for a predetermined time, or until a preset amount of upset takes place. The rotational driving force is discontinued and the rotating workpiece is stopped by the application of a braking force. The friction welding force is maintained or increased for a predetermined time after rotation ceases (forge force). The relationship of direct-drive friction welding parameter characteristics is shown in Figure 1.2.

1.1.2 Inertia Welding

Here, one of the workpieces is connected to a flywheel, and the other is restrained from rotating. The flywheel is accelerated to a predetermined rotational speed, storing the required energy. The drive motor is disengaged and the workpieces are forced together by a friction welding force. This causes the faying surfaces to rub together under pressure. The kinetic energy stored in the rotating flywheel is dissipated as heat, through friction at the weld interface, as the flywheel speed decreases. An increase in the friction welding force may be applied (forging force) before rotation stops. The forge force is maintained for a predetermined time after rotation ceases. The relationship of inertia friction welding parameter characteristics are shown in Figure 1.3.

Further modifications of friction welding include radial, orbital, angular recip-

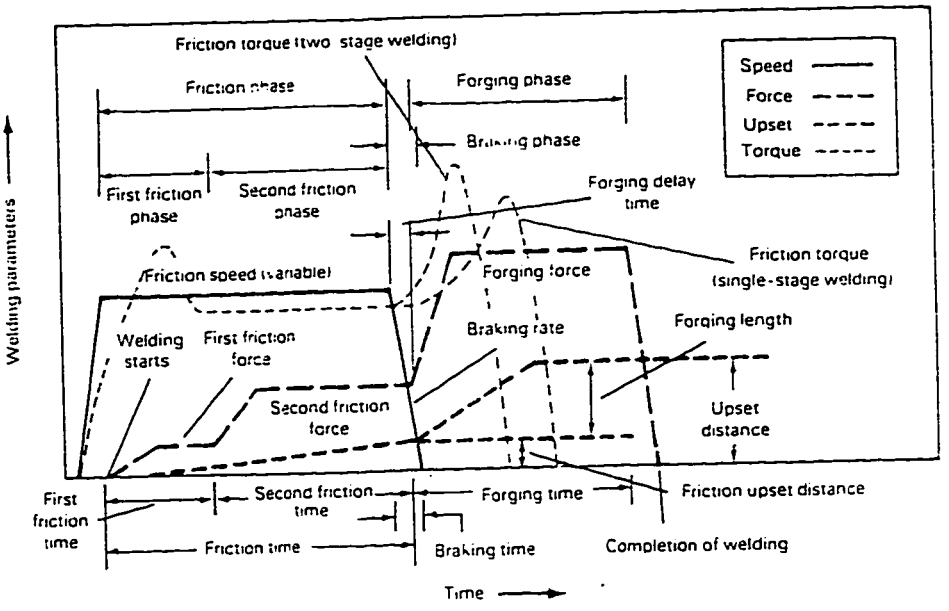

Figure 1.2: Characteristics of Direct-Drive Friction Welding Process

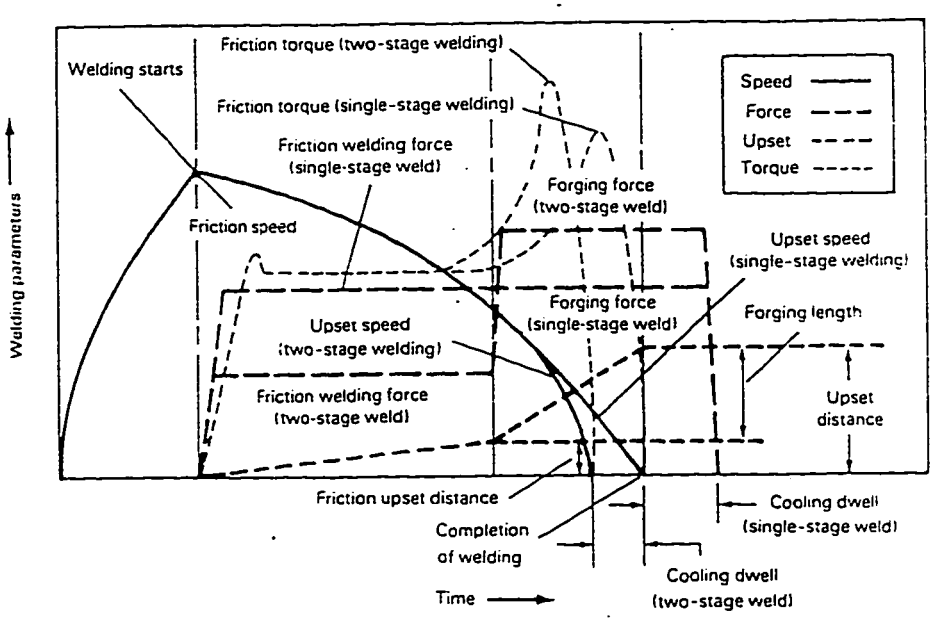

Figure 1.3: Characteristics of Inertia Friction Welding Process

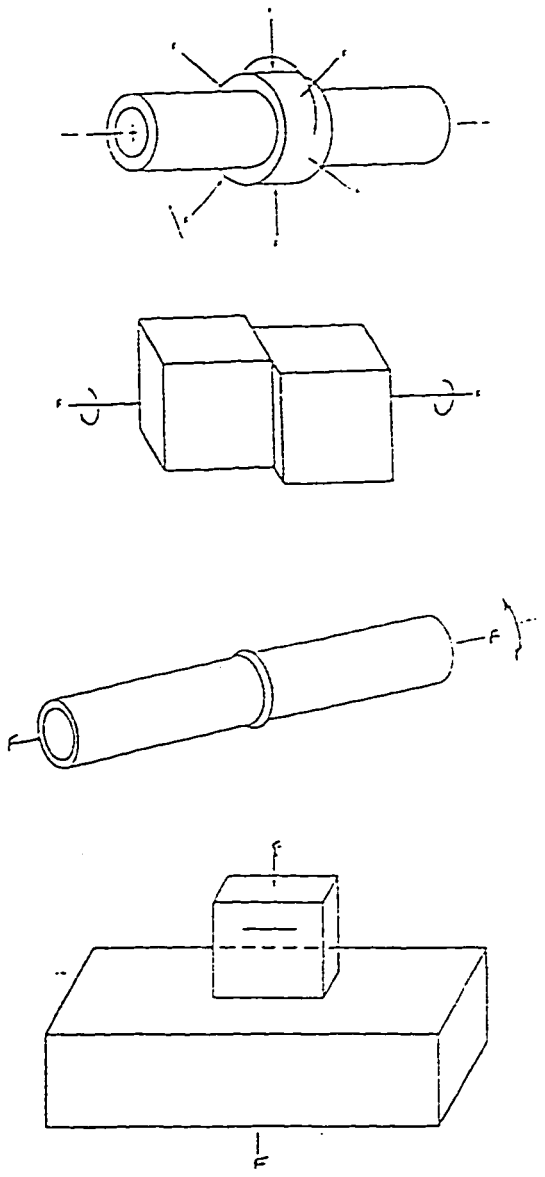

Figure 1.4: Other Forms of Friction Welding

rocating, linear reciprocating, friction welding, and friction surfacing [1]. These processes are shown Figure 1.4. Radial friction welding can be used to join tubular sections where it is undesirable to rotate either of the tubes, or collars to shafts and tubes. Orbital motion may be used to weld noncircular parts. In this application, neither piece rotates about its central axis. The orbital motion provides uniform tangential velocity over the total interface area. When motion ceases, the workpieces are aligned rapidly.

As each name implies, friction is created by various relative motions using either direct-drive motors or kinetic energy form a rotating flywheel.

1.2 Metallurgical Parameters

Friction welding can be used to join a wide range of similar and dissimilar materials. Metals, ceramics, metal-matrix composites, and polymers have all been joined by friction welding, and many of the dissimilar-metal combinations that cannot be joined by conventional fusion welding techniques are readily joined by friction welding methods.

1.2.1 Joining of Similar Metals

The two general requirements for forming good friction welds are, first, that the materials to be joined can be forged and, second, that the materials can generate

friction at the weld interface. The first requirement eliminates similar metal welds in brittle materials such as ceramics, cast irons, and cemented carbides. However, ductile materials can sometimes be joined to these materials. The second requirement eliminates materials that contain alloying elements that provide dry lubrication. Free-machining additives to steel, graphite-containing alloys such as cast iron, and lead alloys may suffer from this requirement. Almost all other metal alloys can be welded to themselves by friction welding techniques.

The relative ease of friction welding metals to themselves is related to the matching properties at the weld interface. Because the materials properties are matched, heat is distributed uniformly on both sides of the joint, and the deformation characteristics are identical on both sides of the joint resulting symmetric welds with good properties. However, there can be a significant variation in processing variables between different classes of materials.

1.2.2 Joining of Dissimilar Metals

While many similar-metal friction welding joints were produced because of economic considerations, many dissimilar-metal friction welding joints are produced because there are no alternative welding methods that can be used. Examples of these types of joints include dissimilar-metal combinations with widely different melting points and dissimilar-metal combinations that form incompatible phases when fusion welded.

The common problems in welding dissimilar materials are

- *Joint Interface:* Highly dissimilar-metal combinations are more sensitive for surface preparation. For example, in stainless steel to aluminum alloy welds, the oxide surface that forms on the aluminum picks up contaminants such as water and hydrocarbons, forming extremely tenacious surface layers. If this layer is not removed prior to welding, poor structural welds may occur.

- *Low-Melting Phase Formation:* Some material combinations have very low melting point phases associated with mixing of constituents at the weld interface. The formation of these phases during the welding cycle is deleterious to the finished weld properties. Examples of this type include iron-base alloys to titanium alloys and aluminum alloys to magnesium alloys. Low melting point eutectics are found in both of these metallurgical systems, and great care must be exercised during parameter development to prevent the formation of liquid phases during the completion of successful welds.

- *Brittle Phase Formation:* Many materials, when combined, are susceptible to the formation of brittle phases. In some combinations, this occurs during the welding cycle; in others, service conditions after welding cause the problem. The reasons for brittle phase formation are

  1. Surface contaminants that embrittle the weld interface

2. Formation of intermetallic phases between normal constituents of the alloys being welded.

- *Differential Thermal Expansion:* Some material combinations are difficult to weld because of the large differences in thermal expansion. Low-expansion materials such as refractory metals, ceramics and low-expansion iron-nickel alloys may fail or be highly stressed during cooling when welded to high-expansion material such as austenitic stainless steels and nickel-base and cobalt-base superalloys.

1.3 Heat Transfer from a Cylinder in Crossflow

Convective heat transfer from a rotating or stationary cylinder has numerous applications in thermal engineering such as cooling of rotating machinery, design of heat exchangers, drying of paper, etc. The crossflow across a cylinder causes temperature gradients to occur within the cylinder. Higher temperature gradients occurs on the side from which the crossflow is being blown.

During friction welding, an inert gas can be blown across the interface of the two bars being joined to prevent the weld from oxidation. This crossflow causes substantial temperature gradients to occur within the two bars. The present study takes into consideration of this crossflow across the interface of the two bars during friction welding.

A literature survey related to the heat transfer duing friction welding till recent times is presented in chapter 2. Most of the literature on friction welding is about the metllurgical aspects of weld and little is found on the heat transfer during friction welding. The governing equations and boundary conditions to the present investigation of three-dimensional, transient temperature analysis of concentric bars during friction welding are discussed in chapter 3. The numerical methodology used to solve the govering equations is also presented.

The effect of various parameters on temperature at the interface, in axial, radial and circumferential directions, is discussed in chapter 4. Large number of results can give a complete picture of the temperature across the interface at any point. Finally, the outcome of the present research and related future work is outlined in chapter 5.

Chapter 2

Literature Survey

2.1 Historical Background

The basic idea of friction welding is not new. A patent was granted as early as 1891 in which the concept of using frictional heat for extrusion and welding purposes was applied [2]. But the first practical use of the principle was perhaps started during World War II for welding thermo-plastic piping. In 1956, the Russian machinist, A. I. Chudikov, revived the old idea and demonstrated successfully the possibility of achieving high-quality butt weld between metal rods [3].

2.2 Literature Review on Heat Transfer During Friction Welding

There have been a number of articles on friction welding of metals published since 1957 in Russian, Polish, German, and Czechoslovakian journals [4], [5], [6], [7].

In 1959, Vill [8] analyzed the energy distribution in friction welding of steel bars. Gel'dman *et al.*, [9] did a similar analysis when welding large size steel pipes. The transient temperature distribution during friction welding of two similar materials (AISI 4140 alloy steel) in tubular form was obtained by Cheng in 1962 [10]. He considered variable thermal properties, time dependent heat inputs and a phase change during welding in his analysis. He also investigated the transient temperature distribution during the friction welding of dissimilar materials in tubular form [11]. The temperature distribution is given in axial direction in the vicinity of the interface.

Much literature can be found on the weldability of the materials, quality of the weld, weld strength. But there were few studies which dealt with the temperature distribution in the materials being welded during the weld cycle. Transient temperature distribution in inertial welding of steels was reported by Wang and Nagappan [12] in 1970. Duffin and Bahrani carried out a series of experiments on the friction welding of mild steel tubular specimens to study the variations in resisting torque, axial force, and axial shortening when the angular speed and axial force are varied [13]. Petrucci reported the spatial temperature variations occured in the friction welding of 12.5 mm diameter mild steel bars in 1978 [14]. Thermocouples were placed on the surface of the non-rotating workpiece at a distance of 5mm from the interface of the two workpieces.

Several mathematical models were developed by Francis [15] which describe various phases of the frictioning stage during friction welding, in particular of the

softened layer which develops close to the weld interface. A one dimensional computational model is presented by Hansson and Kristensen [16] for temperature distribution across the interface during the friction welding of uniform bars having constant cross sectional area. A mathematical treatment of heat flow was developed with a view to select the most realistic possible boundary conditions and including the heat input in the calculations when calculating the temperature distribution in friction welds between dissimilar materials by Na *et al* [17].

Friction welding was modelled by finite element analysis to represent the workpieces and surface contact conditions [18]. Using this model, temperature distributions, thermal expansion and thermoplastic stresses were determined. Nonlinear transient problem of the axisymmetric friction welding, in which the dimensions of the two bars may not be uniform in size, is modelled using finite element analysis [19]. Temperature dependent thermal properties were used in the modelling of this problem. One-dimensional temperature distribution (ie., axial direction) during the friction welding was done by Sluzalec and Sluzalec [20] analytically, experimentally and numerically. In the experimental work, the thermocouples were placed on the surface at the interface and at a distance from the interface. Comparison of analytical, experimental and numerically obtained results are compared to find a good agreement among the results obtained.

2.3 Literature Review on Heat Transfer From a Cylinder in Cross Flow

Convection heat transfer from a cylinder in cross flow is of significance because, most of the realistic boundary conditions are of this type. Earlier studies in heat transfer from a rotating cylinder were done experimentally by Kays, *et al.* [21] and Fand [22]. The local and average coefficients of heat transfer from a rotating cylinder in a uniform flow were measured experimentally for the range of rotating and cross-flow Reynolds numbers from 0-3000 by Ryohachi, *et al* [23]. The flow structure and heat transfer on a rotating cylinder cooled with an air jet was studied by Chiou and Lee [24].

2.4 Summary

The quality of the weld and the strength of the weld obtained by friction welding of two bars depends on the temperature distribution across the interface. It should be noted that the above studies considered the friction welding as a one-dimensional phenomena or a two-dimensional one. The studies did not report the temperature distribution across the interface when realistic boundary conditions such as having a shielding gas across the interface to prevent the weld from oxidation problems. When this cross flow is blown over the interface, there will be great amount of temperature

variations in the circumferential direction which effect the temperature values in other directions as well. The present research considered the temperature variations in axial, radial and circumferential directions, because of which the temperature can be known at any point across the interface of the bars being welded. In chapter 4, temperature profiles are drawn in circumferential, radial and axial directions to give complete temperature distribution across the interface.

Chapter 3

Problem Formulation

3.1 Governing Equations

The problem under consideration is a three-dimensional, transient problem in cylindrical coordiantes. The assumptions made are

- Thermal properties are independent of temperature.
- The pressure at the interface of the two bars is uniform across the cross-section.
- The coefficient of friction at the interface is constant throughout the welding cycle.
- All the thermal properties at the interface of the two bars are taken as the average thermal properties of the two bars.

As shown in Fig. 3.1, the two cylindrical bars with radius R are to be welded to each other. Bar I is rotating with an angular velocity ω, while bar II is stationary. F is the compressive force applied at the interface, k_1, a_1, h_1 and k_2, a_2, h_2 are the thermal

conductivity, thermal diffusivity and the heat transfer coefficient on the surface of the bars, respectively. An inert gas is blown over the weld area to prevent the weld from oxidation. The heat transfer coefficient on the bar I (h_1), which is rotating, is taken as an average heat transfer coefficient and the heat transfer coefficient (h_2) on the stationary bar varies in the circumferential direction. The heat generated at the interface due to the rubbing action, diffuses into both the bars as shown in Fig. 3.1 depending on the thermal properties.

The governing equation for the above said problem is the three-dimensional, transient heat conduction equation in cylindrical coordinates. Since the problem under consideration is analyzing the heat transfer in both the bars, it is considered as a two-domain problem. From here onwards, bar I (which is rotating) is considered as Domain I and bar II (stationary bar) is considered as Domain II.

$$\text{For Domain I} \quad \frac{\partial \psi}{\partial t} = \alpha_1 \left[\frac{1}{r} \frac{\partial}{\partial r} \left(r \frac{\partial \psi}{\partial r} \right) + \frac{1}{r^2} \frac{\partial^2 \psi}{\partial \Phi^2} + \frac{\partial^2 \psi}{\partial z^2} \right] \tag{3.1}$$

$$\text{For Domain II} \quad \frac{\partial \phi}{\partial t} = \alpha_2 \left[\frac{1}{r} \frac{\partial}{\partial r} \left(r \frac{\partial \phi}{\partial r} \right) + \frac{1}{r^2} \frac{\partial^2 \phi}{\partial \Phi^2} + \frac{\partial^2 \phi}{\partial z^2} \right] \tag{3.2}$$

Where $\psi = T_1 - T_\infty$ and $\phi = T_2 - T_\infty$ in which T_∞ is the ambient temperature.

3.1.1 Initial and Boundary Conditions

Initial Condition

$$\psi(r, \Phi, z, 0) = 0; \qquad \phi(r, \Phi, z, 0) = 0; \tag{3.3}$$

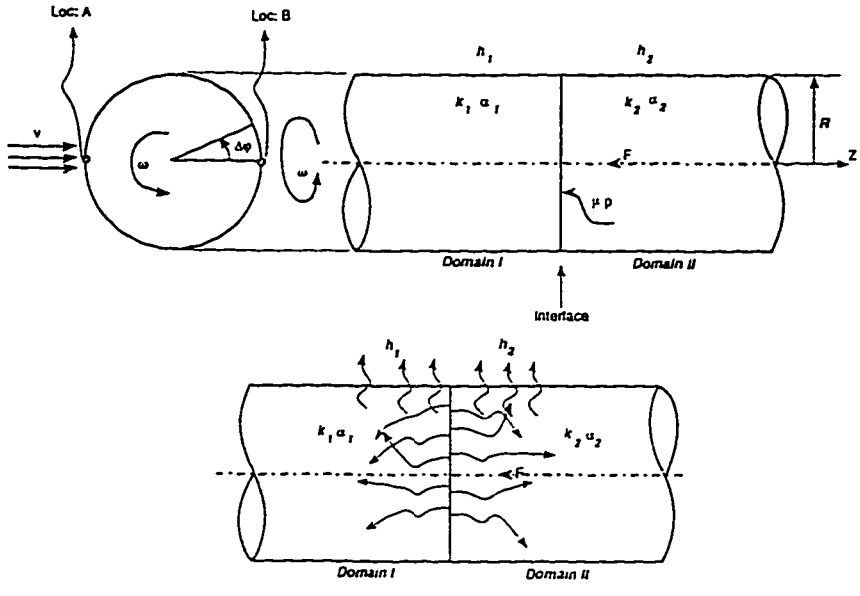

Figure 3.1: Modeling of Friction Welding

Boundary Conditions

- In axial (z-) direction:

  At interface($z = 0$)

$$v(r, \Phi, 0, t) = o(r, \Phi, 0, t) \tag{3.4}$$

  At $z = \infty$, ie., far from interface. an insulated boundary condition is imposed to restrict the length of the bars under consideration.

$$\frac{\partial \psi}{\partial z}(r, \Phi, \infty, t) = 0; \quad \frac{\partial o}{\partial z}(r, \Phi, -\infty, t) = 0; \tag{3.5}$$

- In radial (r-) direction:

  At the center, $(r = 0)$

$$\frac{\partial \psi}{\partial r}(0, \Phi, z, t) = 0; \quad \frac{\partial \phi}{\partial r}(0, \Phi, z, t) = 0; \tag{3.6}$$

  On the surface $(r = R)$, due to the cross-flow, heat transfers from bars to the surroundings. The heat transfer coefficient for the rotating cylinder is taken as an average heat transfer coefficient. For the non-rotating bar, the heat transfer coefficient varies along the surface of the cylinder in the circumferential direction.

$$\frac{\partial \psi}{\partial r}(R, \Phi, z, t) - \frac{h_1}{k_1}\psi(R, \Phi, z, t) = 0; \tag{3.7}$$

$$\frac{\partial \phi}{\partial r}(R, \Phi, z, t) - \frac{h_2(\Phi)}{k_2}\phi(R, \Phi, z, t) = 0; \tag{3.8}$$

- In circumferential (Φ-) direction

  - Temperature continuity

$$\psi(r, 0, z, t) = \psi(r, 2\pi, z, t) \tag{3.9}$$

$$\phi(r, 0, z, t) = \phi(r, 2\pi, z, t) \tag{3.10}$$

  - Heat flux continuity

$$\frac{\partial \psi}{\partial \Phi}(r, 0, z, t) = \frac{\partial \psi}{\partial \Phi}(r, 2\pi, z, t) \tag{3.11}$$

$$\frac{\partial \phi}{\partial \Phi}(r, 0, z, t) = \frac{\partial \phi}{\partial \Phi}(r, 2\pi, z, t) \tag{3.12}$$

- At the interface, the dissipation of heat generated is modelled as [25]

$$-k_1 \frac{\partial \psi}{\partial z}(r,\Phi,0,t) + \mu p(r)\omega r = -k_2 \frac{\partial \phi}{\partial z}(r,\Phi,0,t) \tag{3.13}$$

where μ is the coefficient of friction, p is the pressure applied and ω is the angular speed of the rotating bar.

Using the non-dimensional parameters

$$\tau = \frac{\alpha_1 t}{R^2}, \quad \rho = \frac{r}{R}, \quad \xi = \frac{z}{R}, \quad r_a = \frac{\alpha_2}{\alpha_1}$$

$$r_k = \frac{k_2}{k_1}, \quad B_1 = \frac{h_1 R}{k_1}, \quad B_2 = \frac{h_2 R}{k_2}$$

we get

$$\frac{\partial \psi}{\partial \tau} = \alpha_1 \left[\frac{1}{\rho} \frac{\partial}{\partial \rho} \left(\rho \frac{\partial \psi}{\partial \rho} \right) + \frac{1}{\rho^2} \frac{\partial^2 \psi}{\partial \Phi^2} + \frac{\partial^2 \psi}{\partial \xi^2} \right] \tag{3.14}$$

$$\frac{\partial \phi}{\partial \tau} = \alpha_1 \left[\frac{1}{\rho} \frac{\partial}{\partial \rho} \left(\rho \frac{\partial \phi}{\partial \rho} \right) + \frac{1}{\rho^2} \frac{\partial^2 \phi}{\partial \Phi^2} + \frac{\partial^2 \phi}{\partial \xi^2} \right] \tag{3.15}$$

The non-dimensionalized initial and boundary conditions :

$$\psi(\rho,\Phi,\xi,0) = 0; \quad \phi(\rho,\Phi,\xi,0) = 0; \tag{3.16}$$

$$\frac{\partial \psi}{\partial \xi}(\rho,\Phi,\infty,\tau) = 0; \quad \frac{\partial \phi}{\partial \xi}(\rho,\Phi,-\infty,\tau) = 0; \tag{3.17}$$

$$\frac{\partial \psi}{\partial \rho}(0,\Phi,\xi,\tau) = 0; \quad \frac{\partial \phi}{\partial \rho}(0,\Phi,\xi,\tau) = 0; \tag{3.18}$$

$$\frac{\partial \psi}{\partial \rho}(1,\Phi,\xi,\tau) - B_1 \psi(1,\Phi,\xi,\tau) = 0; \tag{3.19}$$

$$\frac{\partial \phi}{\partial \rho}(1,\Phi,\xi,\tau) - B_2(\Phi) \phi(1,\Phi,\xi,\tau) = 0; \tag{3.20}$$

$$\psi(\rho,\Phi,0,\tau) = \phi(\rho,\Phi,0,\tau) \tag{3.21}$$

Table 3.1: Constants for the Circular Cylinder in Cross Flow

Re_D	C	m
0.4-4	0.989	0.330
4-40	0.911	0.385
40-4000	0.683	0.466
4000-40,000	0.193	0.618
40,000-400,000	0.027	0.805

$$\psi(\rho, 0, \xi, \tau) = \psi(\rho, 2\pi, \xi, \tau) \tag{3.22}$$

$$\phi(\rho, 0, \xi, \tau) = o(\rho, 2\pi, \xi, \tau) \tag{3.23}$$

$$\frac{\partial \psi}{\partial \Phi}(\rho, 0, \xi, \tau) = \frac{\partial \psi}{\partial \Phi}(\rho, 2\pi, \xi, \tau) \tag{3.24}$$

$$\frac{\partial \phi}{\partial \Phi}(\rho, 0, \xi, \tau) = \frac{\partial o}{\partial \Phi}(\rho, 2\pi, \xi, \tau) \tag{3.25}$$

$$\frac{\partial \psi}{\partial \xi}(\rho, \Phi, 0, \tau) + \mu p \omega R^2 = -r_k \frac{\partial o}{\partial \xi}(\rho, \Phi, 0, \tau) \tag{3.26}$$

Because of the nature of governing equations and the boundary conditions, it is extremely difficult to get an analytical solution for the problem under consideration. So, a numerical technique is applied to solve the above equations.

The Nusselt number variation along the periphery of the cylinder is taken from a published article [24]. The values of the Nusselt number are then extrapolated using the following equation [26],

$$\overline{Nu}_D = C Re^m{}_D Pr^{1/3} \tag{3.27}$$

where C and m are tabulated in Table 3.1. The variation of the Nusselt number along the periphery of the rotating cylinder for various Reynolds number is shown in Fig. 3.2.

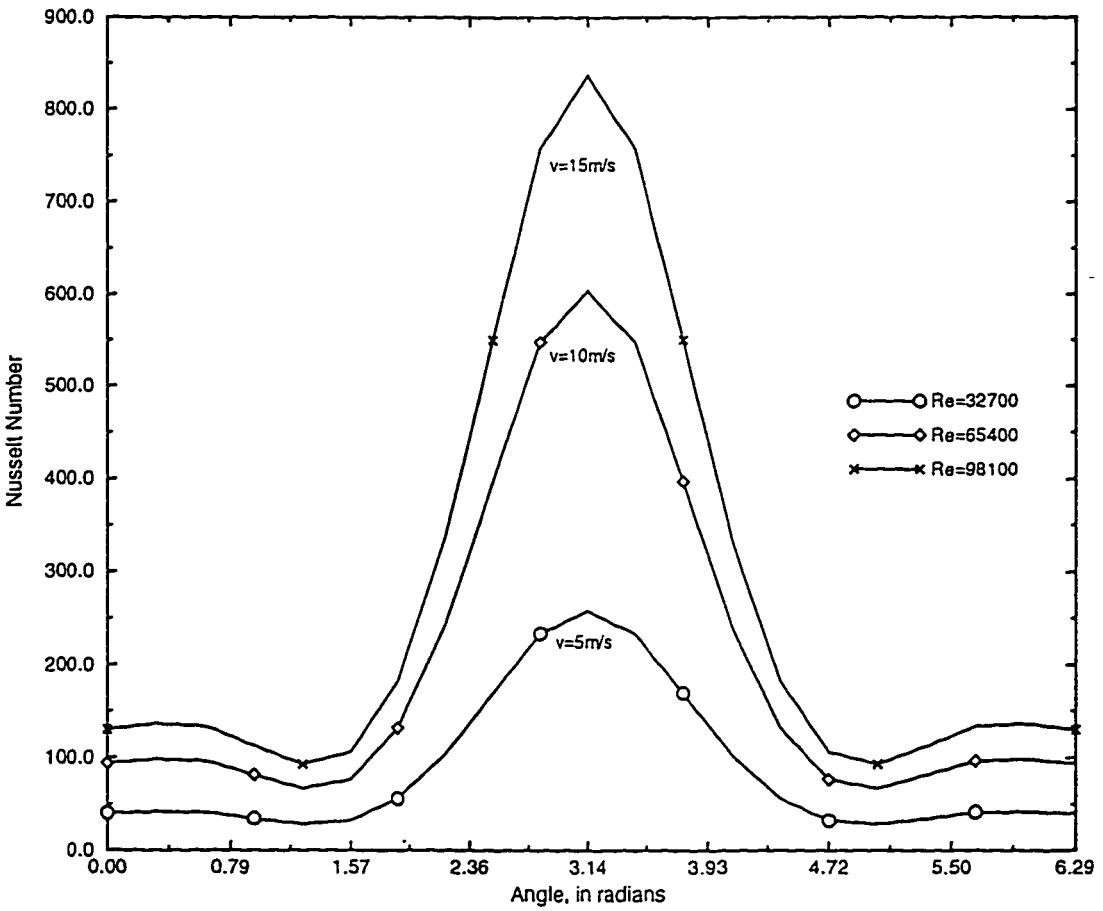

Figure 3.2: Nusselt number variation on the surface of a stationary cylinder

3.2 Finite Difference Formulation

Determination of the temperature distribution numerically dictates that an appropriate conservation equation be written for each of the nodal points of unknown temperature. The resulting set of equations may then be simulaneously solved for the temperature at each node. These simultaneous equations can be obtained either by approximating the partial differential equations or by using the energy balance method. In this formulation, these equations are obtained by using the energy balance method.

3.2.1 Energy Balance Method

The finite difference equation for a node may also be obtained by applying conservation of energy to a control volume about the nodal region. Since the actual direction of heat flow (into or out of the node) is often unknown, it is convenient to formulate the energy balance by assuming that all the heat flow is in to the node. Such a condition is, of course, impossible, but if the rate equations are expressed in a manner consistent with this assumption, the correct form of the finite-difference equation is obtained.

A general form of the energy conservation requirement may then be expressed on a rate basis as [20]

$$\dot{E}_{in} + \dot{E}_g - \dot{E}_{out} = \frac{dE_{st}}{dt} \equiv \dot{E}_{st} \tag{3.28}$$

The descritization of the problem under consideration using energy balance is divided into 3 parts. First, nodes across the cross-section of the interface of the two surfaces are descritized. Secondly, nodes in Domain I are descritized and at last Domain II is considered. Descritization of nodes across the interface is discussed in the subsequent sections. Descritization of the nodes in Domain I and Domain II can be obtained by a similar analysis.

Interface

The center node is given special attention due to its unique nature. Nodal equation for the nodes surrounding the center are treated separately because all of these nodes interact only with the center node in one direction and with different nodes in the other directions as depicted in the Figure 3.3. A general nodal equation is developed for the interior nodes (Equation 3.31). At the surface of the interface, an average of heat transfer coefficients (h_1 and h_2) is taken to calculate the heat transfer coefficient. The descritization of the surface node (at interface) is shown in the Figure 3.5 and the nodal equation is given by Equation 3.32.

Explicit finite difference method is used in obtaining the nodal equations. Central difference approximation is used for the spatial coordinates and forward difference scheme is used for the time domain. Equal size grid elements are taken in radial and axial directions ie., $\Delta r = \Delta z$.

Center Node:

The control volume, in deriving a nodal equation for the center node, is a cylinder of radius dr with dz as its thickness as shown in Figure 3.3. There is no heat generation at the center node because it does not have angular velocity. So the temperature rise of the center node is due to the heat input from the surrounding nodes. Applying the Eqn. 3.28 to the center node, the nodal equation for the center node at interface of the two bars obtained is given by Eqn. 3.29.

$$\Theta'_{(0,j,k)} = \Theta_{(0,j,k)} \left\{1 - 2\,\frac{\Delta\tau}{(\Delta\rho)^2}\,(1+r_k)\left(1 + \frac{\Delta\varphi}{\pi}\right)\right\} + 2\,\frac{\Delta\tau}{(\Delta\rho)^2}\,\frac{r_a}{(r_a+r_k)} *$$

$$\left\{\psi_{1,1,1} + r_k\phi_{1,1,1} + (1+r_k)\frac{\Delta\phi}{\pi} * \sum_{k=2}^{p}\Theta_{0,2,k} + \left(\frac{\mu P\omega R^2}{2\,k_1}\right)\ (\Delta\rho)^2\right\} \quad (3.29)$$

Nodal Equation for Surrounding Nodes to the Center Node

The nodes next to the center node interact with each other in the peripheral direction but all of them interact with the center node in the radial direction. The nodal equation for these nodes is given by Eqn. 3.30

$$\Theta'_{0,2,k} = \left\{1 - \frac{2r_a}{r_a+r_k}\,\frac{\Delta\tau}{(\Delta\rho)^2}\,(1+r_k)\left(2 + \frac{1}{(\Delta\varphi)^2}\right)\right\}\Theta_{0,2,k} + \frac{2r_a}{r_a+r_k}\,\frac{\Delta\tau}{(\Delta\rho)^2} *$$

$$\left\{(1+r_k)\left[\frac{1}{4}\,(\Theta_{0,1,1} + 3\Theta_{0,3,k}) + \frac{1}{2(\Delta\varphi)^2}(\Theta_{0,2,k-1} + \Theta_{0,2,k+1})\right] +\right.$$

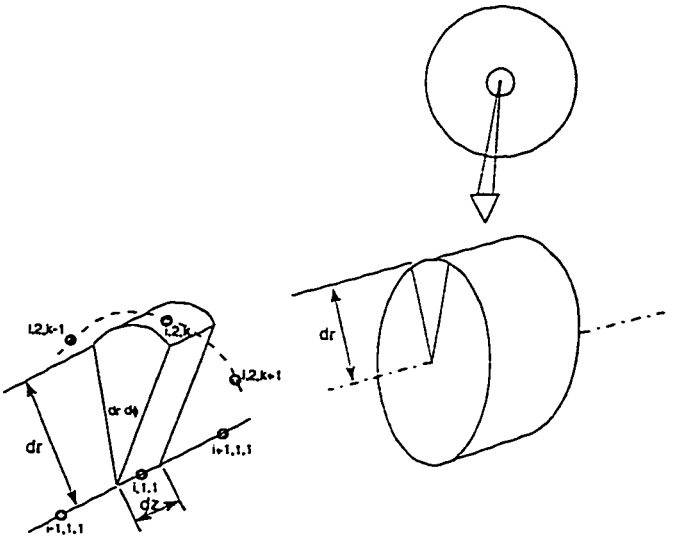

Figure 3.3: Descritization of the Center Node

$$(\psi_{1,2,k} + r_k\phi_{1,2,k}) + \frac{\mu P\omega R^2}{k_1}(\Delta\rho)^2\Big\} \tag{3.30}$$

General Node

Consider applying Equation 3.28 to the control volume about the interior node i, j, k of Figure 3.4. This node is influenced by the heat conduction from its neighboring nodes, (two each in radial direction, axial direction, peripheral direction). Taking the heat coming into the control volume as a positive quantity the nodal equation obtained is given by Equation 3.31.

$$\Theta'_{(0,j,k)} = \Theta_{(0,j,k)} \left\{1 - 2\,\frac{\Delta\tau}{(\Delta\rho)^2}\,\frac{r_a}{(r_a + r_k)}\,(1 + r_k)\left(2 + \frac{1}{(j-1)^2(\Delta\phi)^2}\right)\right\} +$$

$$\frac{2r_a}{(r_a+r_k)}\frac{\Delta\tau}{(\Delta\rho)^2}\left\{\psi_{1,j,k}+r_k\phi_{1,j,k}+\left(\frac{1+r_k}{2}\right)\left[\left(1-\frac{1}{2(j-1)}\right)\Theta_{0,j-1,k}+\right.\right.$$

$$\left.\left(1+\frac{1}{2(j-1)}\right)\Theta_{0,j+1,k}\right]+\left(\frac{1+r_k}{2}\right)\frac{1}{(j-1)^2(\Delta\phi)^2}\left(\Theta_{0,j,k-1}+\Theta_{0,j,k+1}\right)+$$

$$\left.\left(\frac{\mu P\omega R^2}{k_1}\right)(j-1)(\Delta\rho)^2\right\} \tag{3.31}$$

Surface Node

The nodal equation for the node on the surface at the interface can be written as

$$\Theta'_{(0,n+1,k)} = \Theta_{(0,n+1,k)}\left\{1-4\frac{\Delta\tau}{(\Delta\rho)^2}\frac{r_a}{(r_a+r_k)}\left(\frac{1+r_k}{1-\frac{1}{4n}}\right)\left[(3-\frac{1}{n})+\left(\frac{\Delta\rho}{\Delta\phi}\right)^2+\right.\right.$$

$$\left.\left.\frac{(B_1+r_k)B_2}{(1+r_k)}\Delta\rho\right]\right\}+2\frac{r_a}{(r_a+r_k)}\frac{\Delta\tau}{(\Delta\rho)^2}\{4(\psi_{1,n+1,k}+r_k\,\phi_{1,n+1,k})+$$

$$\left(\frac{\Delta\rho}{\Delta\phi}\right)^2\left(\frac{1+r_k}{1-\frac{1}{4n}}\right)(\Theta_{0,n+1,k+1}+r_k\,\Theta_{0,n+1,k-1})+$$

$$2(1+r_k)\left(\frac{1-\frac{1}{2n}}{1-\frac{1}{4n}}\right)\Theta_{0,n,k}+2\left(\frac{\mu P\omega R^2}{k_1}\right)n(\Delta\rho)^2\Big\} \tag{3.32}$$

3.2.2 Stability Analysis

The accuracy of the explicit finite-difference solution depends upon the size of the element in each direction and the increment in time for each iteration. The stability

criteria obtained is valid for any type of material combinations, ie., either both the bars are of the same materials or of different materials but holds good only when the bar with lower conductivity is rotating. The equation for the surrounding nodes to the center node at interface (Equation 3.30) requires the minimum time increment value for stability of the solution. Therefore, the time increment ($\Delta\tau$) value can be found from the following equation

$$\Delta\tau \leq \frac{(\Delta\rho)^2}{2\left(2+\frac{1}{(\Delta\Phi)^2}\right)} \tag{3.33}$$

From Equation 3.33, the time step can be found given the size of the grid in the radial (or axial) direction and in the peripheral direction. But the effect of the value of $\Delta\Phi$ is negligible making Eqn. 3.33 more vulnerable to the size of the element in the radial (or axial) direction. So, smaller the grid size, smaller is the timestep ($\Delta\tau$).

Different stability criteria is needed when the bar with lower conductivity is kept stationary. The timestep in this case can be obtained from the general nodal equation at the interface (Eqn. 3.31).

$$\Delta\tau \leq \frac{(r_a+r_k)\,(\Delta\rho)^2}{2r_a\,(1+r_k)\left(2+\frac{1}{(\Delta\Phi)^2}\right)} \tag{3.34}$$

3.2.3 Method of Solution

A computer program is developed to solve the above algebraic equations. It consists of various subroutines interacting with the MAIN program. The algorithm is shown

in the Fig. 3.6. In the main program, the variables such as number of nodes in each direction, the jet velocity, the angular velocity, the pressure, etc, have to be defined. The value of the time-step is determined from the stability criteria. The calculation procedure is as follows:

1. The calculations starts by computing the center node temperature at the interface.

2. Then the program steps forward in the radial direction by an increment of Δr and computes the temperatures of the nodes in the circumferential direction at that radius.

3. Thus, the calculation procedure continues for all the radii including the surface.

4. Then the program steps forward in the axial direction by a distance Δr and compute the nodal temperatures at that cross-section as described in steps (1), (2), (3) and (4).

5. After determining all the nodal temperatures for the present time step, the program marches into the time domain by an amount determined by the stability. The temperatures calculated for the present time step are utilised for the next time-step. And the steps described above are repeated until the plastic range temeperatures are obtained in one of the two bars.

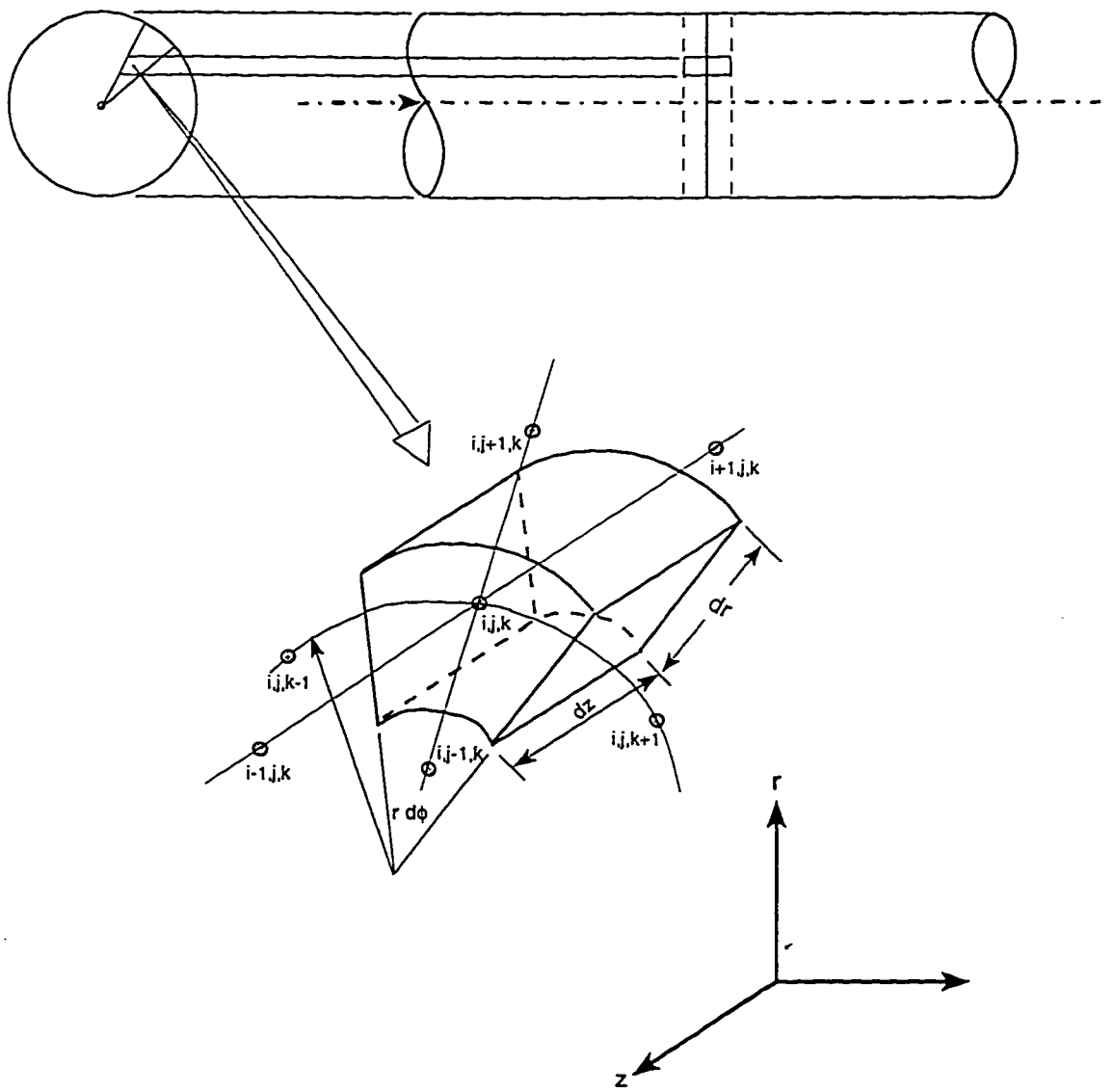

Figure 3.4: Descritization of the General Node

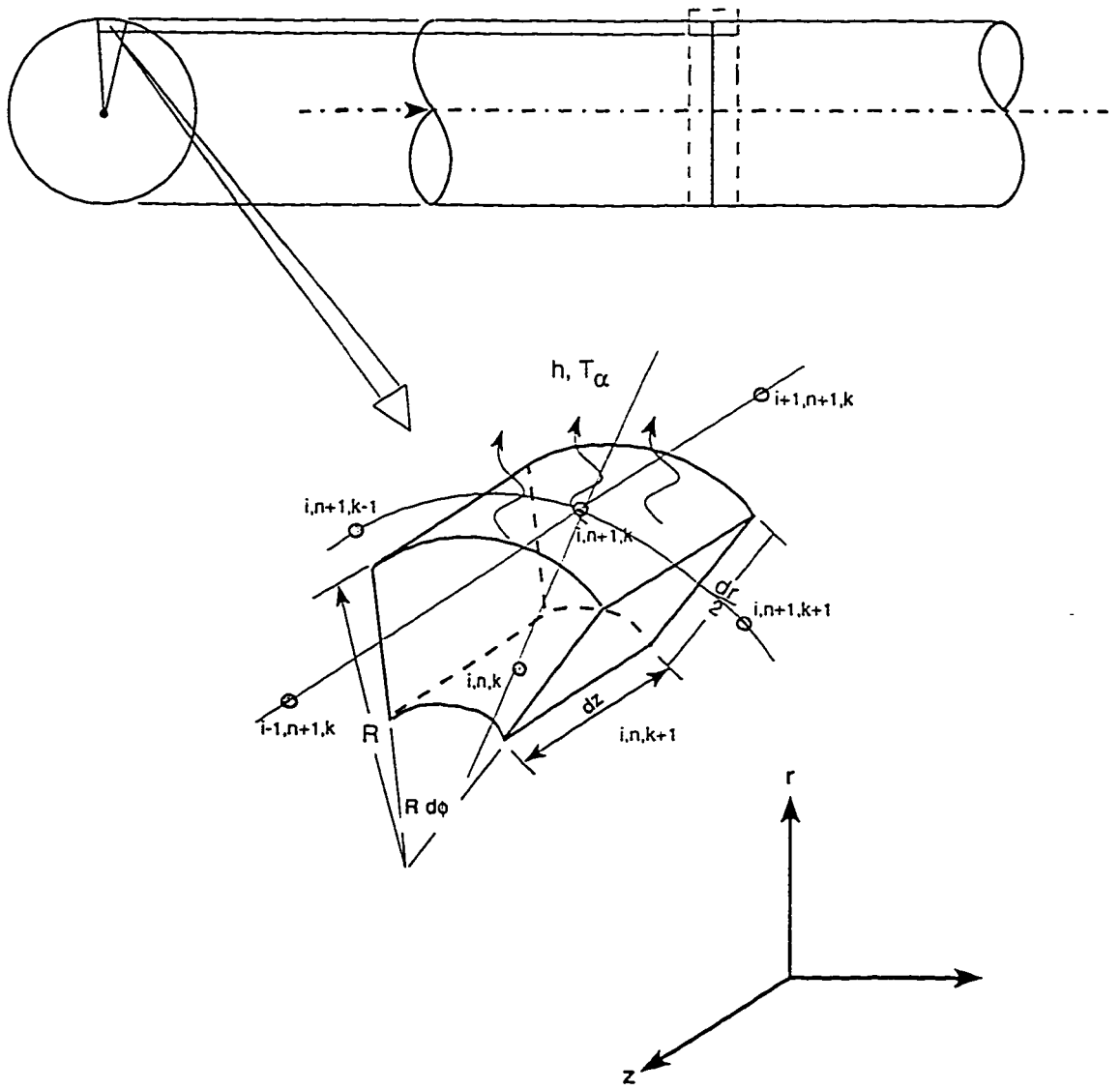

Figure 3.5: Descritization of the Surface Node

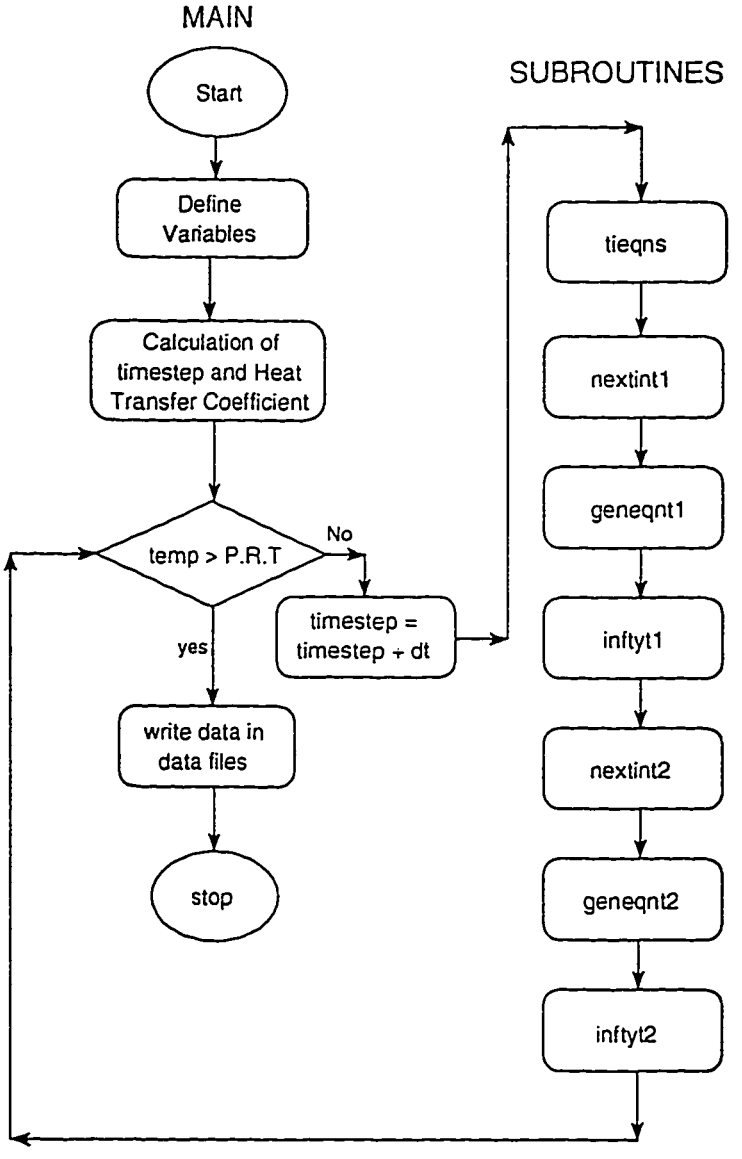

Figure 3.6: Algorithm of the computer program

Chapter 4

Results and Discussion

Three material combinations are chosen for the results of the analysis. These are steel-steel, steel-aluminum and steel-copper. The results obtained for steel-copper are presented first and then the results for steel-steel and finally the analysis for steel-aluminum case are discussed. In each of the cases, temperature profiles are given in circumferential, radial and axial directions for different angular speeds and for different jet velocities. Temperature rise with time at the back and front stagnation points are also discussed. A grid test is also performed to prove the accuracy of the considered grid size.

4.1 Accuracy

A grid test has been done to get an optimum grid size to obtain accurate results with minimum computation time. The grid test is done using the steel-steel friction weld with an rpm of 2000 and a jet velocity of 10 m/s and at 10.0 s. The back stagnation point on the surface at the interface is selected to show the effect of the

number of nodes in each direction.

Since the distance between the two nodes (Δr) is determined by the number of nodes in the radial direction, a ratio has to be maintained between the number of nodes in the axial direction to the nodes in the radial direction in order to reduce the end effect of the boundary condition at the end of the bar. The effect of this ratio is shown in Figure 4.1. There is a sudden decline in temperature by about 16.0 °C when this ratio is increased from 2.0 to 2.66. And the temperature does not change considerably when this ratio is further increased to 3.0. So, to have a compromise between the accuracy and the computation time, a ratio of 2.66 (ie., nodes in axial direction, m=40, nodes in radial direction, n=15) is selected for steel-steel case. For steel-copper and steel-aluminum cases, considering the high conductivity of copper and aluminum, a ratio of 3.33 (ie., m=50, n=15) is selected to reduce the end effect of the boundary condition at end of the bars. Figure 4.2 shows the temperature at the back stagnation point on the surface of a steel-steel weld at interface and at 10.0 s with the number of nodes on the x-axis. There is a large variation in temperature when the number of nodes in the axial direction are increased from 20 to 40 keeping the nodes in the radial and circumferential directions as 15 and 21 respectively. This variation is negligible when the nodes in the axial direction are further increased. So,the number of nodes in the axial direction are considered as 40 when the nodes in the radial direction are 15, thus keeping a ratio of 2.66 between them. For steel-copper and steel-aluminum combinations, 50 nodes are considered

in the axial direction to reduce the end effect of the boundary condition.

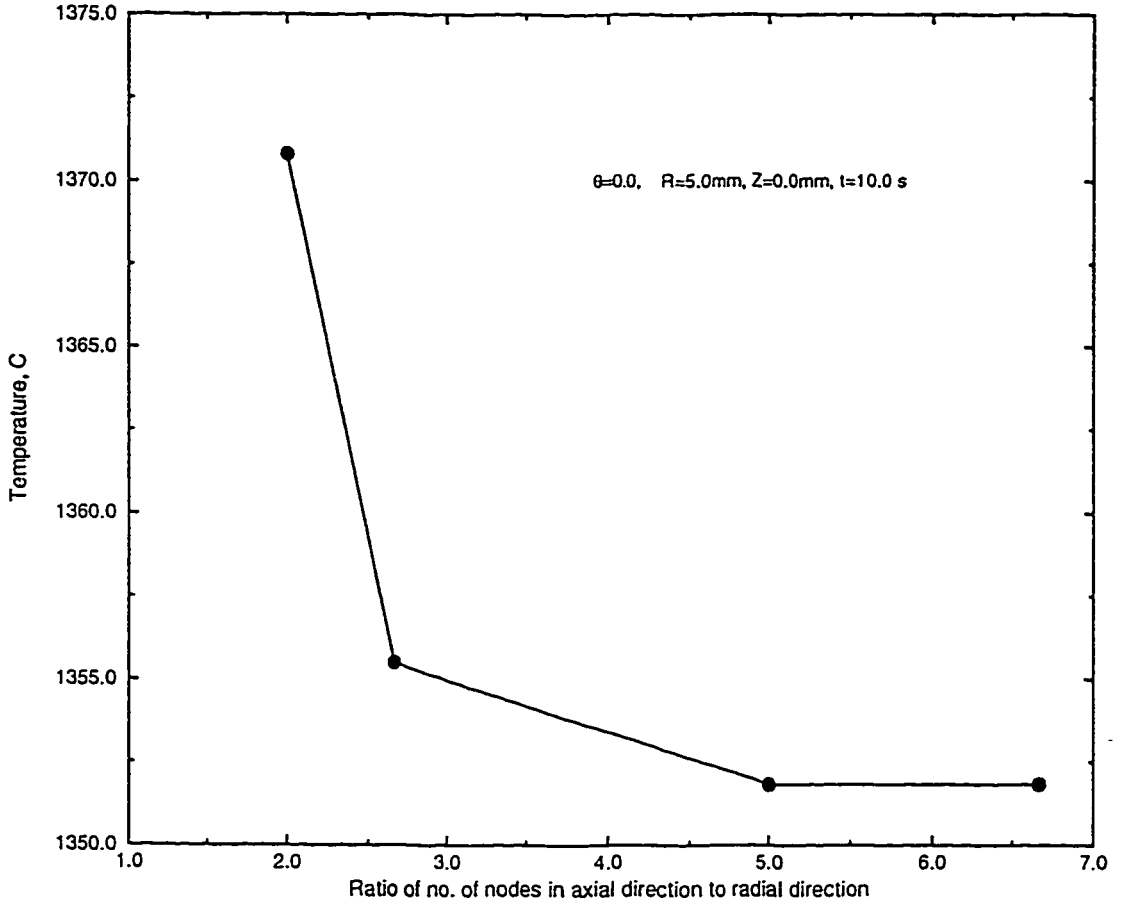

Figure 4.1: Effect of the ratio of the number of nodes in axial direction to the radial direction on the temperature of the back stagnation point on the surface at interface of a steel-steel friction weld with 15 nodes in radial direction.

In the circumferential direction, the variation in temperature is about 15 °C when the number of nodes is increased from 15 to 21 keeping the nodes in radial and axial direction as 15 and 40 respectively. But this difference is negligible when a further increase in number of nodes in circumferential direction is considered.

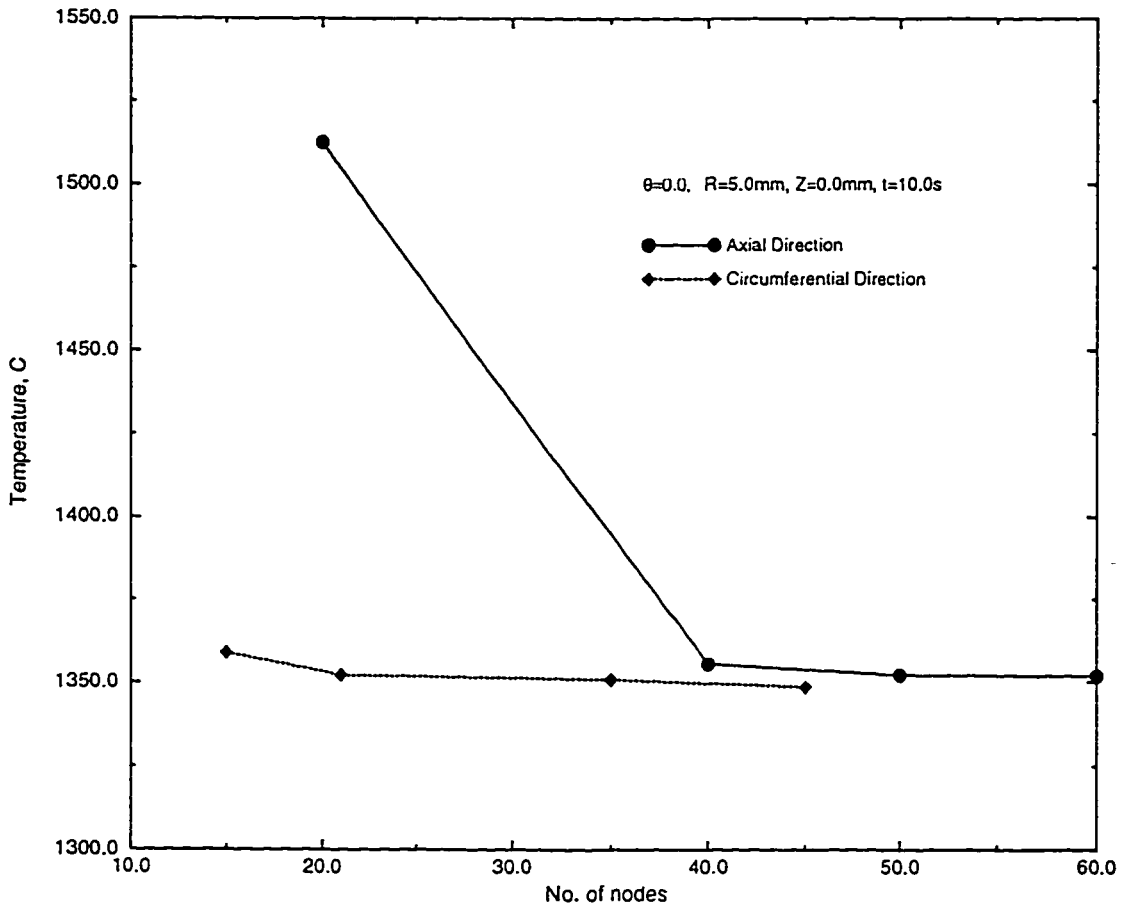

Figure 4.2: Effect of increasing the number of nodes in axial and circumferential directions on the temperature back stagnation point on the surface at interface of a steel-steel friction weld.

4.2 Steel-Copper

The grid size used for this case is 15 × 21 × 50. Large number of nodes in the axial direction are taken to reduce the end effect of the boundary conditions at both ends of the bars on the accuracy of temperature profiles in the vicinity of the interface. Two angular speeds and three jet velocities are used for the comparison of the results.

4.2.1 Effect of Jet Velocity

Case 1: RPM = 2500

Figure 4.3 shows the circumferential temperature profiles on the surface for an rpm of 2500 with different jet velocities at 11.0 s. The temperature reaches around 1225 °C within 11.0 s when a jet velocity of 5 m/s is used. A large decrease in temperature occurs when the jet velocity is increased to 10 m/s. The decrease in temperature is due to the increase in cooling effect. Temperature of about 800 °C is reached for the same time of 11.0 s when the jet velocity is further increased to 15 m/s. The profiles are symmetric in the circumferential direction because the jet flow profile taken was a symmetric one. The point of jet incidence is at $\theta = \pi$, where the lowest temperature occurs for each profile. The difference in temperature at two points, ie., $\theta = 0.0$ and $\theta = \pi$, increases as the jet velocity increases.

Figure 4.4 shows the comparison of temperature profiles in circumferential direc-

tion at mid-radius (r=2.5 mm). The difference between the values of temperature in Figure 4.3 Figure 4.4 is due to the fact that the heat generation is directly proportional to the radius. So, the heat generation at surface is much higher than that of at mid-radius.

Figure 4.5 shows the comparison of the radial temperature profiles at $\theta = 0.0$, where the heat transfer coefficient is minimum, for an rpm of 2500 and for different jet velocities. Due to the low heat transfer coefficient, higher temperatures are obtained in this direction. At 11.0 s, the profiles are similar but they differ in temperature values for different jet velocities. The large gap in profiles for a jet velocity of 5 m/s and 10 m/s is due to the increase in cooling effect. Moreover, the effect of heat generation was much more pronounced than the heat taken away by the jet flow when a jet velocity of 5 m/s is used. Figure 4.6 shows the comparison of the radial temperature profiles at the front stagnation point ($\theta = \pi$), where the heat transfer coefficient is maximum. Hence, the temperature values are considerably lower than those of profiles in Figure 4.5, if they are compared individually.

Figure 4.7 shows the comparison of the axial temperature profiles on the surface at $\theta = 0.0$ at time t=11.0 s with an rpm of 2500 for different jet velocities. Interesting point to note here is the large difference in temperatures in each profile in Domain I and Domain II. Due to its low thermal conductivity, the temperature decreases more rapidly in steel bar in the axial direction when compared to that of the copper bar which has high thermal conductivity. The effect of higher jet velocities is again

pronounced at the interface (Z=0.0 mm) in this Figure that indicates the importance of careful selection of the proper jet velocity. Figure 4.8 shows the comparison of axial centerline temperature profiles with an angular speed of 2500 for different jet velocities. The values are much lower when the temperature profiles are compared with those of in Figure 4.7, again due to the direct proportionality of the heat generation to the radius.

Figure 4.10 shows the comparison of rise in temperature values at $\theta = 0.0$, Z=0.0 mm, and R=5.0 mm with time for an rpm of 2500 for different jet velocities. For a jet velocity of 5 m/s, the rise in temperature is much faster yielding a temperature of around 1200 °C in 11.0 s. With the increase in jet velocity to 10 m/s, it takes 20.0 s to reach a temperature of about 1170 °C. The increase in temperature early in the welding process is sharp and the profile became flat after 8.0 s, suggesting thata steady state temperature variation is being approached. For a jet velocity of 15 m/s, the temperature reached in 20 s is about 840 °C suggesting that it may not be possible to reach the plastic range temperature of 1200 °C.

Figure 4.9 shows the similar comparison of rise in temperature as that discussed for Figure 4.10 except at the location where $\theta = \pi$, Z=0.0 mm, and R=5.0 mm.

Case 2: RPM = 3000

Figure 4.11 shows the comparison of circumferential temperature profiles on the surface at 8.0 s for an rpm of 3000 with different jet velocities. Due to the increase

in rpm, the heat generation across the interface increases resulting reduction in time (to 8.0 s compared to 11.0 s when $\omega = 2500$). Higher temperatures can be noticed for the profiles with jet velocities of 10 m/s and 15 m/s when compared with those in Figure 4.3 which is due to the rate of heat generation. The same is the reason with Figure 4.12 when compared with Figure 4.4. Similar discussion can be made for Figures 4.13-4.16 comparing with Figures 4.5-4.8 respectively. Temperature rise at front and back stagnation points is much sharp in Figure 4.18 and Figure 4.17 when compared with Figure 4.10 and Figure 4.9 for a jet velocity of 5 m/s respectively. For a jet velocity of 10 m/s, it takes 17.0 s to reach a temperature of about 1200 °C. A steady-state profile is approached after 10 s for the profile with jet velocity of 15 m/s.

4.2.2 Effect of Angular Speed

Case 1: Jet Velocty = 5 m/s

Figures 4.19-4.25 show the effect of angular velocity at 8.0 s with a jet velocity of 5 m/s. The large variation in temperatures (of about 200 °C) results from the fact of increase in angular speed which results in increase in heat generation rate across the interface. Figure 4.19 and Figure 4.20 shows the comparison of circumferential temperature profiles on the surface and at mid-radius. Figure 4.21 and Figure 4.22 compares the radial temperature profiles at back and front stagnation points at

8.0 s. Figure 4.23 and Figure 4.24 shows the axial temperature profiles at back stagnation point on the surface and at the center respectively. In all the curves at 8.0 s, the profile for 3000 rpm has high temperature of about 1200 °C at the surface of interface when compared to the profile with 2500 rpm which has a temperature of around 1000 °C at same location. Figure 4.26 and Figure 4.25 shows the comparison of rise in temperature with time at front and back stagnation points on the surface at the interface.

Case 2: Jet Velocty = 10 m/s

Figures 4.27-4.33 show the comparison of temperature profiles for a jet velocity of 10 m/s at time 17.0 s. Similar discussion can be made as done for the case of 5 m/s with some exceptions. In Figure 4.27 and Figure 4.28, due to the increase in velocity and also due to longer exposure to the jet, the temperature difference between back and front stagnation points (ie., at $\theta = 0.0$ and $\theta = \pi$) is 50 °C which can be a considerable difference for steel-copper weld. Because of this difference, the copper bar may experience some thermal stresses after the completion of the weld and also solidification defects may occur. In Figure 4.34 and Figure 4.33 which show the rise the temperature at front and back stagnation points, the profile with rpm of 2500 is approaching to the steady-state nature after about 16.0 s.

Case 3: Jet Velocty = 15 m/s

Figures 4.35-4.41 show the comparison of temperature profiles for a jet velocity of 15 m/s and at time 20.0 s. Due to the increase in jet velocity, cooling effect increases and more time is needed to reach a desired temperature of about 1200 °C. Limitation of computation time allowed to run the program for 20.0 s for which the profile with rpm of 3000 reached around 1045 °C and the profile with rpm of 2500 rpm reach around 875 °C. Slightly higher temperature difference occurs between the front and back stagnation points as the rpm increases as shown in Figure 4.35. Similar discussion can be made as above for other Figures with a jet velocity of 15 m/s.

4.3 Steel-Steel

For this combination of materials diffusion of heat is slow because of low conductivity and hence less number of nodes are considered in the axial direction. The grid size used in this case is 15 × 21 × 40. Three angular velocities and three jet velocities are considered for the purpose of analysis.

4.3.1 Effect of Jet Velocity

Case 1: RPM = 2000

Figure 4.46 and Figure 4.47 shows the comparison of temperature profiles in the circumferential direction on the surface and at mid-radius respectively. At 10.0 s, the temperature difference in Figure 4.46 among the profiles for the three jet velocities, namely 5 m/s, 10 m/s and 15 m/s, is of the range of about 350 °C at the back stagnation point and about 500 °C at the front stagnation point where the heat transfer coefficient has its maximum value. These large difference in the temperature values is attributed to the low thermal conductivity of steel. The effect of the increase in jet velocity can be seen when the profile for a jet velocity of 5 m/s is compared with that of 15 m/s. The temperature difference between the front and back stagnation points ($\theta = \pi$ and $\theta = 0.0$) is about 125 °C for 5 m/s and this difference increases to about 210 °C for 10 m/s and 240 °C for a jet velocity of 15 m/s. At mid-radius, as can be seen in Figure 4.47, the temperatures are lower because of the low heat generatrion and the temperature difference between the front and back stagnation points is also lower because of its distance from the point of incidence of the jet. The range of temperature difference is 50-100 °C with the smallest value for 5 m/s and the highest for the profile with jet velocity of 15 m/s.

Figure 4.48 and Figure 4.49 shows the comparison of temperature profiles in the radial direction at front and back stagnation points. A large variation in temperature

of about 340 °C can be observed in Figure 4.48 between the profiles with jet velocities 5 m/s and 10 m/s at 10.0 s. This difference is reduced between the profiles for 10 m/s and 15 m/s suggesting that if the jet velocity is further increased then the temperature profiles become closer and closer. The maximum temperature is on the surface at back stagnation point for the profile with the jet velocity of 5 m/s but it occurs at inner nodes for the profiles with jet velocities of 10 m/s and 15 m/s. This discrepancy is due to the increase in cooling effect at the surface with the increase in jet velocity. In Figure 4.49 which shows the comparison of the temperature profiles at front stagnation point at 10.0 s, the profiles have less slope than those of in Figure 4.48. This is due to the high heat transfer coefficient due to which more heat is taken away and the profiles become flat. Moreover, maximum temperature occurs far from surface in this direction at a radius of around 4.0 mm. This distance from the surface increase with the increase in jet velocity. There is no difference in temperature at center node.

Figure 4.50 and Figure 4.51 shows the comparison of the axial temperature profiles on the surface at back stagnation point and at center respectively at 10.0 s for different jet velocities. The temperature increased very sharp near the interface as can be seen from Figure 4.50. High temperatures occured in the vicinity of the interface conform the narrow heat-affected zone during the process. At 10.0 mm on either side of the interface, the temperature is about 200 °C which means that there is no effect of the boundary conditions at both ends on the interface temperature. The

temperature at the center of the interface is around 1300 °C. The low temperature at this point is due to the fact that there is no heat generation at this point. And the temperature rise at this point occurs only due to the contribution from the surrounding nodes to this center node.

Figure 4.52 and Figure 4.53 shows the comparison of rise of temperature at front and back stagnation points on the surface. As shown in Figure 4.52, a temperature of about 1450 °C is reached in 10.0 s for the profile with a jet velocity of 5 m/s. The other two profiles have a sharp rise in temperature in the initial phase of the process but after 8.0 s both the profiles are fast approaching a steady-state profile. Similar trend occured in Figure 4.53.

Case 2: RPM = 2500

Figures 4.54-4.61 show the the comparison of temperature profiles at 5.0 s in the order as discussed for the case with rpm of 2000. Similar discussion can be made as done for Figures 4.46 and 4.47 for Figures 4.54 and 4.55. In Figure 4.48, which shows the comparison of temperature profiles in the radial direction at back stagnation point, a difference of 400 °C is observed for the profile with a jet velocity of 5 m/s. This large difference in temperature is due to high increase in rate of heat generation with the increase in radius and partly due to the low conductivity of steel. This difference is subsequently decreased with the increase in jet velocity. At front stagnation point where the heat transfer coefficient is maximum, this difference

is reduced to about 300 °C for the profile with jet velocity of 5 m/s and this difference is further reduced to about 180 °C for the profile with jet velocity of 10 m/s and 130 °C for 15 m/s. And also the maximum temperature point occurs in the radial direction at around 4.5 mm with 5 m/s jet velocity and its distance from surface increased with the increase in jet velocity and the reason being again is the increase in cooling effect with the increase in jet velocity.

The temperature rise becomes sharper in Figures 4.58 and 4.59 when compared to Figures 4.50 and 4.51. This is due to the increase in heat generation rate with the increase in rpm. Sharp rise in temperature occured at front and back stagnation points on the surface as can be seen in Figures 4.60 and 4.61. Similar discussion can be made Figures 4.60 and 4.61 as done for Figures 4.52 and 4.53.

Case 3: RPM = 3000

Similar discussion applies for Figures 4.62-4.69 in the same order as done for Figures 4.46-4.53 with some exceptions. The slope of the curves in Figures 4.64 and 4.65 is high as compared to Figures 4.48 and 4.49 respectively. The reason being the high rate of heat generation and the small duration of the process. So, the difference in temperatures at the surface and at the center also increased. A difference of 200 °C is observed at front stagnation point and this difference is reduced at back stagnation point between the profiles with jet velocity of 5 m/s and 15 m/s.

4.3.2 Effect of Angular Speed

Case 1: Jet Velocity = 5 m/s

Figures 4.70-4.77 show the comparison of temperature profiles for three angular velocities, namely 2000, 2500 and 3000 rpm, at 3.0 s. In Figures 4.70-4.75, the difference in between the profiles is due to the increase in heat generation rate with the increase in rpm. In Figure 4.72, the difference in temperature values between the node at back stagnation point on the surface and the center node is about 500 °C for the profile with rpm of 3000 and this difference decreased to about 400 °C for rpm 2500 and it further reduced to approximately 360 °C for the profile with rpm of 2000. Similar trend is observed in at front stagnation point also in the radial direction as shown in Figure 4.73. Narrow high temperature zones occured near the interface even with the increase of rpm as can be noticed in Figure 4.74 and Figure 4.75. With the increase in rpm, the slope of profiles in Figure 4.76 and Figure 4.77 increases indicating the increase in rpm results in increase in heat generation rate.

Case 2: Jet Velocity = 10 m/s

With the increase in jet velocity, the difference in temperature values at $\theta = 0.0$ and $\theta = \pi$ increased due to the increase in cooling effect when Figure 4.70 and Figure 4.71 are compared to Figure 4.78 and Figure 4.79 respectively. There is also a considerable decrease in temperature difference between the center and at

back stagnation point when Figure 4.80 and Figure 4.81 are compared to Figure 4.72 Figure 4.73 respectively. Due to the increase in jet velocity cooling effect increases and hence the maximum temperature occurs inside the material and not on the surface as can be seen in Figure 4.81. This looks contrary to the direct proportionality of heat generation with radius. But the high jet velocity offsets the increase in heat generation rate with increase in radius. Similar discussion can be made for Figures 4.82-4.85 as done for Figures 4.74 and 4.77.

Case 3: Jet Velocity = 15 m/s

Again the difference in temperatures between points $\theta = 0.0$ and $\theta = \pi$, the back and front stagnation points on the surface, increased with the increase in jet velocity. This difference stands at 250 °C for profile with rpm of 3000 and it decreased with the decrease in rpm as 200 °C for 2500 rpm and 150 °C for 2000 rpm as can be seen in Figure 4.86. And a similar trend occured at mid-radius as shown in Figure 4.87. For Figures 4.88-4.93, a similar discussion can be made as done for Figures 4.80-4.85.

4.4 Steel-Aluminum

The grid size used for these combination of materials is 15 × 21 × 50. The large number of nodes considered in the axial direction is to reduce the effect of the

boundary condition at both ends of the bars, especially at end of the aluminum bar. Two angular velocities, namely 2000 and 2500, and three jet velocities, 5, 10 and 15 m/s are considered for the analysis.

4.4.1 Effect of Jet Velocity

Case 1: RPM = 2000

Figure 4.94 and Figure 4.95 show the effect of jet velocities for an rpm of 2000 after 4.0 s. As can be seen from both the Figures, the difference in temperature at $\theta = 0.0$ and $\theta = \pi$ (at back and front stagnation point) increases with the increase in jet velocity owing to the increase in the cooling effect. This difference is about 17 °C for the profile with jet velocity of 5 m/s and increased to 35 °C for a jet velocity of 10 m/s and further increased to 45 °C for the profile with a jet velocity of 15 m/s as shown in the Figure 4.94. Similar trend is observed at mid-radius with less temperature differences as shown in Figure 4.95.

Comparing each profile in the Figure 4.96 with Figure 4.97 at R=5.0 mm which gives the comparison of temperature profiles in radial direction at back and front stagnation points at 4.0 s, a difference of around 15 °C occurs for the profile with a jet velocity of 5 m/s and this difference is increased with the increase in jet velocity as about 35 °C for 10 m/s and about 45 °C for a jet velocity of 15 m/s.

Figures 4.98 and 4.99 can be explained with the same discussion as done for

Figures 4.7 and 4.8. Figures 4.100 and 4.101 show the comparison of temperature rise at back and fornt stagnation point on the surface at interface. For a jet velocity of 5 m/s, about 700 °C is reached in 4.0 s and it took 5.0 s and 7.0 s for 10 m/s and 15 m/s respectively to reach around 675 °C as shown in Figure 4.100. Similar trend is observed in Figure 4.101

Case 2: RPM = 2500

Similar discussion can be made for Figures 4.102-4.105 as was done for Figures 4.94-4.97. The effect of jet velocity has a minimum effect in the axial direction at back stagnation point on the surface, especially in the steel bar as a very small temperature differences occur among the three profiles for the three jet velocities. This is due to the very short duration welding cycle of 2.0 s. Similar trend occurs in Figure 4.107. In Figures 4.108 and 4.109, the temperature difference between the curves with jet velocities of 10 m/s and 15 m/s at 3.0 s is around 50 °C. This difference is attributed to the increase in the cooling effect with the increase in jet velocity.

4.4.2 Effect of Angular Speed

Figures 4.110-4.117 shows the comparison of temperature profiles with a jet velocity of 5 m/s for two angular speeds at 2.0 s. The large temperature difference between the profiles in Figures 4.110-4.114 is due to the increase rpm which increases the

heat generation rate. Figures 4.116 and 4.117 show the comparison of temperature rise at front and back stagnation point on the surface at interface. The temperature rises very sharply during the whole cycle because of low jet velocity.

A similar discussion can be made for Figures 4.118-4.133 as was done for Figures 4.19-4.42.

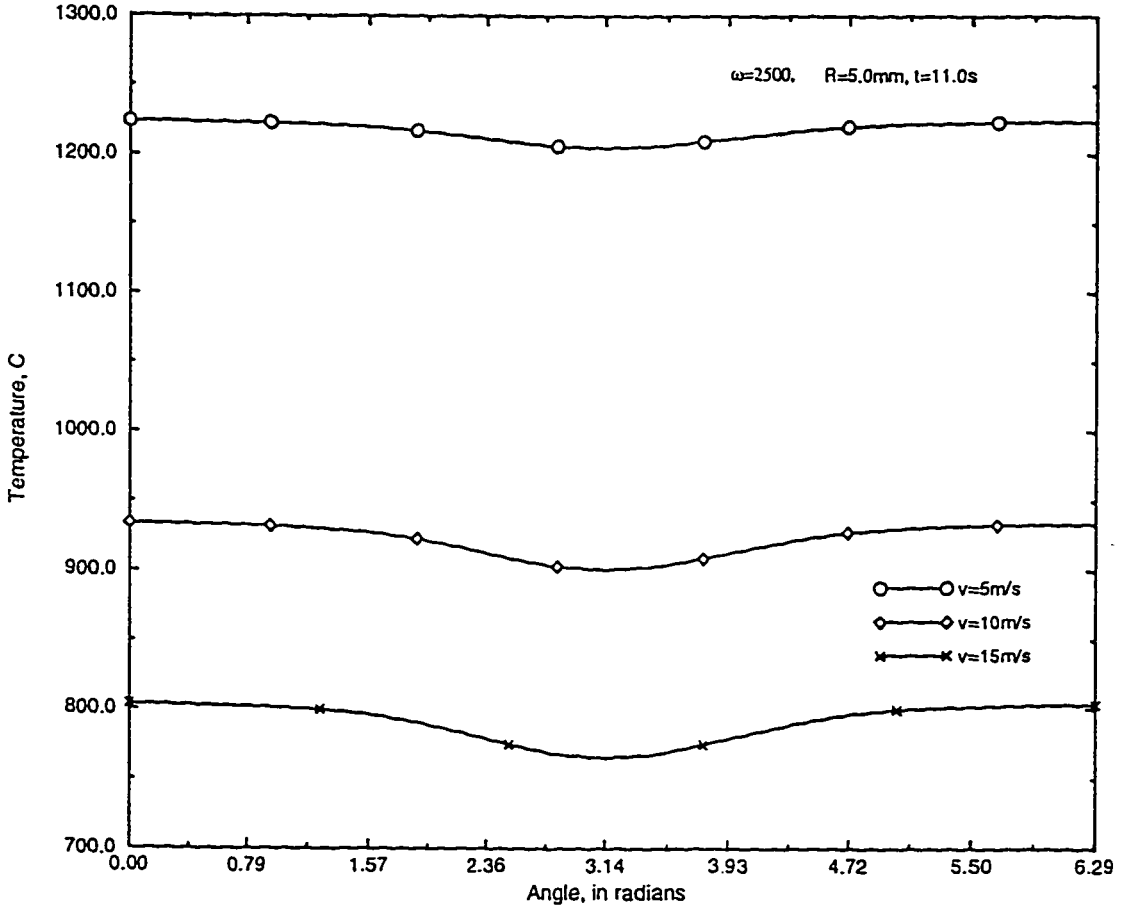

Figure 4.3: Comparison of circumferential temperature profiles on the surface of a steel-copper friction weld at time t=11.0 s with an angular speed of 2500 rpm for different jet velocities.

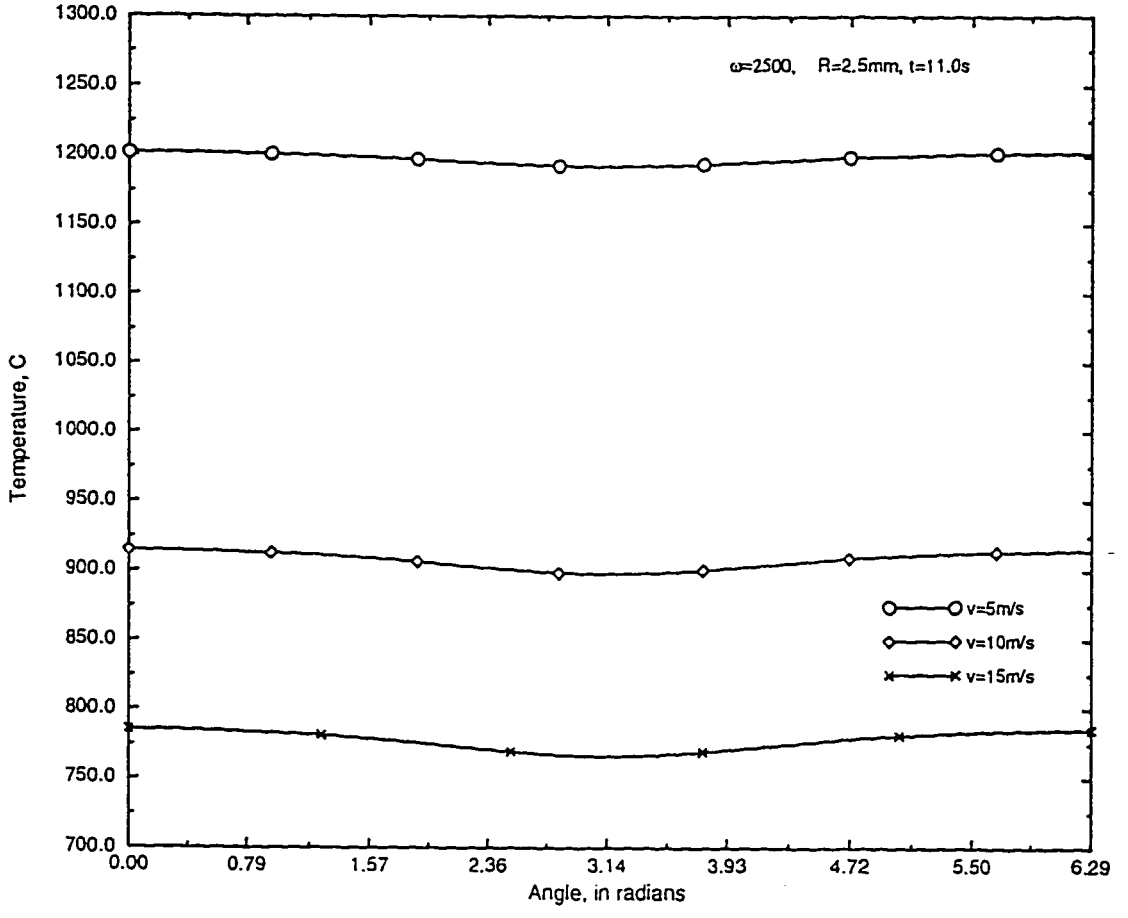

Figure 4.4: Comparison of circumferential temperature profiles at mid-radius of a steel-copper friction weld at time t=11.0 s with an angular speed of 2500 rpm for different jet velocities.

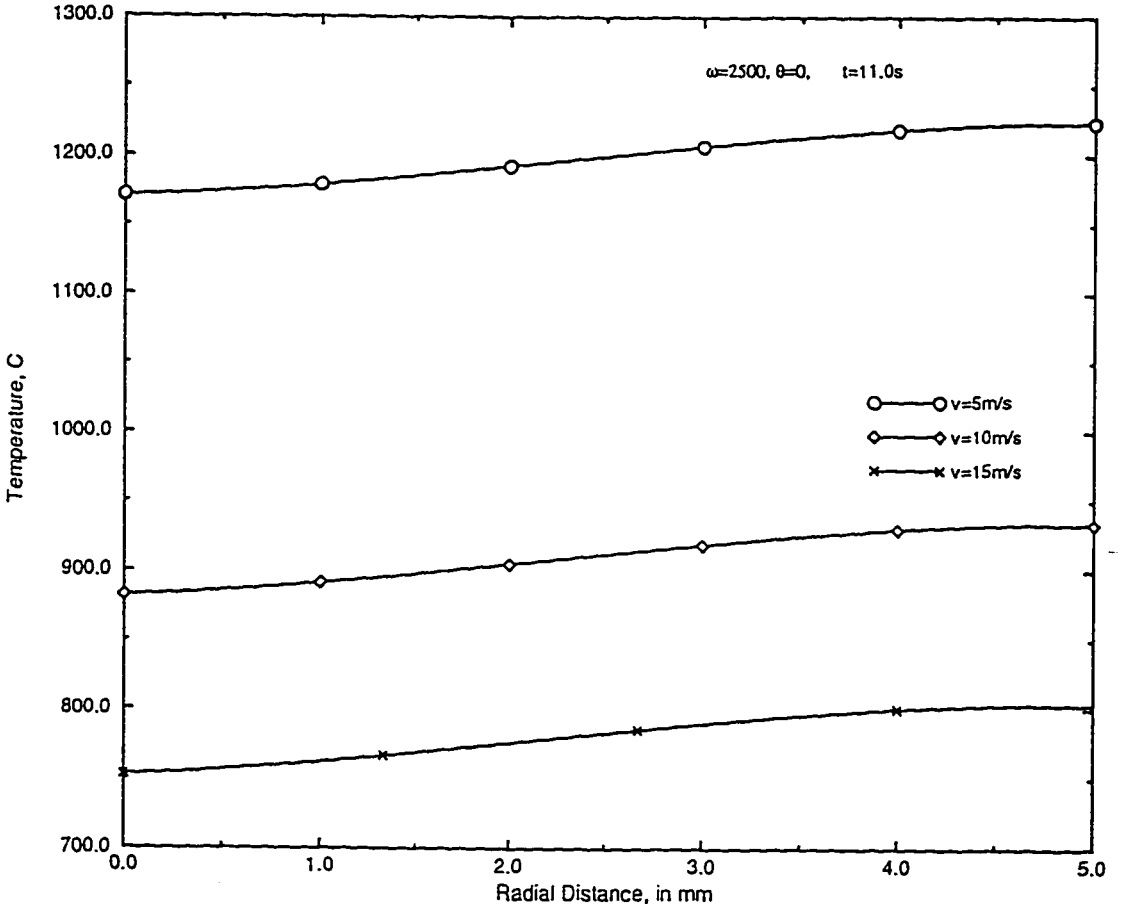

Figure 4.5: Comparison of radial temperature profiles at back stagnation point of a steel-copper friction weld at time t=11.0 s with an angular speed of 2500 rpm for different jet velocities.

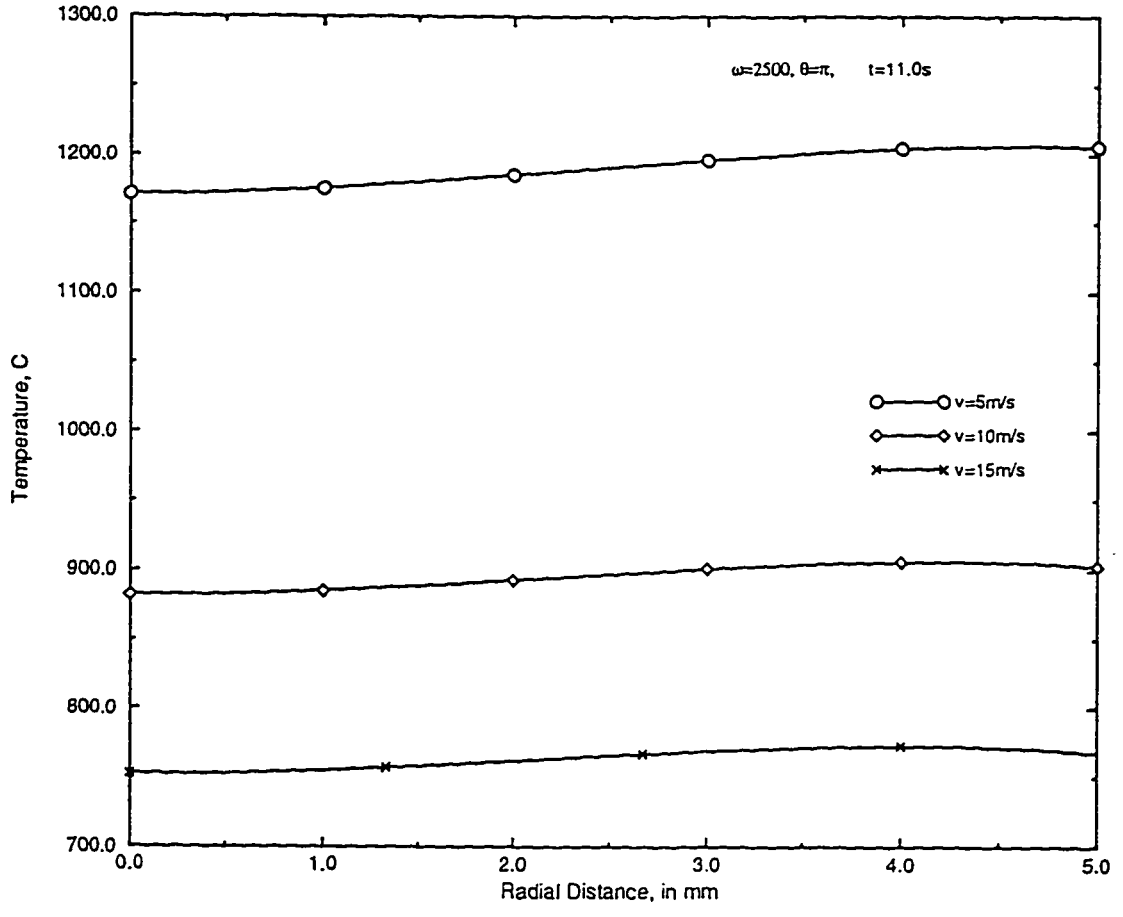

Figure 4.6: Comparison of radial temperature profiles at front stagnation point of a steel-copper friction weld at time t=11.0 s with an angular speed of 2500 rpm for different jet velocities.

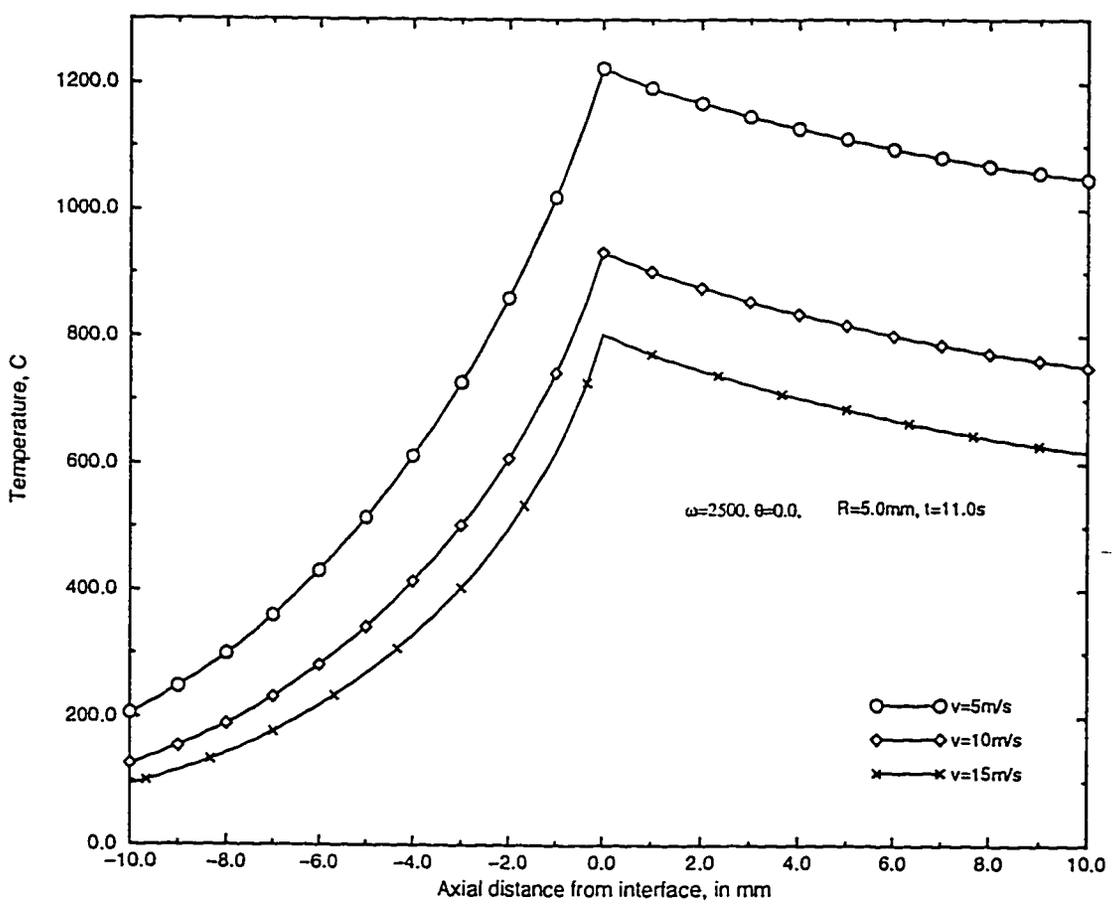

Figure 4.7: Comparison of axial temperature profiles on the surface along the back stagnation point of a steel-copper friction weld at time t=11.0 s with an angular speed of 2500 rpm for different jet velocities.

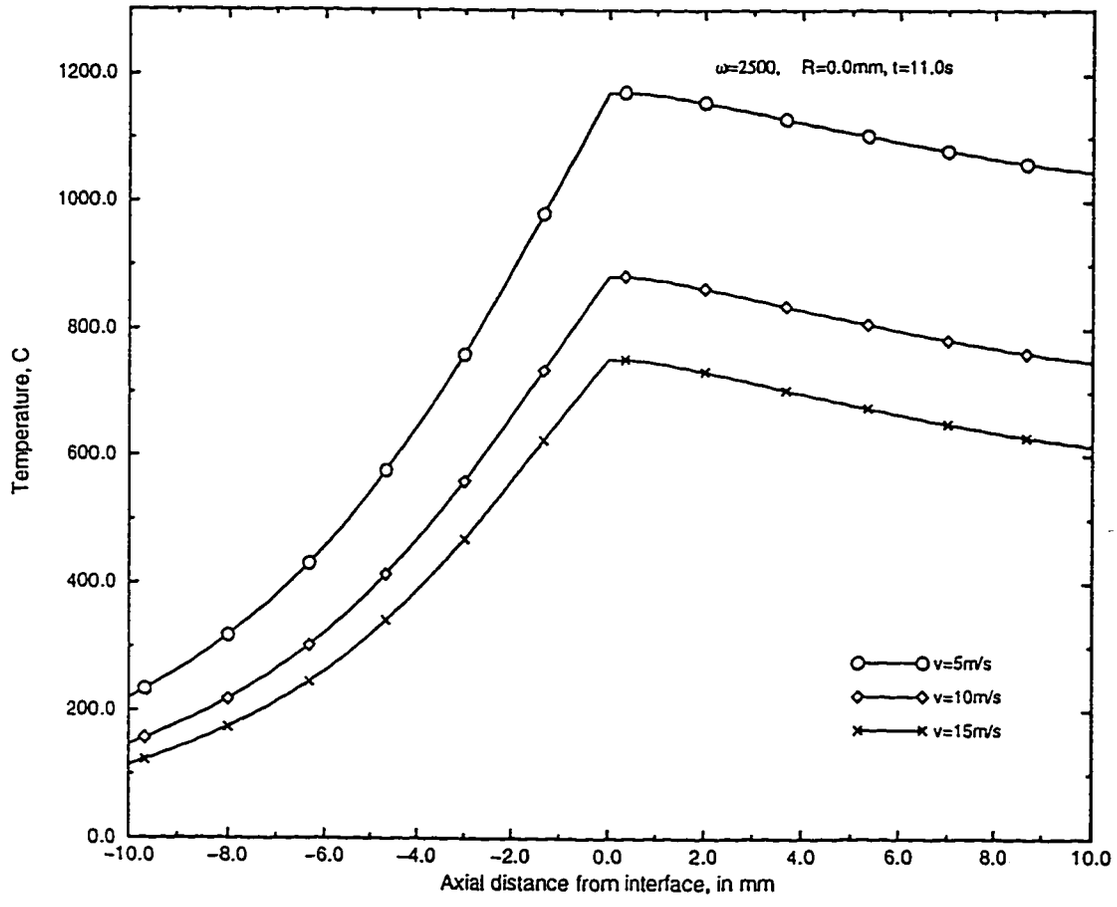

Figure 4.8: Comparison of centerline temperature profiles of a steel-copper friction weld at time t=11.0 s with an angular speed of 2500 rpm for different jet velocities.

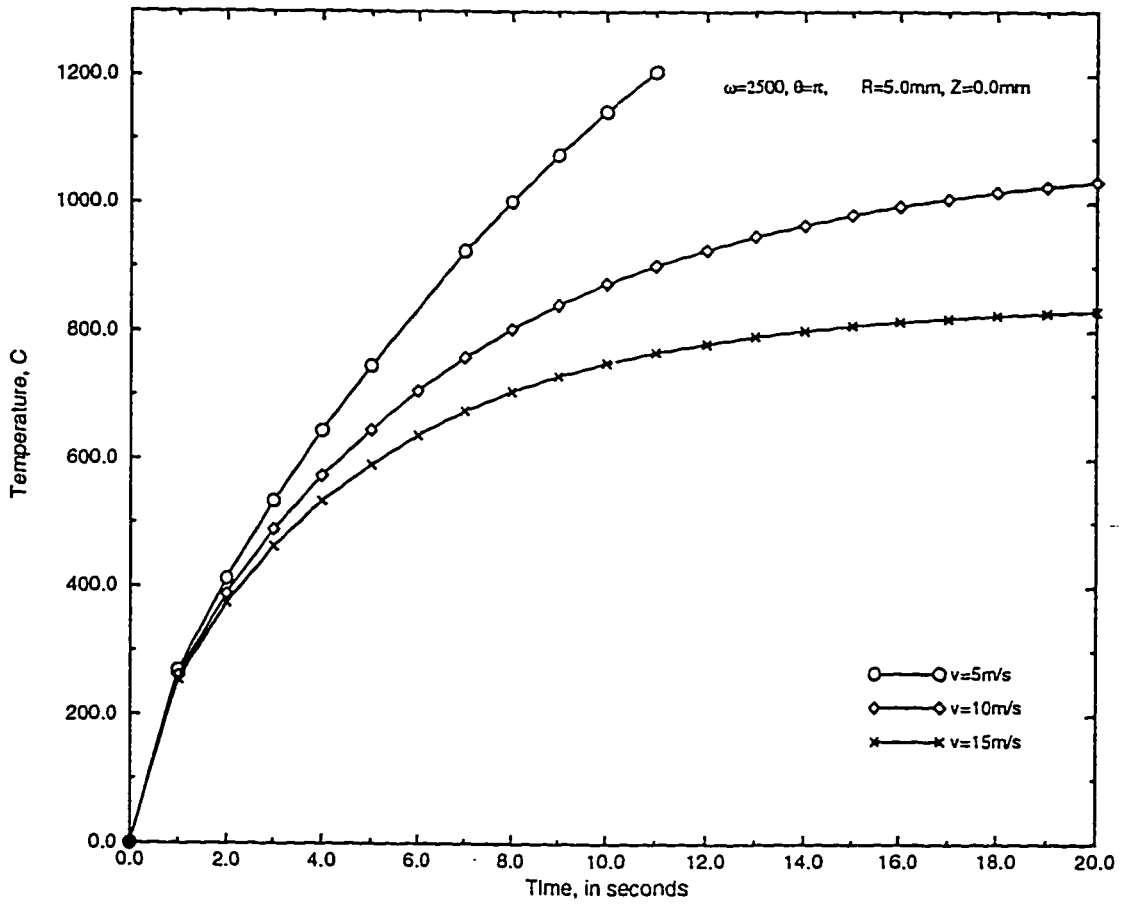

Figure 4.9: Comparison of temeprature rise at front stagnation point of a steel-copper friction weld with an angular speed of 2500 rpm for different jet velocities.

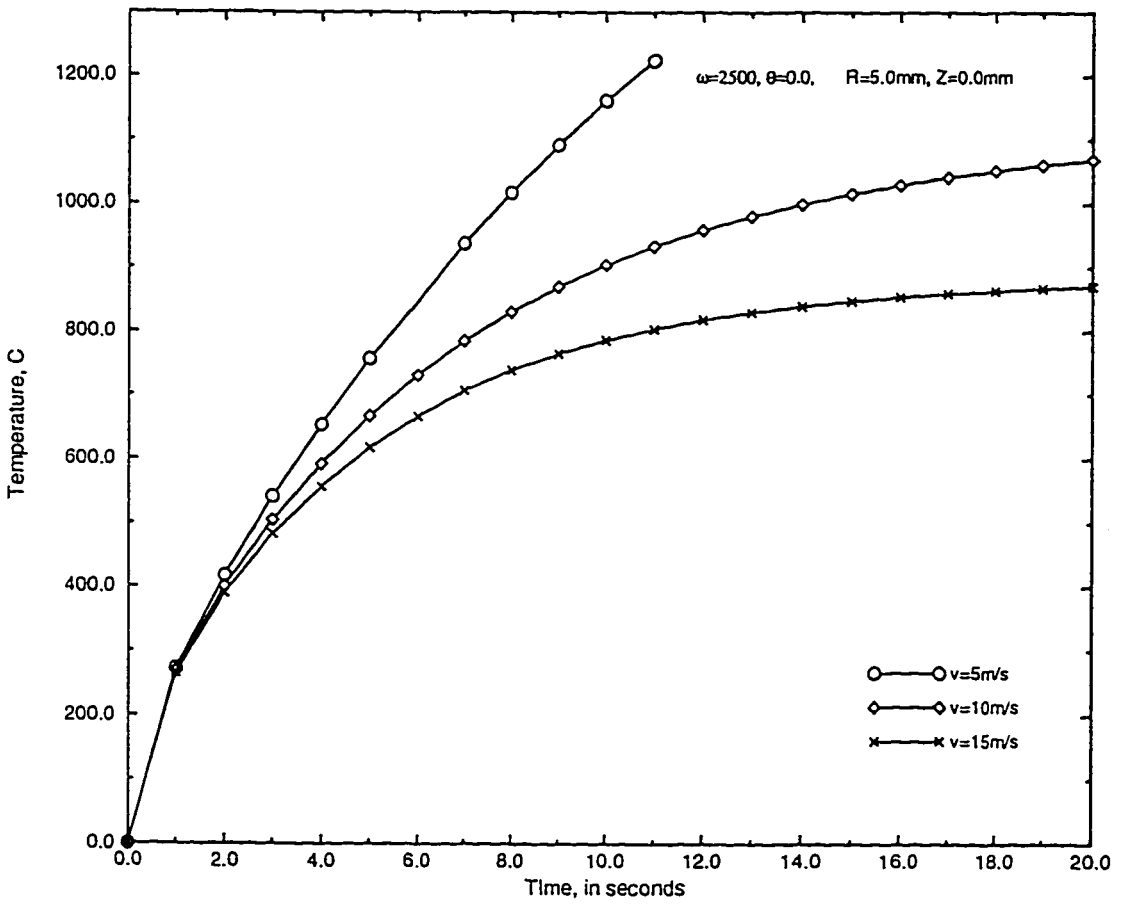

Figure 4.10: Comparison of temeprature rise at back stagnation point of a steel-copper friction weld with an angular speed of 2500 rpm for different jet velocities.

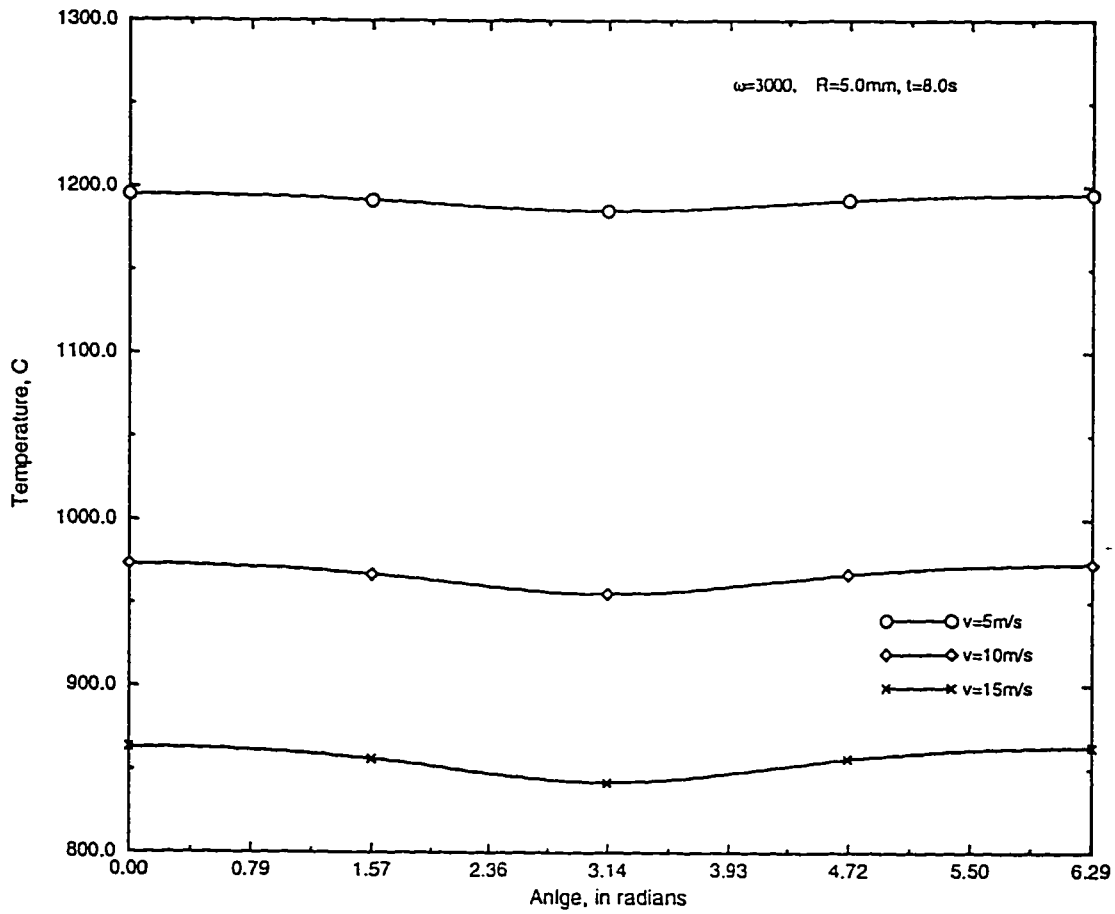

Figure 4.11: Comparison of circumferential temperature profiles on the surface of a steel-copper friction weld at time t=8.0 s with an angular of 3000 rpm for different jet velocities.

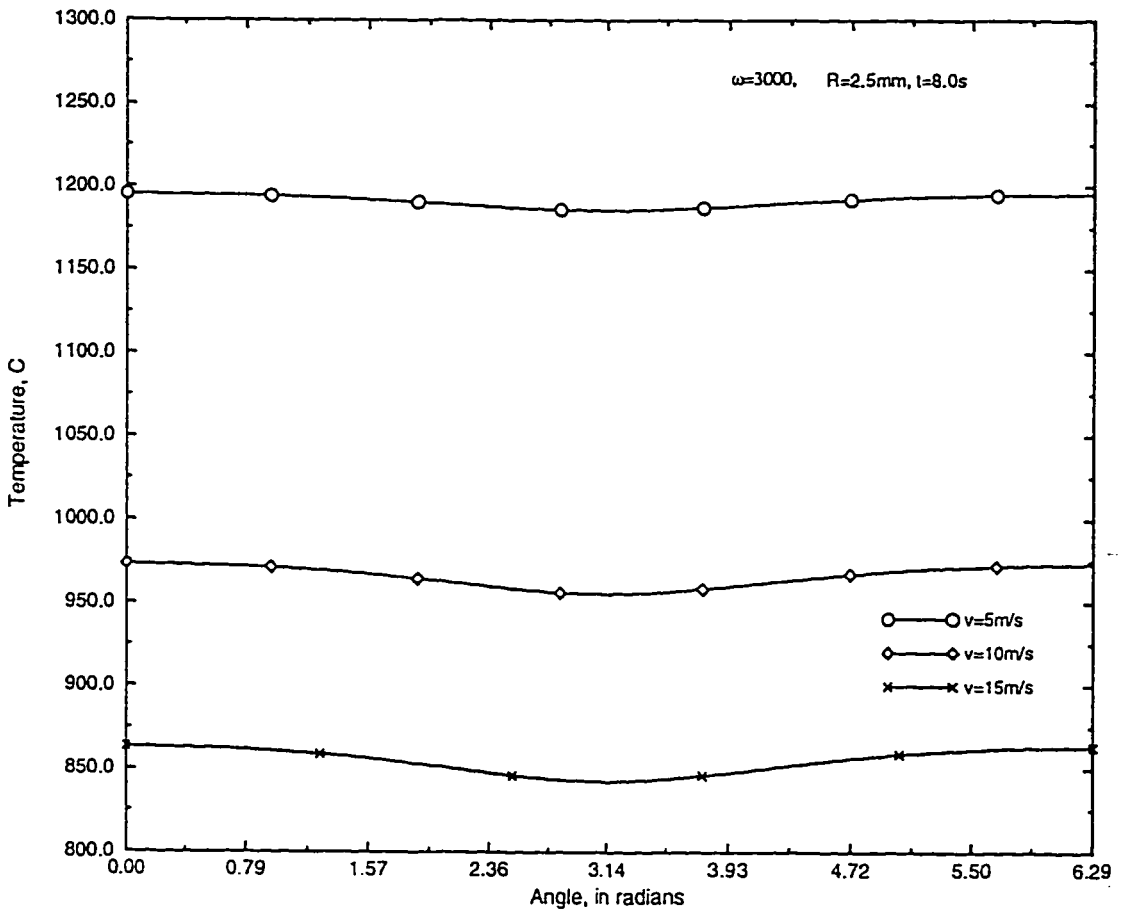

Figure 4.12: Comparison of circumferential temperature profiles at mid-radius of a steel-copper friction weld at time t=8.0 s with an angular of 3000 rpm for different jet velocities.

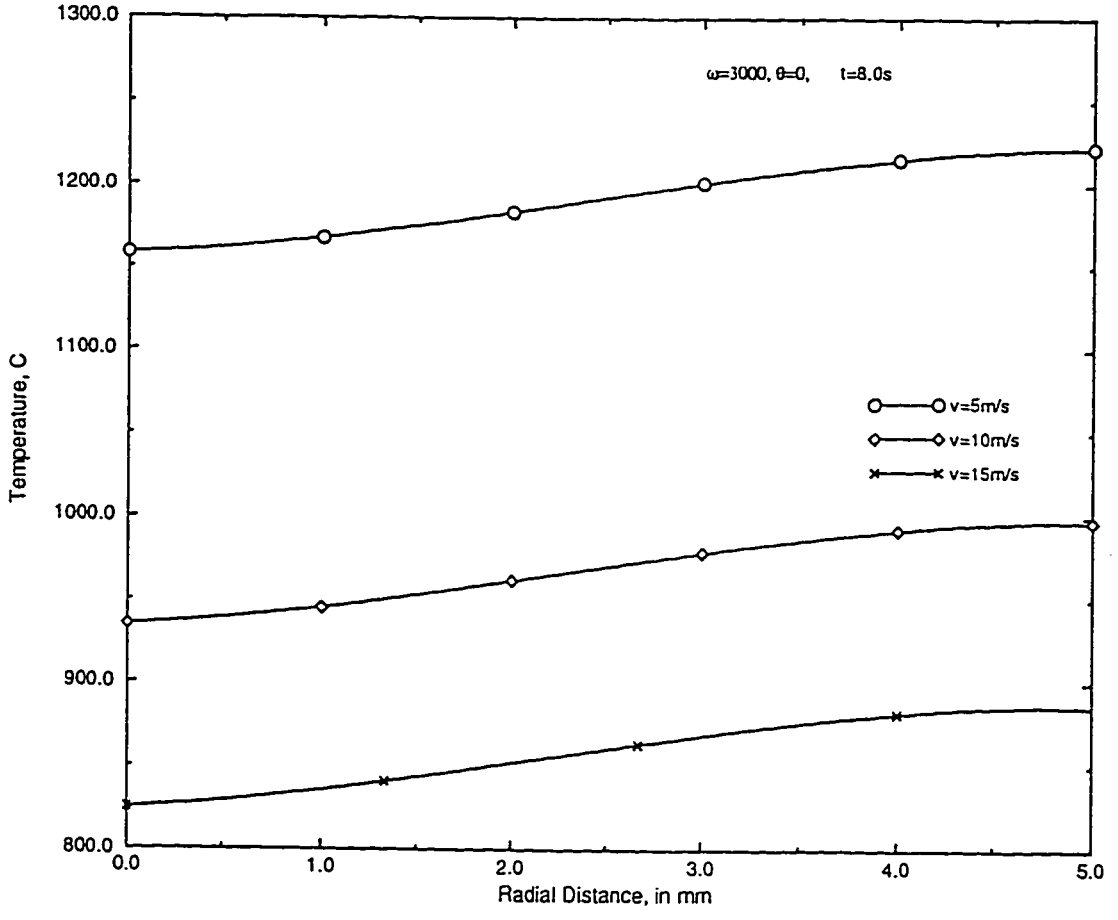

Figure 4.13: Comparison of radial temperature profiles at back stagnation point of a steel-copper friction weld at time t=8.0 s with an angular of 3000 rpm for different jet velocities.

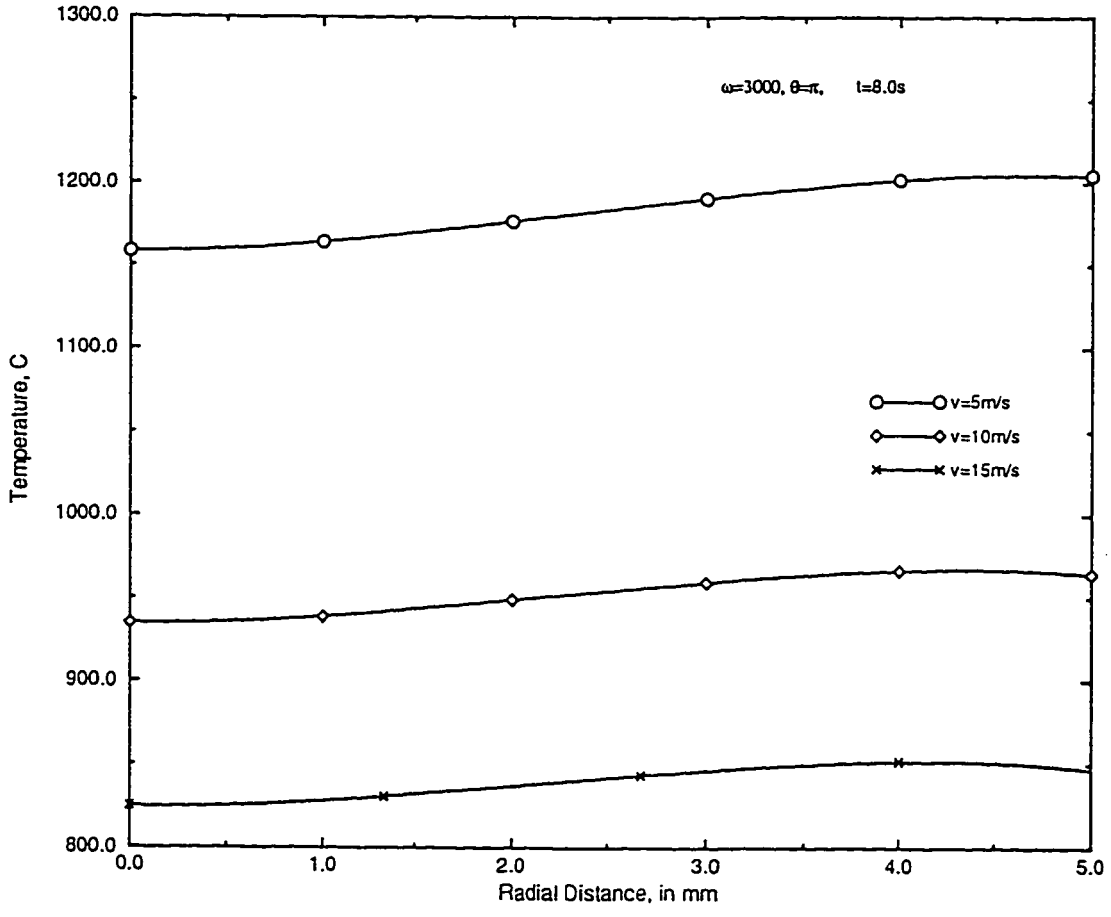

Figure 4.14: Comparison of radial temperature profiles at front stagnation point of a steel-copper friction weld at time t=8.0 s with an angular of 3000 rpm for different jet velocities.

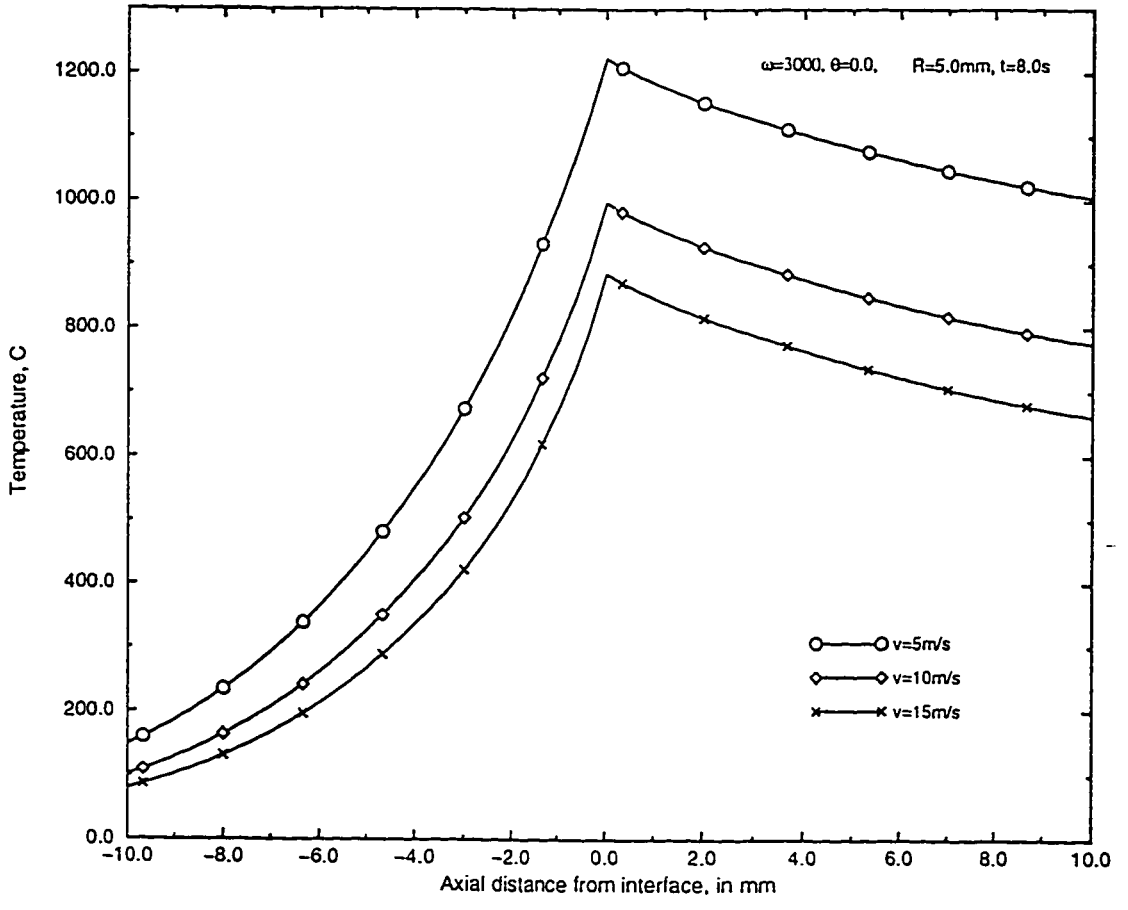

Figure 4.15: Comparison of axial temperature profiles on the surface at back stagnation point of a steel-copper friction weld at time t=8.0 s with an angular of 3000 rpm for different jet velocities.

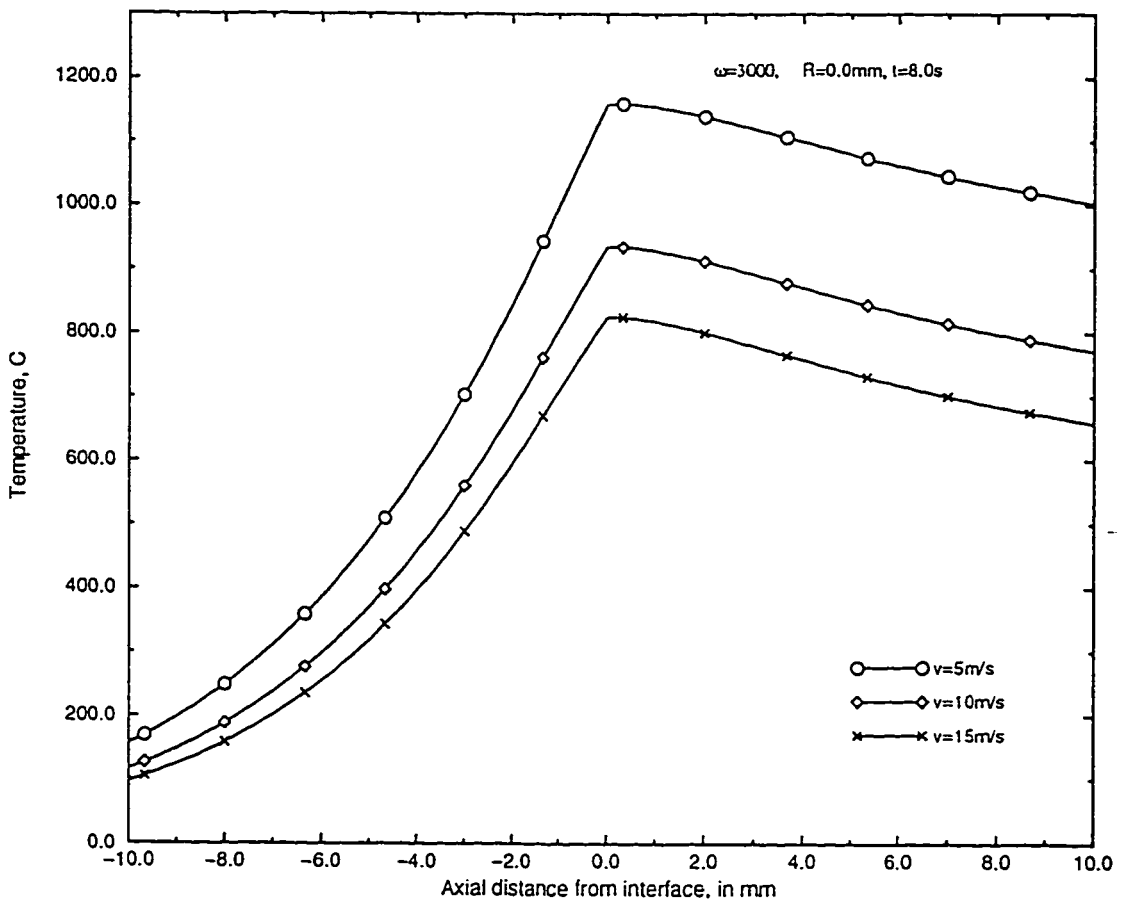

Figure 4.16: Comparison of centerline temperature profiles of a steel-copper friction weld at time t=8.0 s with an angular of 3000 rpm for different jet velocities.

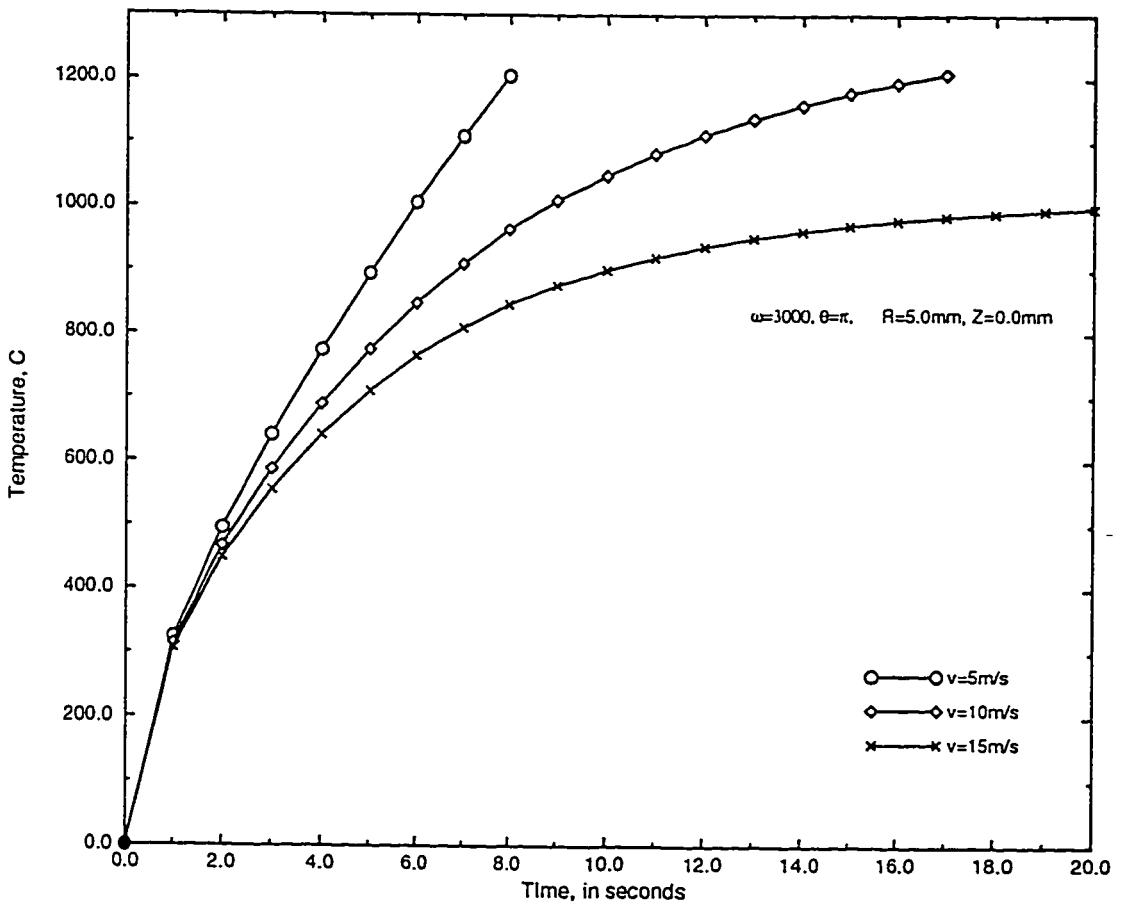

Figure 4.17: Comparison of temeprature rise at front stagnation point of a steel-copper friction weld with an angular speed of 3000 rpm for different jet velocities.

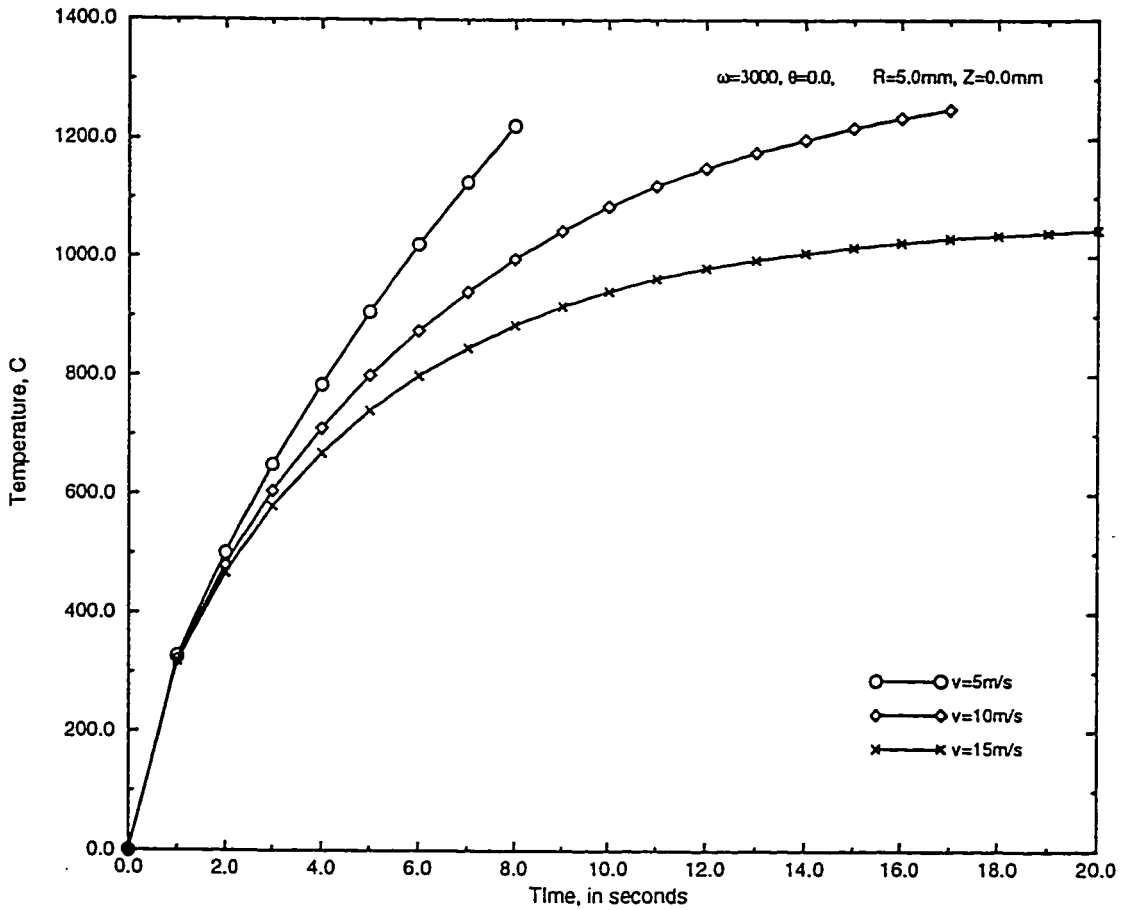

Figure 4.18: Comparison of temeprature rise at back stagnation point of a steel-copper friction weld with an angular speed of 3000 rpm for different jet velocities.

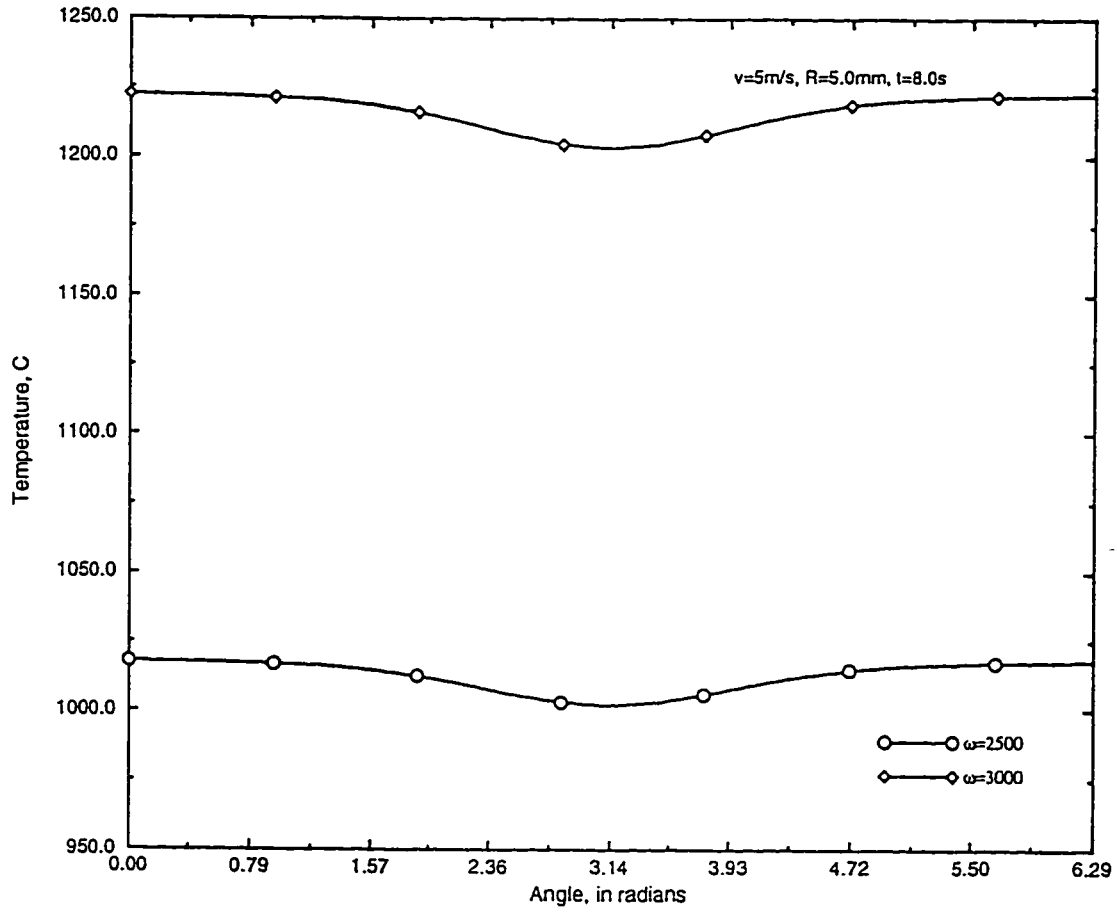

Figure 4.19: Comparison of circumferential temperature profiles on the surface of a steel-copper friction weld at time time t=8.0 s with a jet velocity of v=5 m/s for different angular speeds.

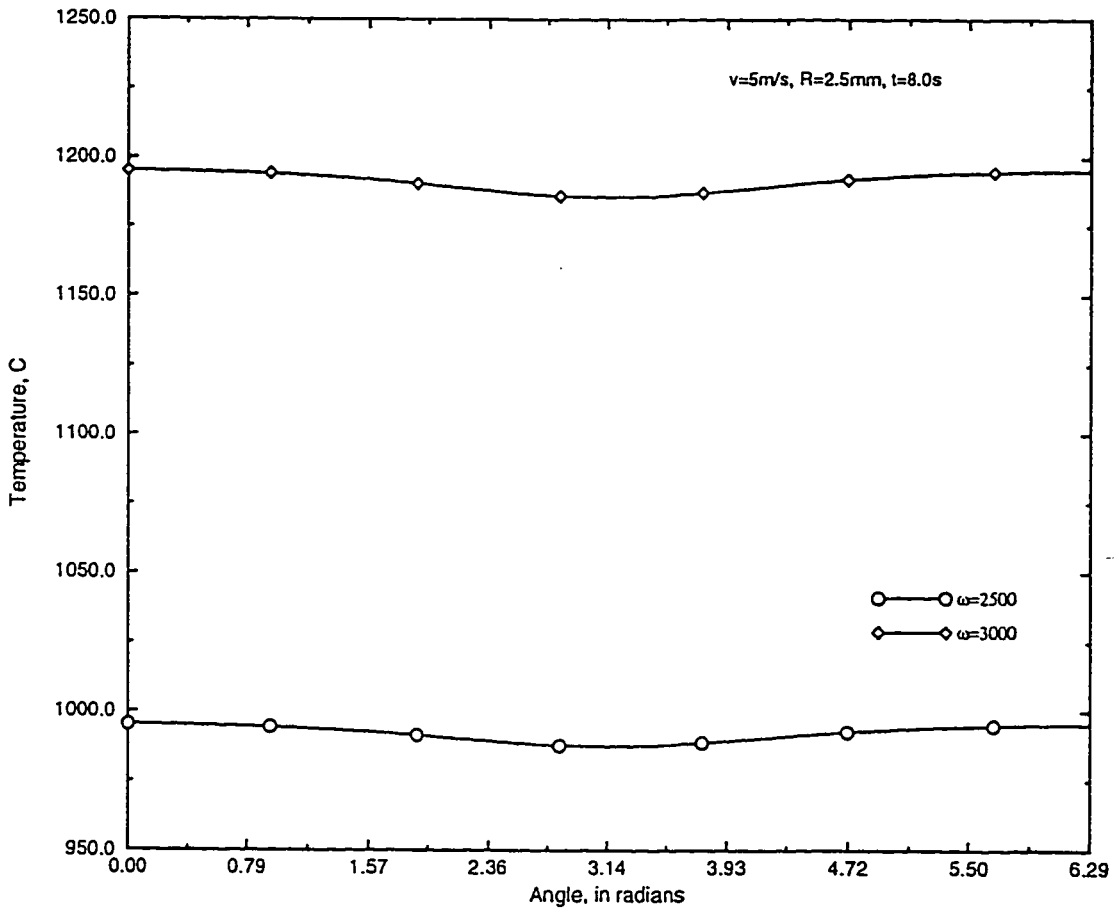

Figure 4.20: Comparison of circumferential temperature profiles at mid-radius of a steel-copper friction weld at time time t=8.0 s with a jet velocity of v=5 m/s for different angular speeds.

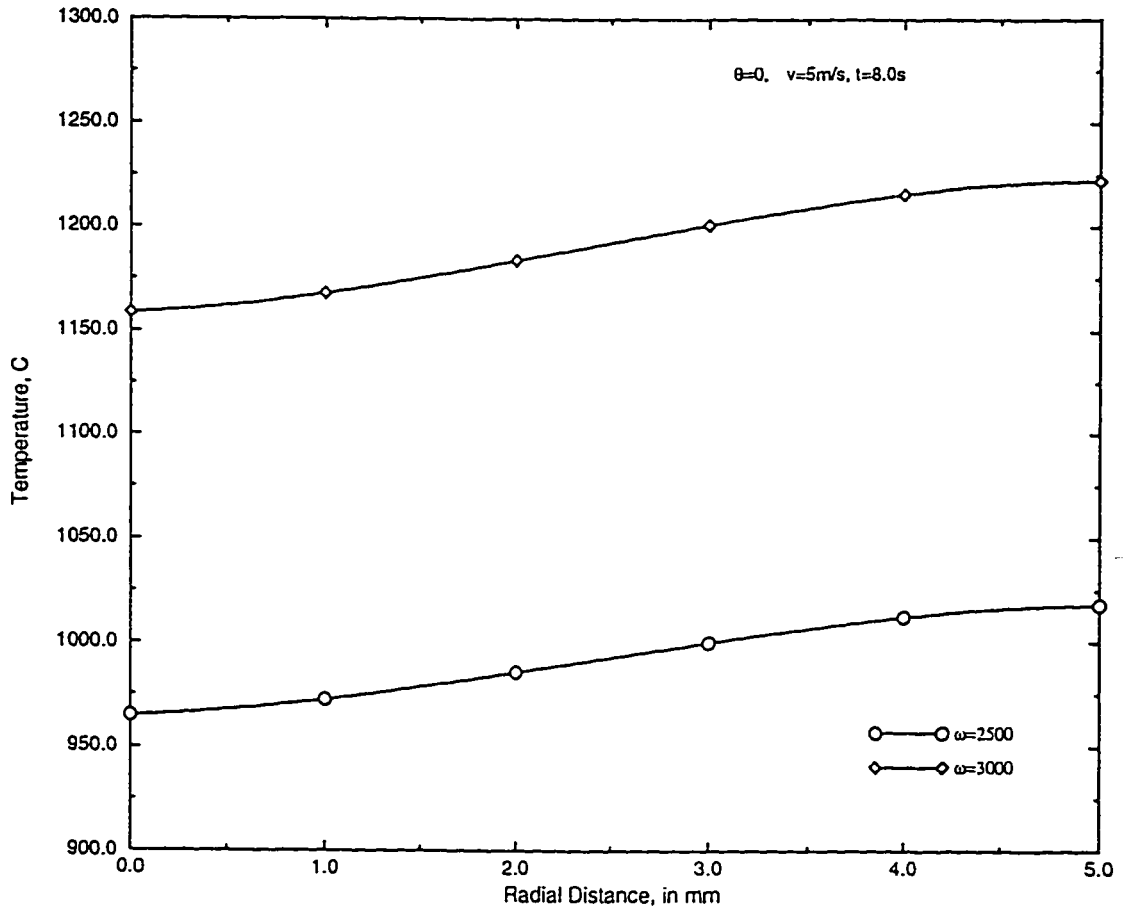

Figure 4.21: Comparison of axial temperature profiles at back stagnation point of a steel-copper friction weld at time time t=8.0 s with a jet velocity of v=5 m/s for different angular speeds.

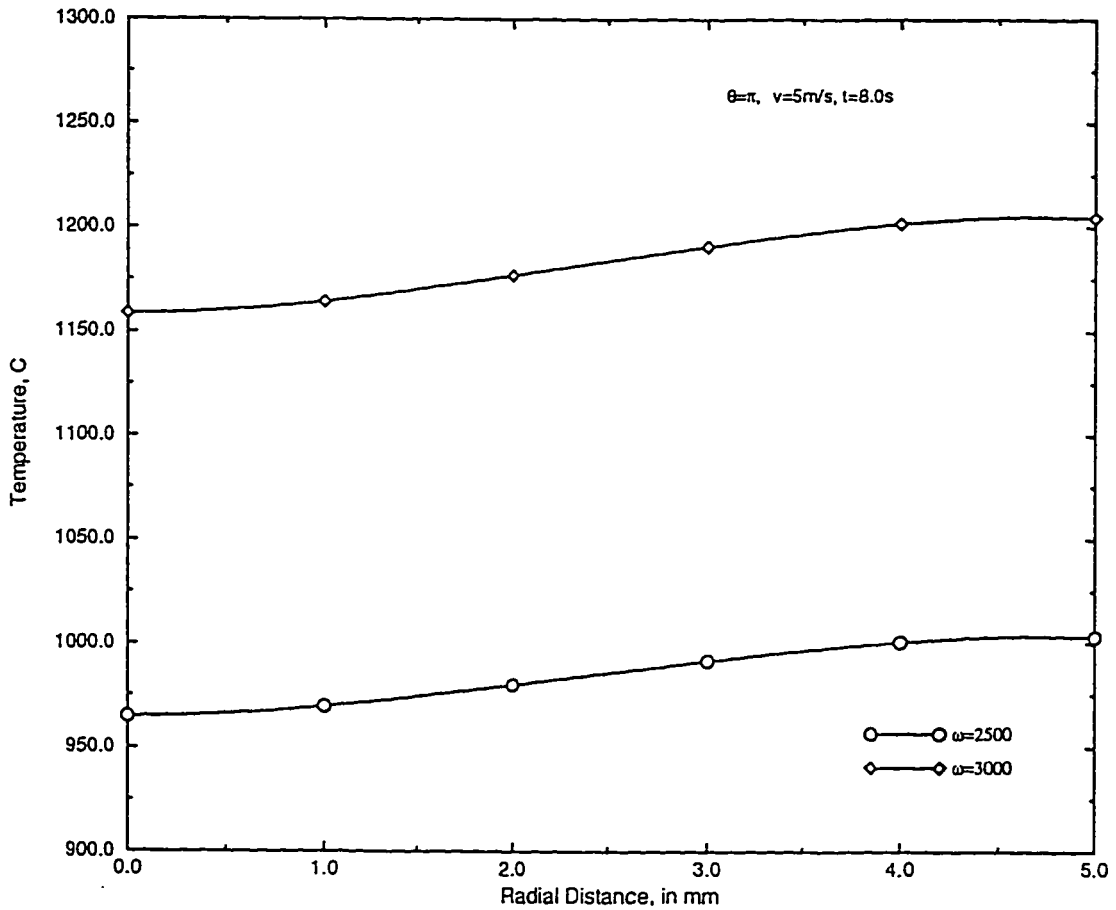

Figure 4.22: Comparison of radial temperature profiles at front stagnation point of a steel-copper friction weld at time time t=8.0 s with a jet velocity of v=5 m/s for different angular speeds.

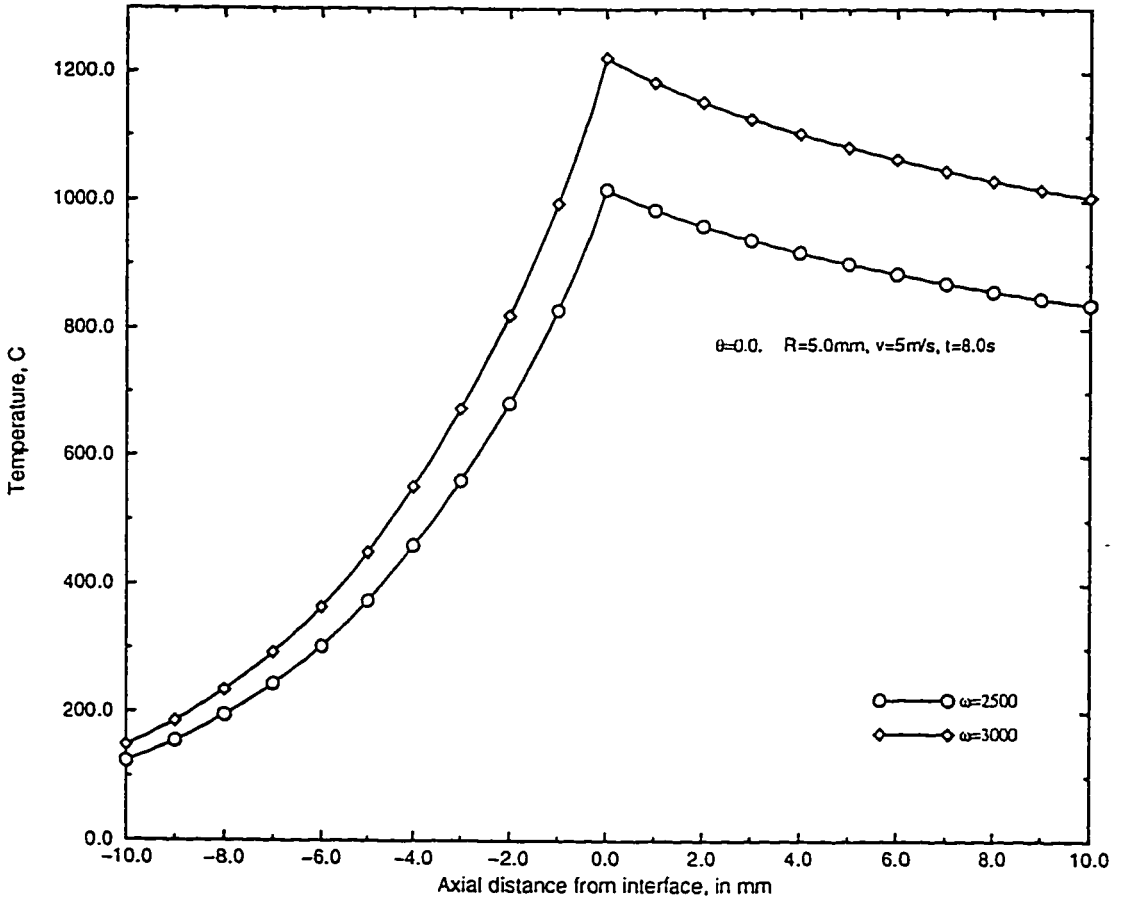

Figure 4.23: Comparison of axial temperature profiles on the surface at back stagnation point of a steel-copper friction weld at time time t=8.0 s with a jet velocity of v=5 m/s for different angular speeds.

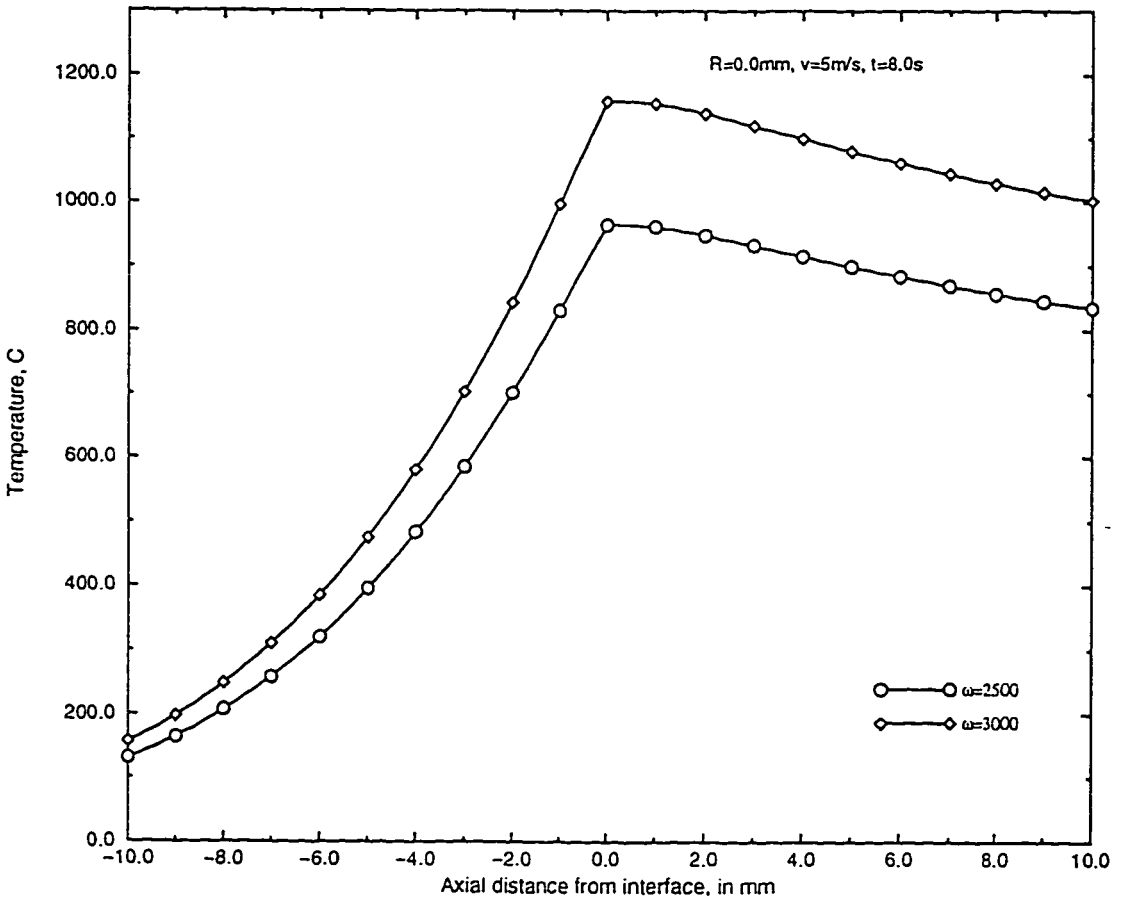

Figure 4.24: Comparison of centerline temperature profiles of a steel-copper friction weld at time time t=8.0 s with a jet velocity of v=5 m/s for different angular speeds.

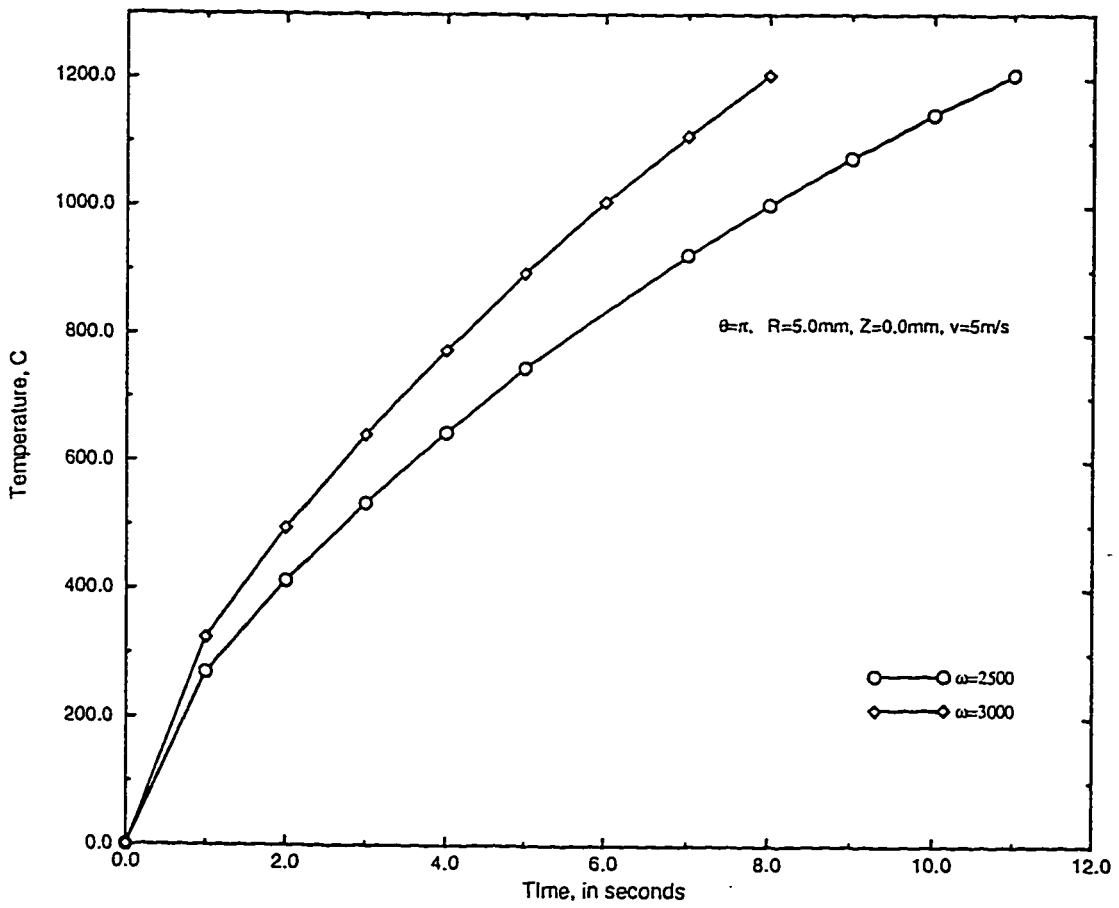

Figure 4.25: Comparison of temperature profiles with increase in time at front stagnation point of a steel-copper friction weld with a jet velocity of v=5 m/s for different anglular speeds.

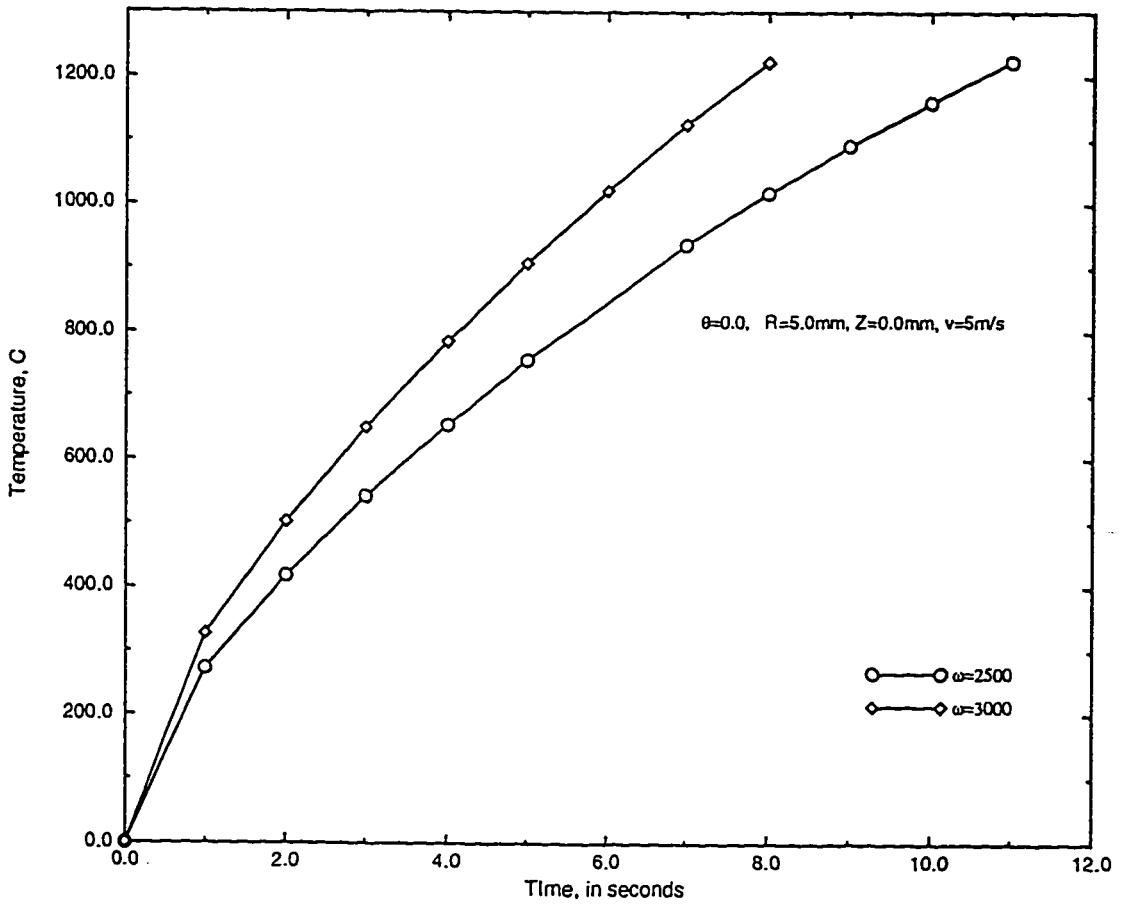

Figure 4.26: Comparison of temperature rise at back stagnation point of a steel-copper friction weld with a jet velocity of v=5 m/s for different anglular speeds.

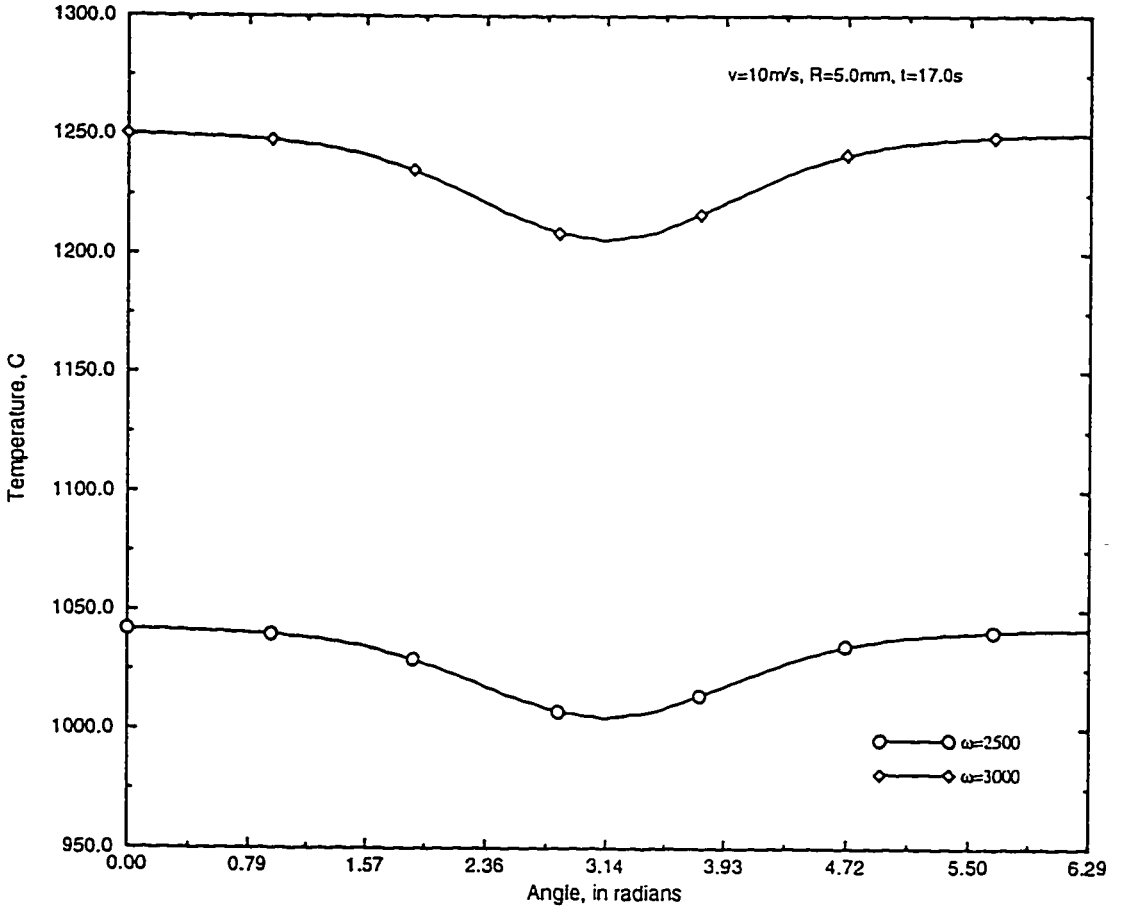

Figure 4.27: Comparison of circumferential temperature profiles on the surface of a steel-copper friction weld at time t=17.0 s with a jet velocity of v=10 m/s for different anglular speeds.

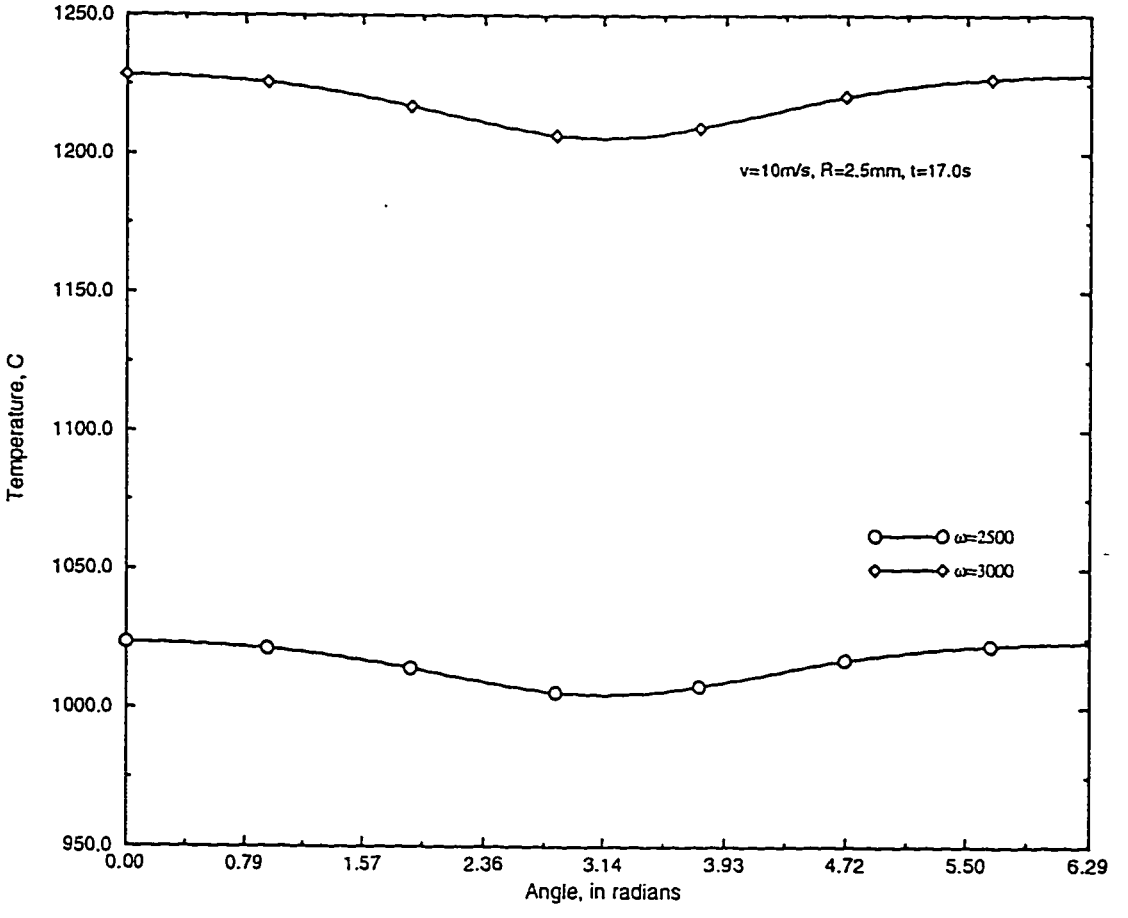

Figure 4.28: Comparison of circumferential temperature profiles at mid-radius of a steel-copper friction weld at time t=17.0 s with a jet velocity of v=10 m/s for different anglular speeds.

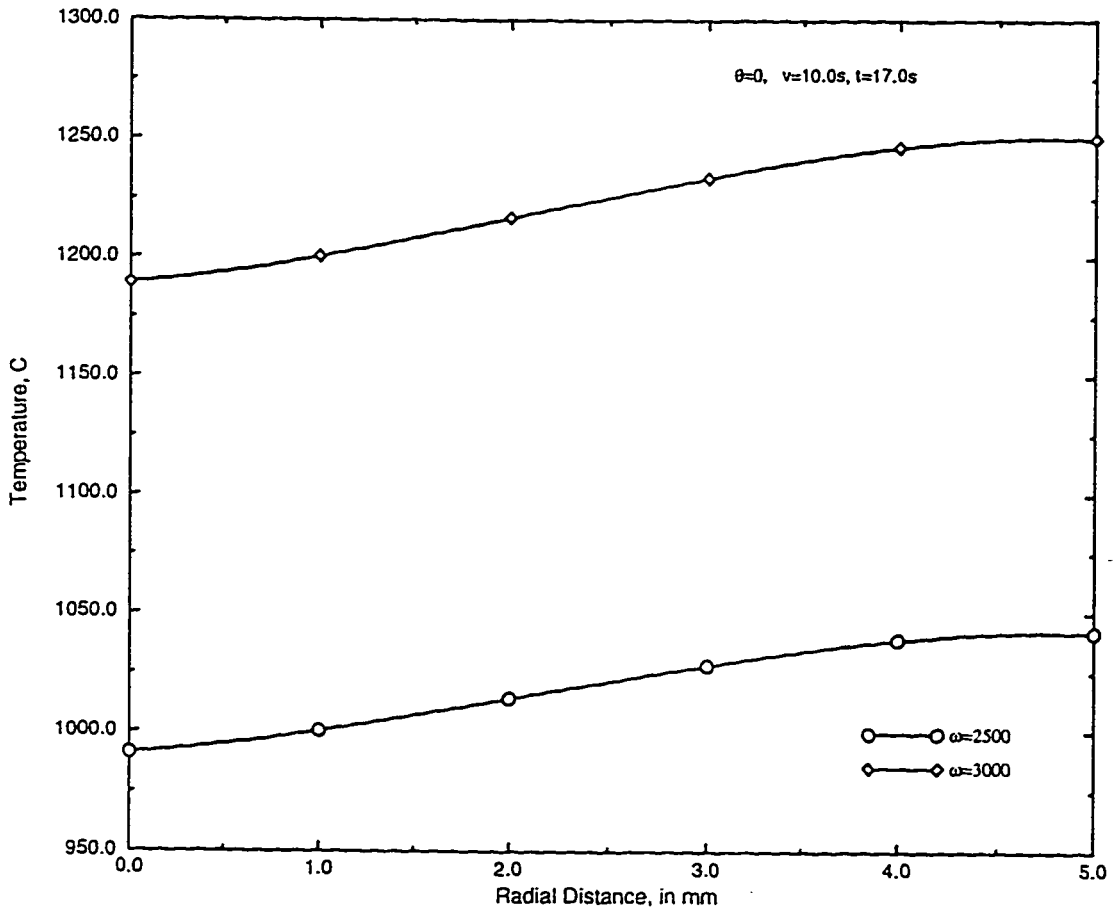

Figure 4.29: Comparison of radial temperature profiles at back stagnation point of a steel-copper friction weld at time t=17.0 s with a jet velocity of v=10 m/s for different anglular speeds.

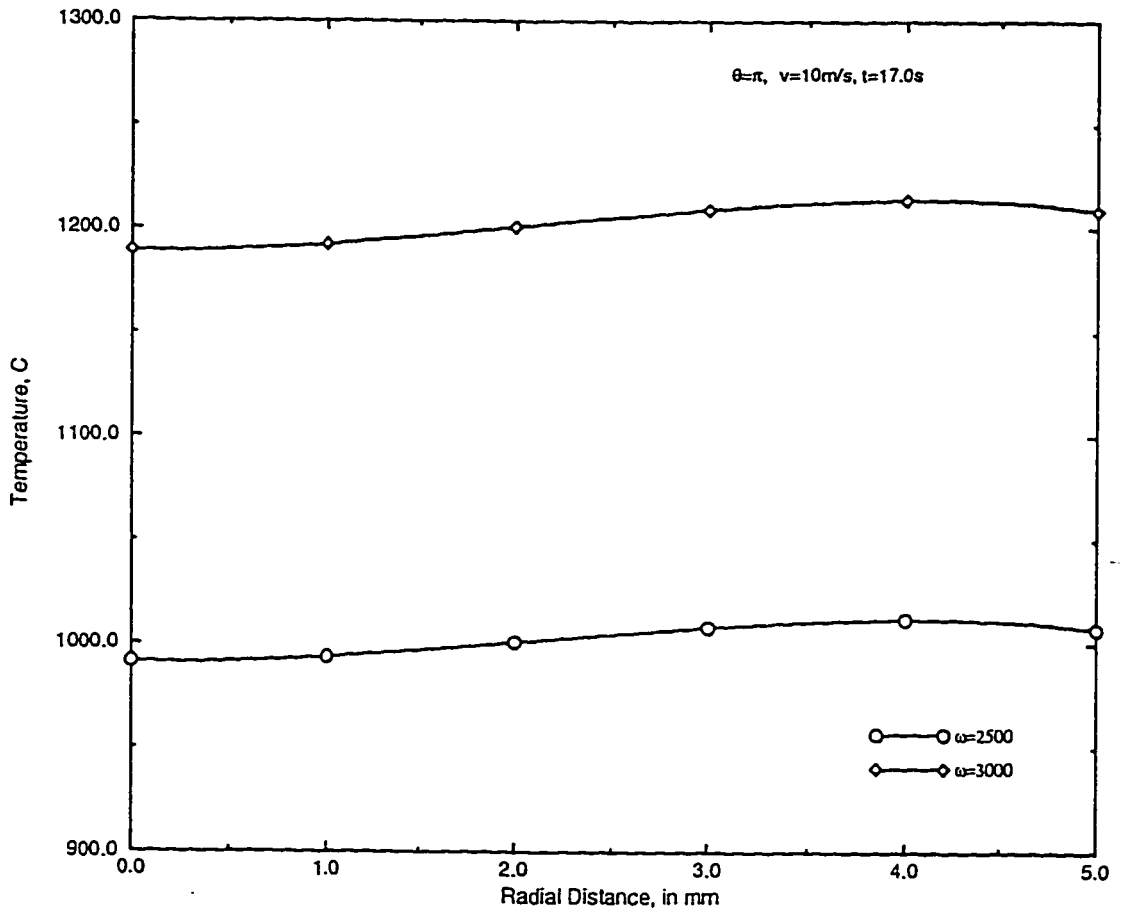

Figure 4.30: Comparison of radial temperature profiles at front stagnation point of a steel-copper friction weld at time t=17.0 s with a jet velocity of v=10 m/s for different anglular speeds.

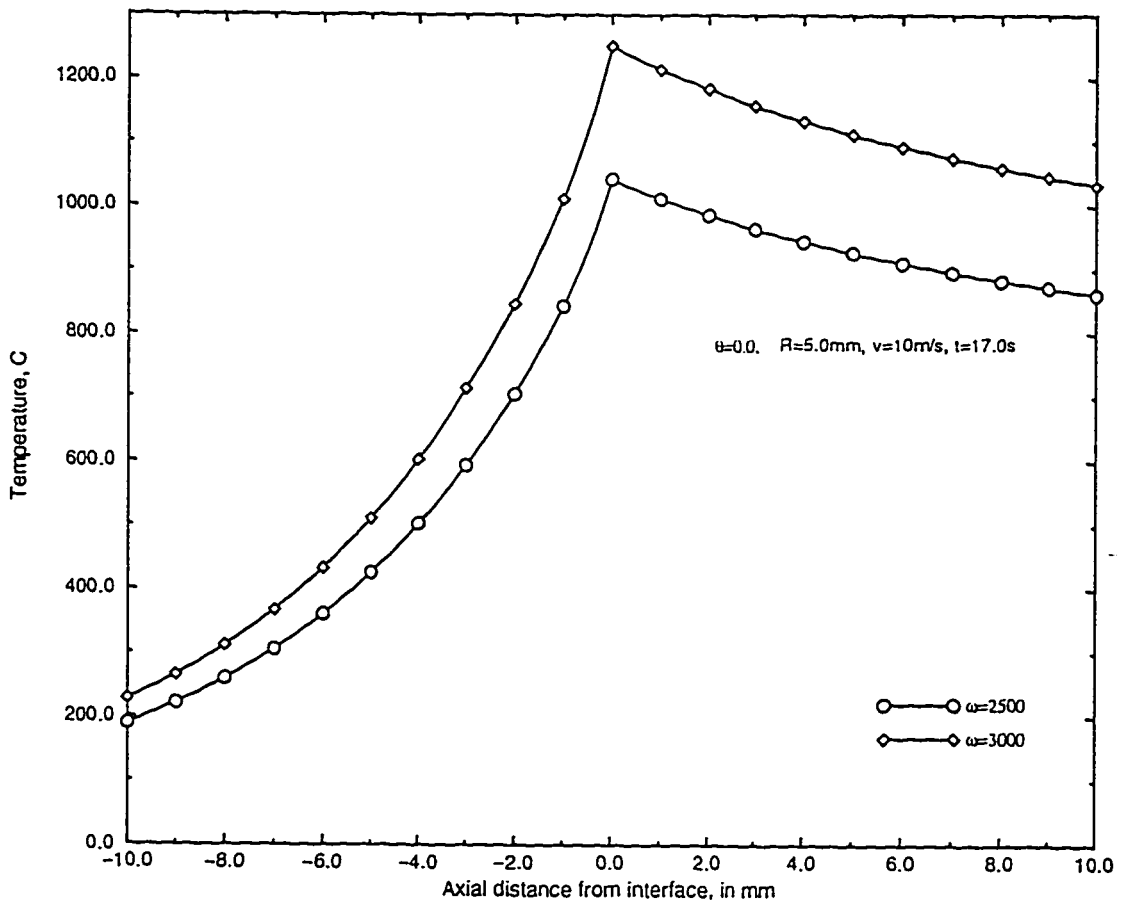

Figure 4.31: Comparison of axial temperature profiles on the surface at back stagnation point of a steel-copper friction weld at time t=17.0 s with a jet velocity of v=10 m/s for different anglular speeds.

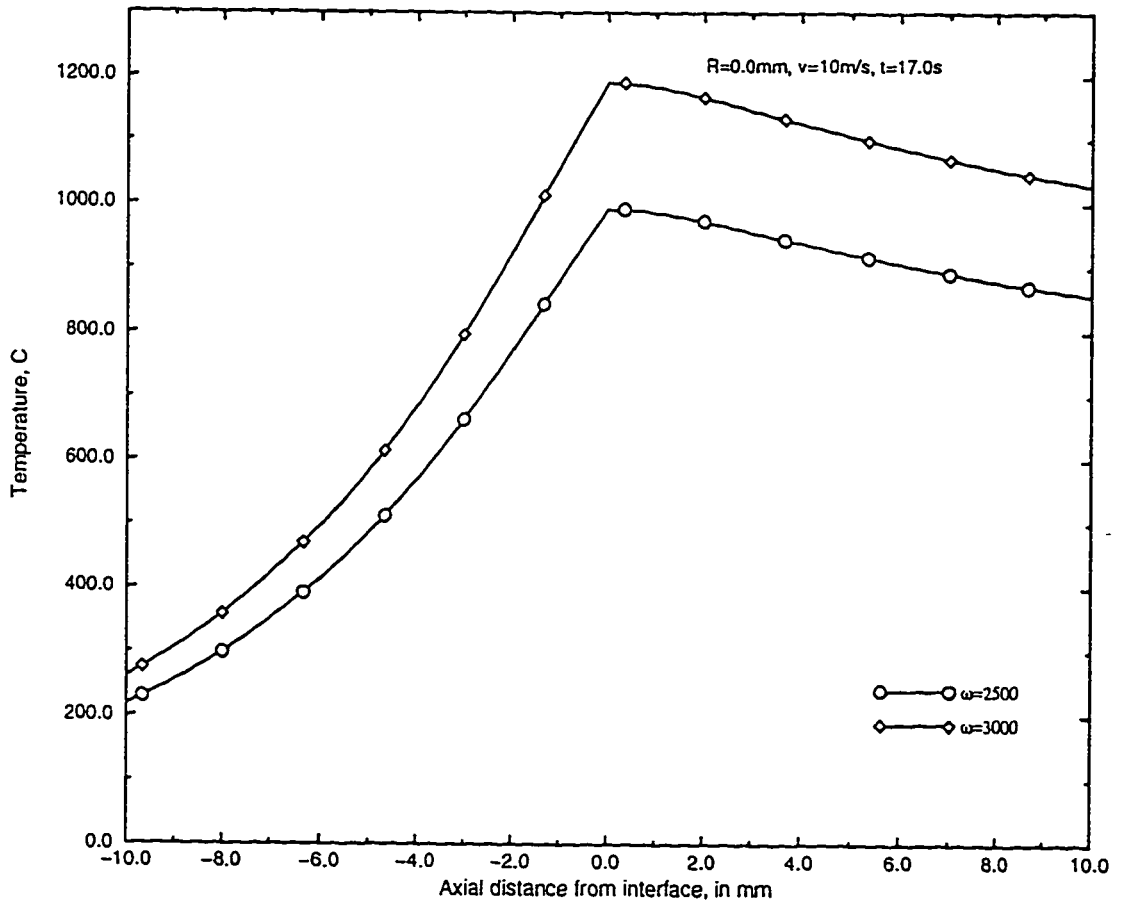

Figure 4.32: Comparison of centerline temperature profiles of a steel-copper friction weld at time t=17.0 s with a jet velocity of v=10 m/s for different anglular speeds.

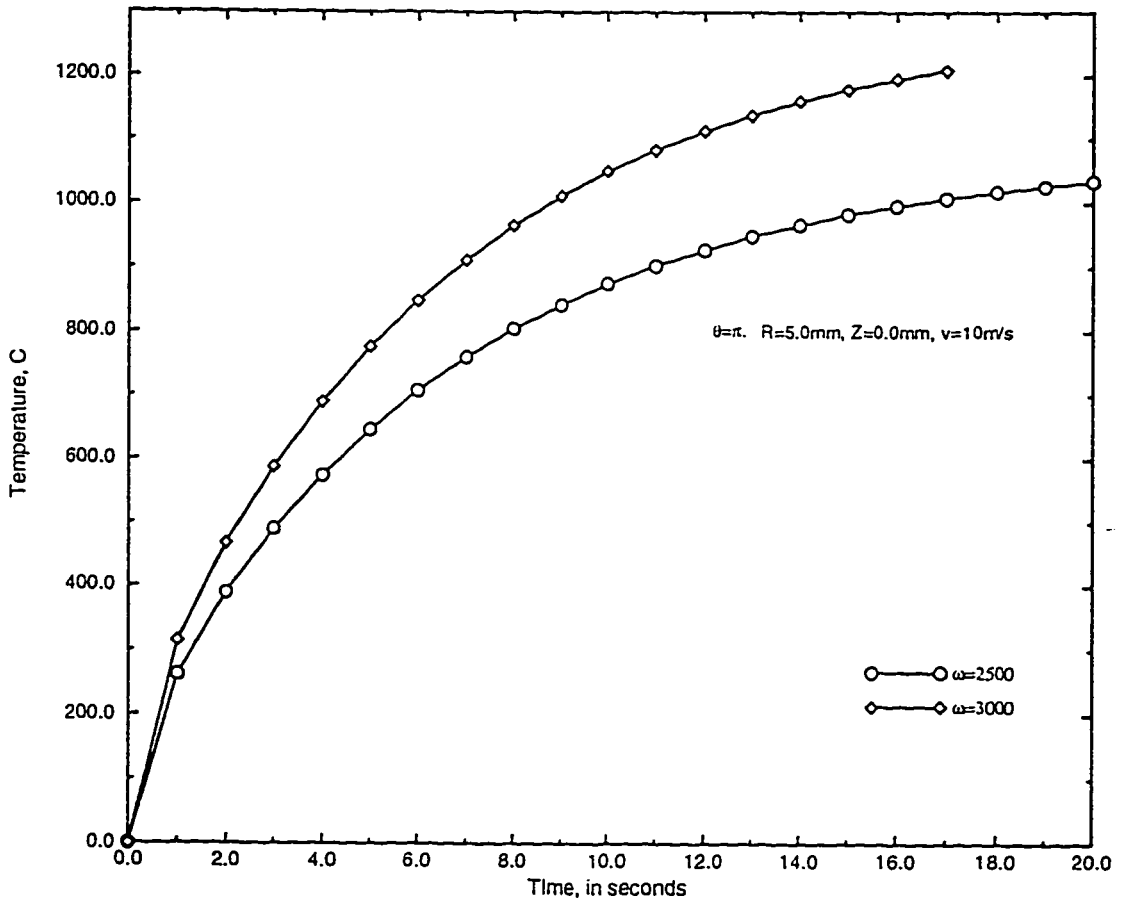

Figure 4.33: Comparison of temperature rise at front stagnation point of a steel-copper friction weld with a jet velocity of v=10 m/s for different anglular speeds.

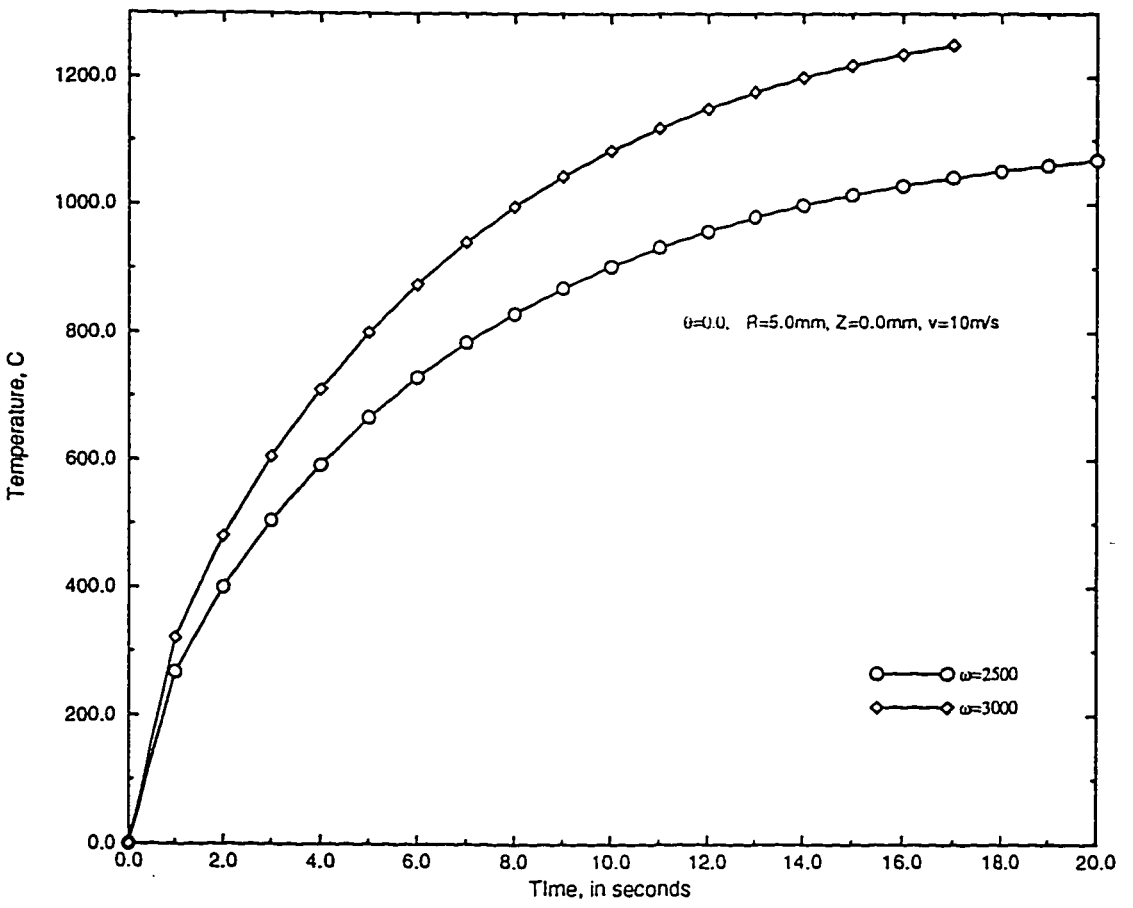

Figure 4.34: Comparison of temperature rise at back stagnation point of a steel-copper friction weld with a jet velocity of v=10 m/s for different anglular speeds.

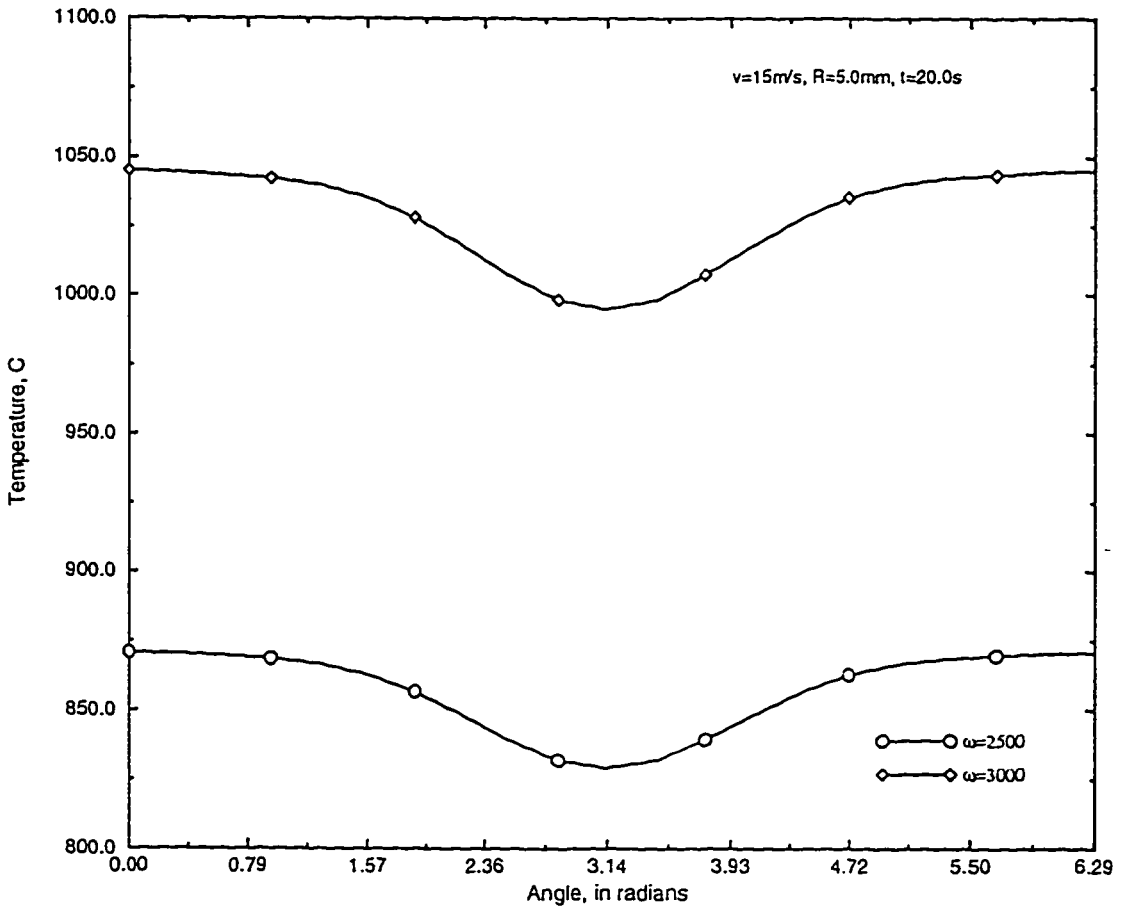

Figure 4.35: Comparison of circumferential temperature profiles on the surface of a steel-copper friction weld at time t=20.0 s with a jet velocity of v=15 m/s for different anglular speeds.

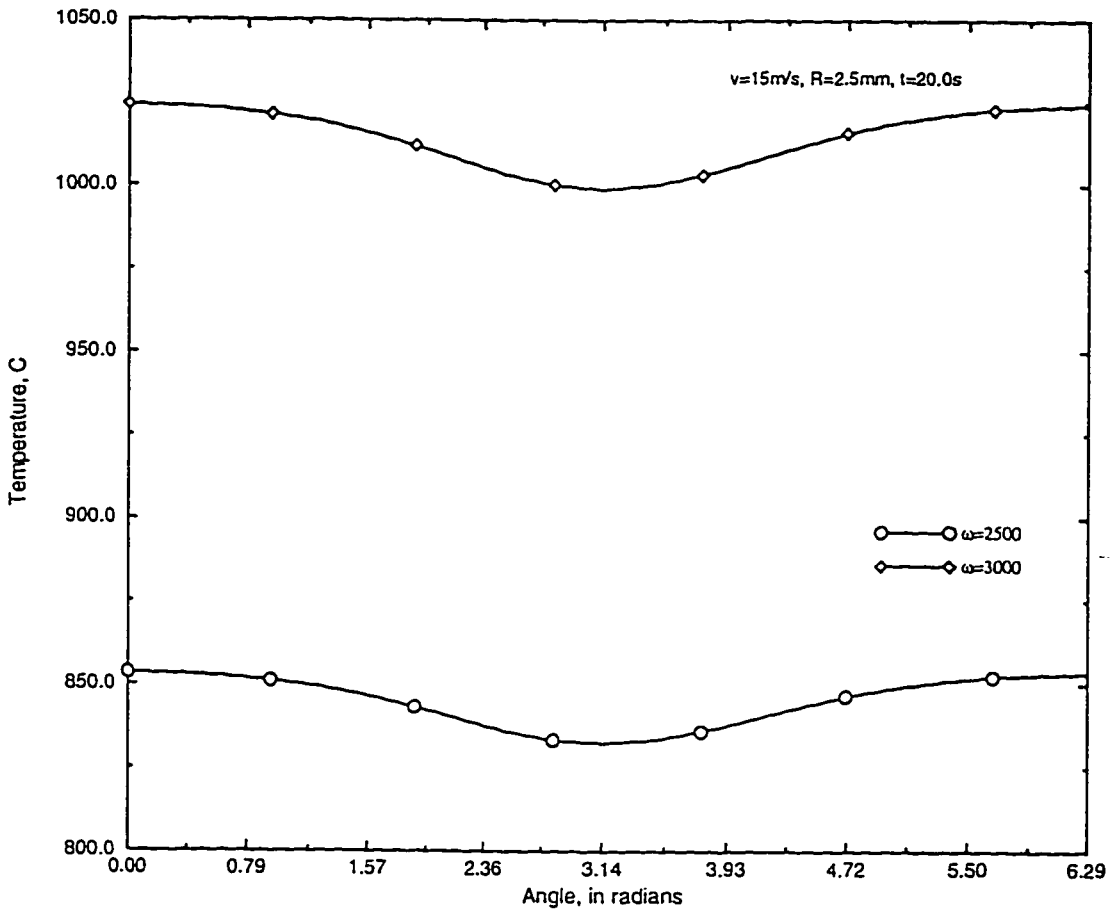

Figure 4.36: Comparison of circumferential temperature profiles at mid-radius of a steel-copper friction weld at time t=20.0 s with a jet velocity of v=15 m/s for different anglular speeds.

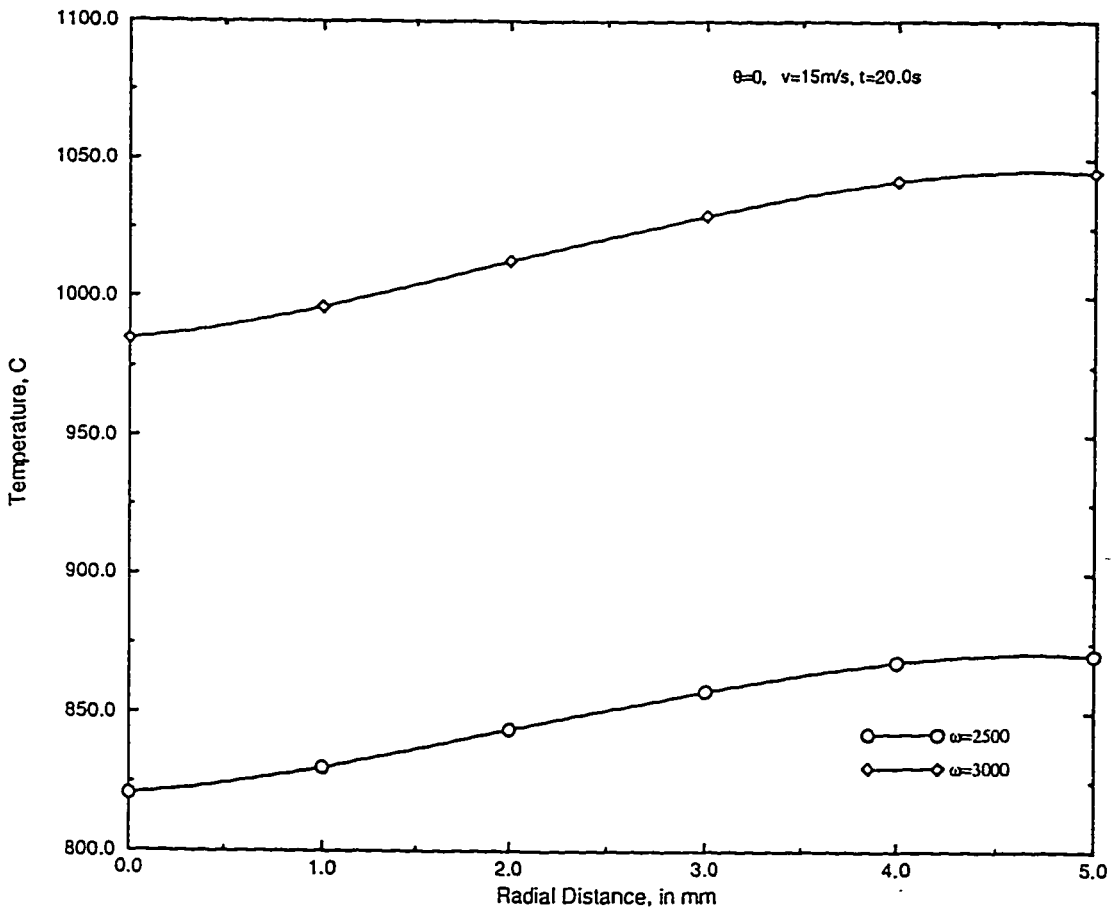

Figure 4.37: Comparison of radial temperature profiles at back stagnation point of a steel-copper friction weld at time t=20.0 s with a jet velocity of v=15 m/s for different anglular speeds.

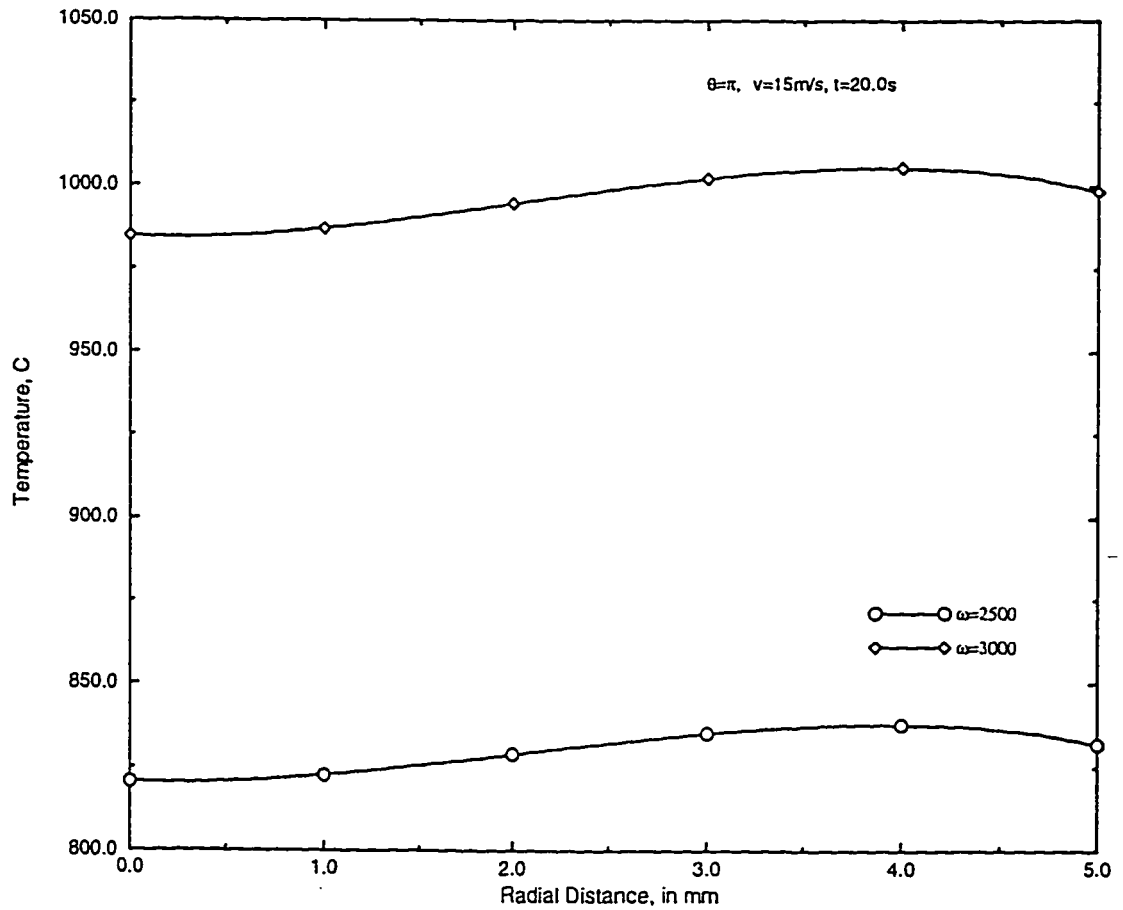

Figure 4.38: Comparison of radial temperature profiles at front stagnation point of a steel-copper friction weld at time t=20.0 s with a jet velocity of v=15 m/s for different anglular speeds.

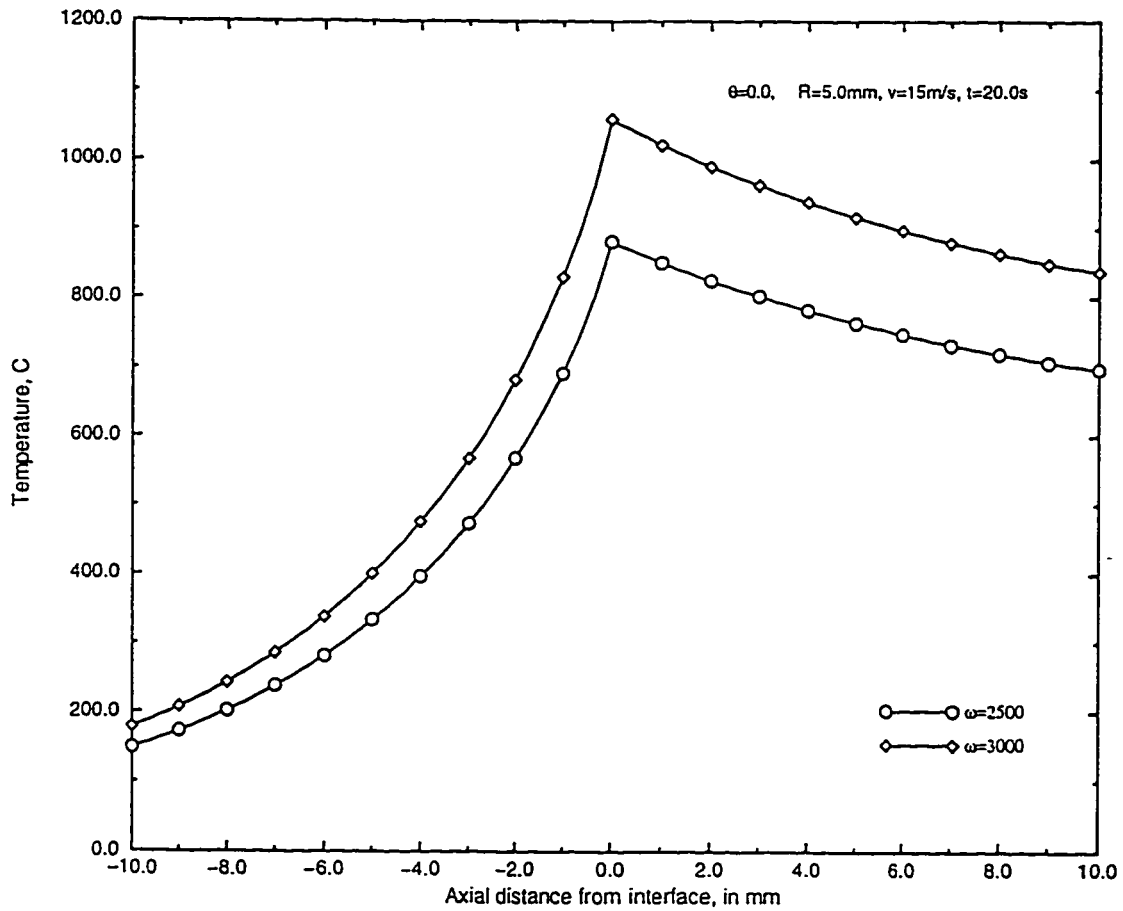

Figure 4.39: Comparison of axial temperature profiles on the surface at back stagnation point of a steel-copper friction weld at time t=20.0 s with a jet velocity of v=15 m/s for different anglular speeds.

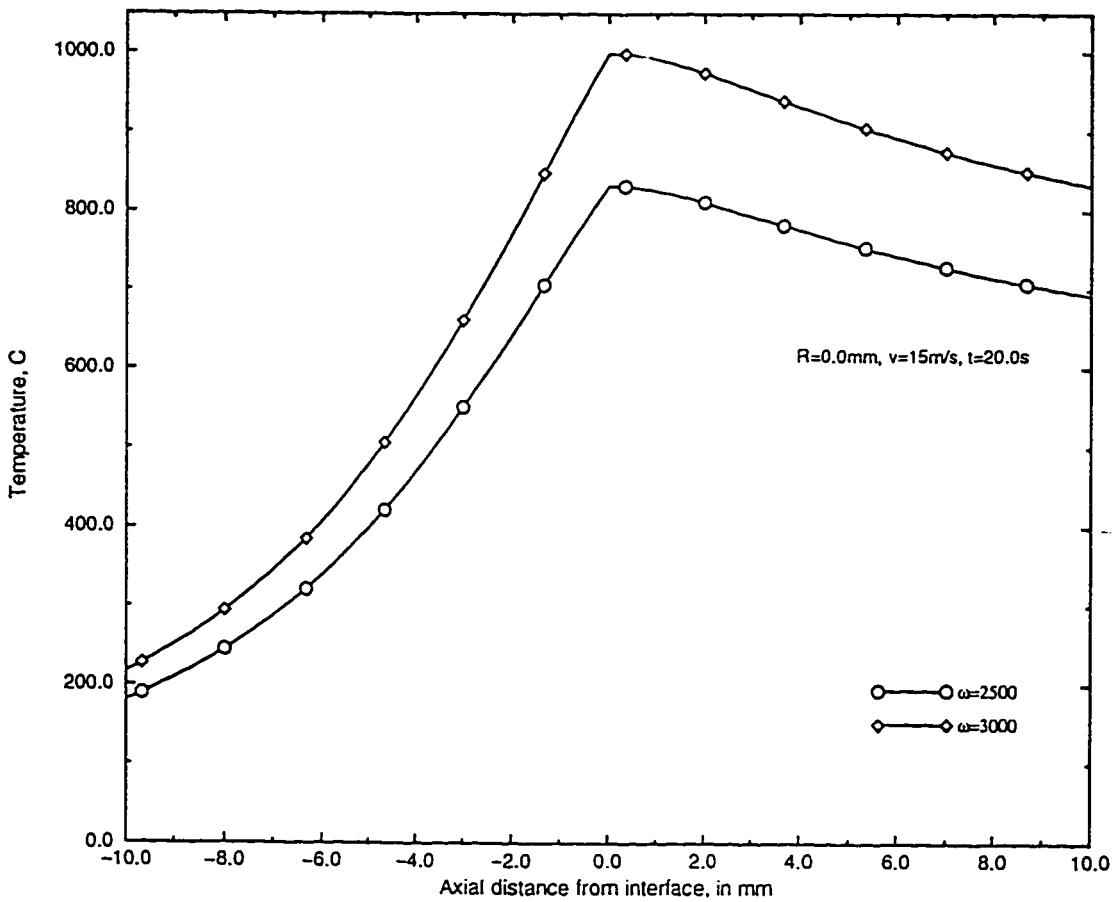

Figure 4.40: Comparison of centerline temperature profiles of a steel-copper friction weld at time t=20.0 s with a jet velocity of v=15 m/s for different anglular speeds.

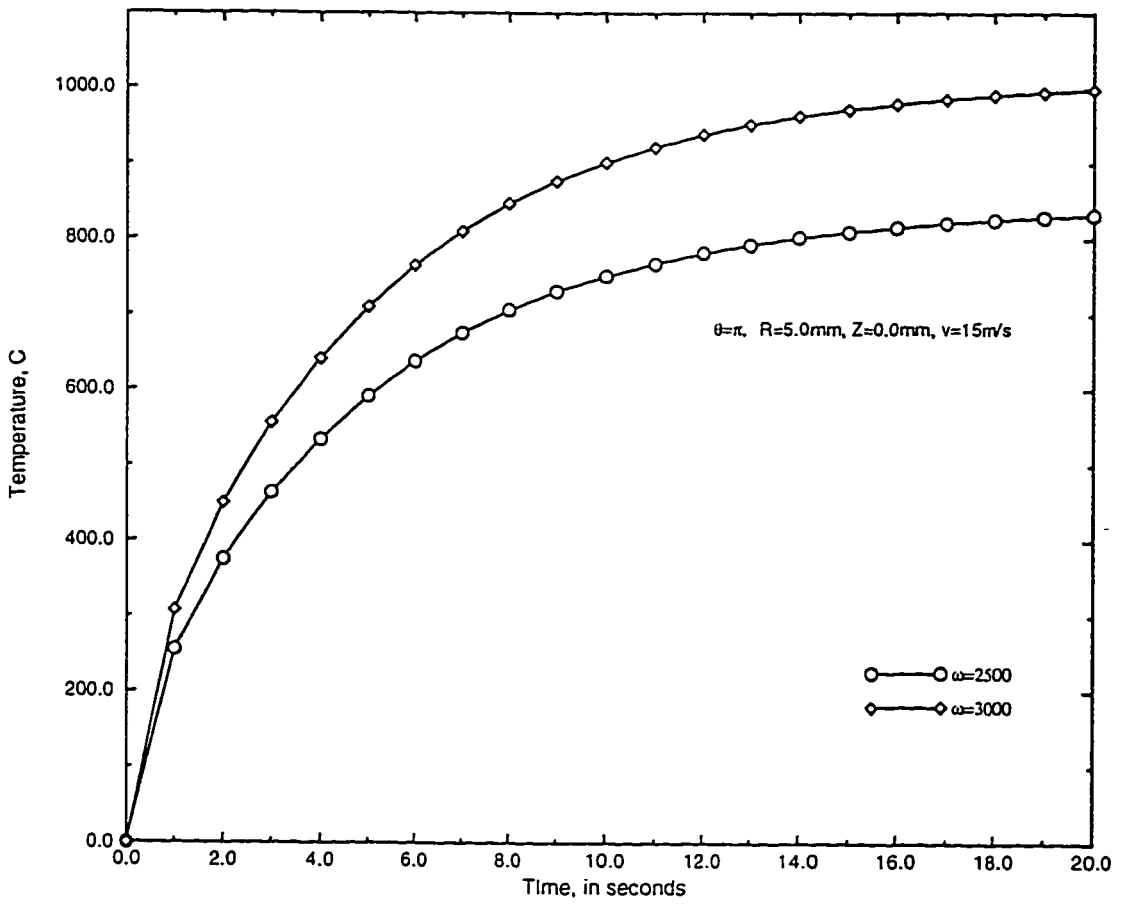

Figure 4.41: Comparison of temperature rise at front stagnation point of a steel-copper friction weld with a jet velocity of v=15 m/s for different anglular speeds.

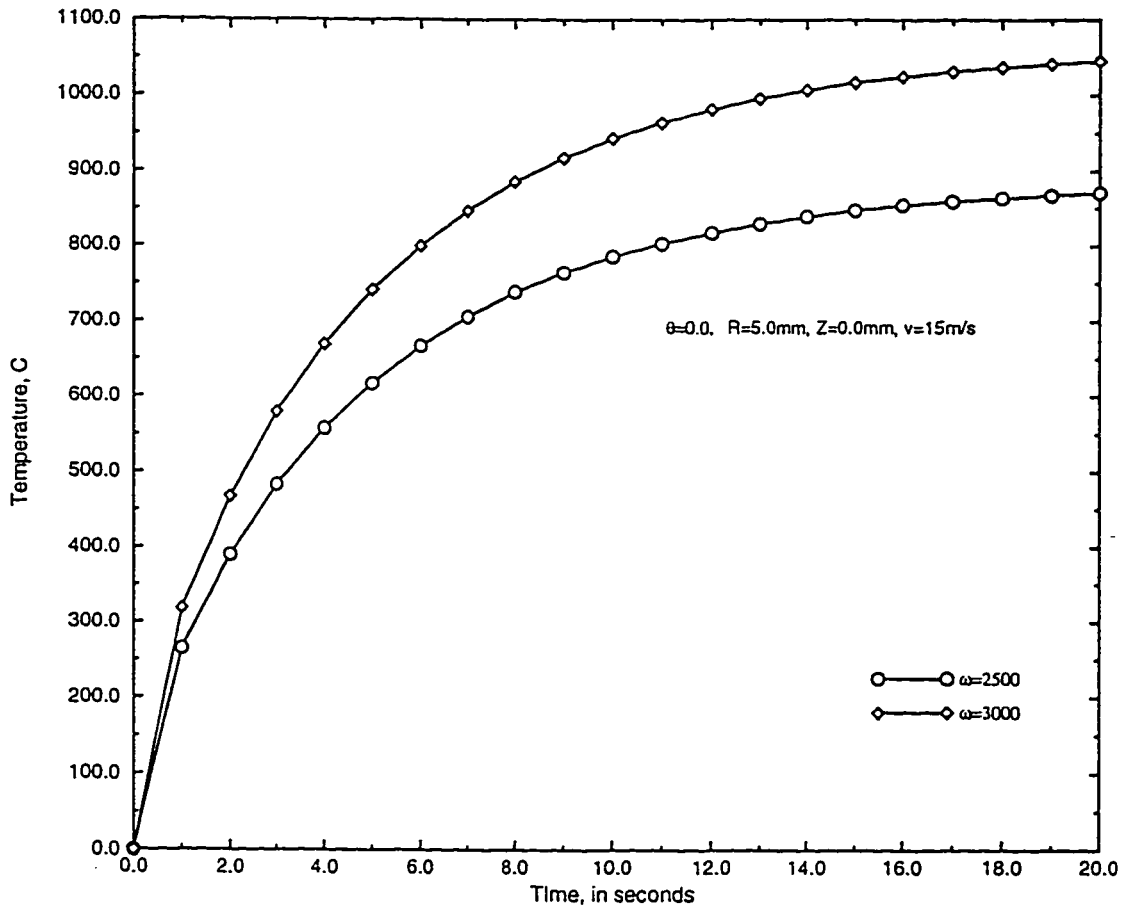

Figure 4.42: Comparison of temperature rise at back stagnation point of a steel-copper friction weld with a jet velocity of v=15 m/s for different anglular speeds.

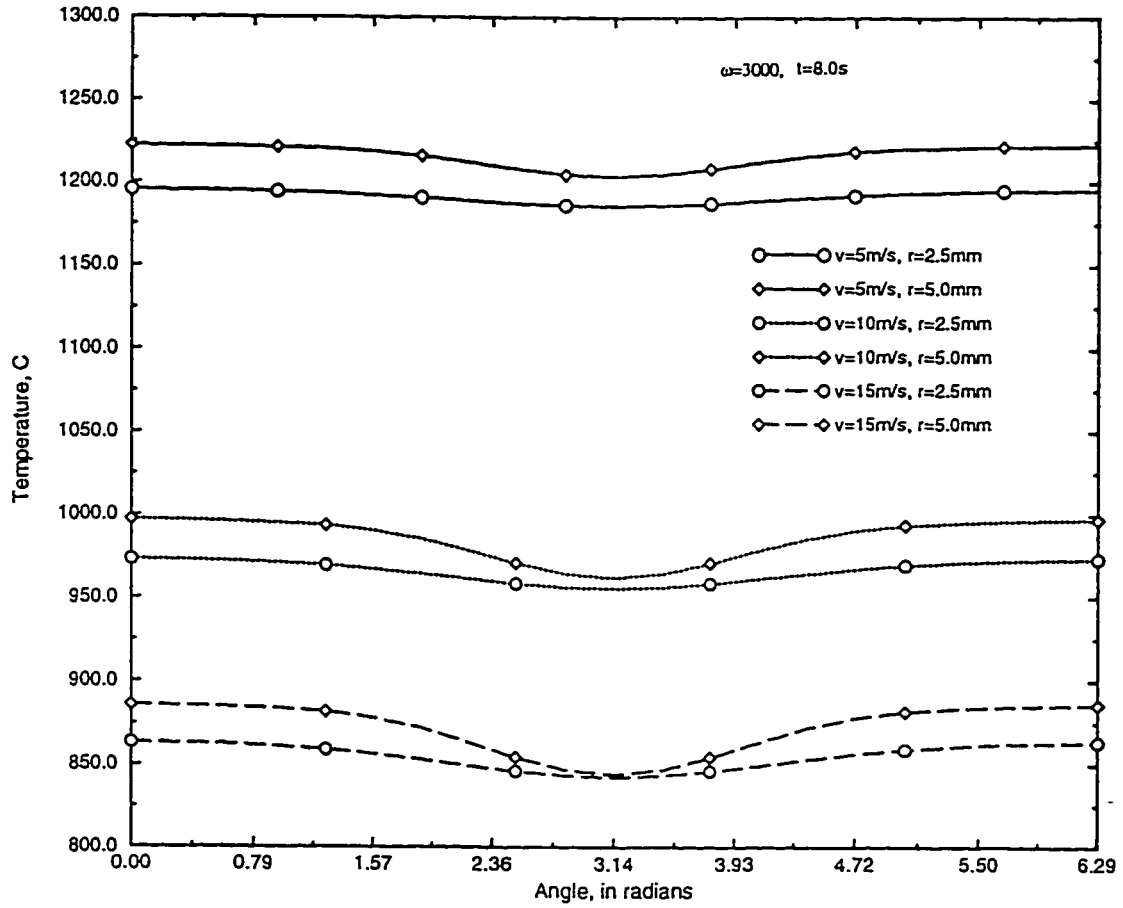

Figure 4.43: Comparison of circumferential temperature profiles on the surface and mid-radius of a steel-copper friction weld at time t=8.0 s with an angular speed of 3000 rpm for different jet velocities.

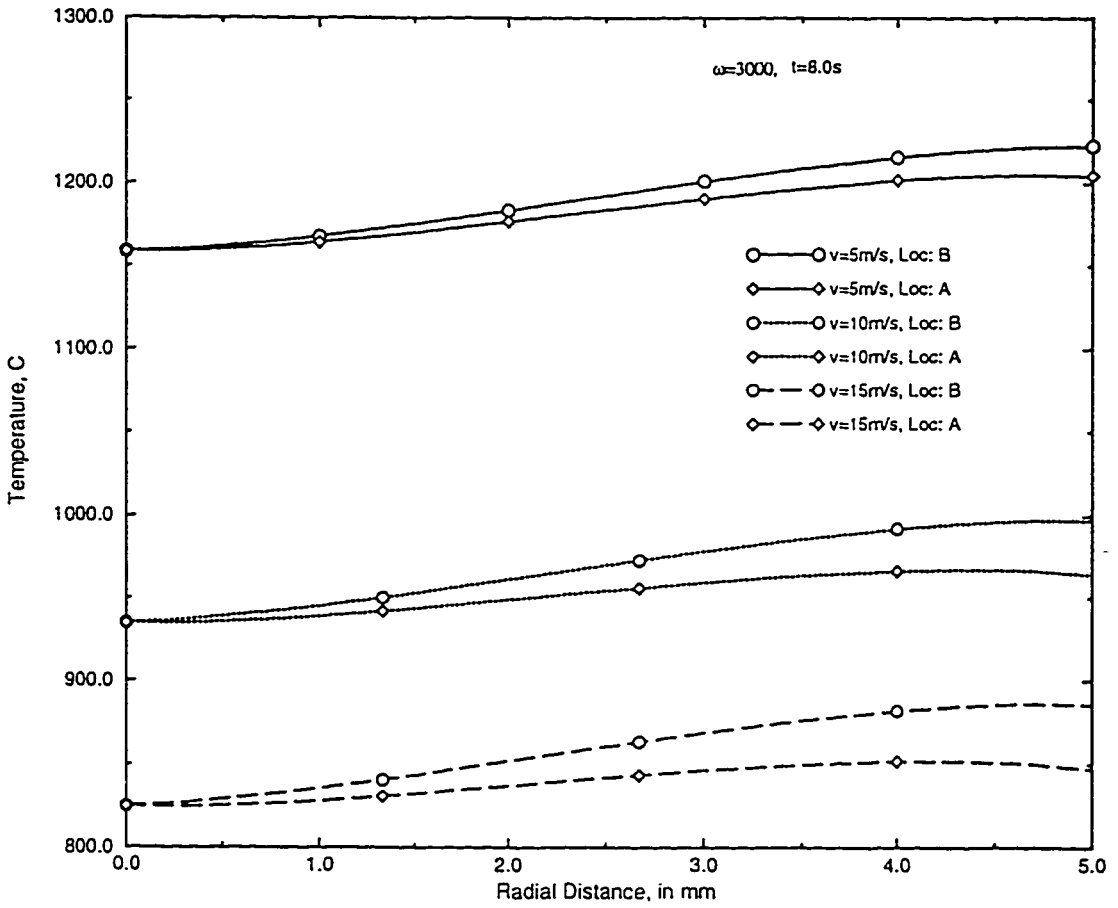

Figure 4.44: Comparison of radial temperature profiles at $\theta = 0.0$ and $\theta = \pi$ of a steel-copper friction weld at time t=8.0 s with an angular speed of 3000 rpm for different jet velocities.

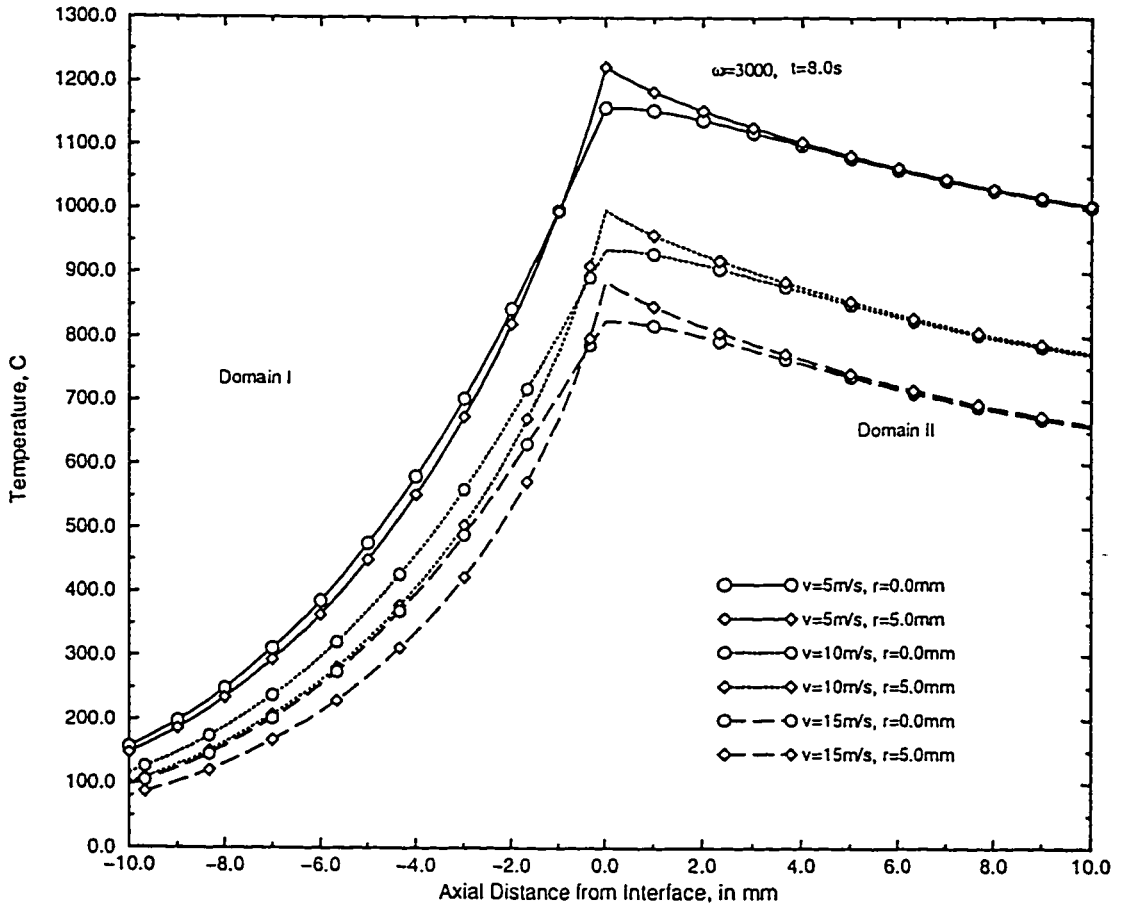

Figure 4.45: Comparison of axial temperature profiles at back stagnation point on the surface and at the center of a steel-copper friction weld at time t=8.0 s with an angular speed of 3000 rpm for different jet velocities.

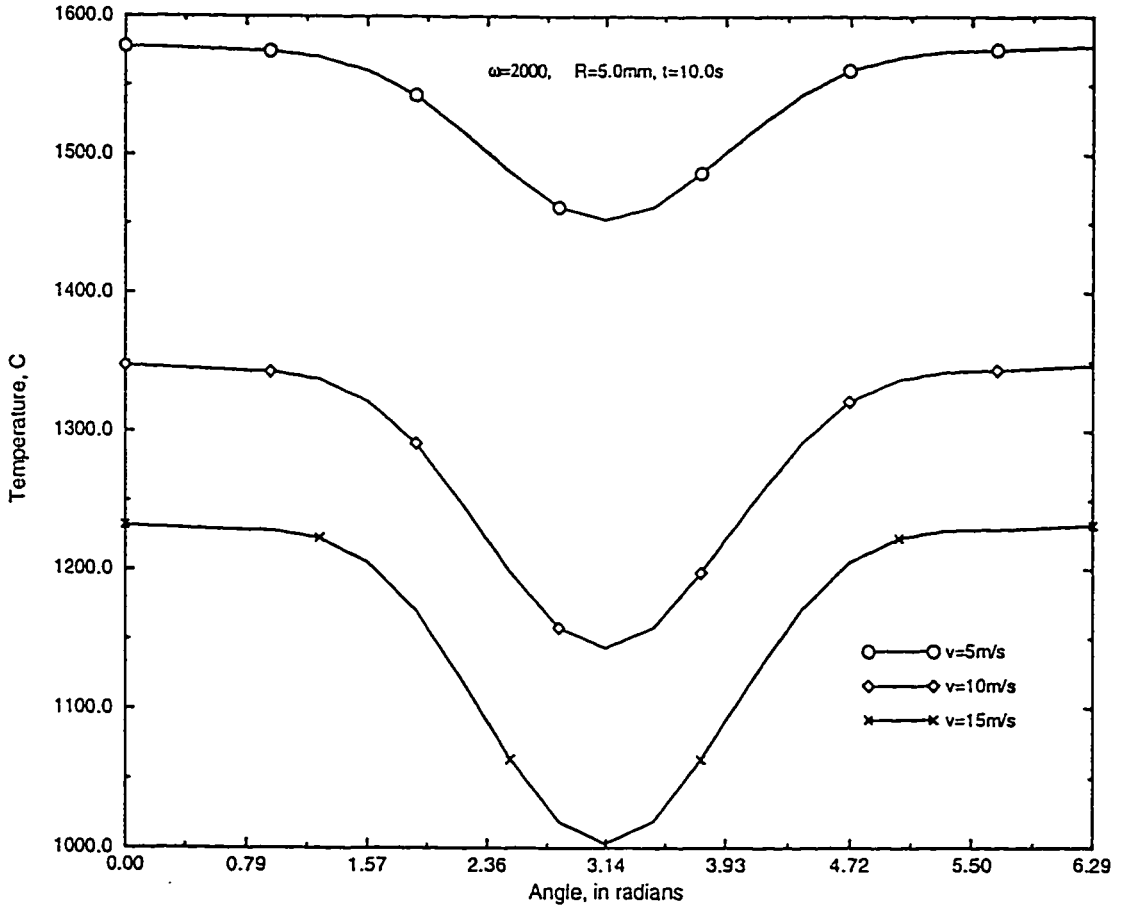

Figure 4.46: Comparison of circumferential temperature profiles on the surface of a steel-steel friction weld at time t=10.0 s with an angular speed of 2000 rpm for different jet velocities.

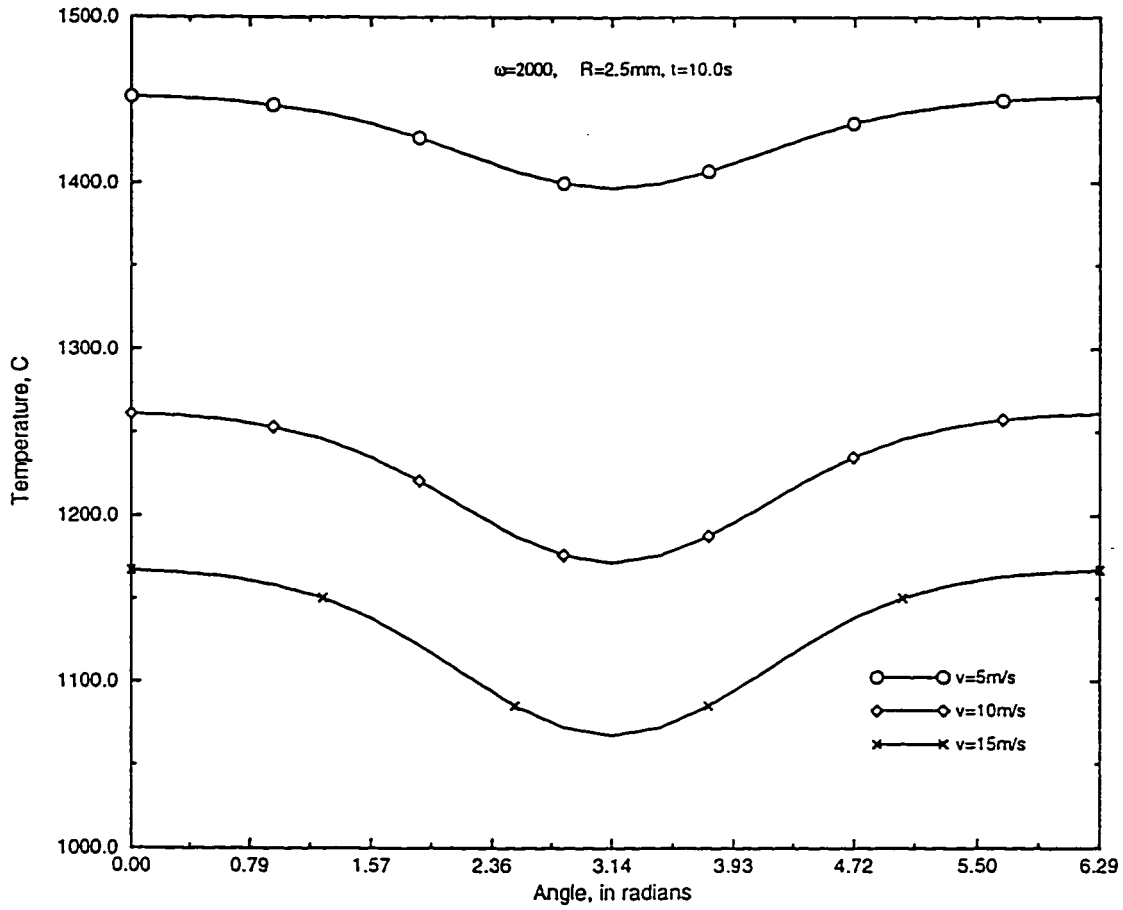

Figure 4.47: Comparison of circumferential temperature profiles at mid-radius of a steel-steel friction weld at time t=10.0 s with an angular speed of 2000 rpm for different jet velocities.

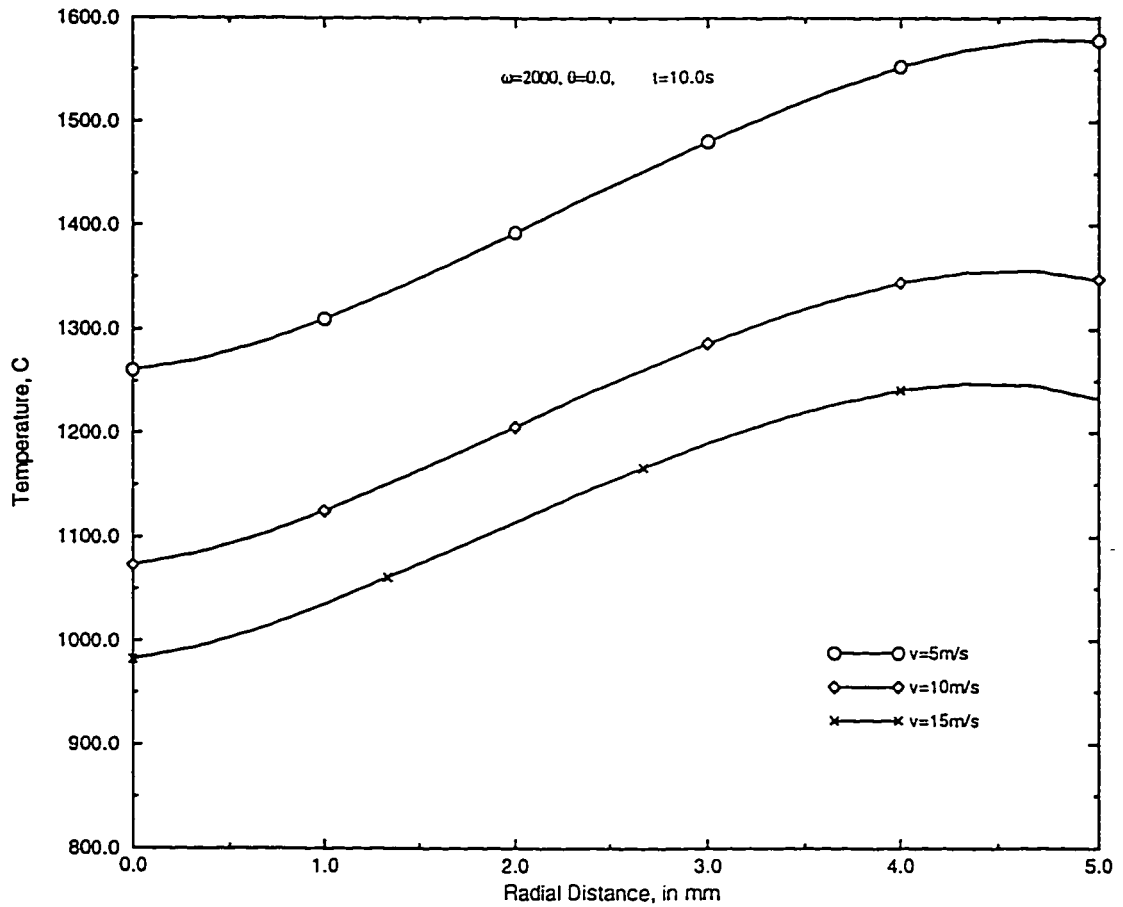

Figure 4.48: Comparison of radial temperature profiles at back stagnation point of a steel-steel friction weld at time t=10.0 s with an angular speed of 2000 rpm for different jet velocities.

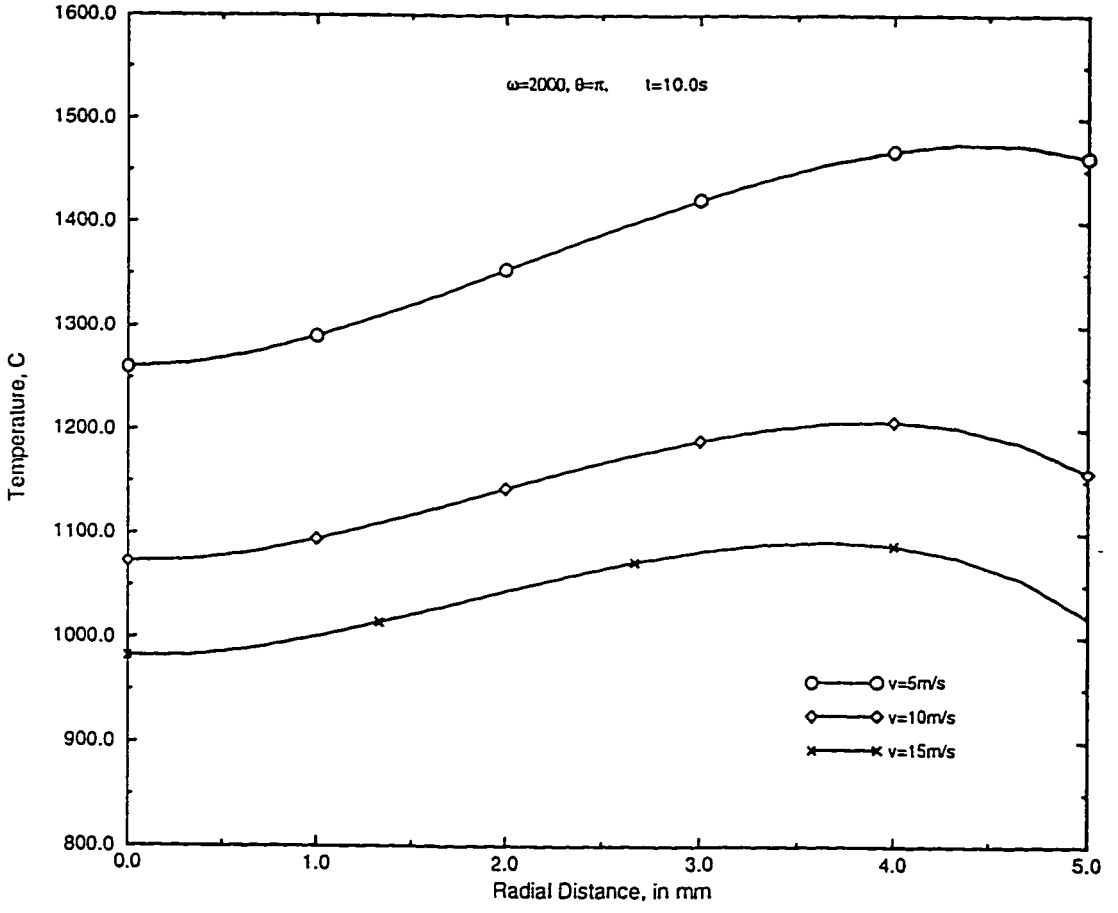

Figure 4.49: Comparison of radial temperature profiles at front stagnation point of a steel-steel friction weld at time t=10.0 s with an angular speed of 2000 rpm for different jet velocities.

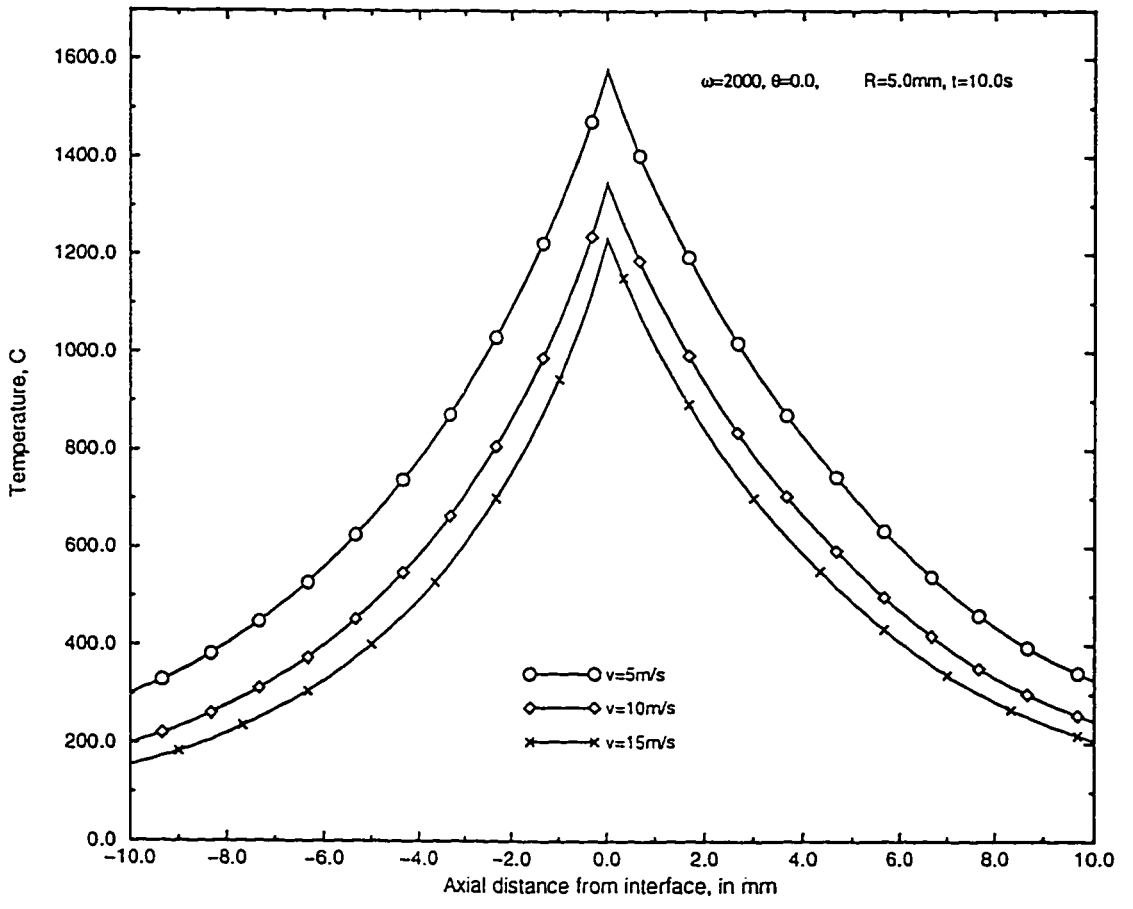

Figure 4.50: Comparison of axial temperature profiles on the surface at back stagnation point of a steel-steel friction weld at time t=10.0s with an angular speed of 2000 rpm for different jet velocities.

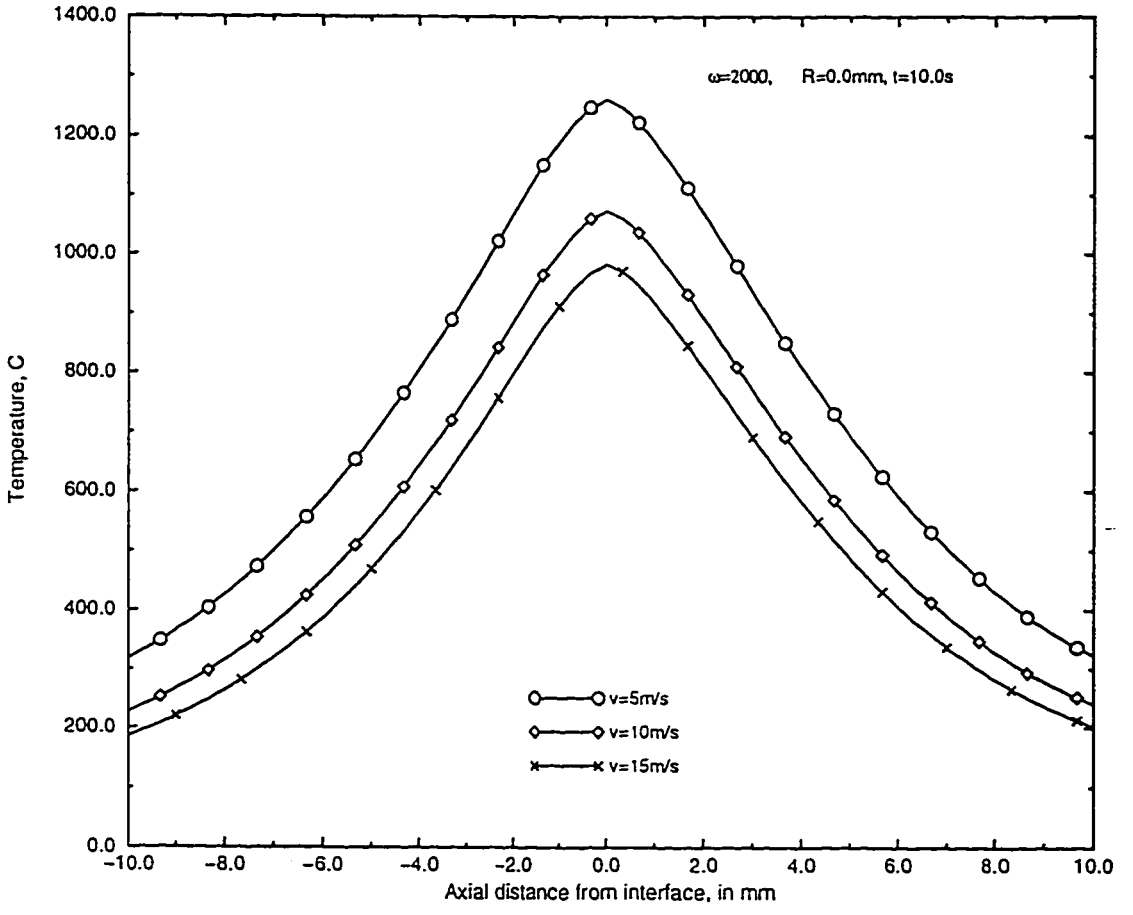

Figure 4.51: Comparison of centerline temperature profiles of a steel-steel friction weld at time t=10.0s with an angular speed of 2000 rpm for different jet velocities.

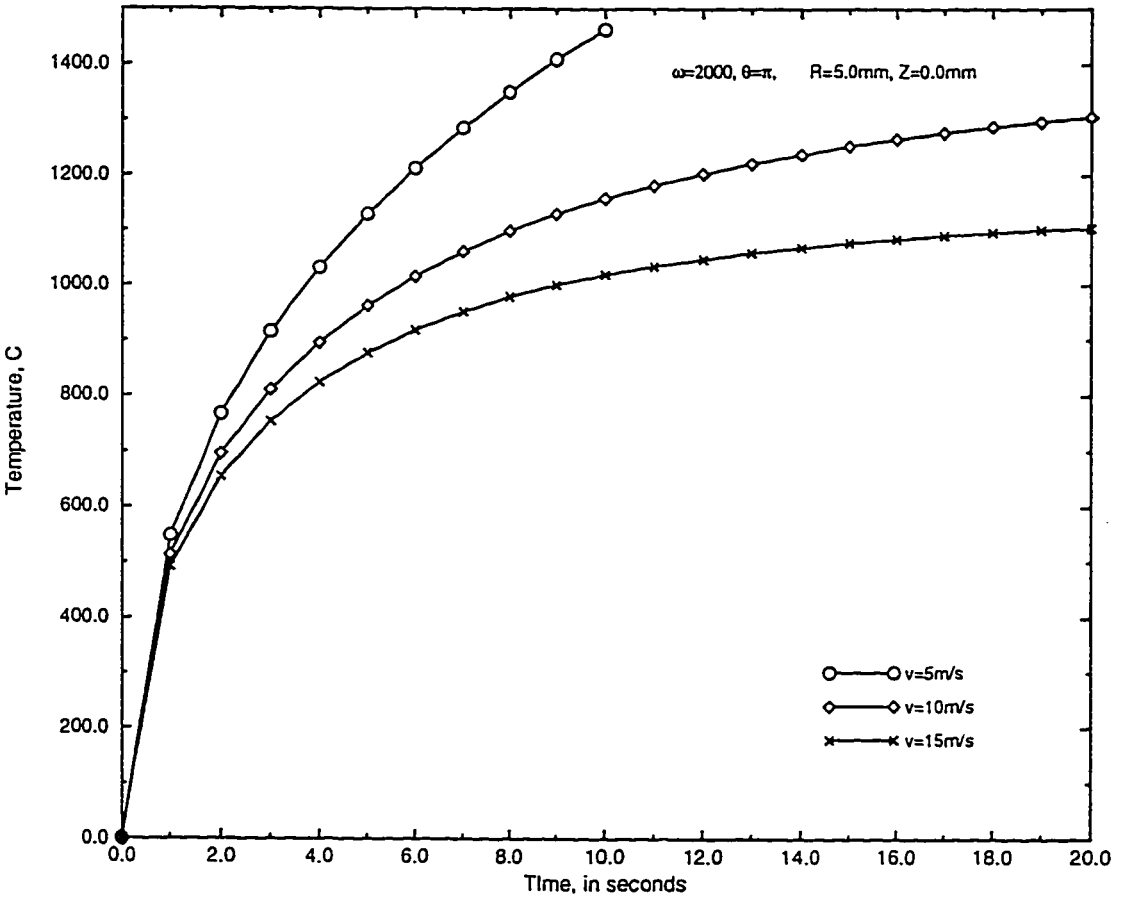

Figure 4.52: Comparison of temperature raise at front stagnation point of a steel-steel friction weld with an angular speed of 2000 rpm for different jet velocities.

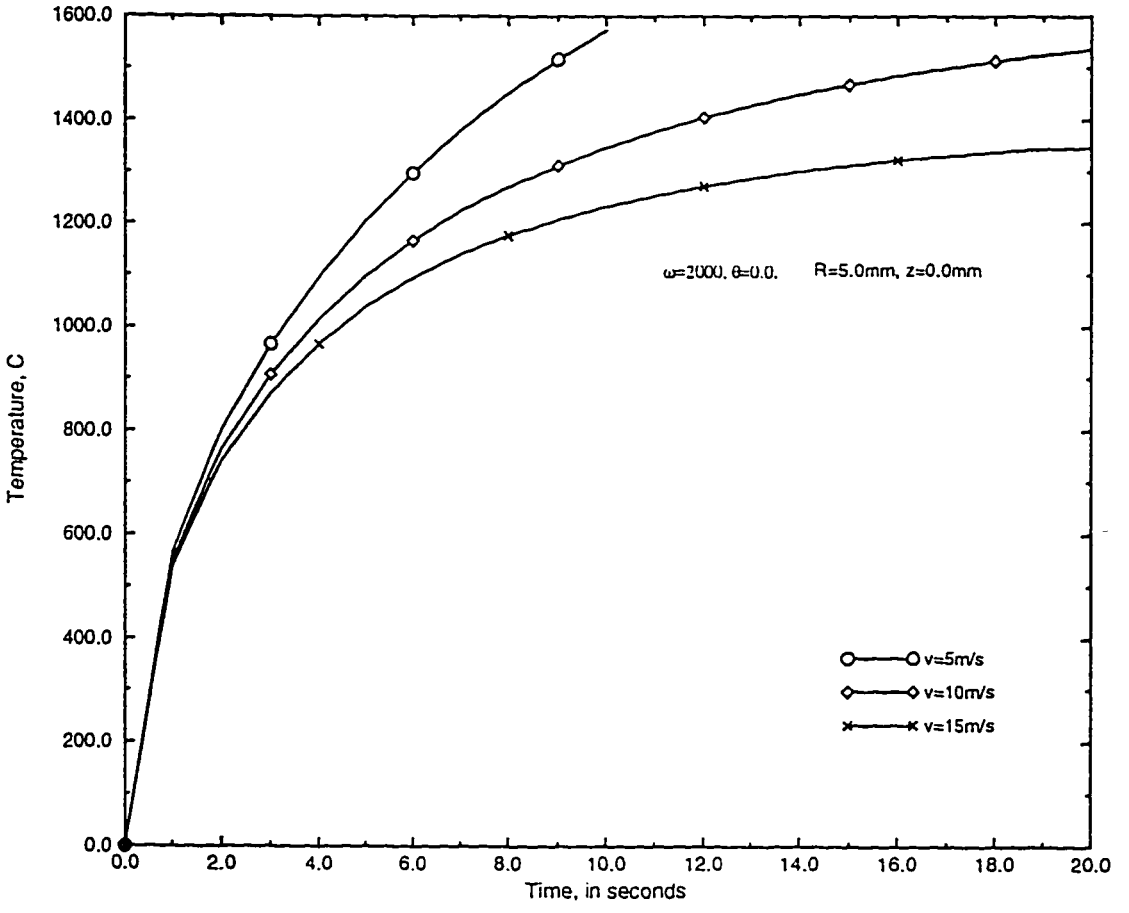

Figure 4.53: Comparison of temperature raise at back stagnation point of a steel-steel friction weld with an angular speed of 2000 rpm for different jet velocities.

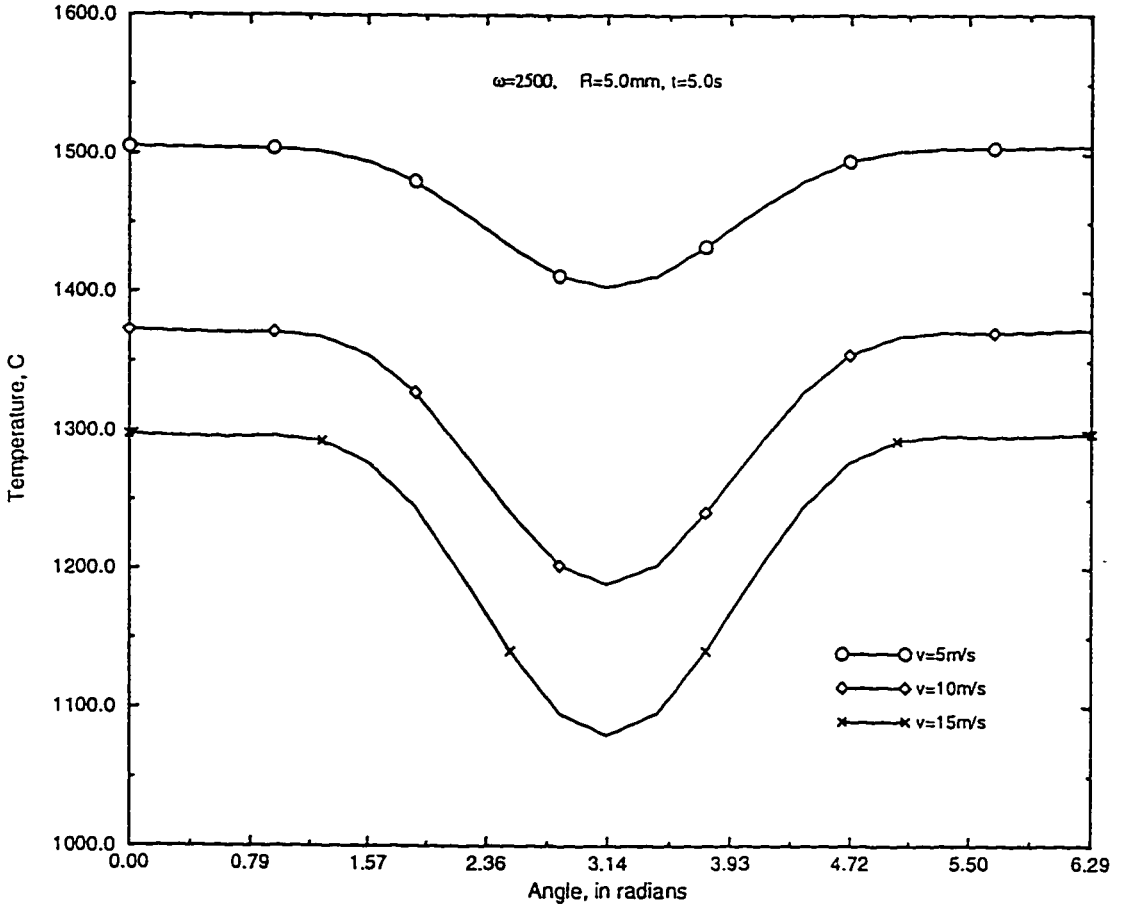

Figure 4.54: Comparison of circumferential temperature profiles on the surface of a steel-steel friction weld at time t=5.0 s with an angular speed of 2500 rpm for different jet velocities.

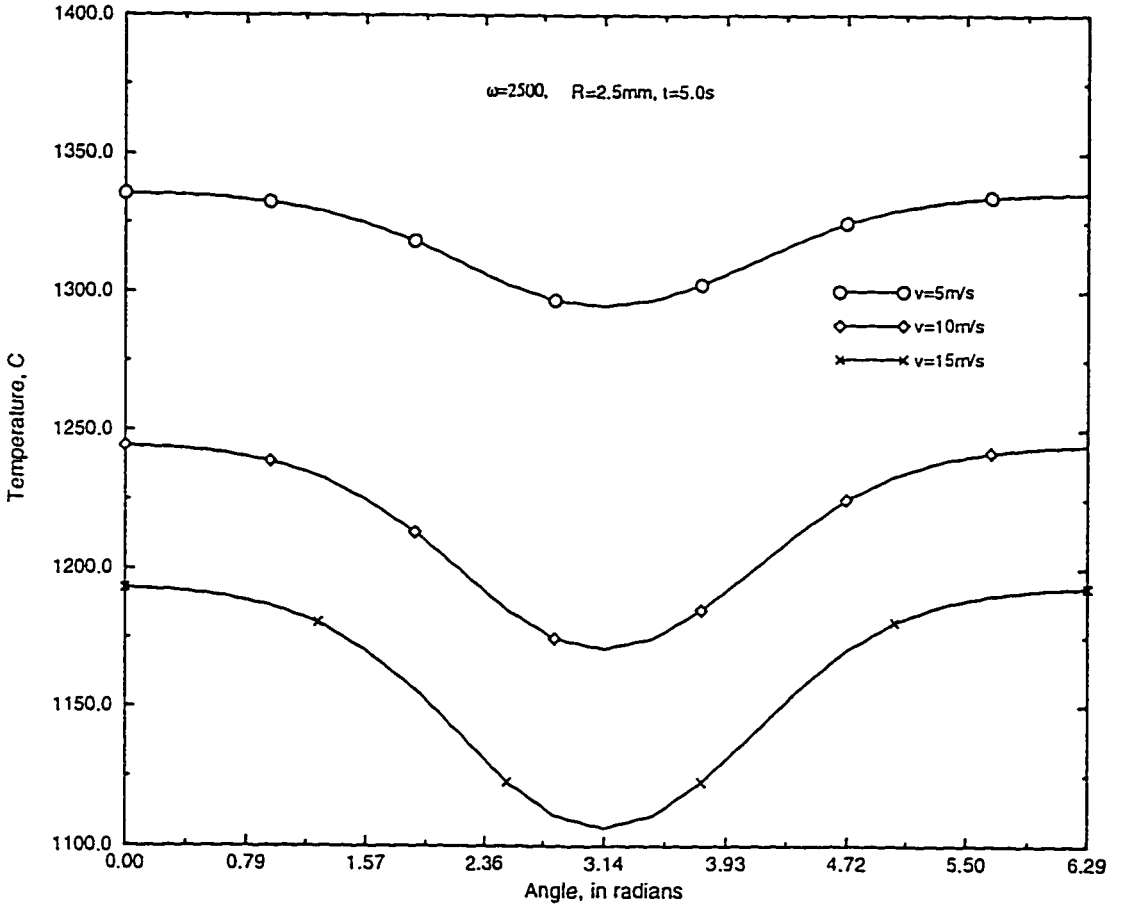

Figure 4.55: Comparison of circumferential temperature profiles at mid-radius of a steel-steel friction weld at time t=5.0 s with an angular speed of 2500 rpm for different jet velocities.

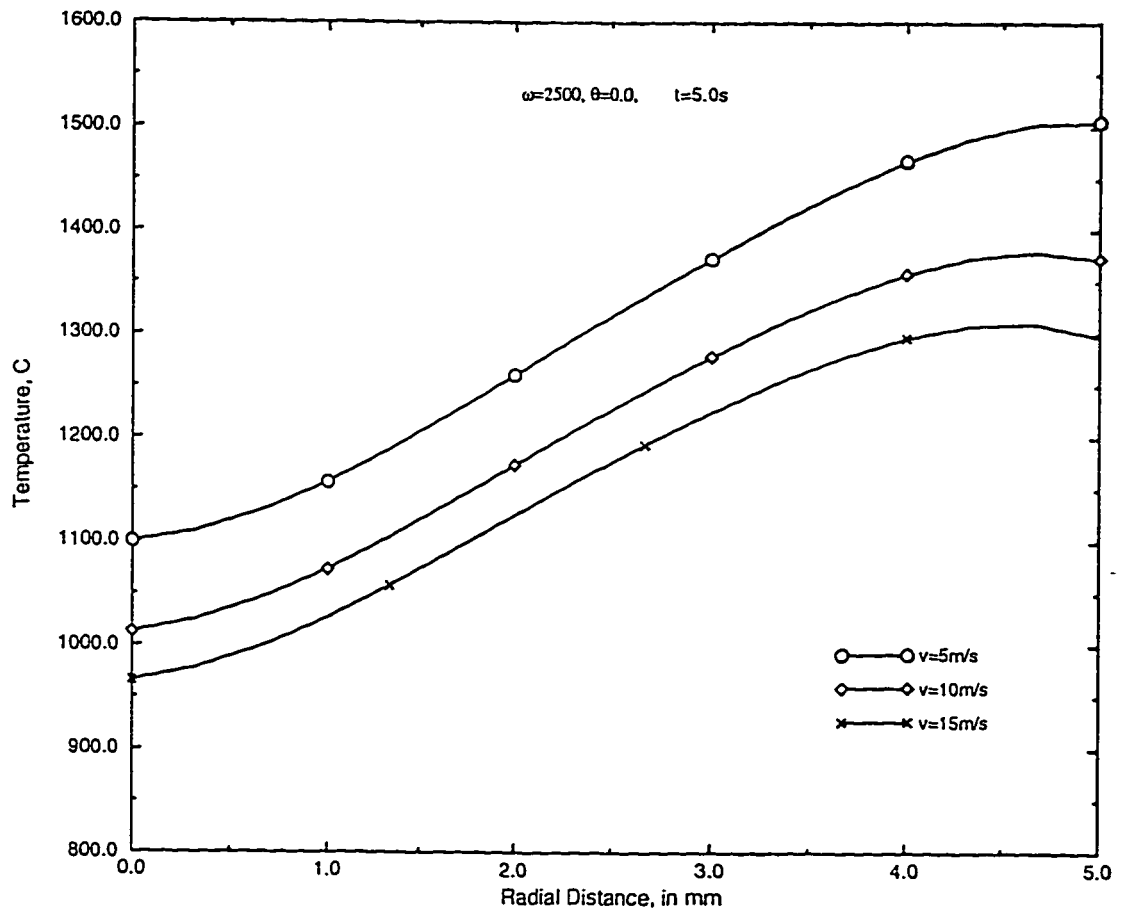

Figure 4.56: Comparison of radial temperature profiles at back stagnation point of a steel-steel friction weld at time t=5.0 s with an angular speed of 2500 rpm for different jet velocities.

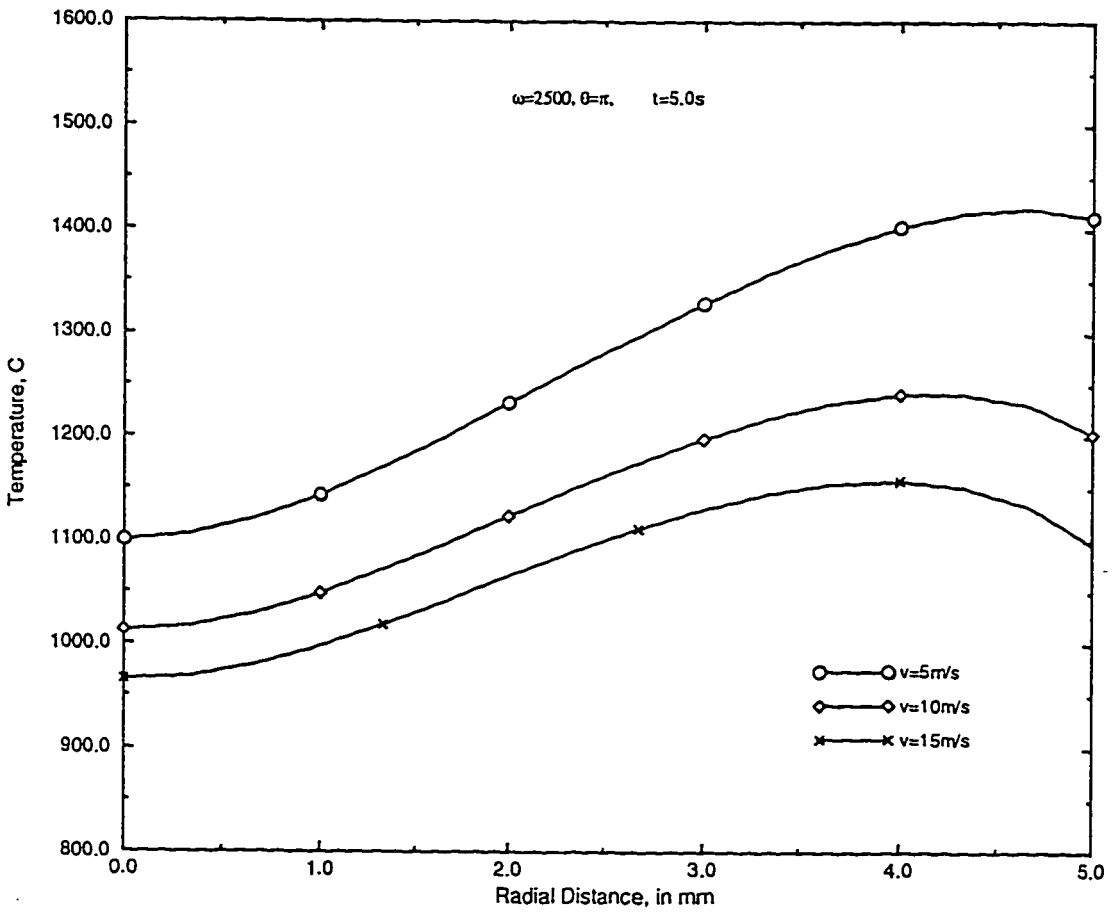

Figure 4.57: Comparison of radial temperature profiles at front stagnation point of a steel-steel friction weld at time t=5.0 s with an angular speed of 2500 rpm for different jet velocities.

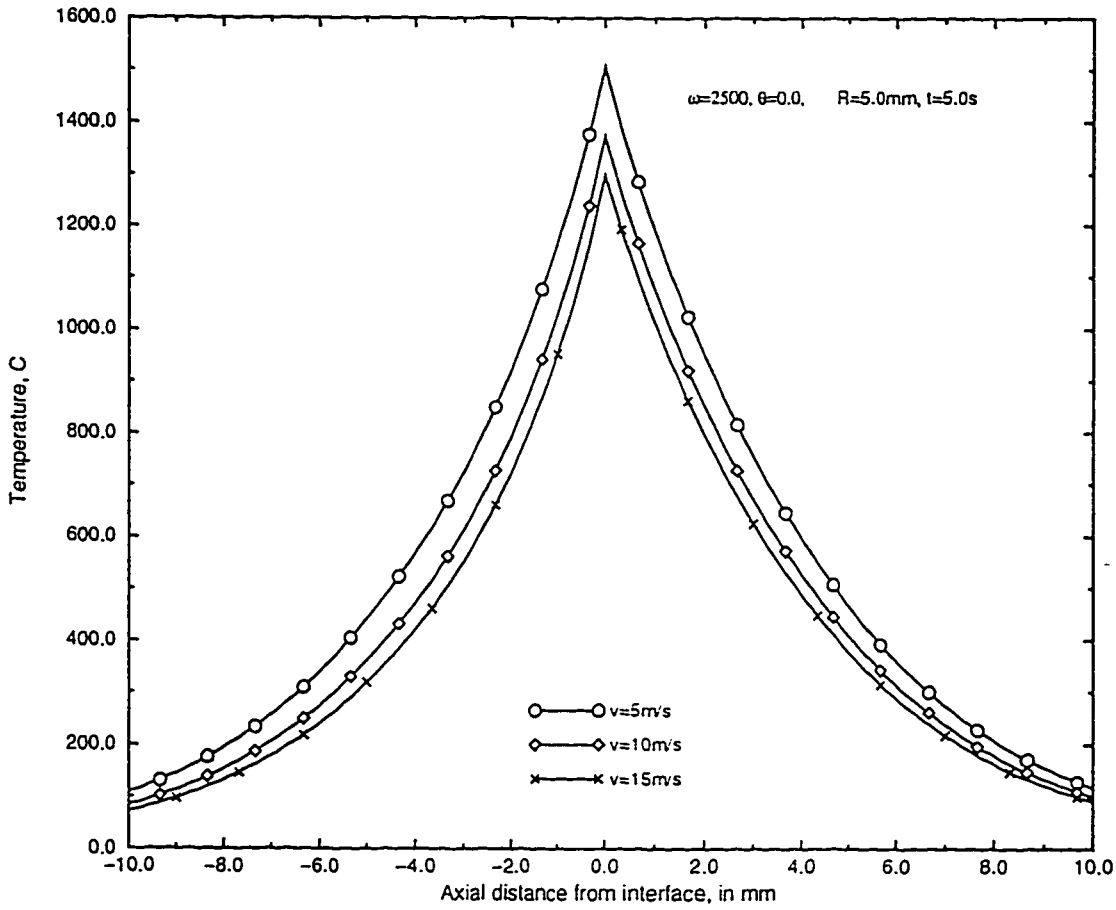

Figure 4.58: Comparison of axial temperature profiles on the surface at back stagnation point of a steel-steel friction weld at time t=5.0s with an angular speed of 2500 rpm for different jet velocities.

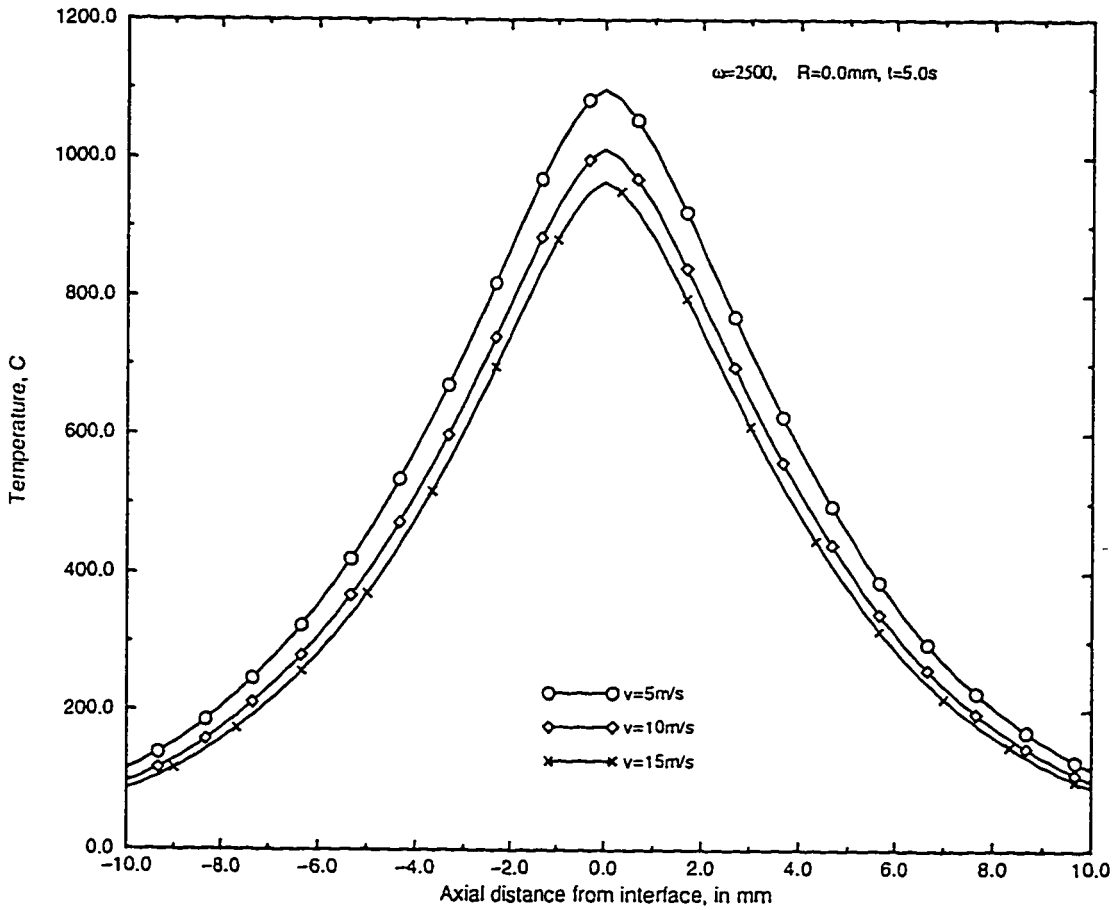

Figure 4.59: Comparison of centerline temperature profiles of a steel-steel friction weld at time t=5.0s with an angular speed of 2500 rpm for different jet velocities.

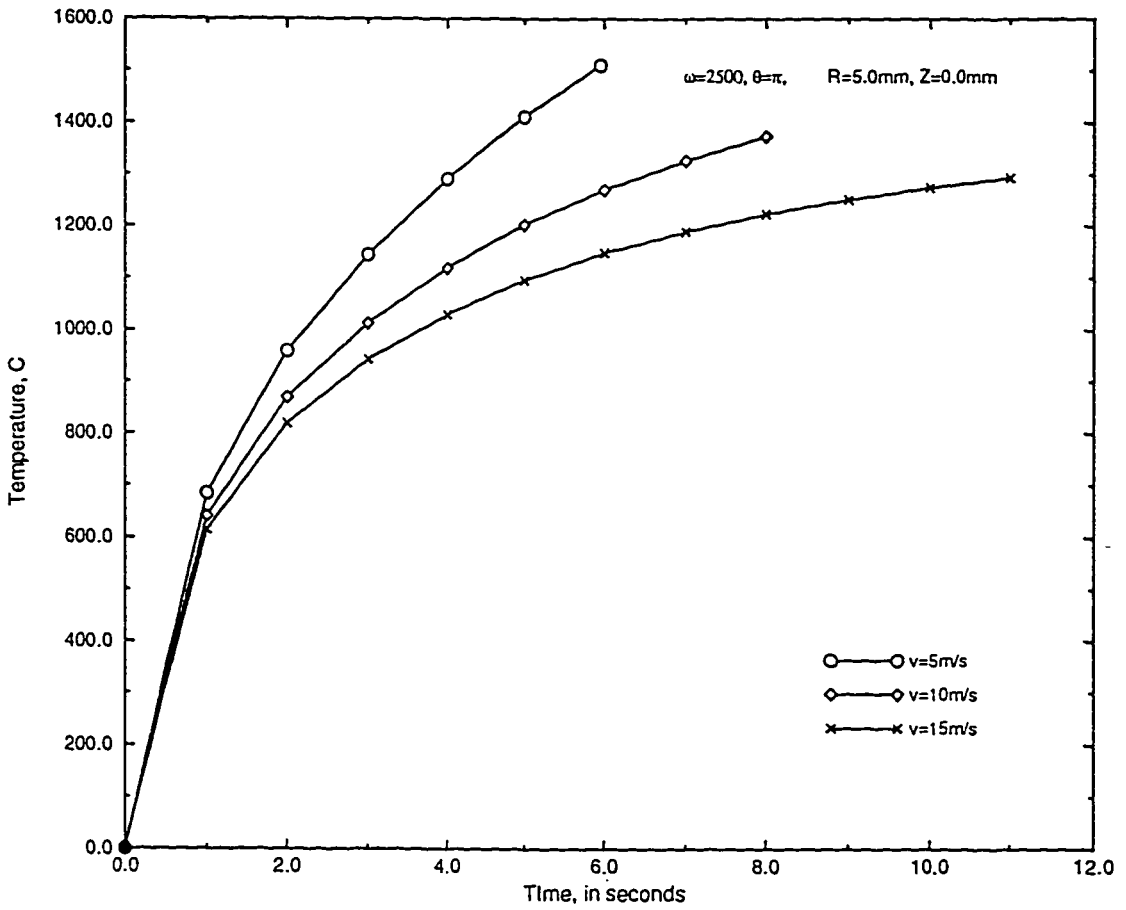

Figure 4.60: Comparison of temperature raise at front stagnation point of a steel-steel friction weld with an angular speed of 2500 rpm for different jet velocities.

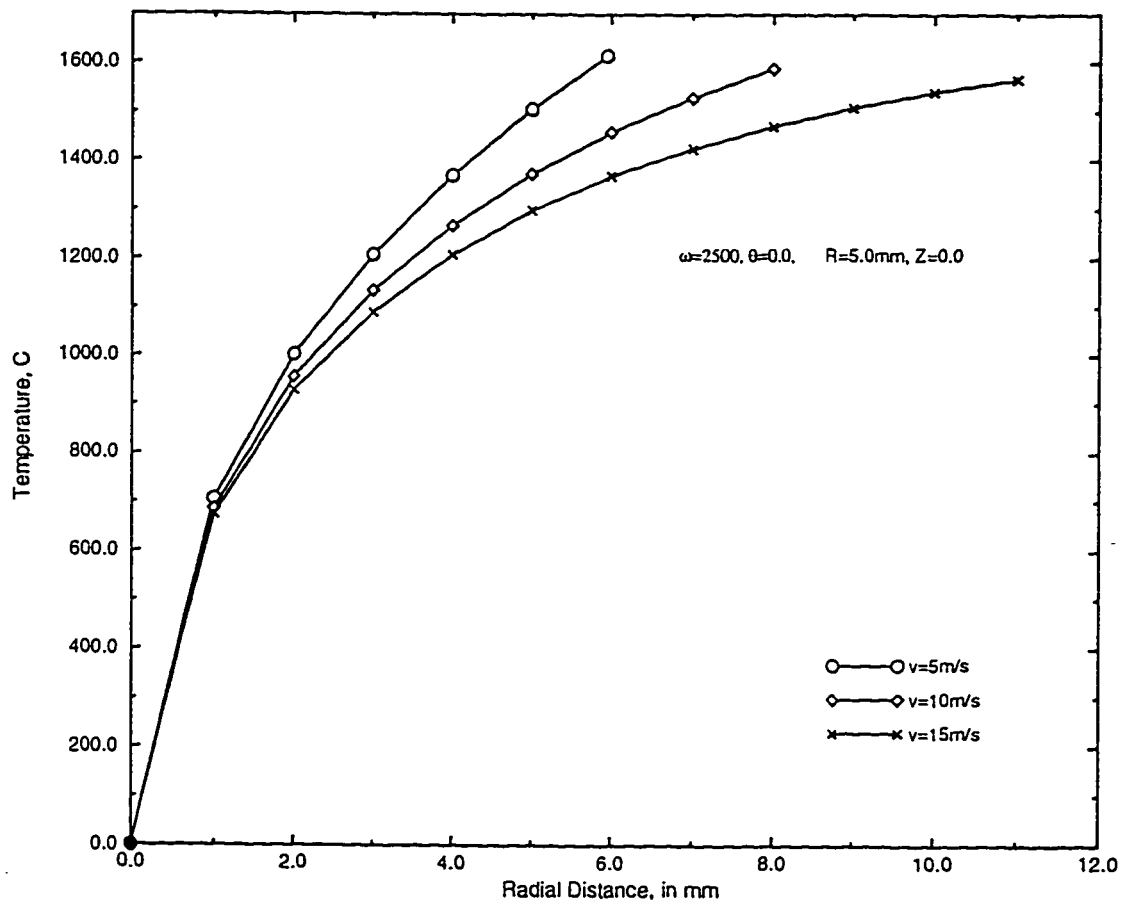

Figure 4.61: Comparison of temperature raise at back stagnation point of a steel-steel friction weld with an angular speed of 2500 rpm for different jet velocities.

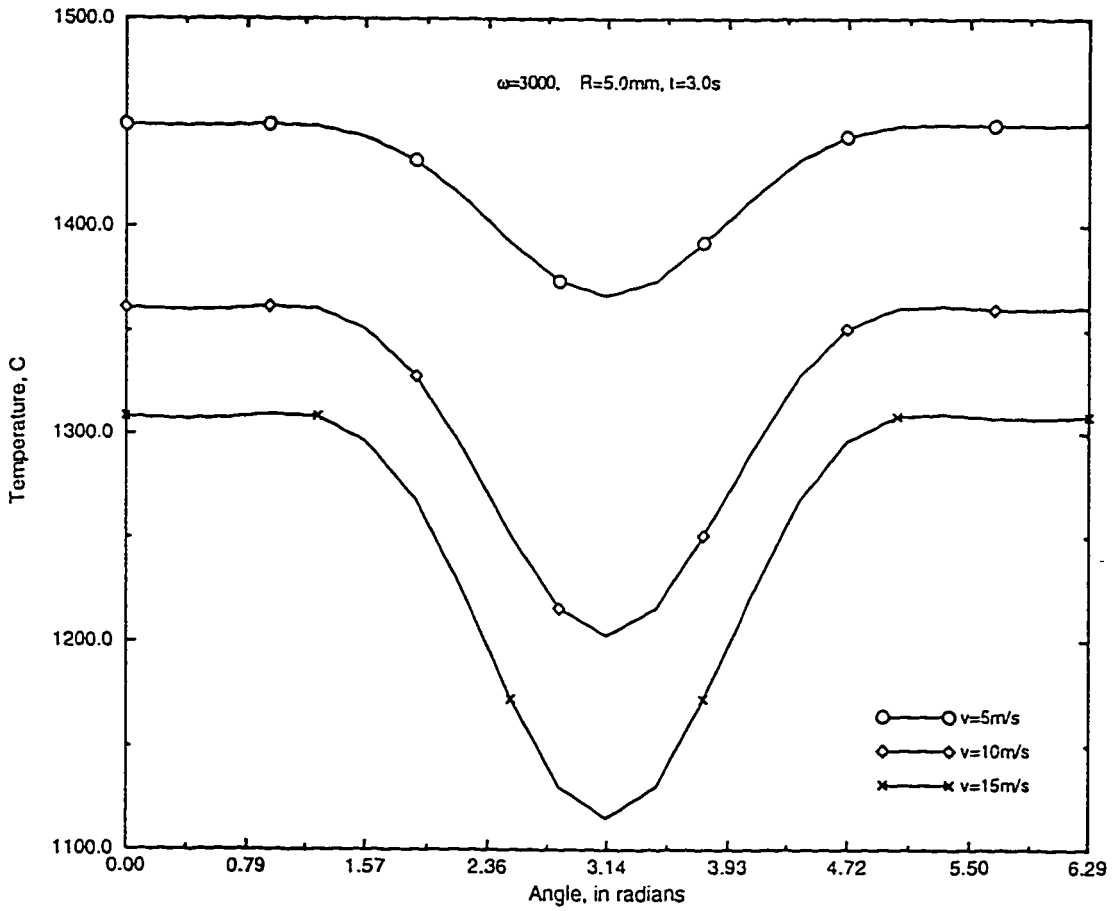

Figure 4.62: Comparison of circumferential temperature profiles on the surface of a steel-steel friction weld at time t=3.0s with an angular speed of 3000 rpm for different jet velocities.

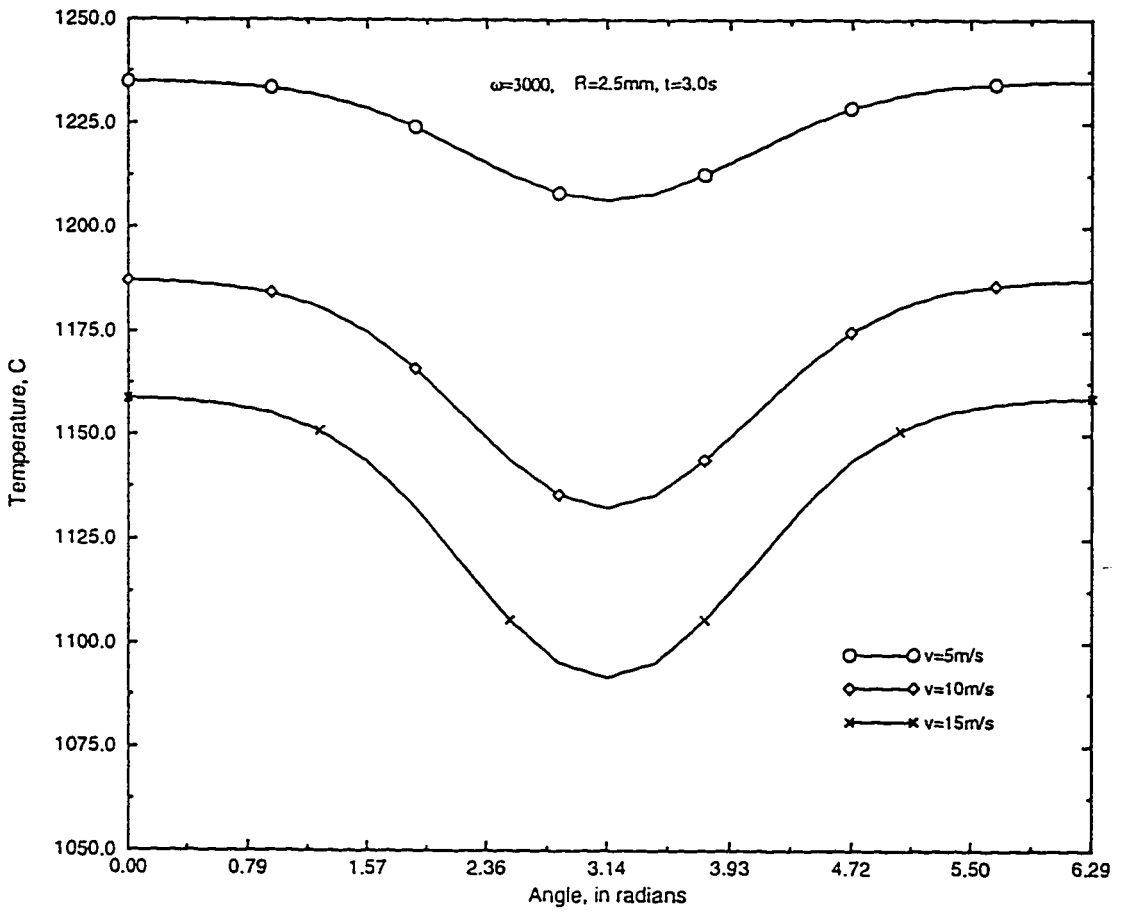

Figure 4.63: Comparison of circumferential temperature profiles at mid-radius of a steel-steel friction weld at time t=3.0s with an angular speed of 3000 rpm for different jet velocities.

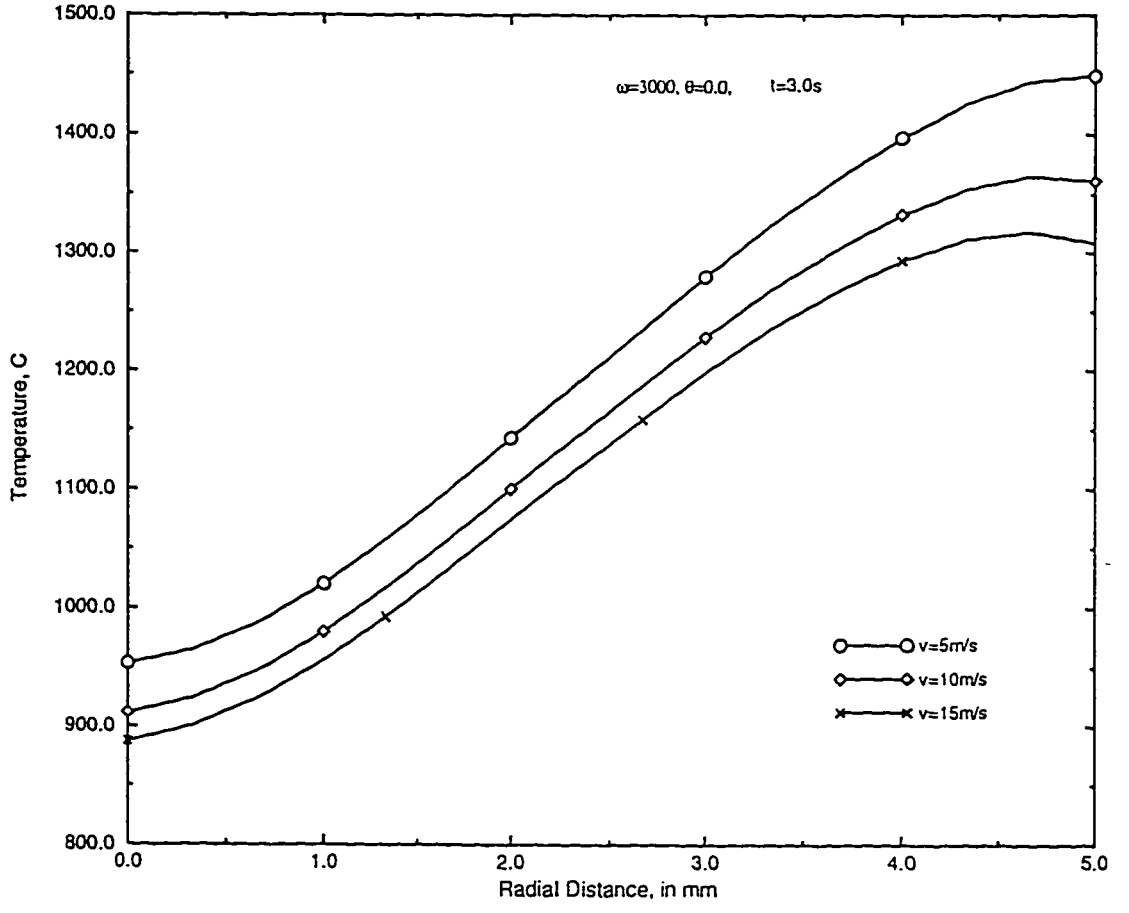

Figure 4.64: Comparison of radial temperature profiles at back stagnation point of a steel-steel friction weld at time t=3.0s with an angular speed of 3000 rpm for different jet velocities.

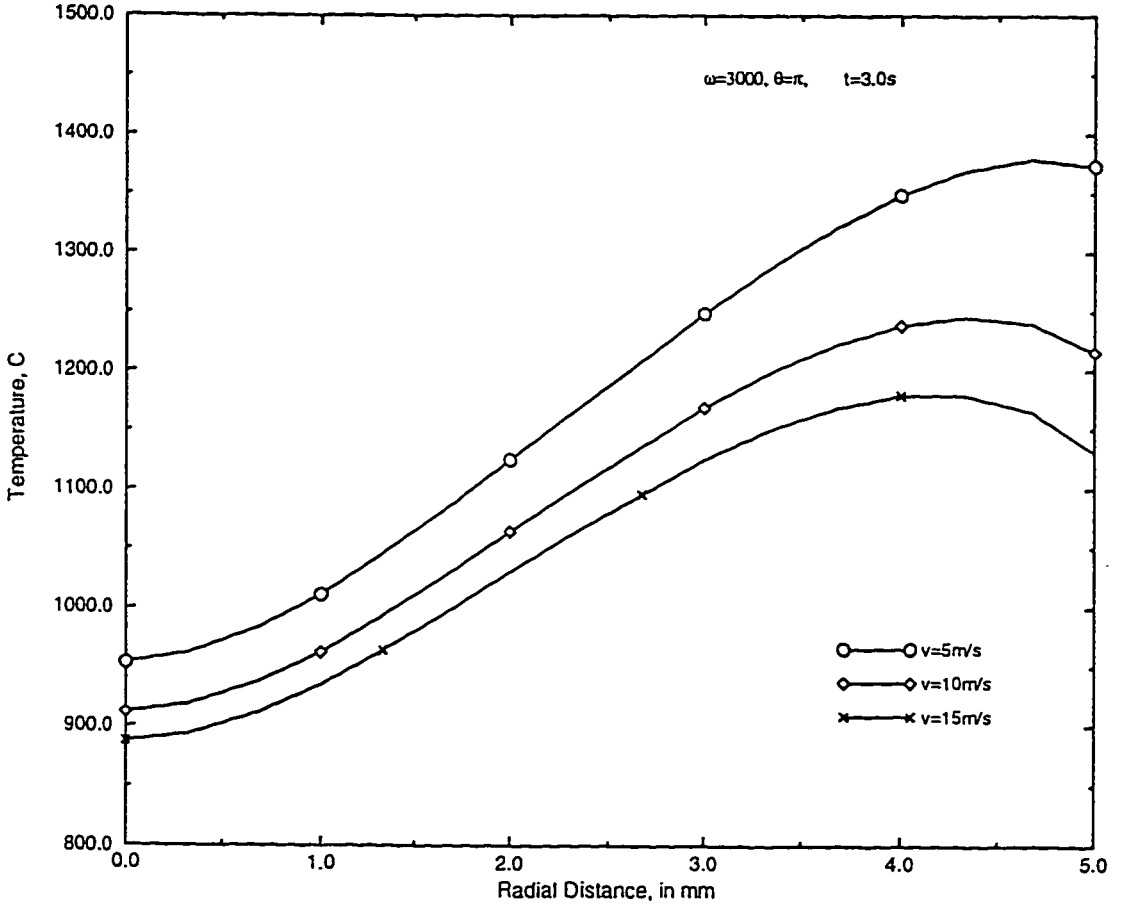

Figure 4.65: Comparison of radial temperature profiles at front stagnation point of a steel-steel friction weld at time t=3.0s with an angular speed of 3000 rpm for different jet velocities.

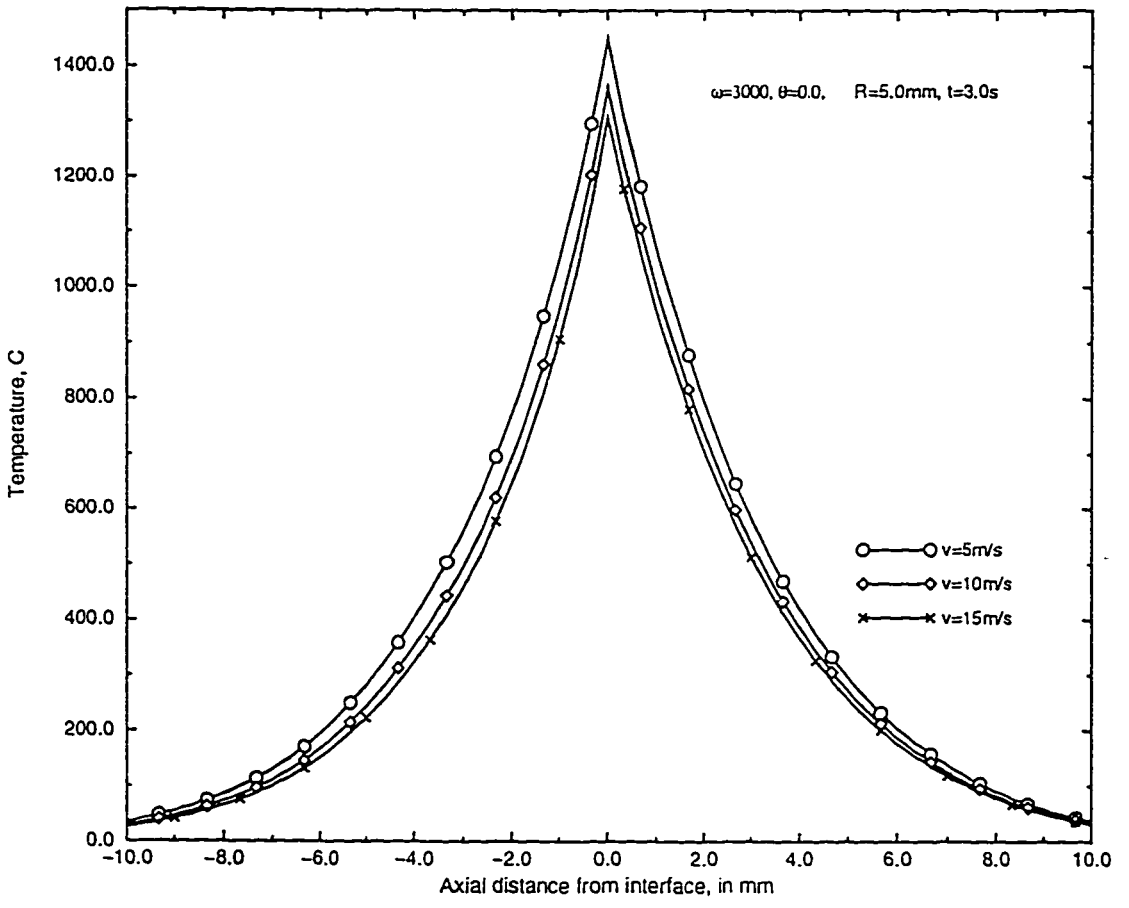

Figure 4.66: Comparison of axial temperature profiles on the surface at back stagnation point of a steel-steel friction weld at time t=3.0s with an angular speed of 3000 rpm for different jet velocities.

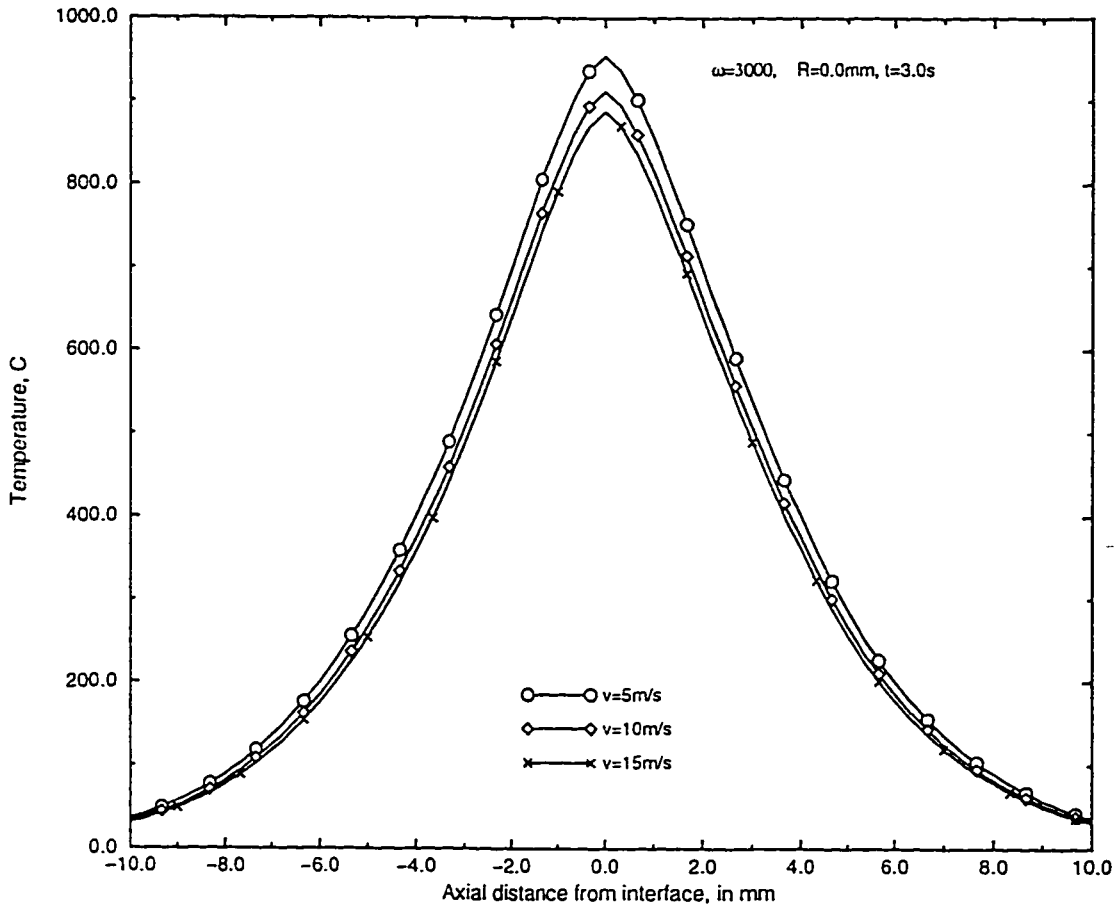

Figure 4.67: Comparison of centerline temperature profiles of a steel-steel friction weld at time t=3.0s with an angular speed of 3000 rpm for different jet velocities.

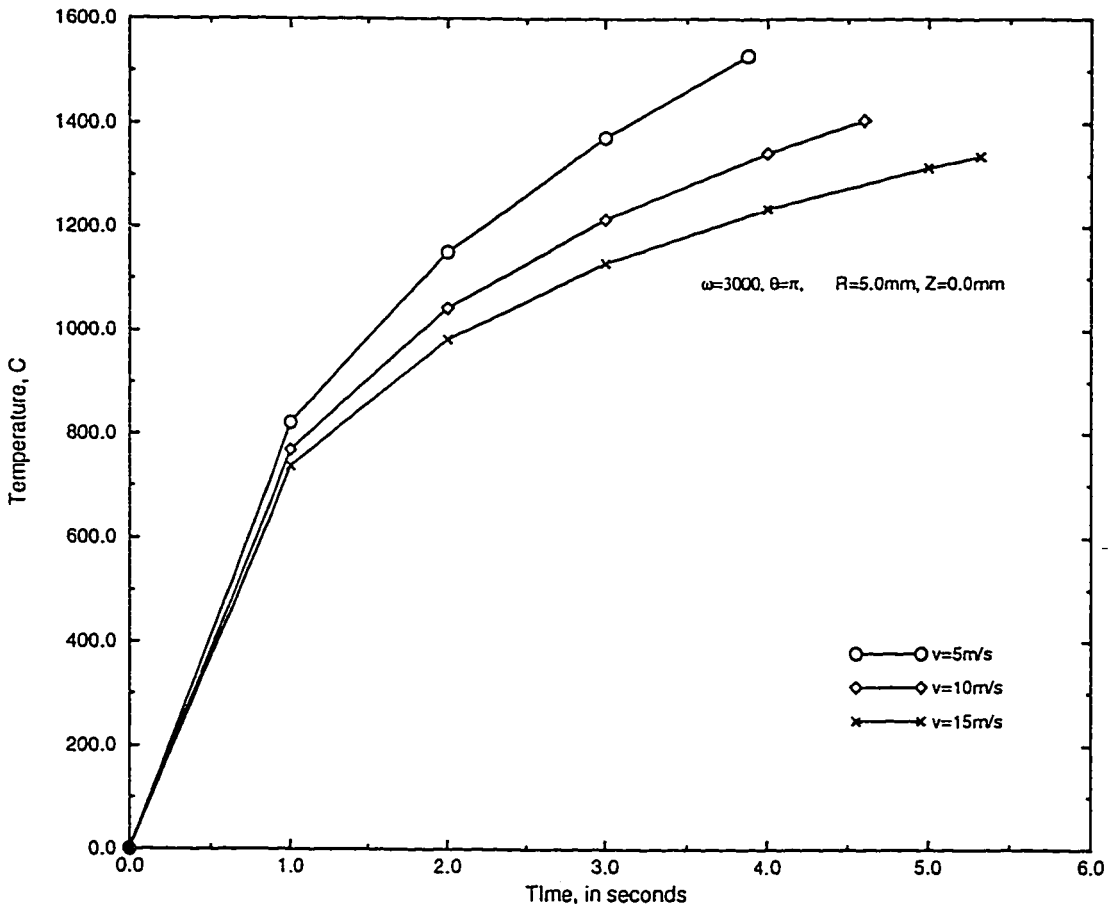

Figure 4.68: Comparison of temperature raise at front stagnation point of a steel-steel friction weld with an angular speed of 3000 rpm for different jet velocities.

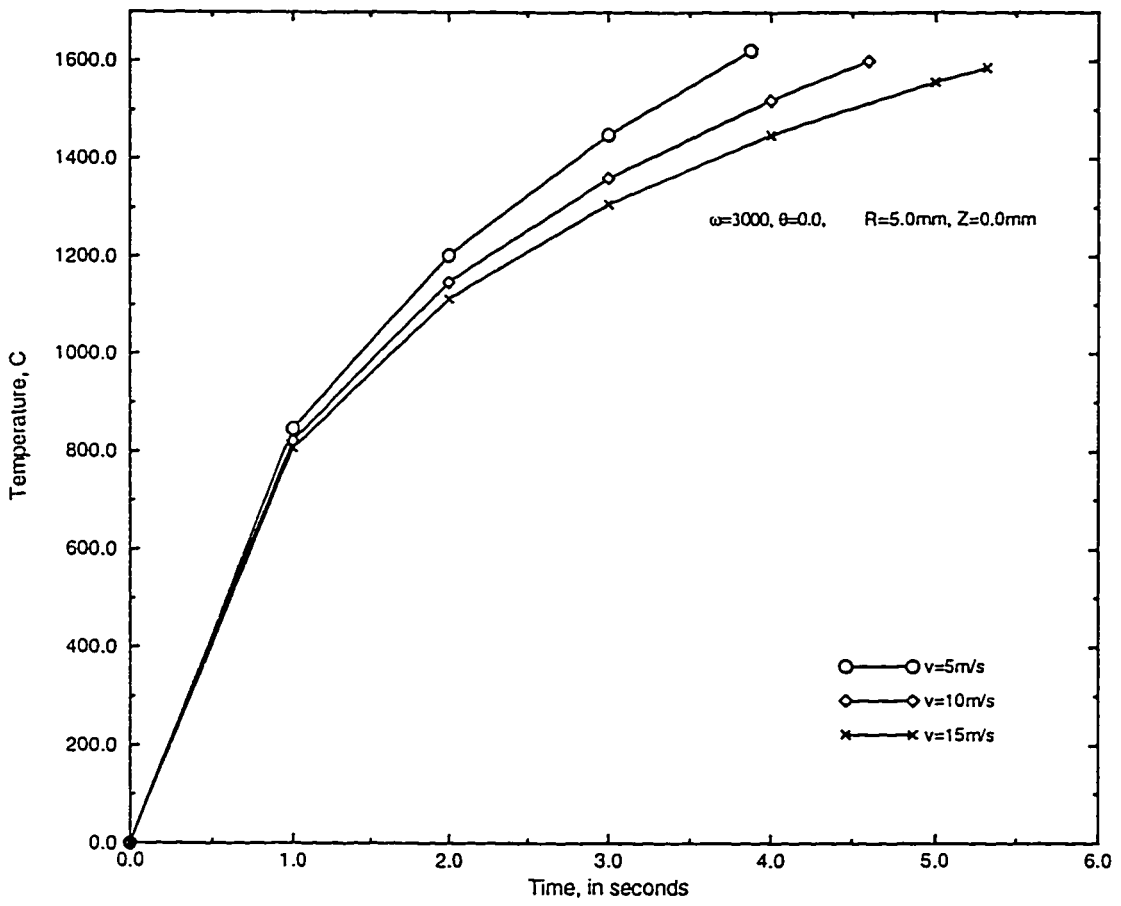

Figure 4.69: Comparison of temperature raise at back stagnation point of a steel-steel friction weld with an angular speed of 3000 rpm for different jet velocities.

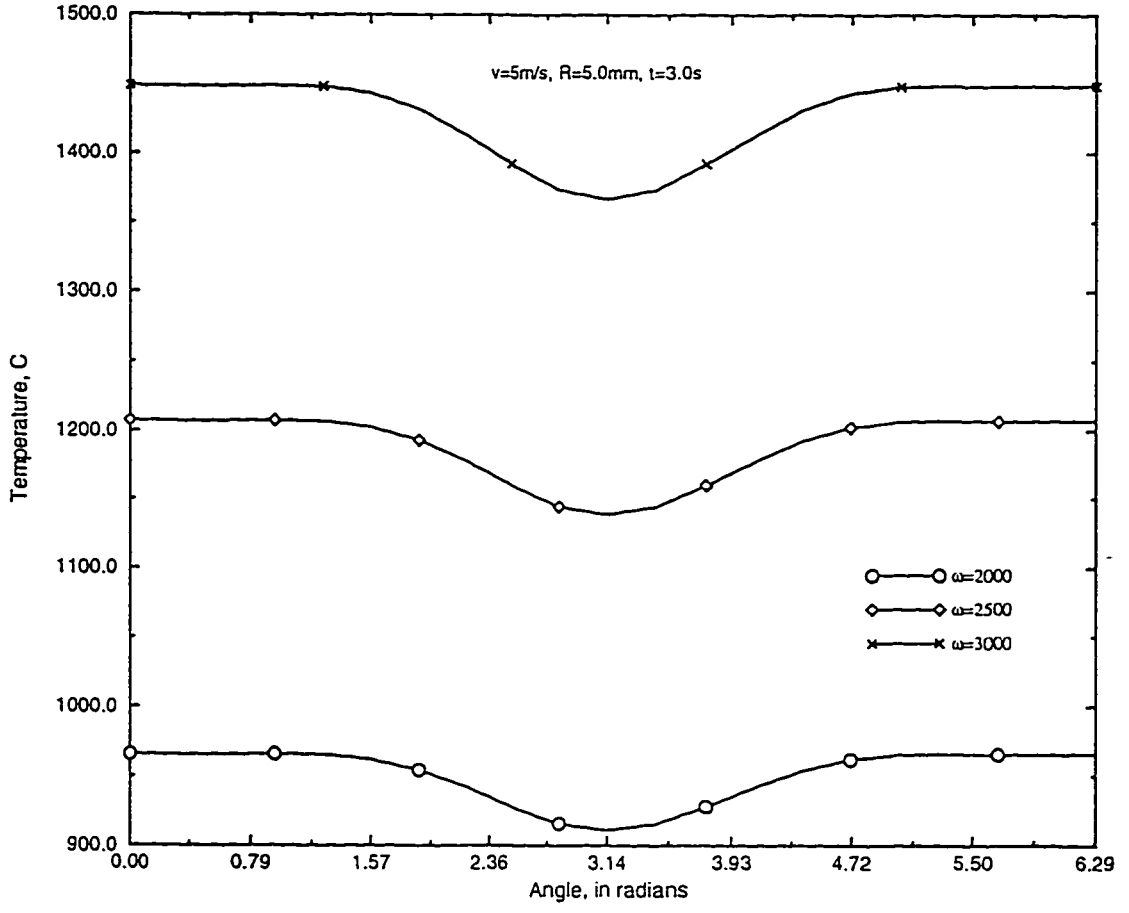

Figure 4.70: Comparison of circumferential temperature profiles on the surface of a steel-steel friction weld at time t=3.0 s with a jet velocity of v=5 m/s for different angular speeds.

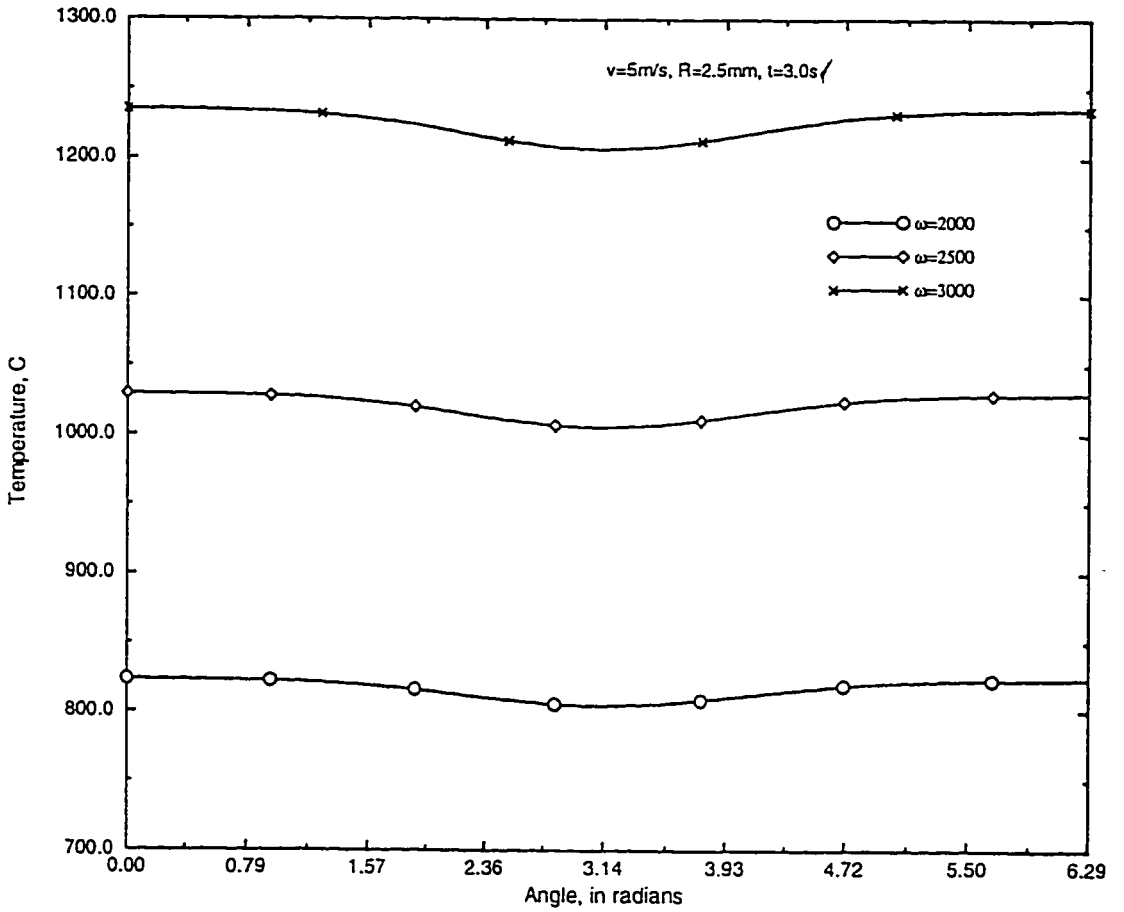

Figure 4.71: Comparison of circumferential temperature profiles at mid-radius of a steel-steel friction weld at time t=3.0 s with a jet velocity of v=5 m/s for different angular speeds.

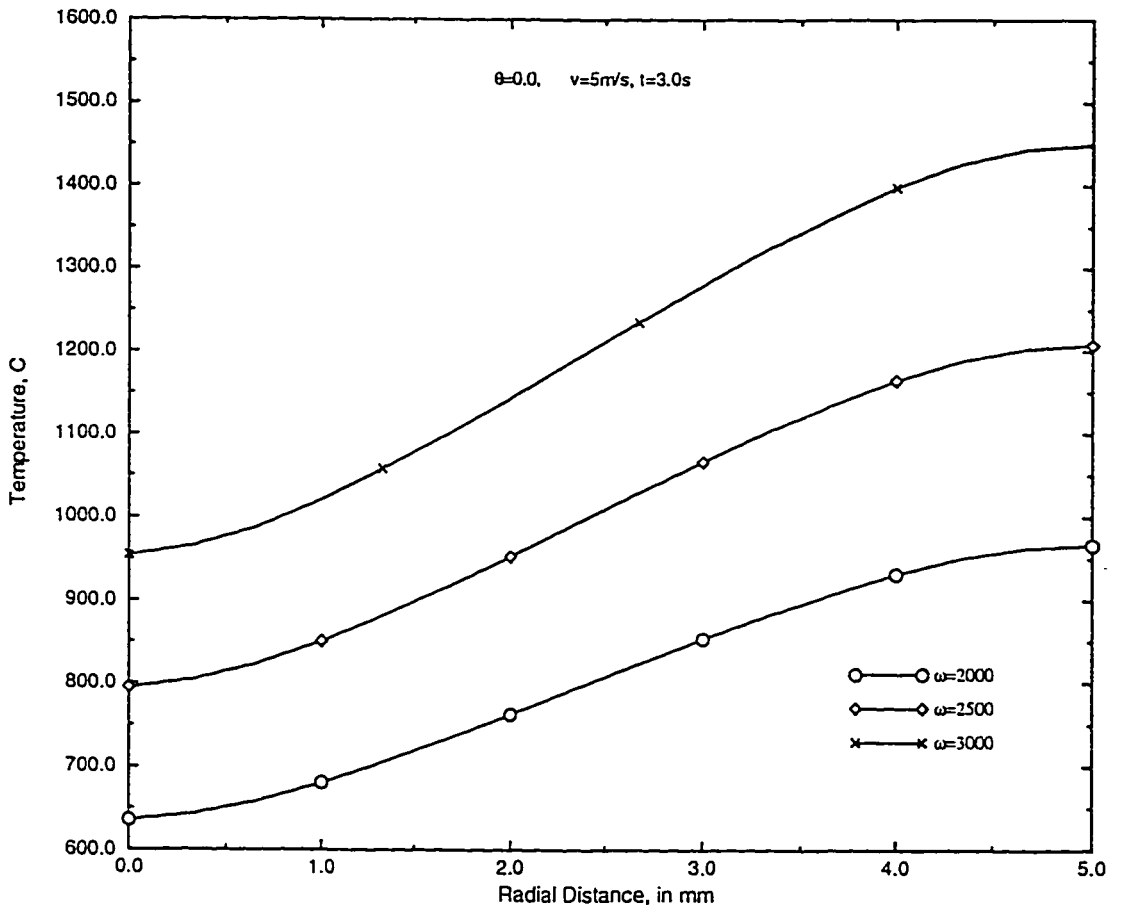

Figure 4.72: Comparison of radial temperature profiles at back stagnation point of a steel-steel friction weld at time t=3.0 s with a jet velocity of v=5 m/s for different angular speeds.

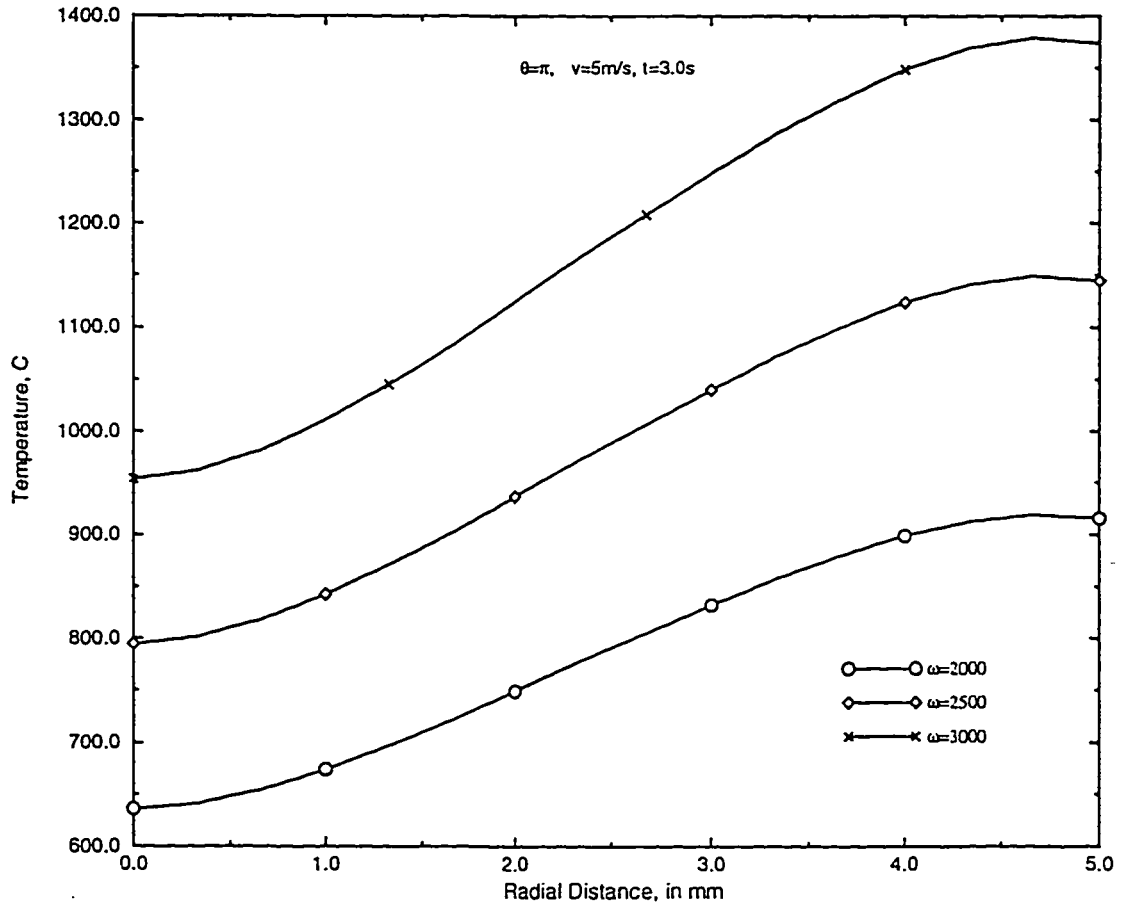

Figure 4.73: Comparison of radial temperature profiles at front stagnation point of a steel-steel friction weld at time t=3.0 s with a jet velocity of v=5 m/s for different angular speeds.

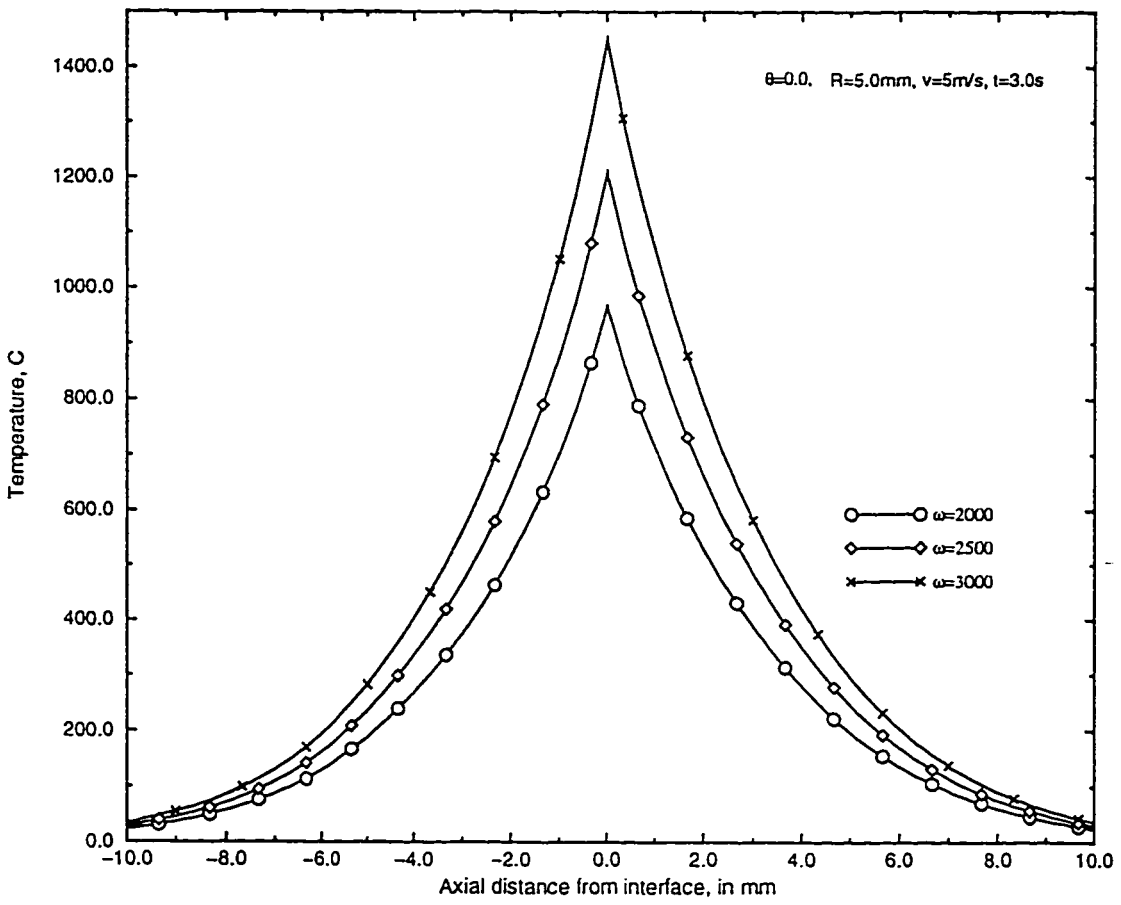

Figure 4.74: Comparison of radial temperature profiles at back stagnation point of a steel-steel friction weld at time t=3.0 s with a jet velocity of v=5 m/s for different angular speeds.

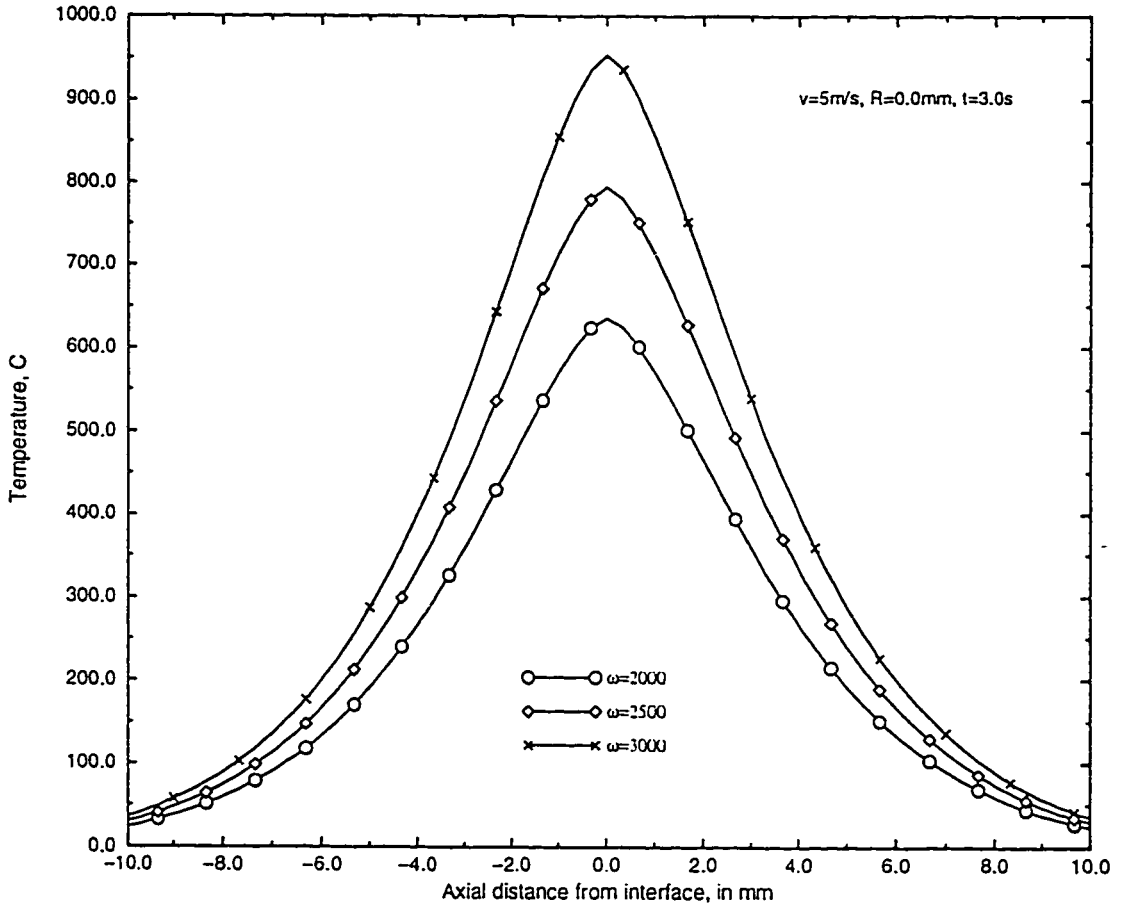

Figure 4.75: Comparison of centerline temperature profiles of a steel-steel friction weld at time t=3.0 s with a jet velocity of v=5 m/s for different angular speeds.

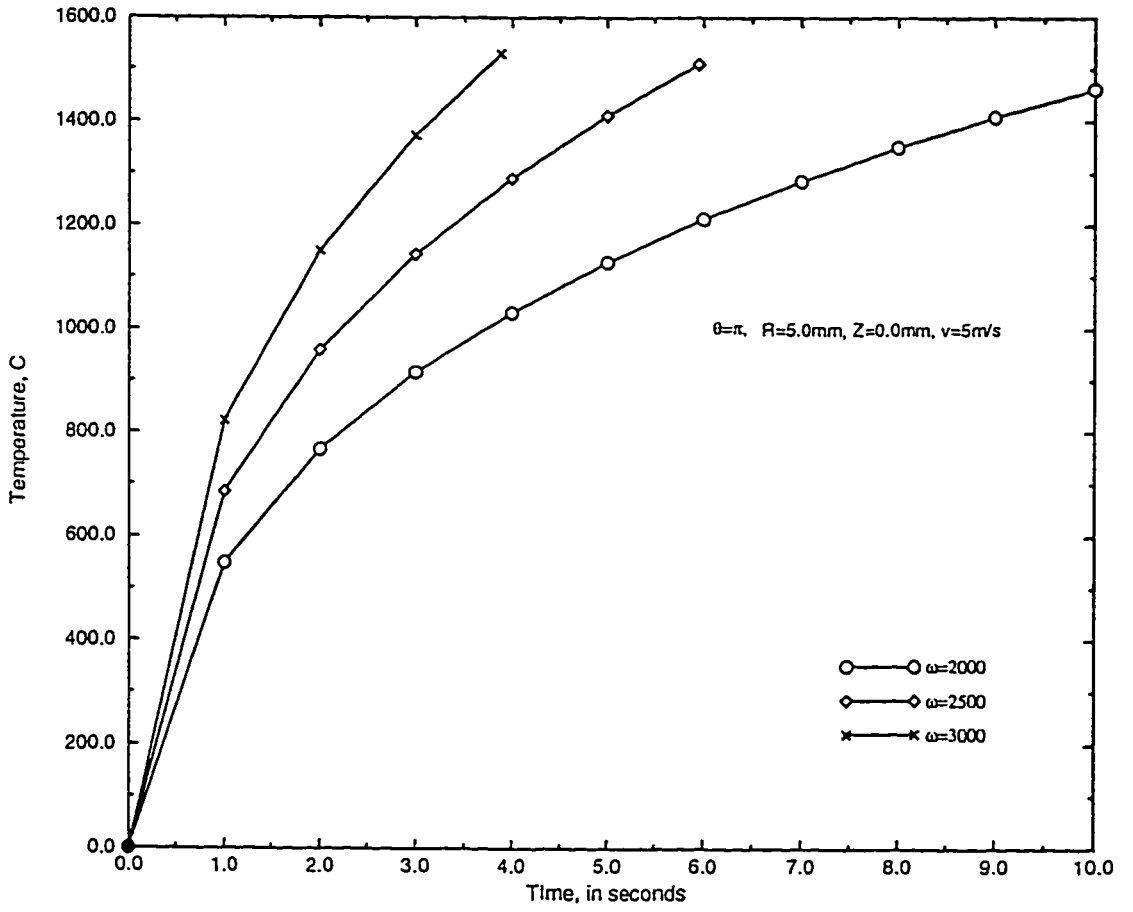

Figure 4.76: Comparison of temperature profiles with increase in time at front stagnation point of a steel-steel friction weld with a jet velocity of v=5 m/s for different angular speeds.

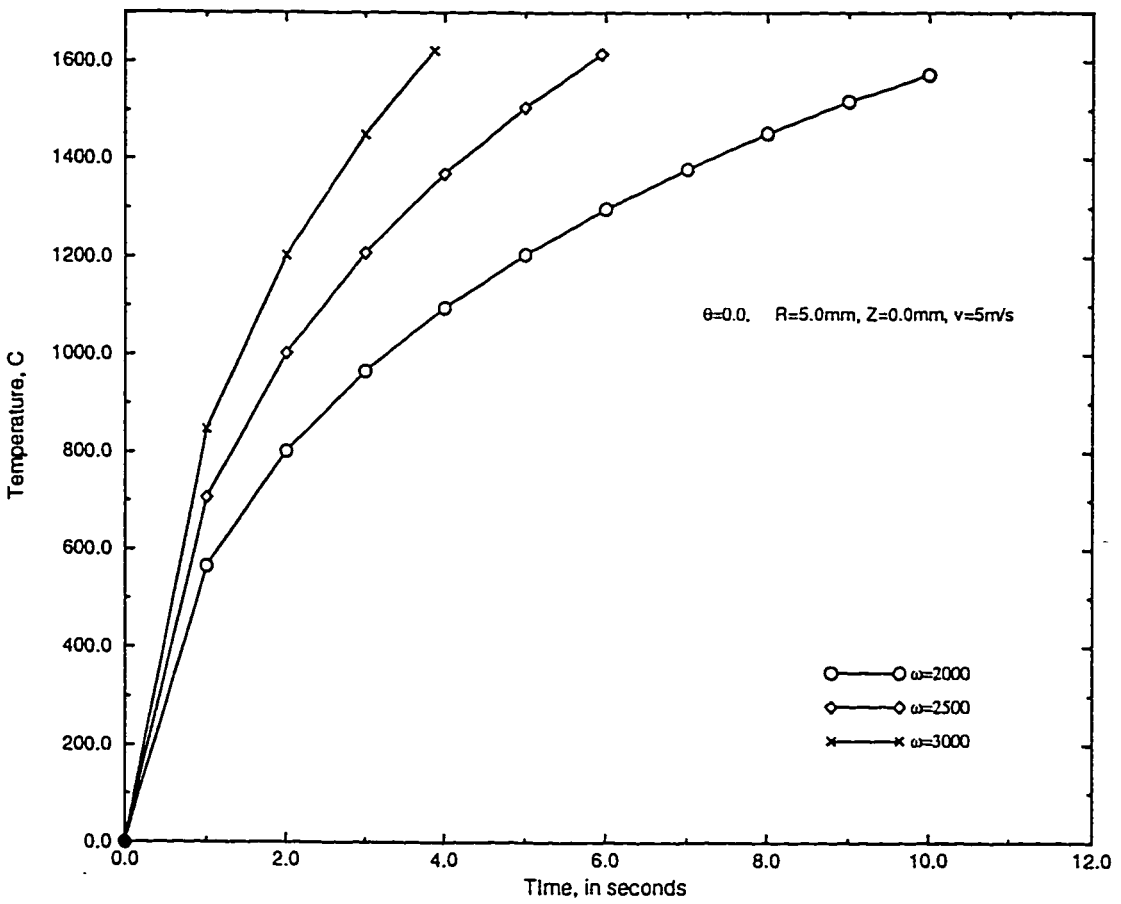

Figure 4.77: Comparison of temperature raise at back stagnation point of a steel-steel friction weld with a jet velocity of v=5 m/s for different angular speeds.

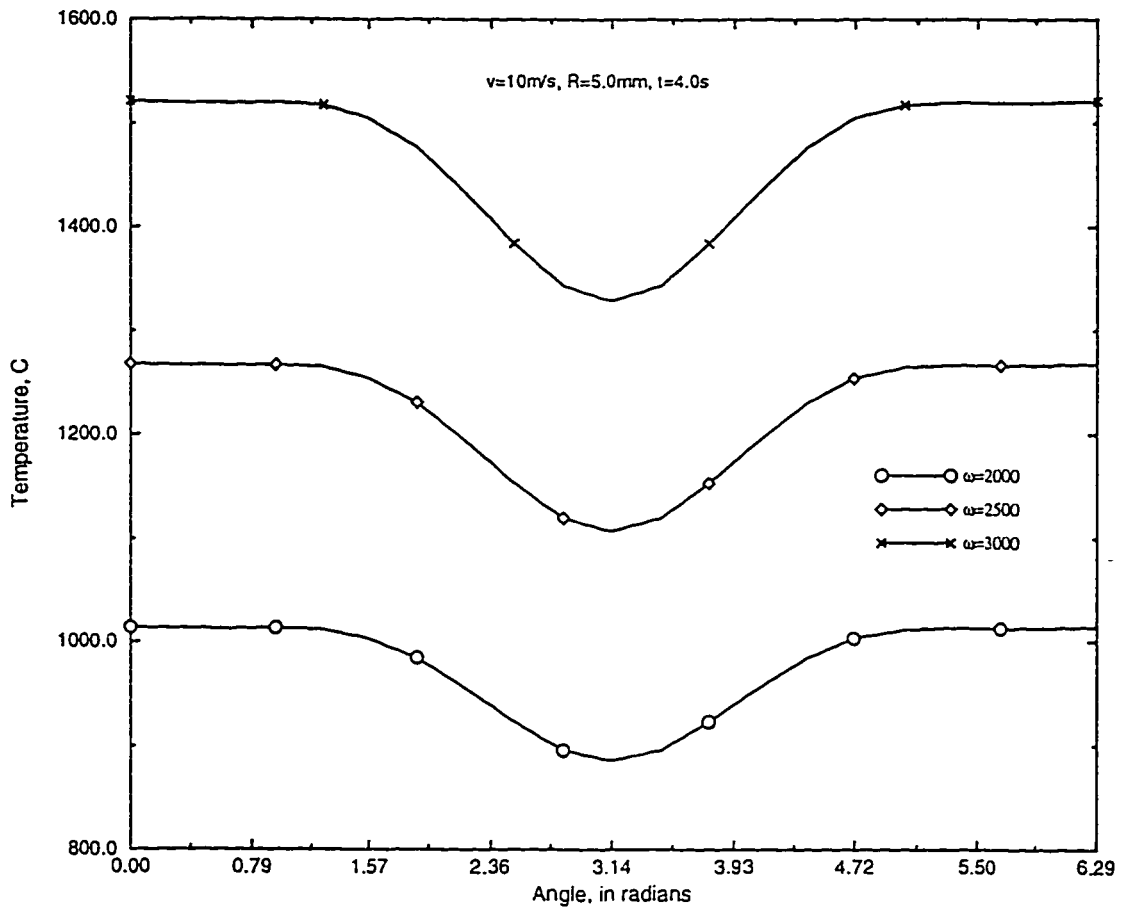

Figure 4.78: Comparison of circumferential temperature profiles on the surface of a steel-steel friction weld at time t=4s with a jet velocity of v=10 m/s for different angular speeds.

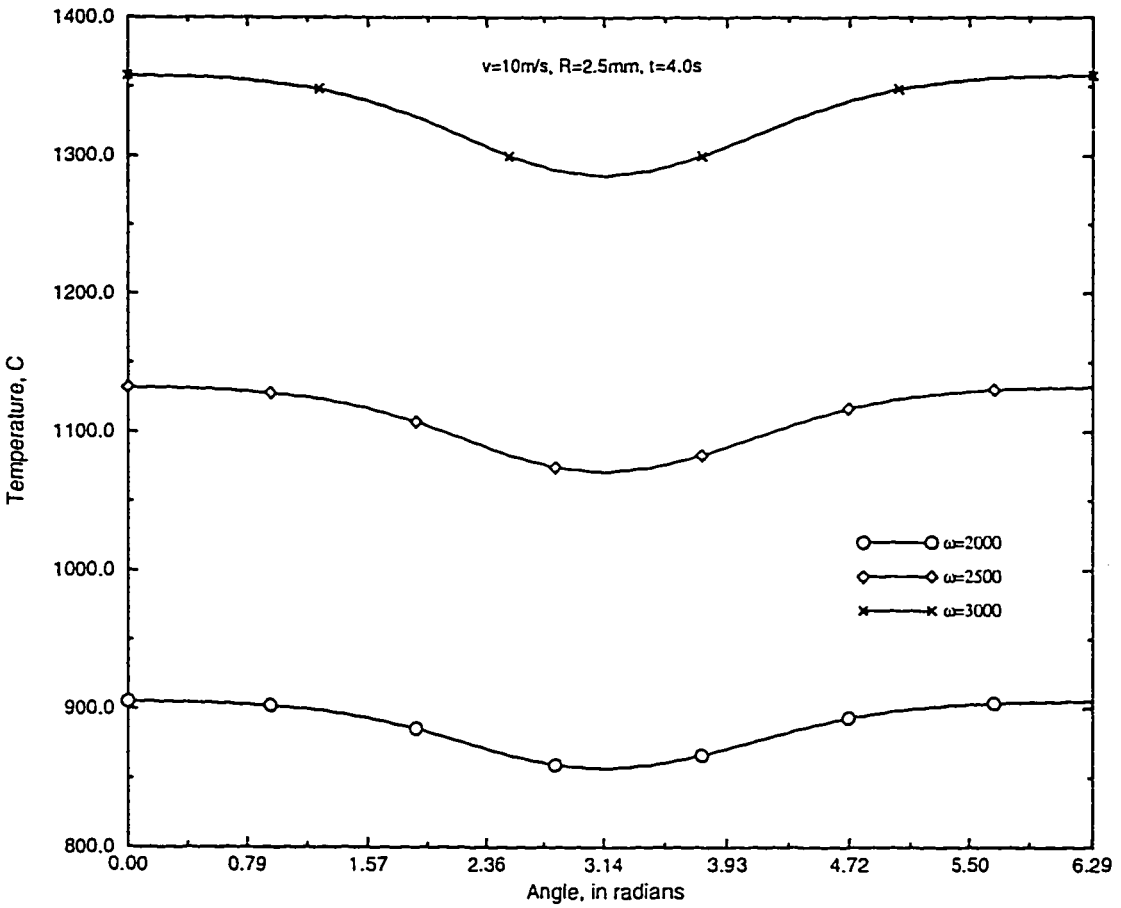

Figure 4.79: Comparison of circumferential temperature profiles at mid-radius of a steel-steel friction weld at time t=4s with a jet velocity of v=10 m/s for different angular speeds.

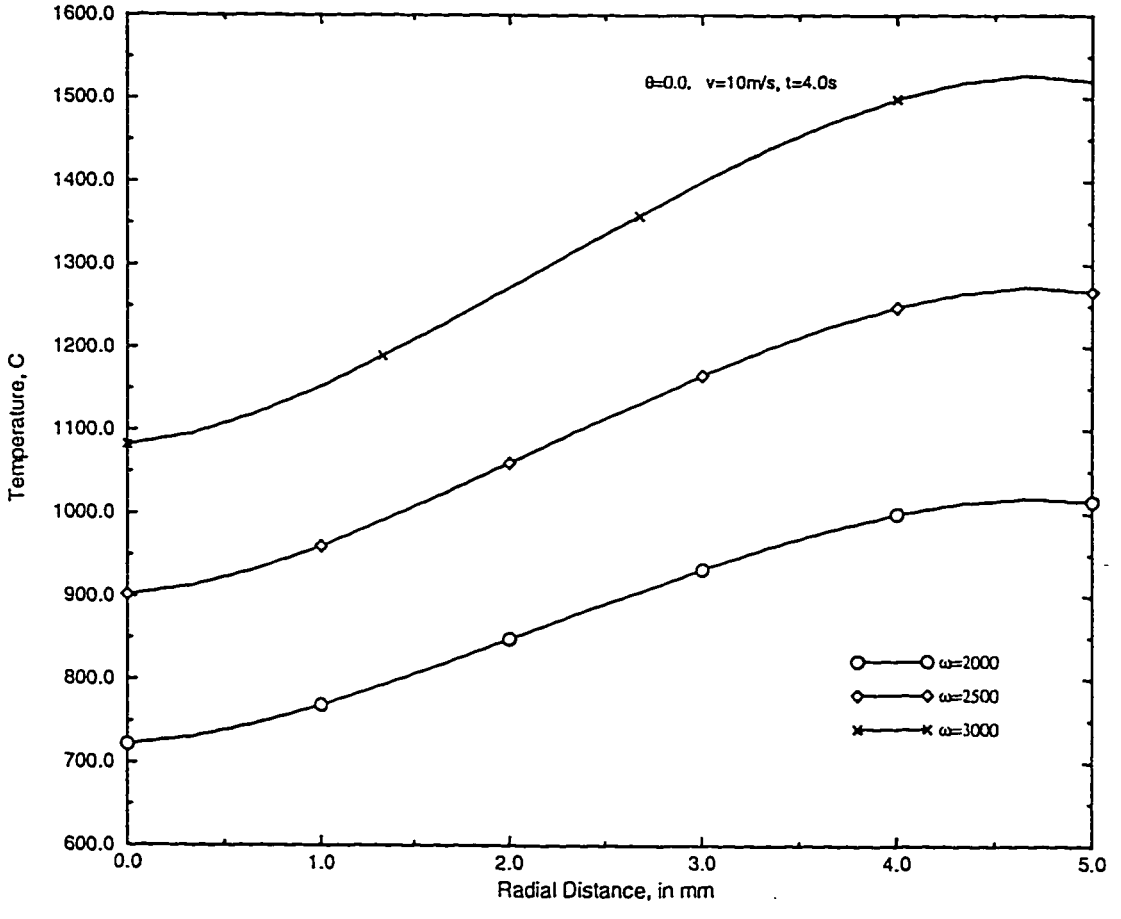

Figure 4.80: Comparison of radial temperature profiles at back stagnation point of a steel-steel friction weld at time t=4s with a jet velocity of v=10 m/s for different angular speeds.

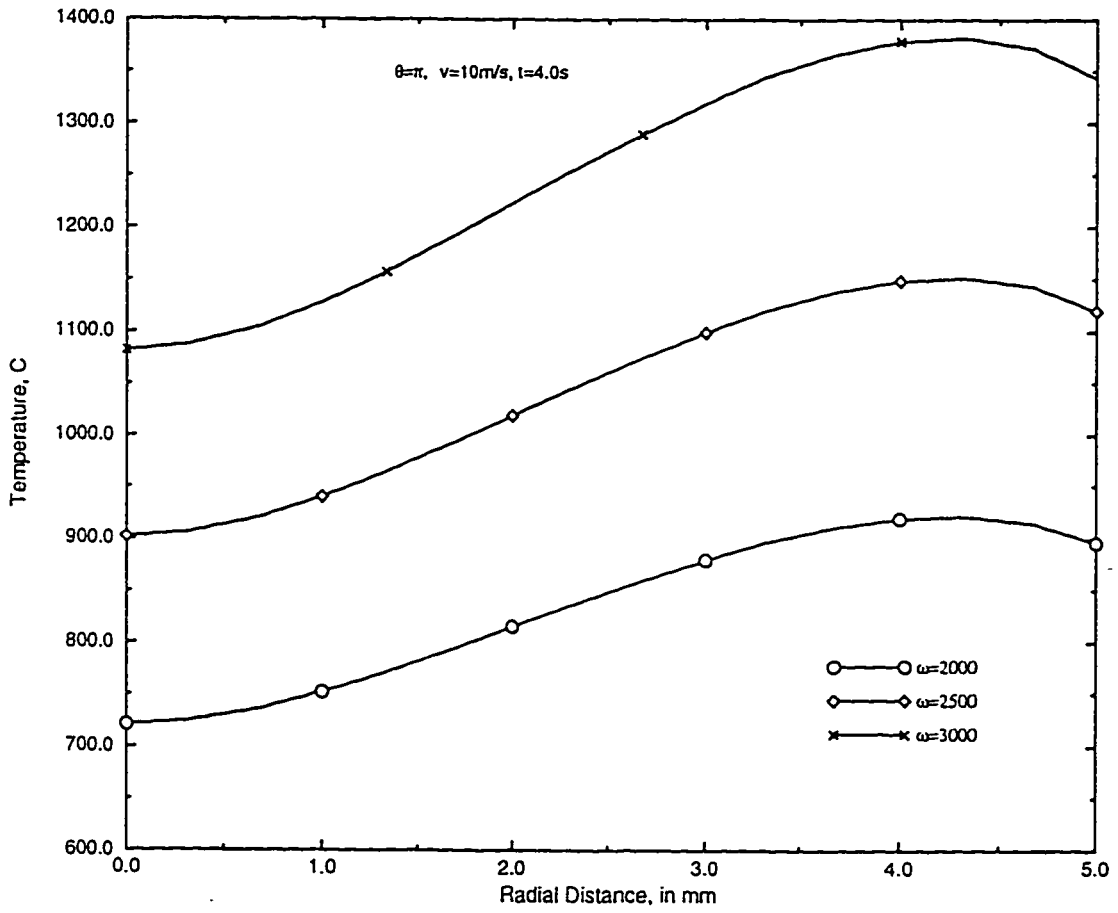

Figure 4.81: Comparison of radial temperature profiles at front stagnation point of a steel-steel friction weld at time t=4s with a jet velocity of v=10 m/s for different angular speeds.

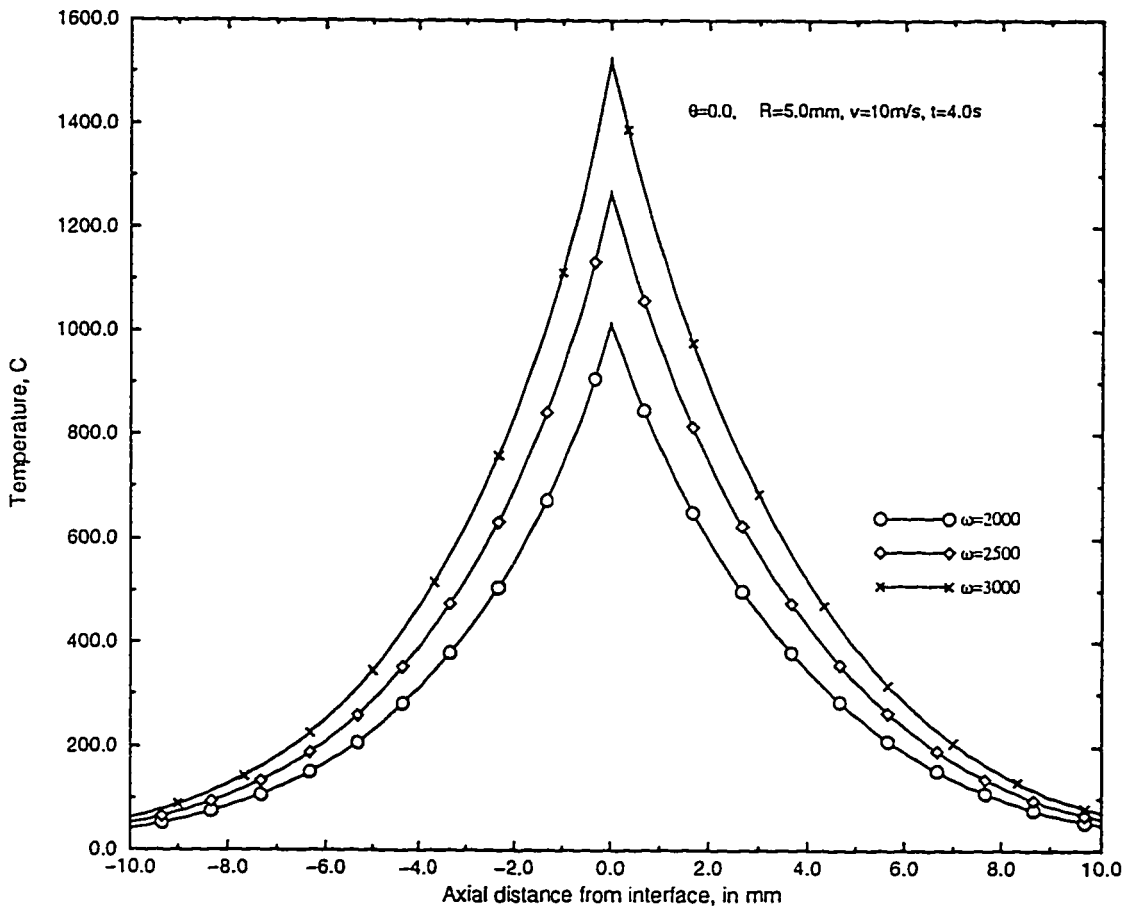

Figure 4.82: Comparison of radial temperature profiles at back stagnation point of a steel-steel friction weld at time t=4s with a jet velocity of v=10 m/s for different angular speeds.

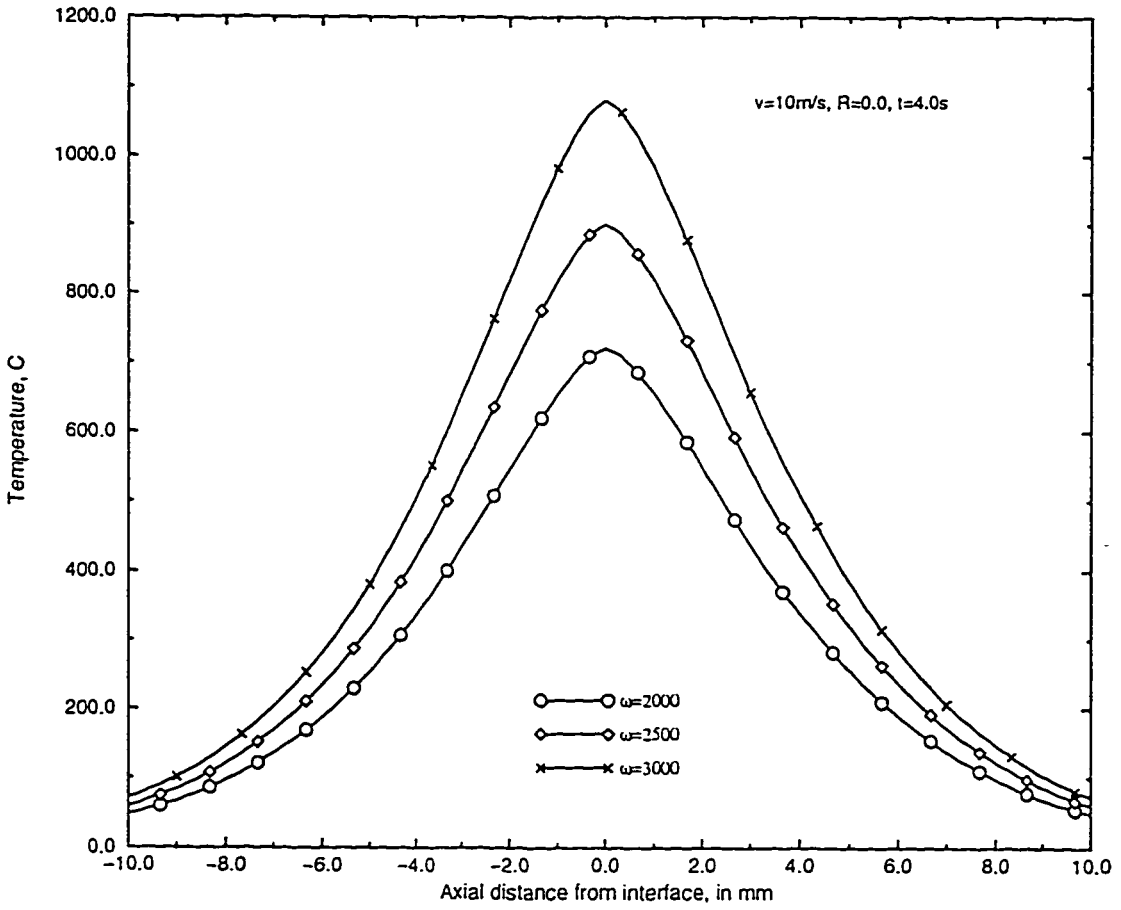

Figure 4.83: Comparison of centerline temperature profiles of a steel-steel friction weld at time t=4s with a jet velocity of v=10 m/s for different angular speeds.

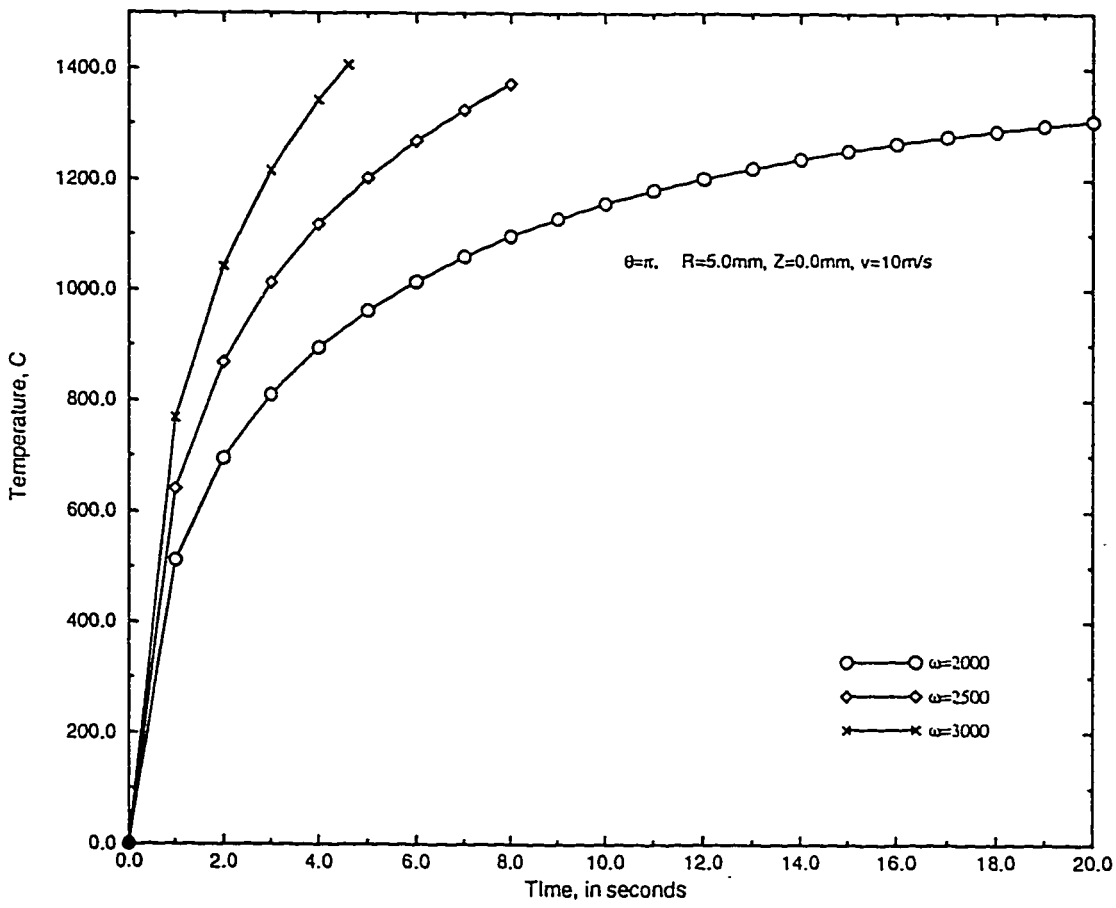

Figure 4.84: Comparison of temperature raise at front stagnation point of a steel-steel friction weld with a jet velocity of v=10 m/s for different angular speeds.

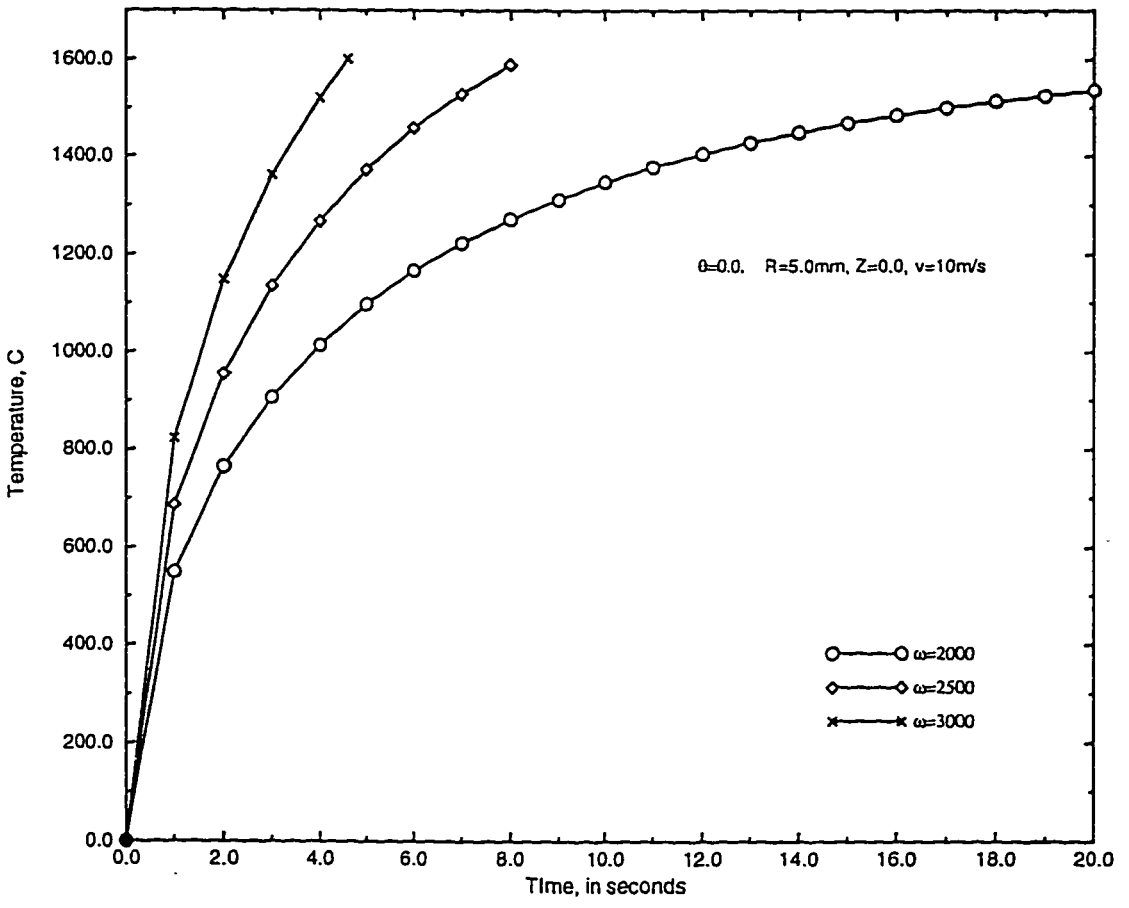

Figure 4.85: Comparison of temperature raise at back stagnation point of a steel-steel friction weld with a jet velocity of v=10 m/s for different angular speeds.

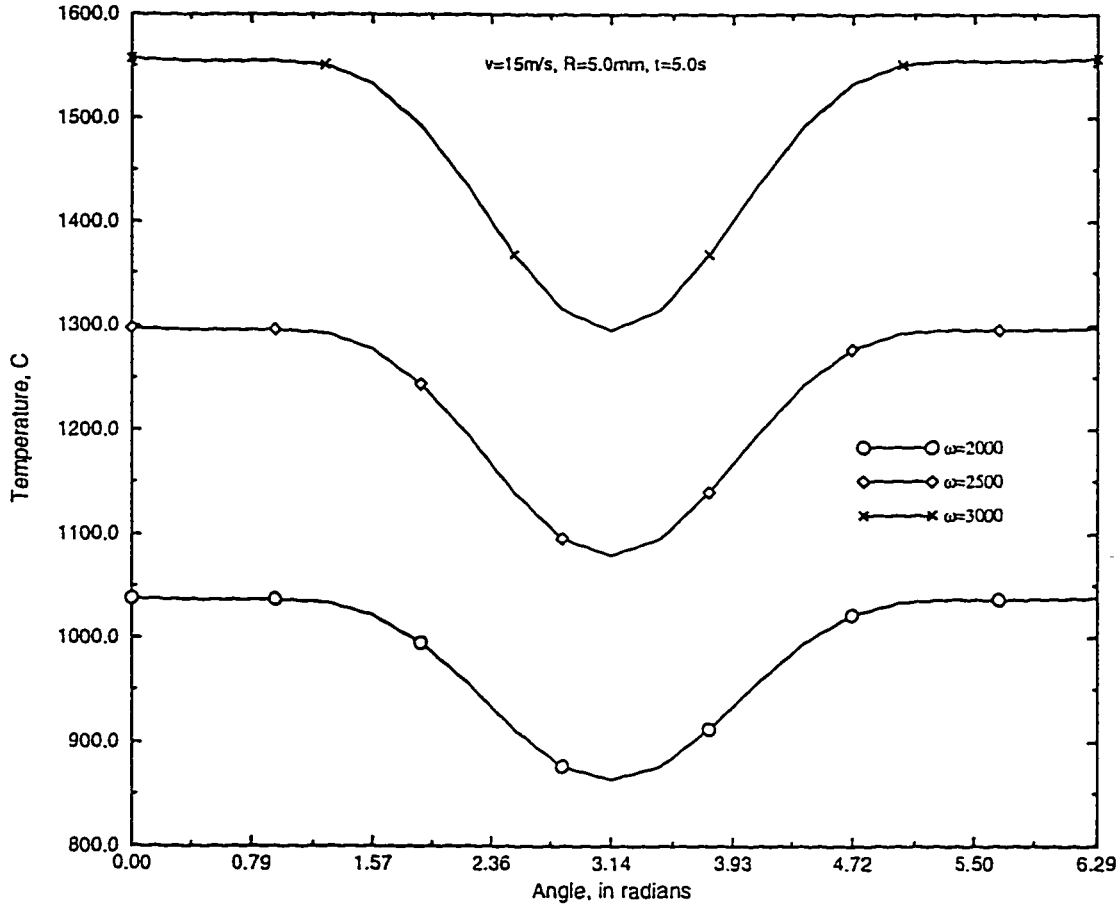

Figure 4.86: Comparison of circumferential temperature profiles on the surface of a steel-steel friction weld at time t=5.0 s with a jet velocity of v=15 m/s for different angular speeds.

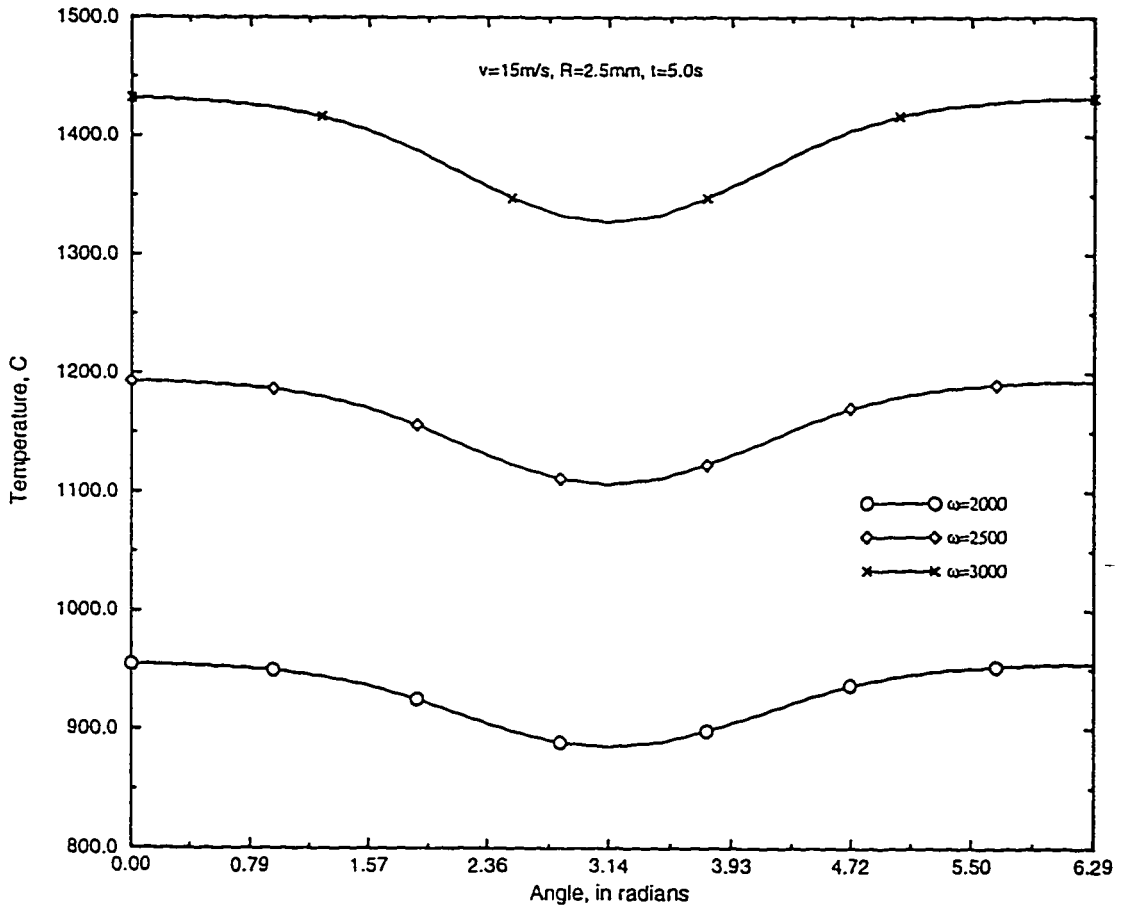

Figure 4.87: Comparison of circumferential temperature profiles at mid-radius of a steel-steel friction weld at time t=5.0 s with a jet velocity of v=15 m/s for different angular speeds.

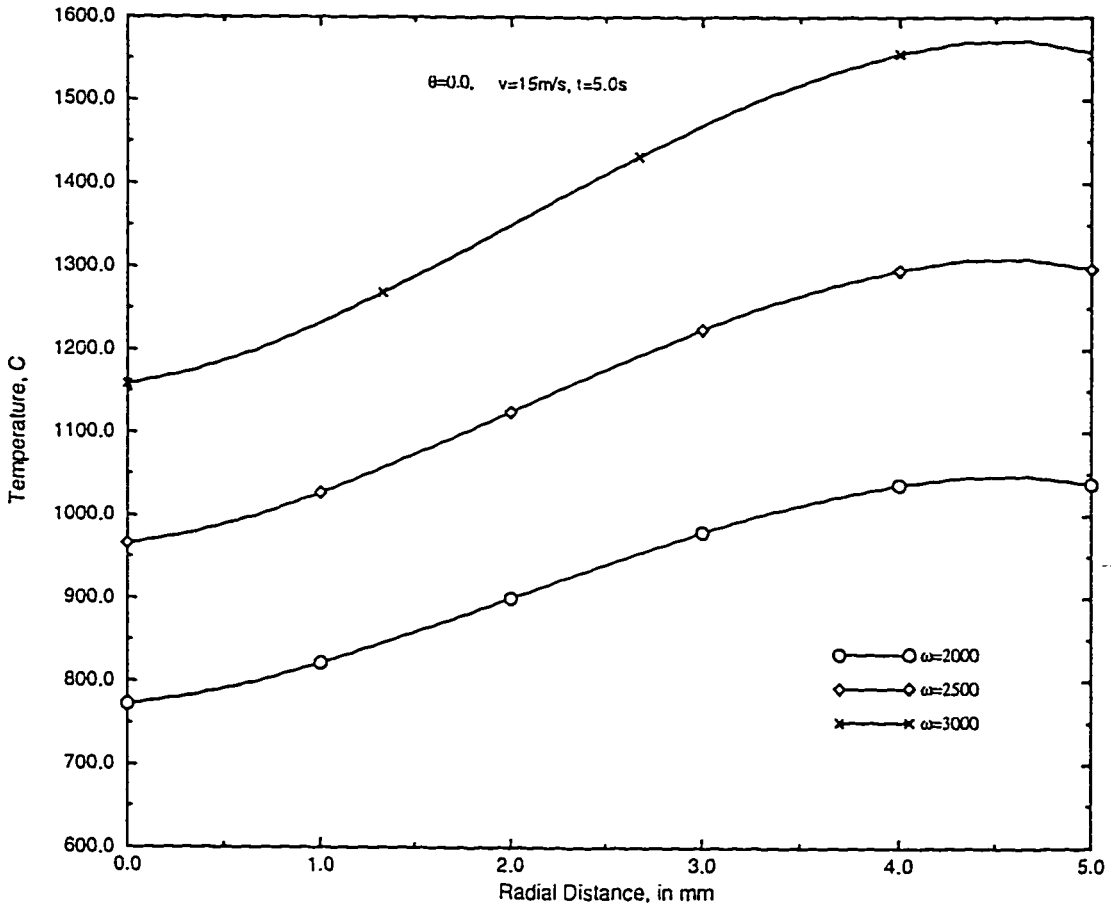

Figure 4.88: Comparison of radial temperature profiles at back stagnation point of a steel-steel friction weld at time t=5.0 s with a jet velocity of v=15 m/s for different angular speeds.

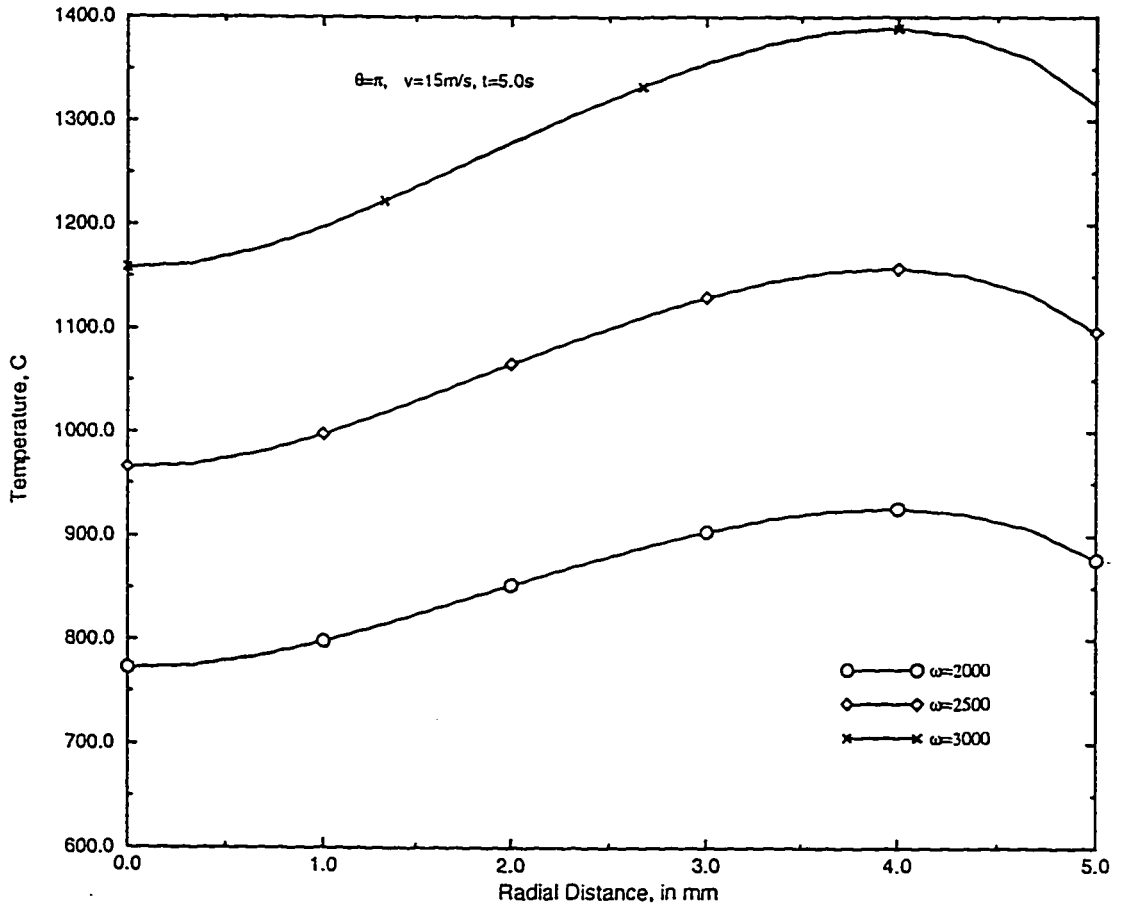

Figure 4.89: Comparison of radial temperature profiles at front stagnation point of a steel-steel friction weld at time t=5.0 s with a jet velocity of v=15 m/s for different angular speeds.

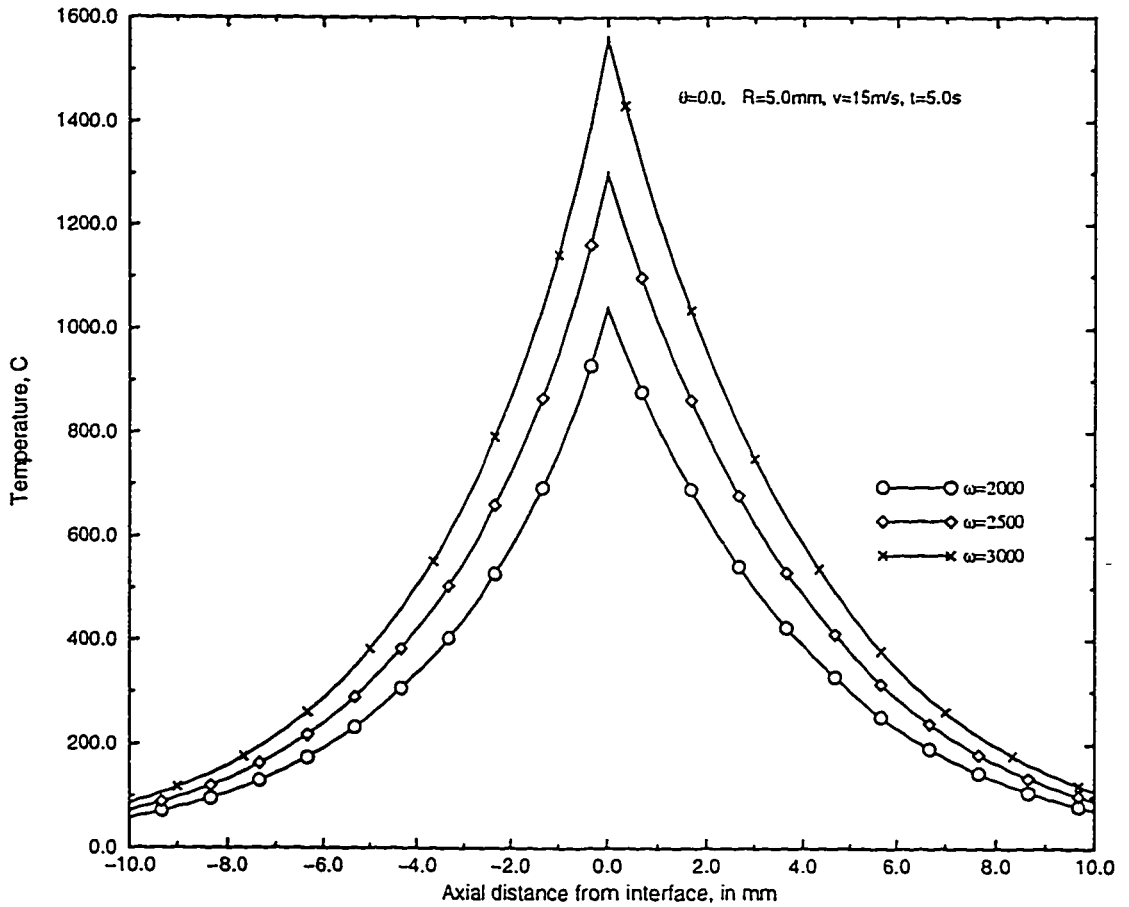

Figure 4.90: Comparison of radial temperature profiles at back stagnation point of a steel-steel friction weld at time t=5.0 s with a jet velocity of v=15 m/s for different angular speeds.

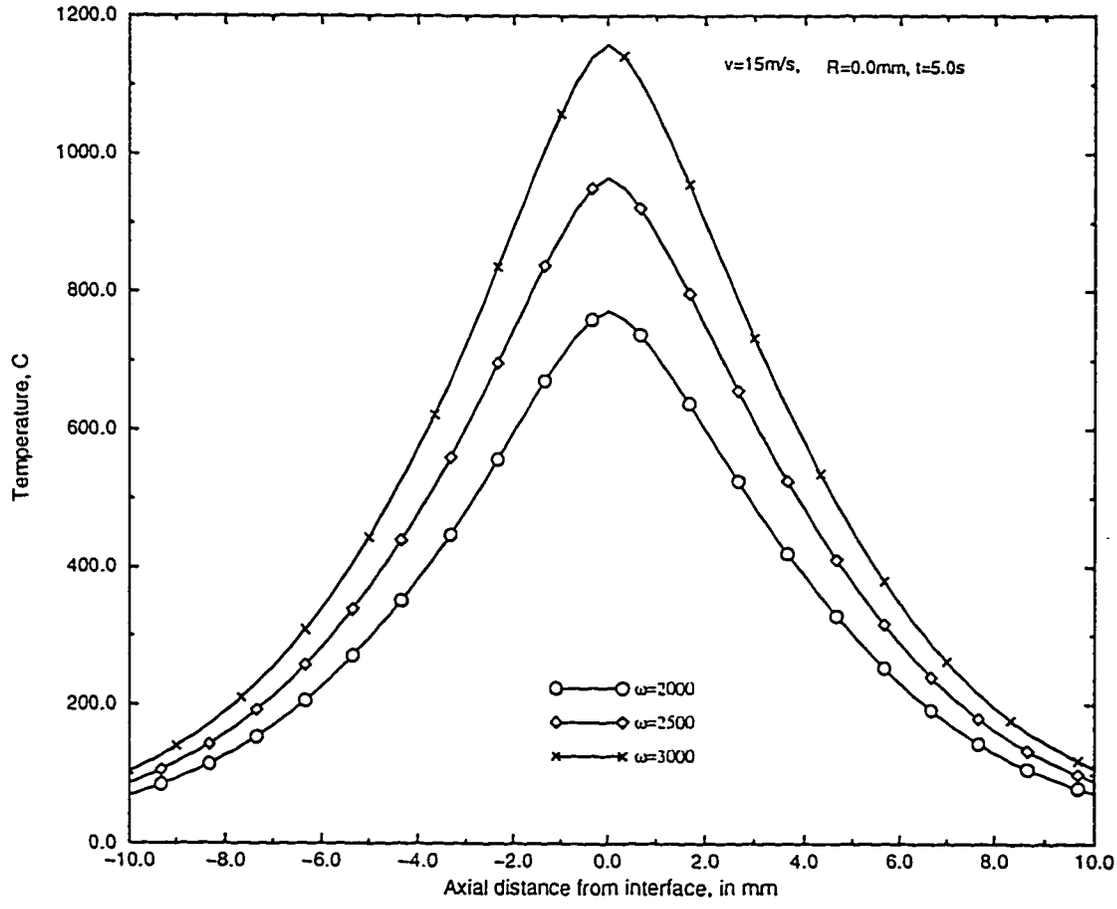

Figure 4.91: Comparison of centerline temperature profiles of a steel-steel friction weld at time t=5.0 s with a jet velocity of v=15 m/s for different angular speeds.

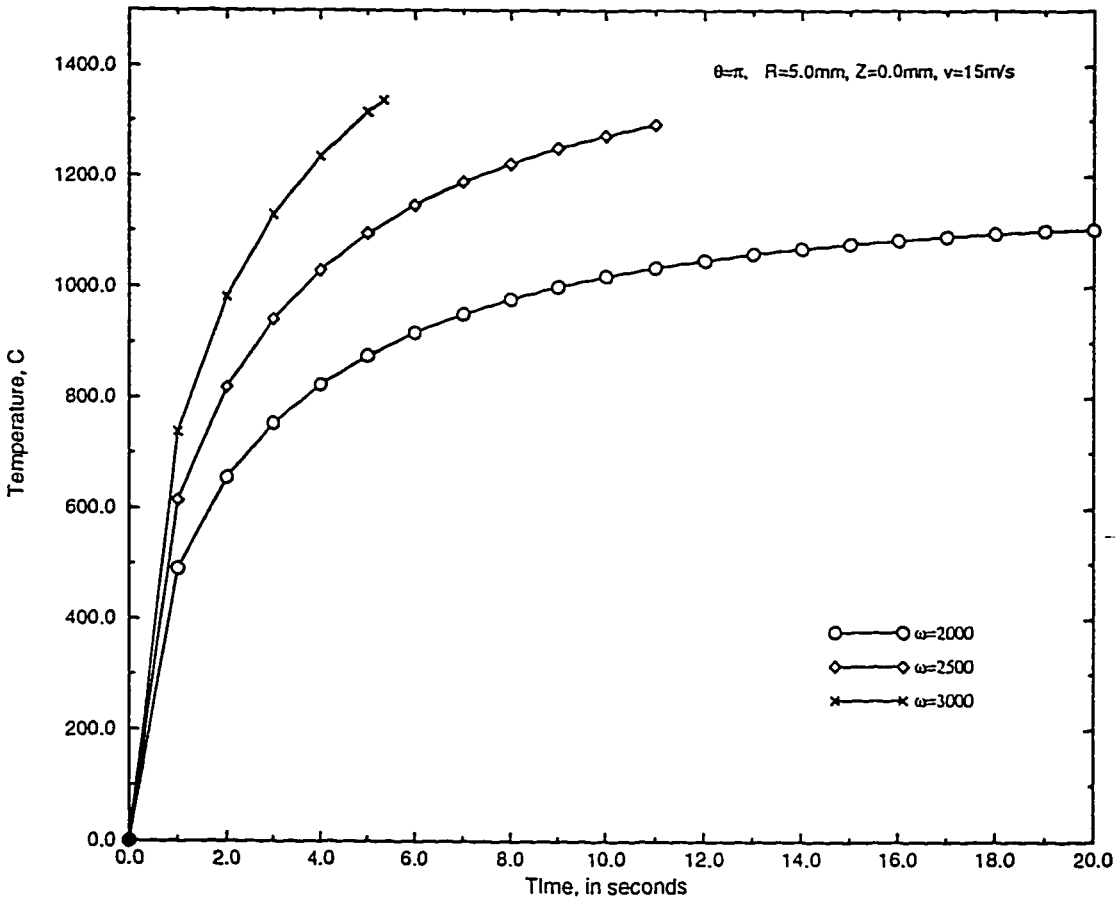

Figure 4.92: Comparison of temperature raise at front stagnation point of a steel-steel friction weld with a jet velocity of v=15 m/s for different angular speeds.

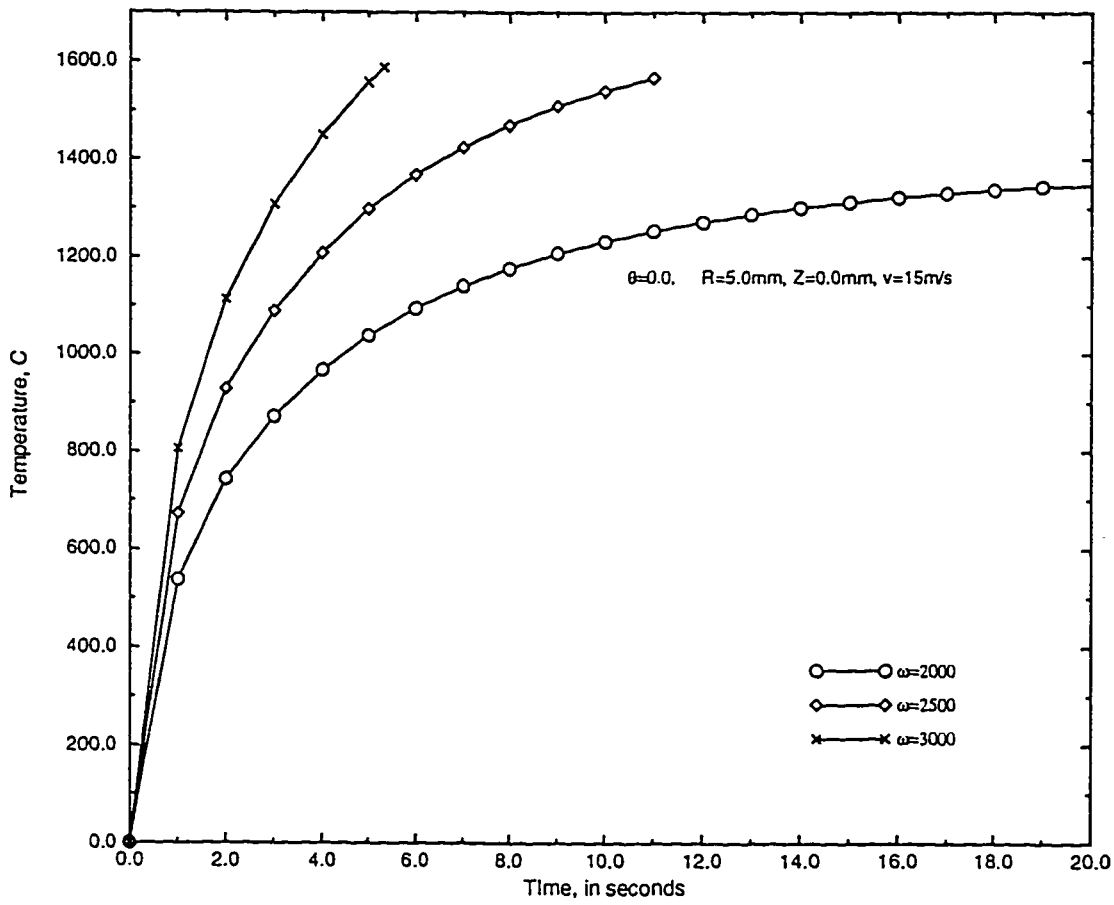

Figure 4.93: Comparison of temperature raise at back stagnation point of a steel-steel friction weld with a jet velocity of v=15 m/s for different angular speeds.

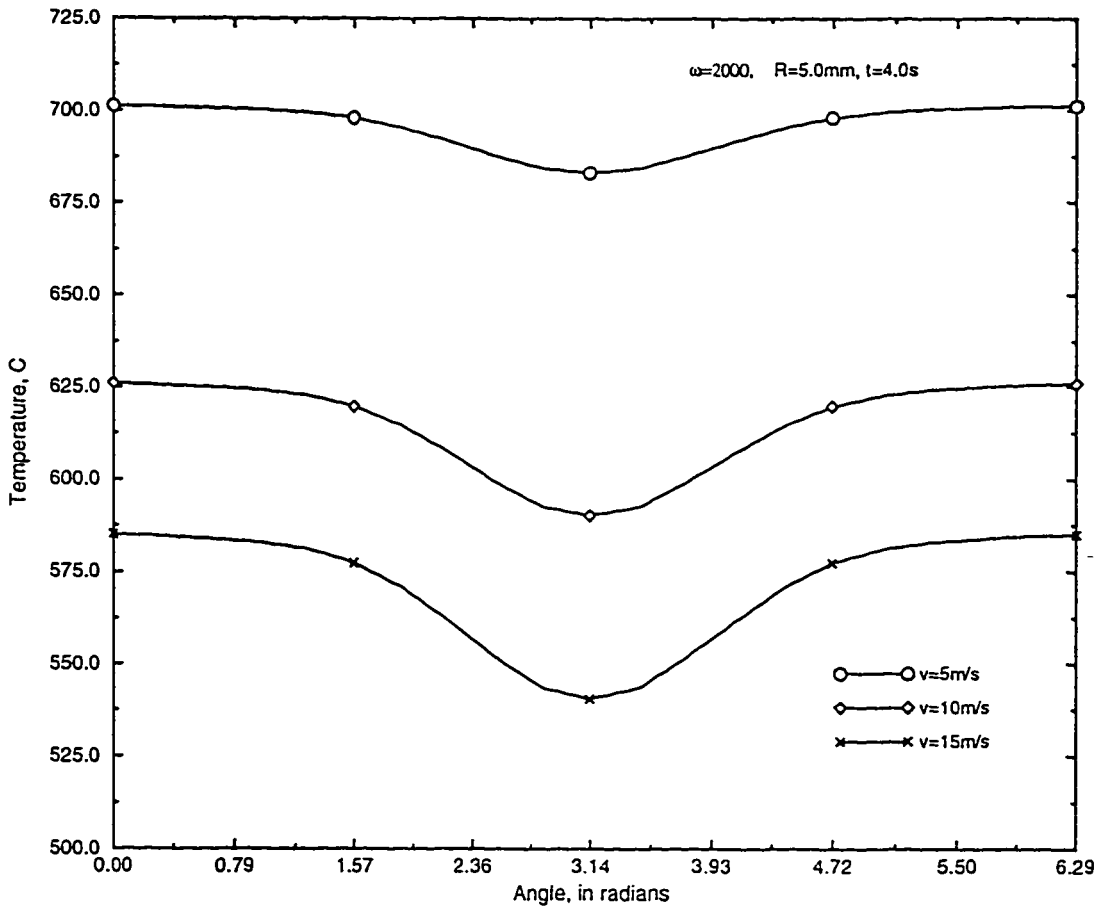

Figure 4.94: Comparison of circumferential temperature profiles on the surface of a steel-aluminum friction weld at time t=4.0 s with an angular speed of 2000 rpm for different jet velocities.

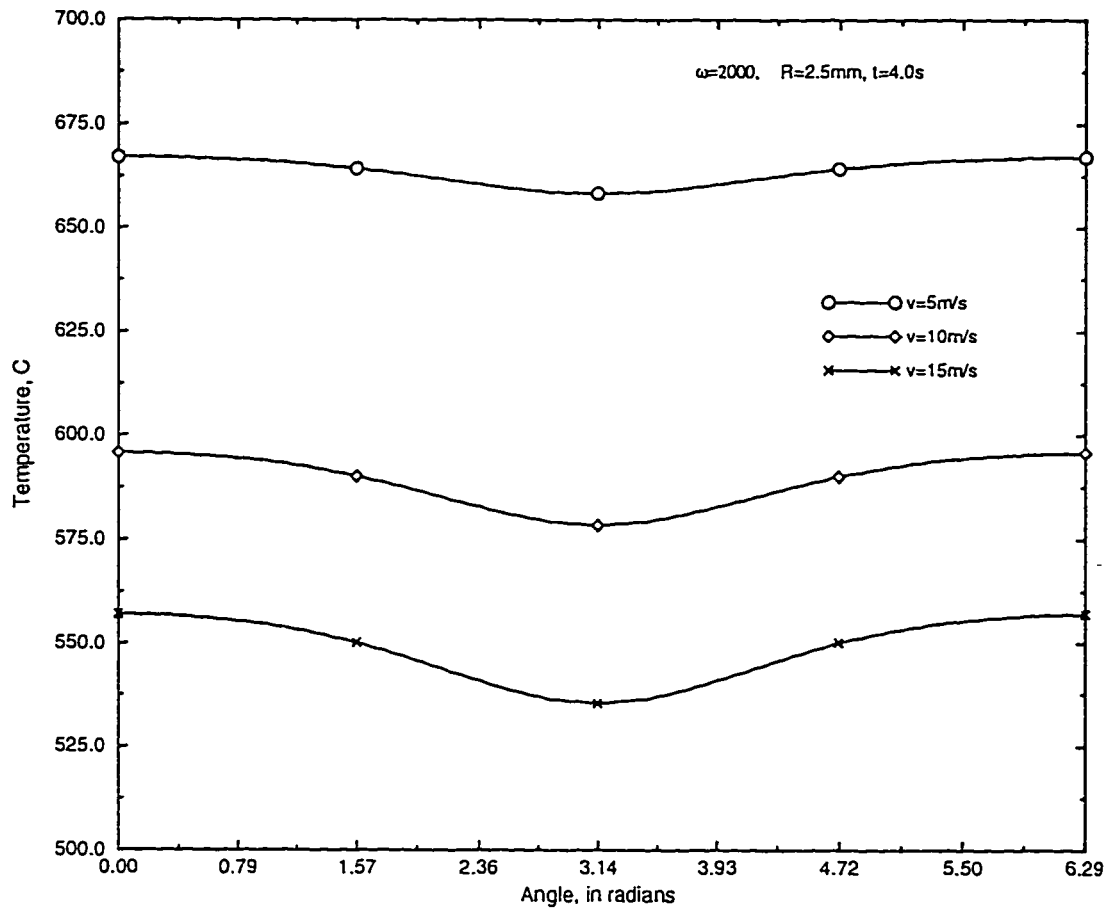

Figure 4.95: Comparison of circumferential temperature profiles at mid-radius of a steel-aluminum friction weld at time t=4.0 s with an angular speed of 2000 rpm for different jet velocities.

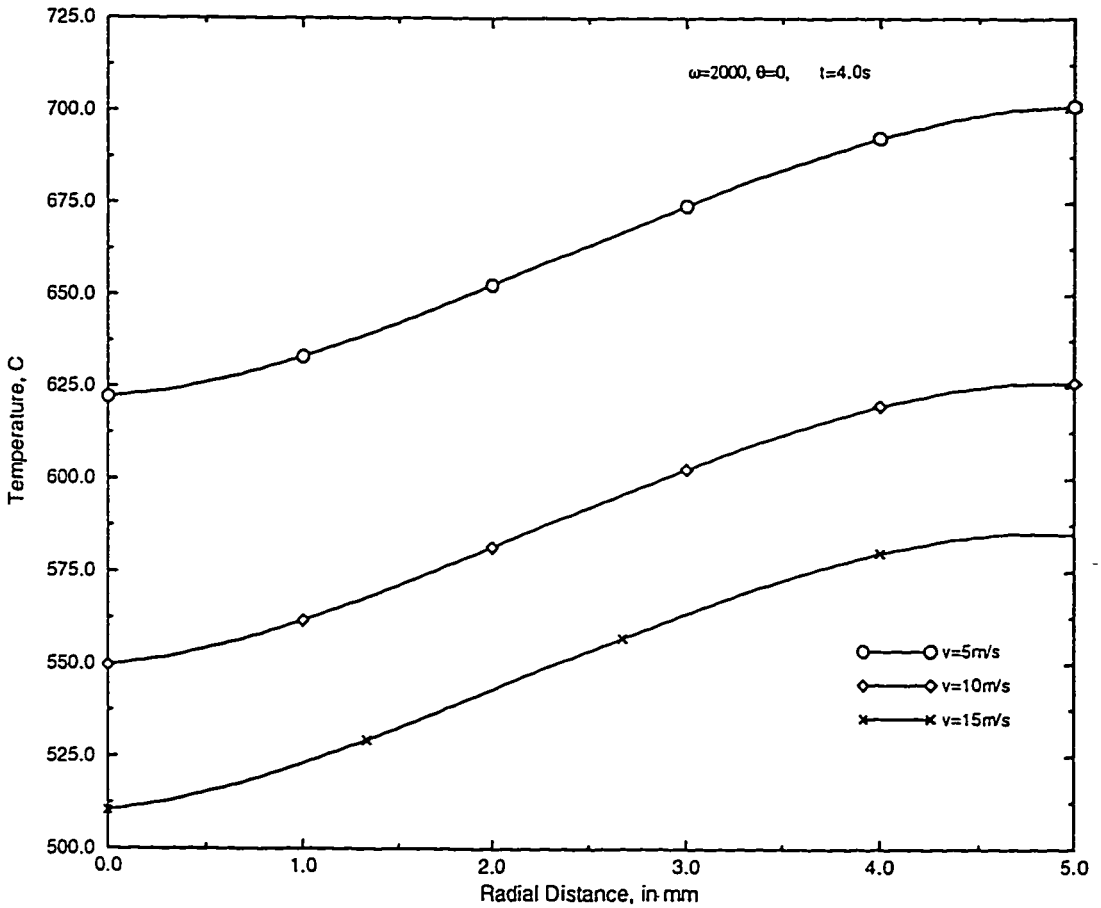

Figure 4.96: Comparison of radial temperature profiles at back stagnation point of a steel-aluminum friction weld at time t=4.0 s with an angular speed of 2000 rpm for different jet velocities.

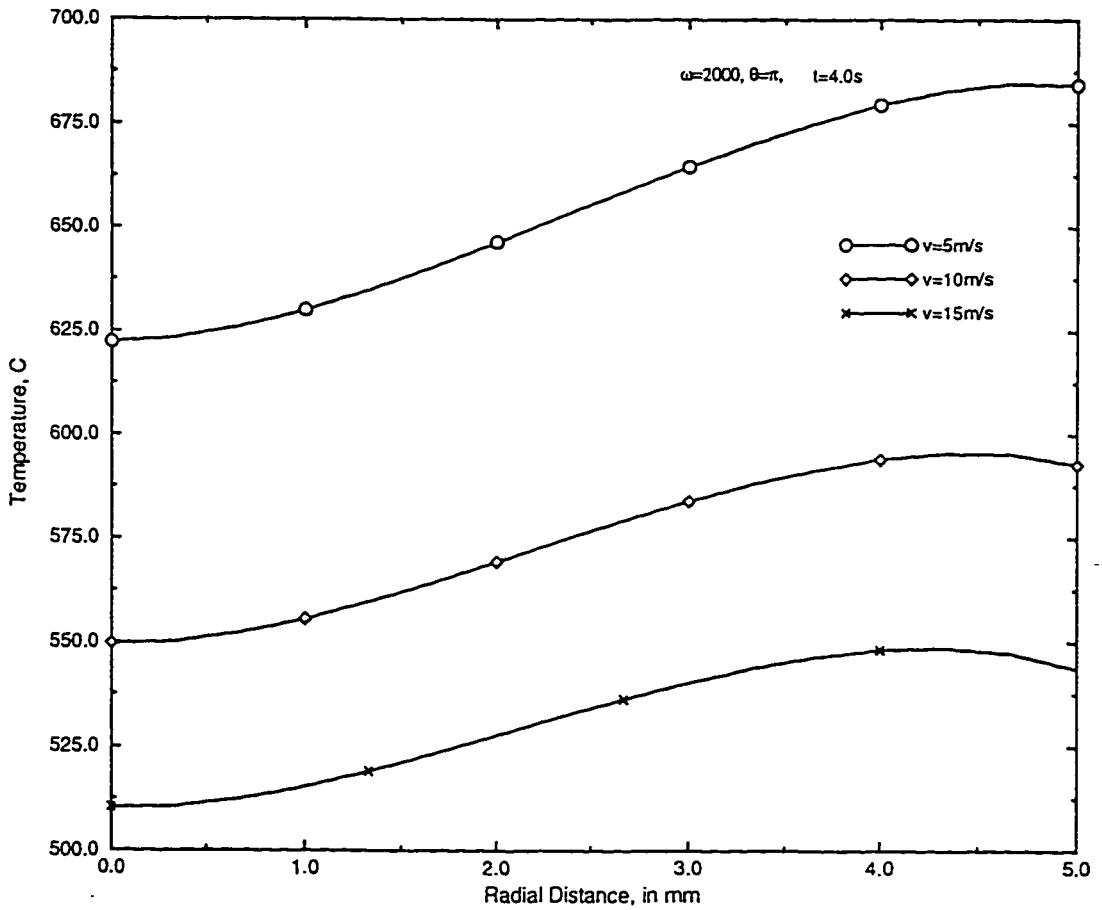

Figure 4.97: Comparison of radial temperature profiles at front stagnation point of a steel-aluminum friction weld at time t=4.0 s with an angular speed of 2000 rpm for different jet velocities.

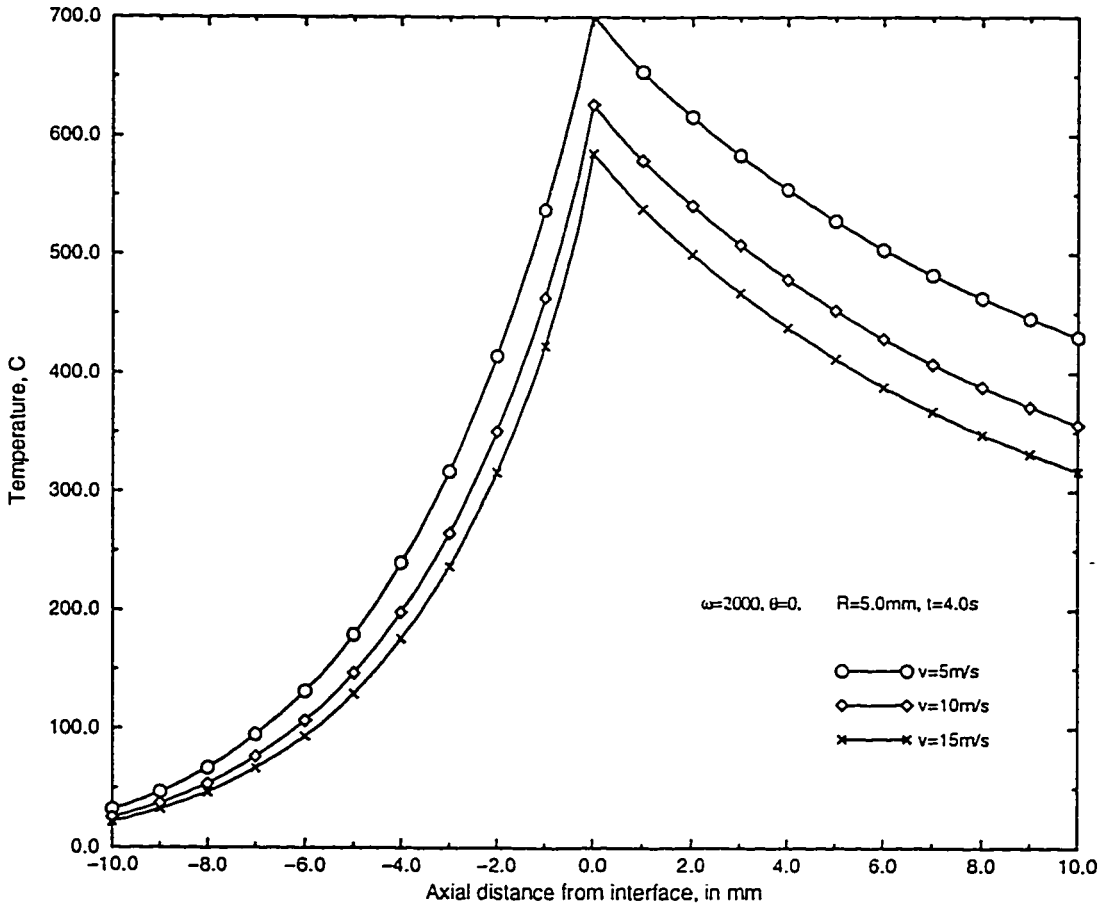

Figure 4.98: Comparison of axial temperature profiles at back stagnation point of a steel-aluminum friction weld at time t=4.0 s with an angular speed of 2000 rpm for different jet velocities.

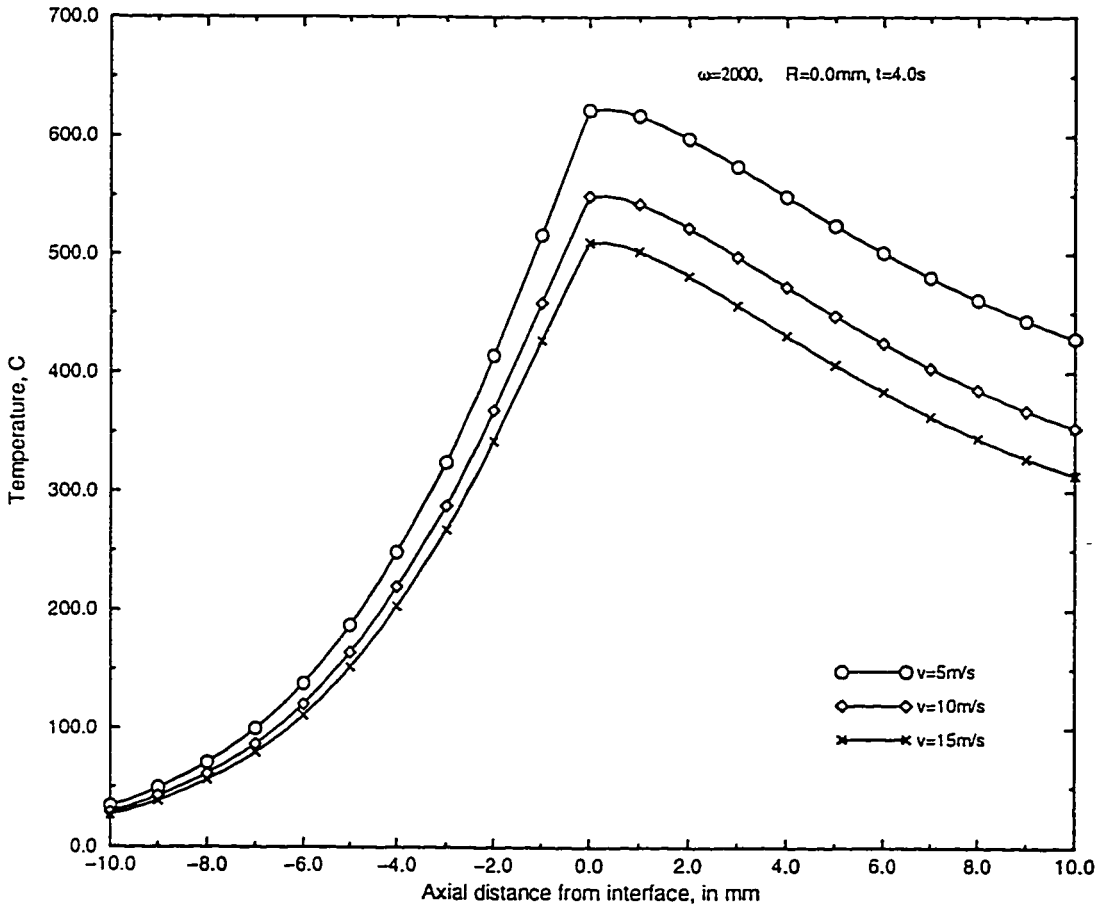

Figure 4.99: Comparison of centerline temperature profiles with theof a steel-aluminum friction weld with an angular speed of 2000 rpm for different jet velocities.

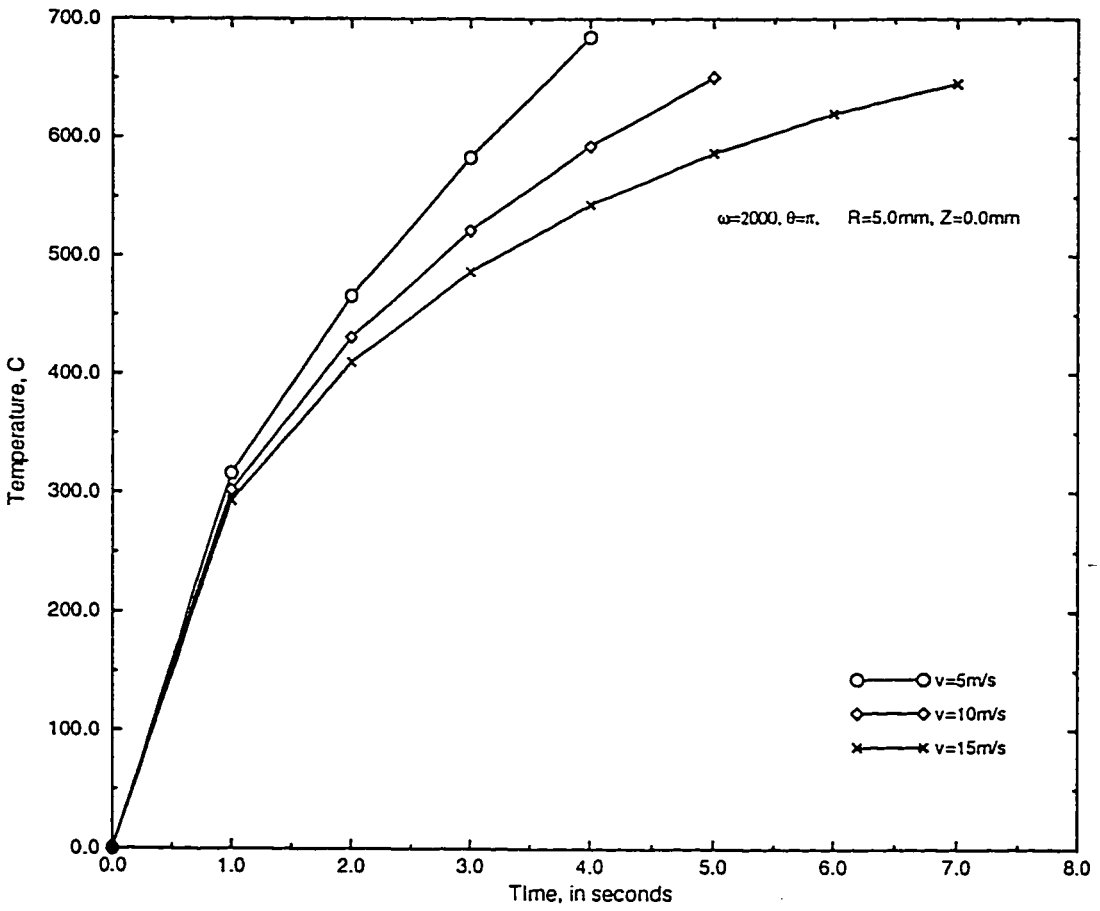

Figure 4.100: Comparison of temperature profiles with the increase of time at front stagnation point of a steel-aluminum friction weld with an angular speed of 2000 rpm for different jet velocities.

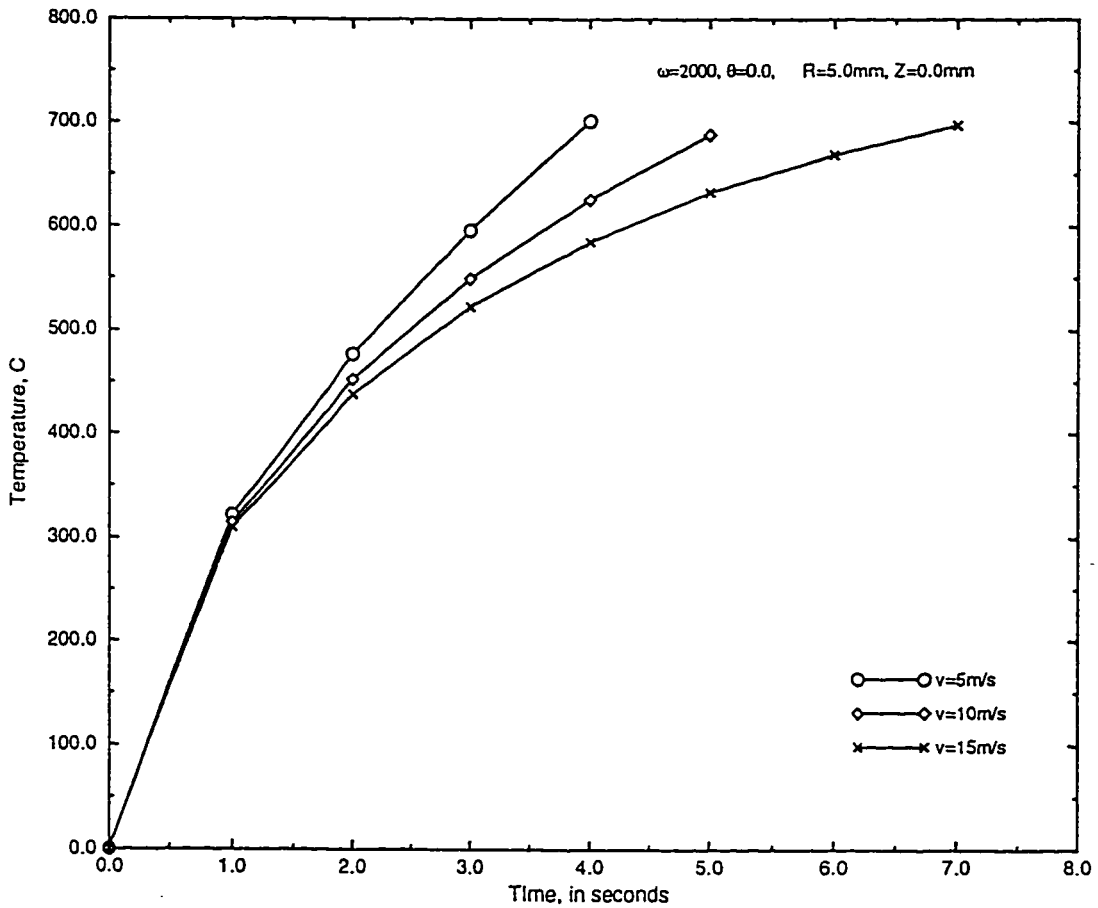

Figure 4.101: Comparison of temperature profiles with the increase of time at back stagnation point of a steel-aluminum friction weld with an angular speed of 2000 rpm for different jet velocities.

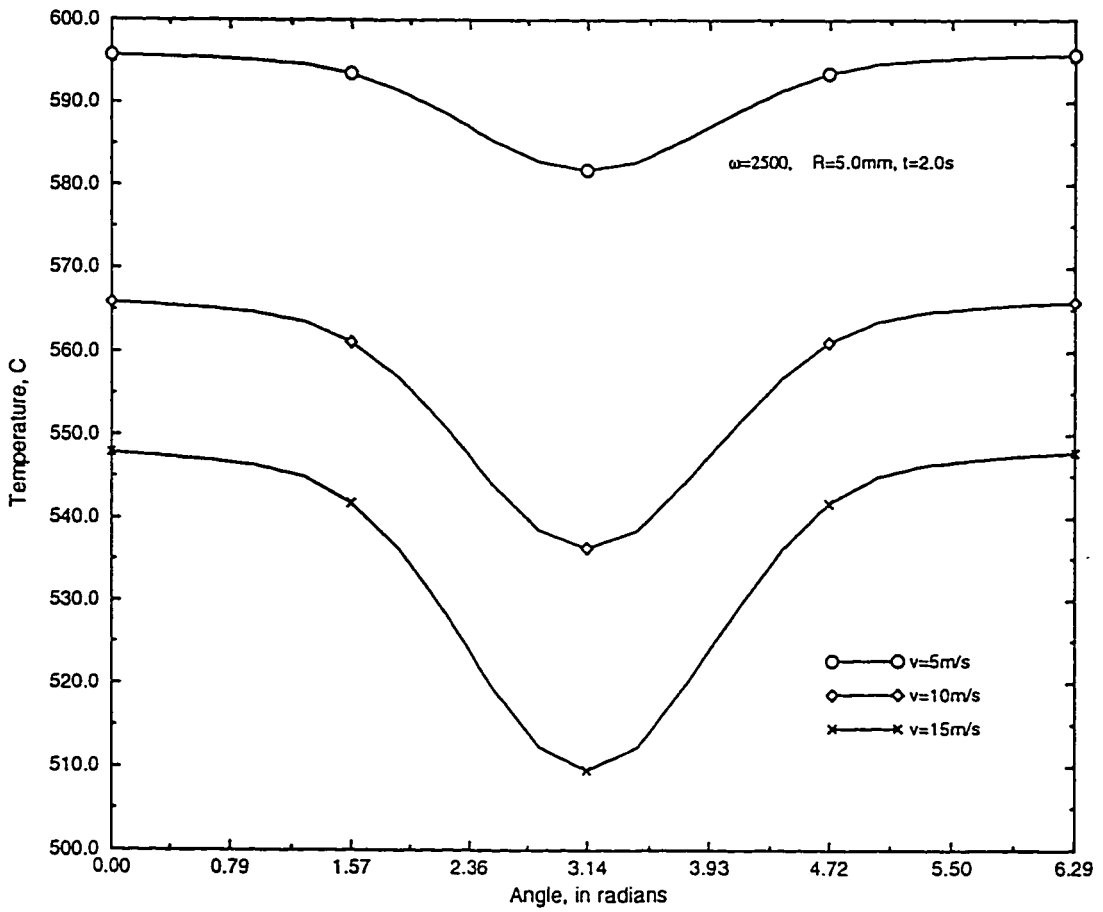

Figure 4.102: Comparison of circumferential temperature profiles on the surface of a steel-aluminum friction weld at time t=2.0 s with an angular speed of 2500 rpm for different jet velocities.

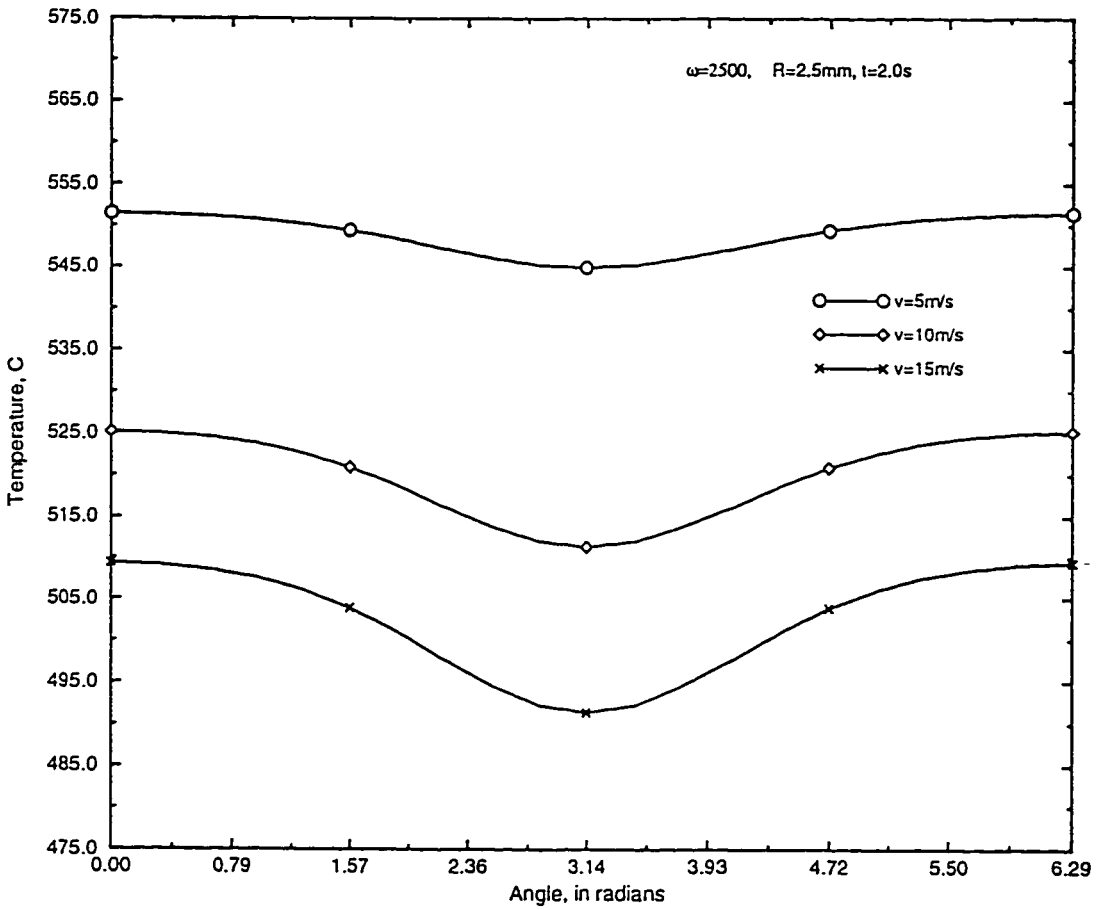

Figure 4.103: Comparison of circumferential temperature profiles at mid-radius of a steel-aluminum friction weld at time t=2.0 s with an angular speed of 2500 rpm for different jet velocities.

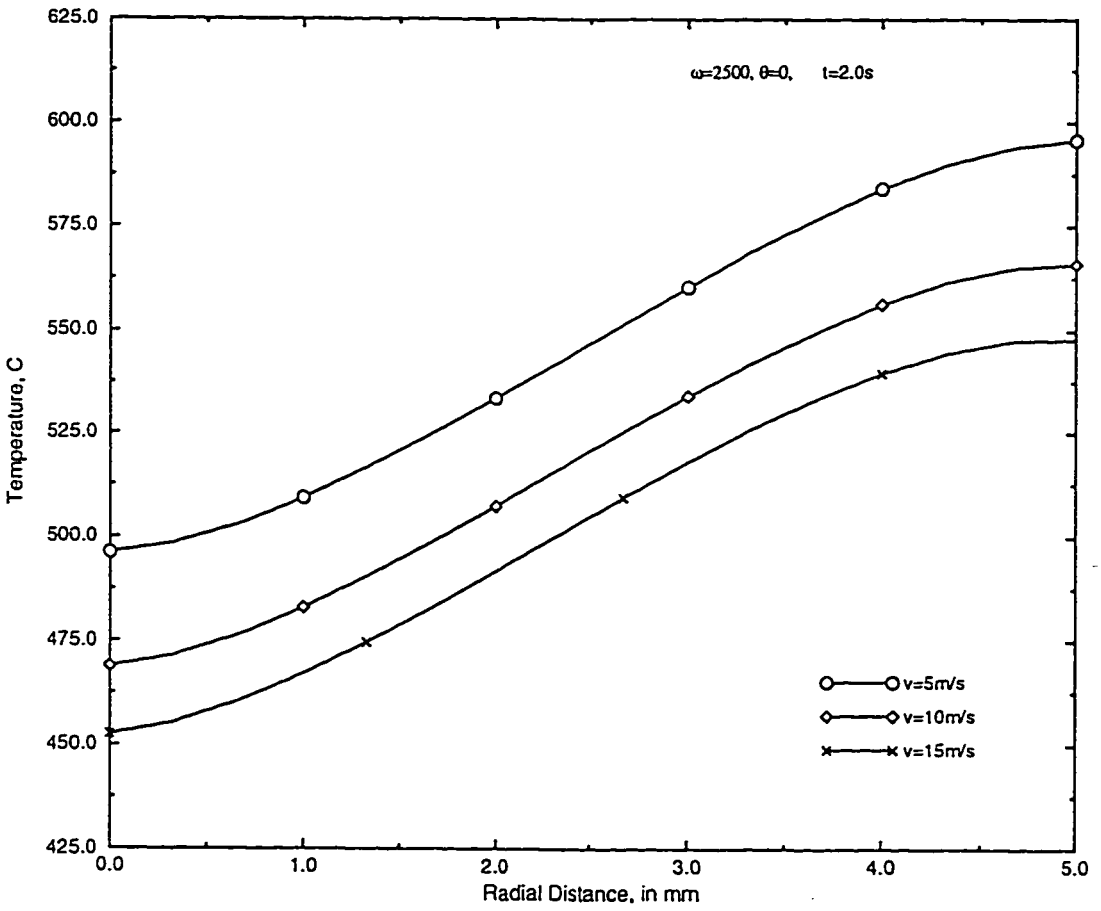

Figure 4.104: Comparison of radial temperature profiles at back stagnation point of a steel-aluminum friction weld at time t=2.0 s with an angular speed of 2500 rpm for different jet velocities.

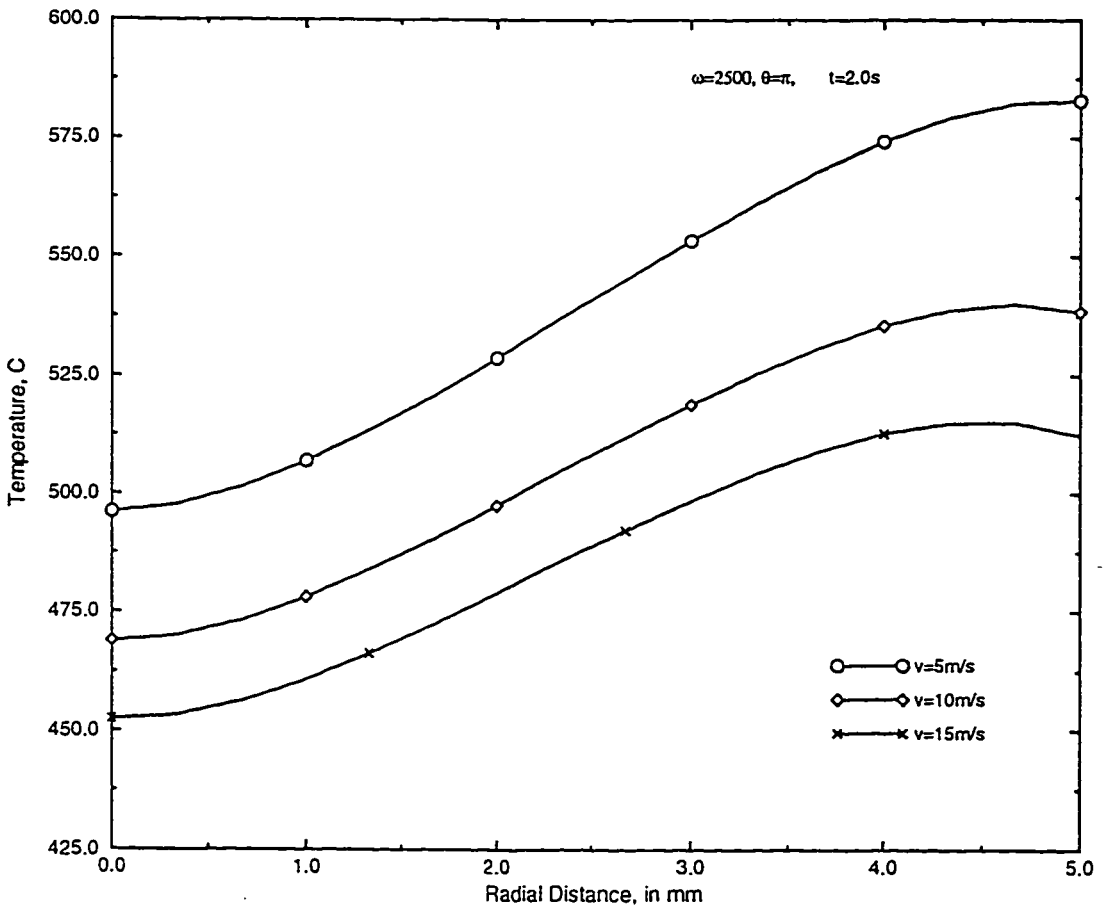

Figure 4.105: Comparison of radial temperature profiles at front stagnation point of a steel-aluminum friction weld at time t=2.0 s with an angular speed of 2500 rpm for different jet velocities.

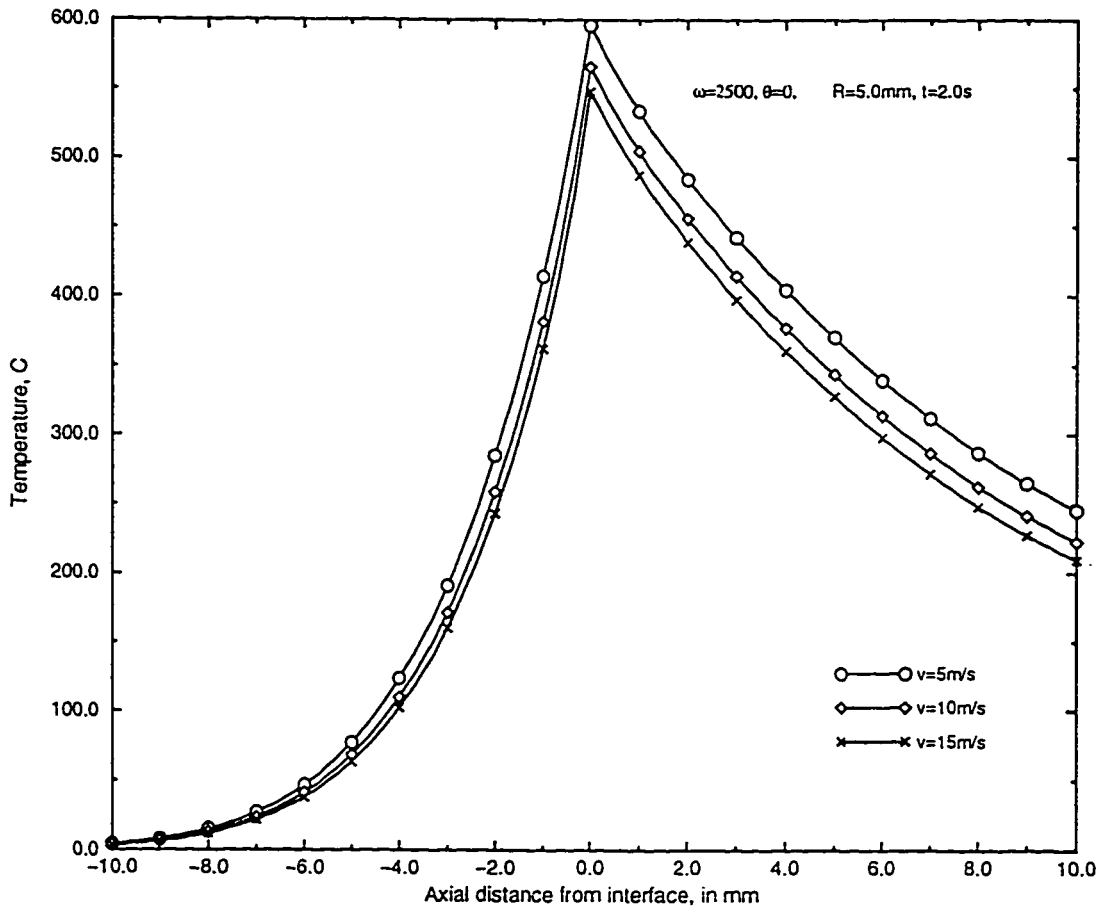

Figure 4.106: Comparison of axial temperature profiles at back stagnation point of a steel-aluminum friction weld at time t=2.0 s with an angular speed of 2500 rpm for different jet velocities.

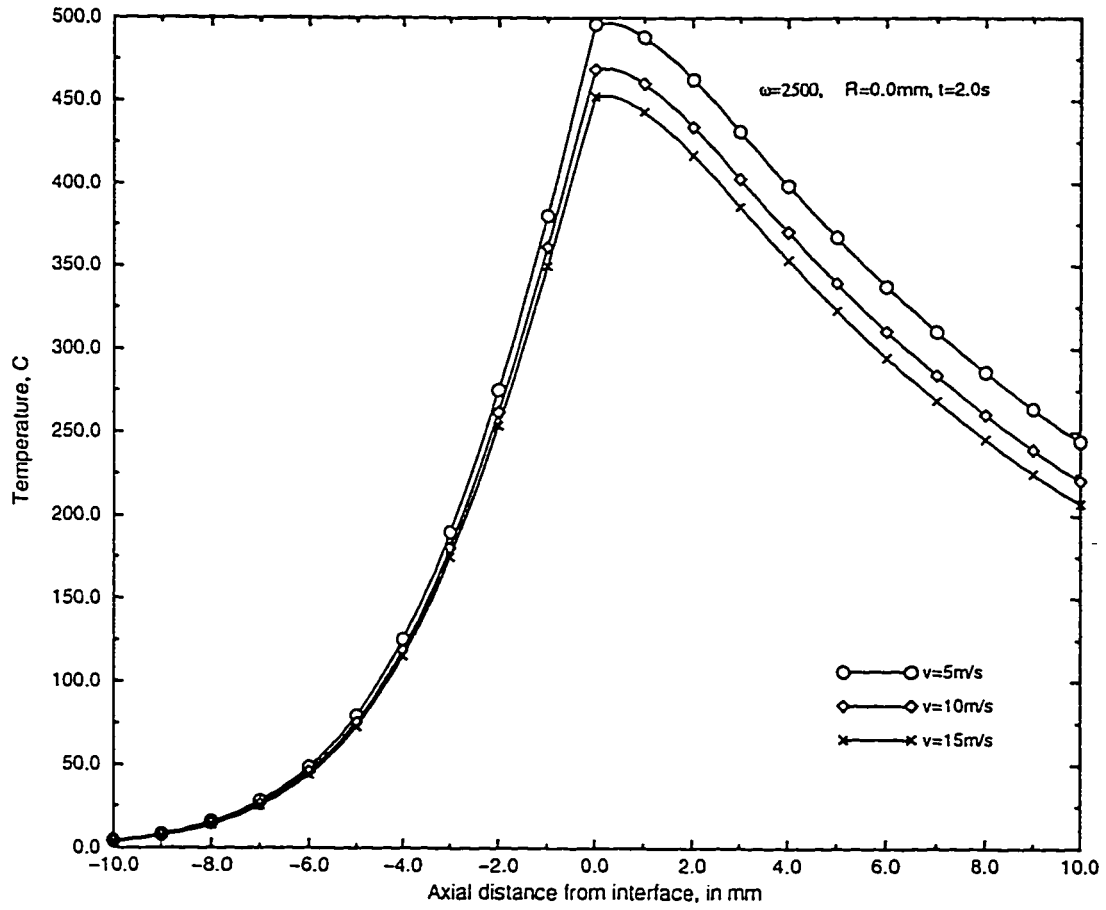

Figure 4.107: Comparison of centerline temperature profiles with theof a steel-aluminum friction weld with an angular speed of 2500 rpm for different jet velocities.

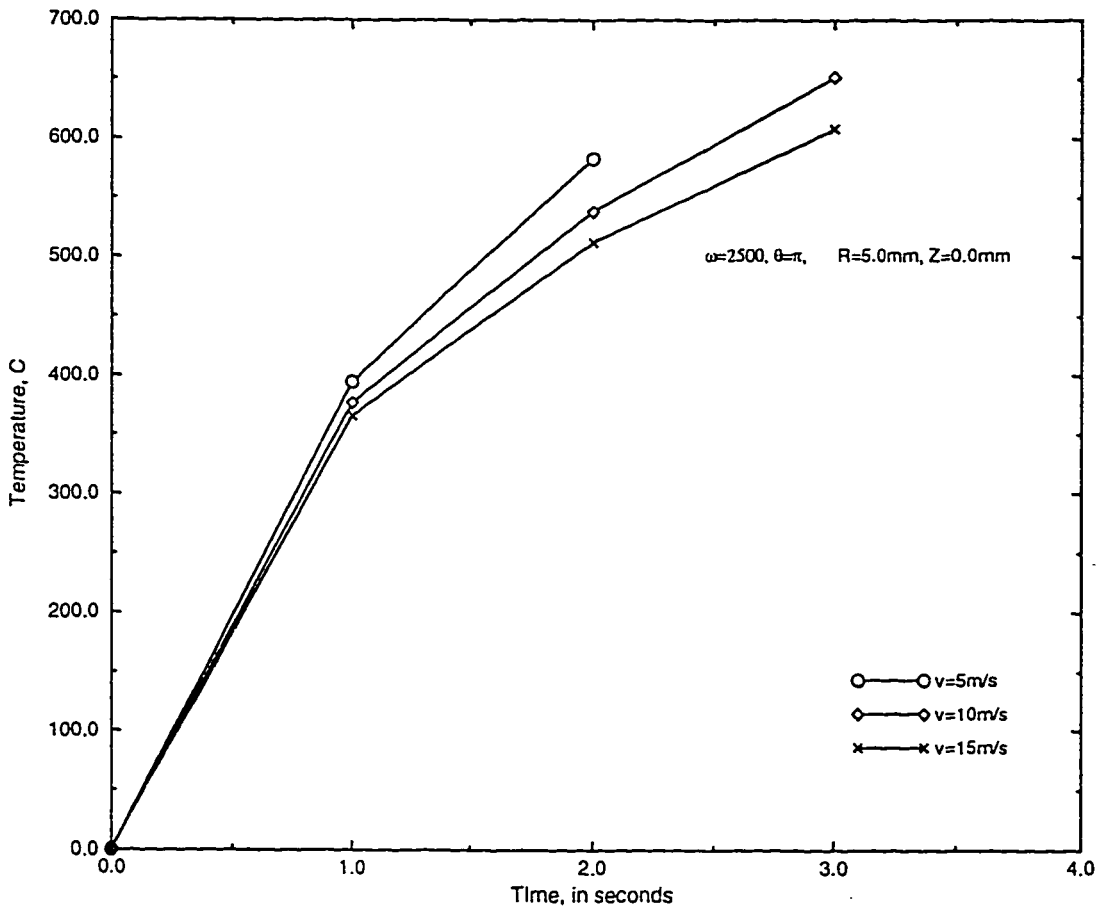

Figure 4.108: Comparison of temperature profiles with the increase of time at front stagnation point of a steel-aluminum friction weld with an angular speed of 2500 rpm for different jet velocities.

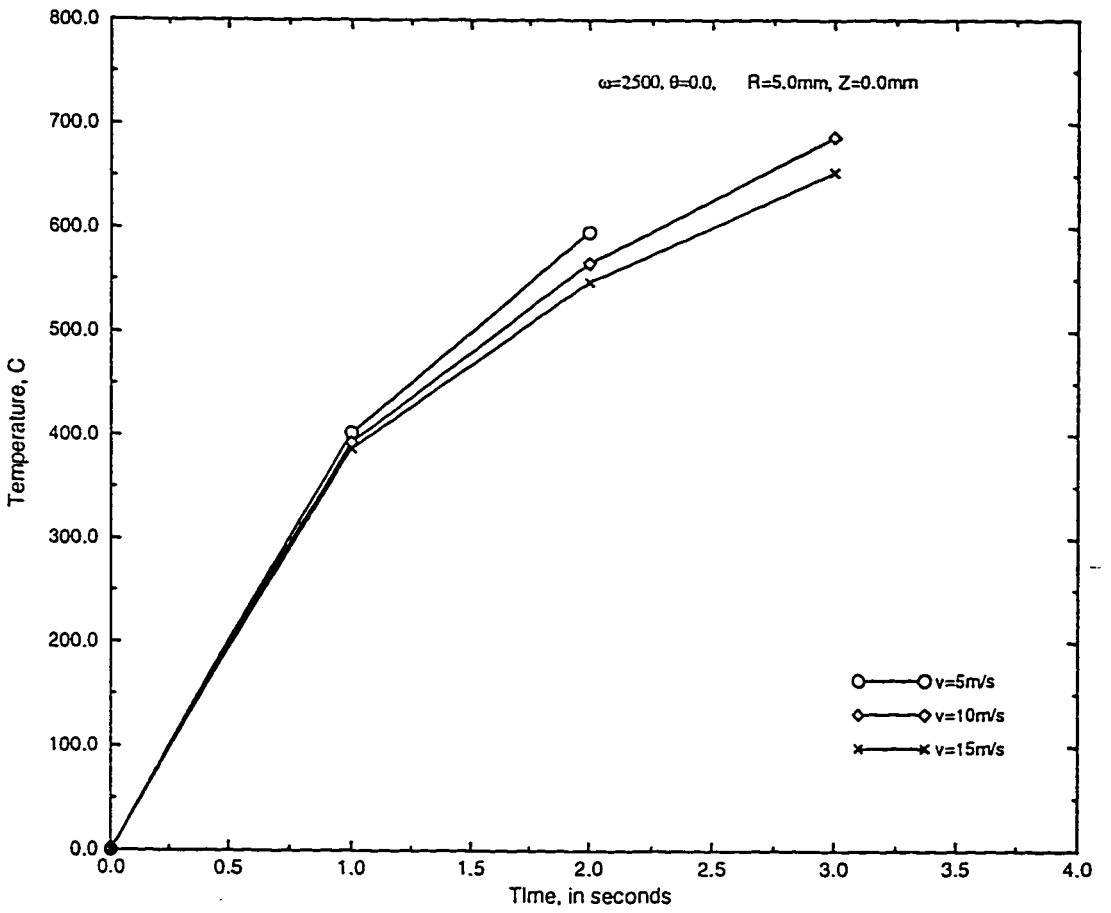

Figure 4.109: Comparison of temperature profiles with the increase of time at back stagnation point of a steel-aluminum friction weld with an angular speed of 2500 rpm for different jet velocities.

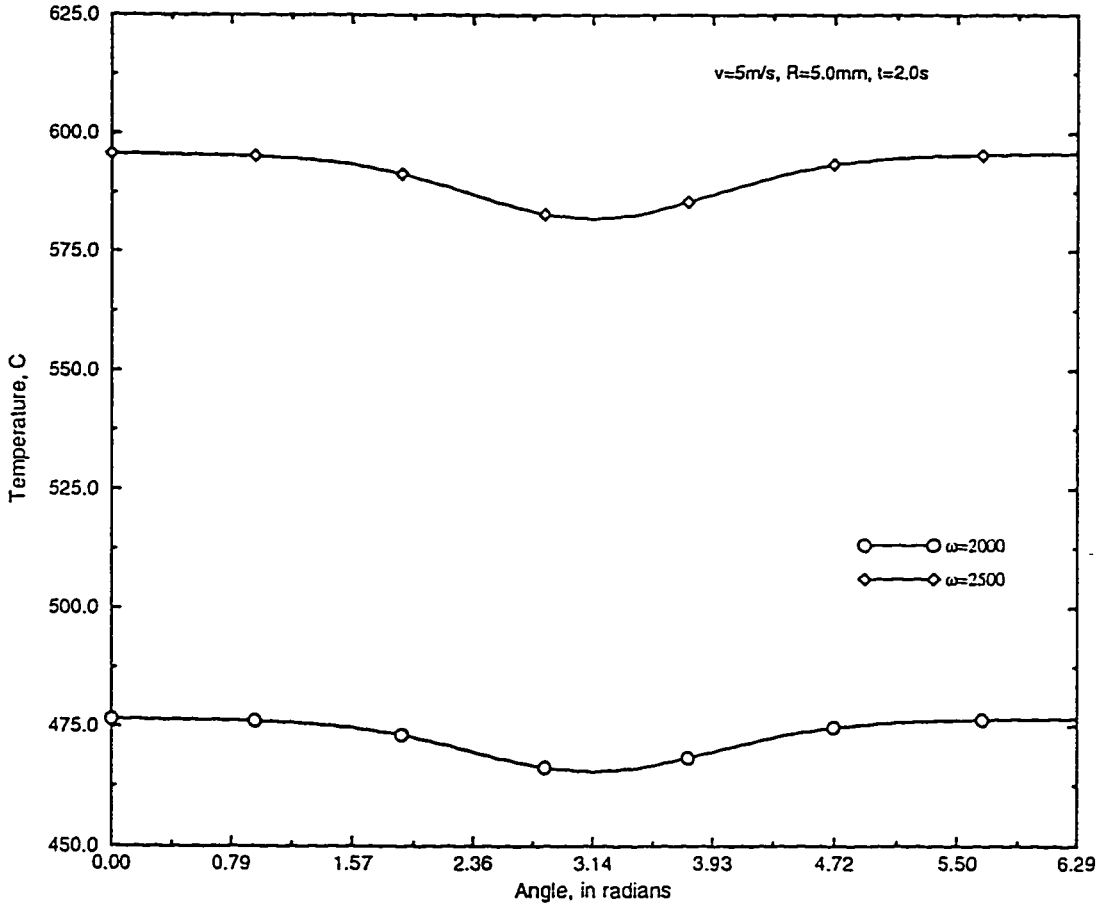

Figure 4.110: Comparison of circumferential temperature profiles on the surface of a steel-aluminum friction weld at time t=2.0 s with a jet velocity of v=5 m/s for different angular speeds.

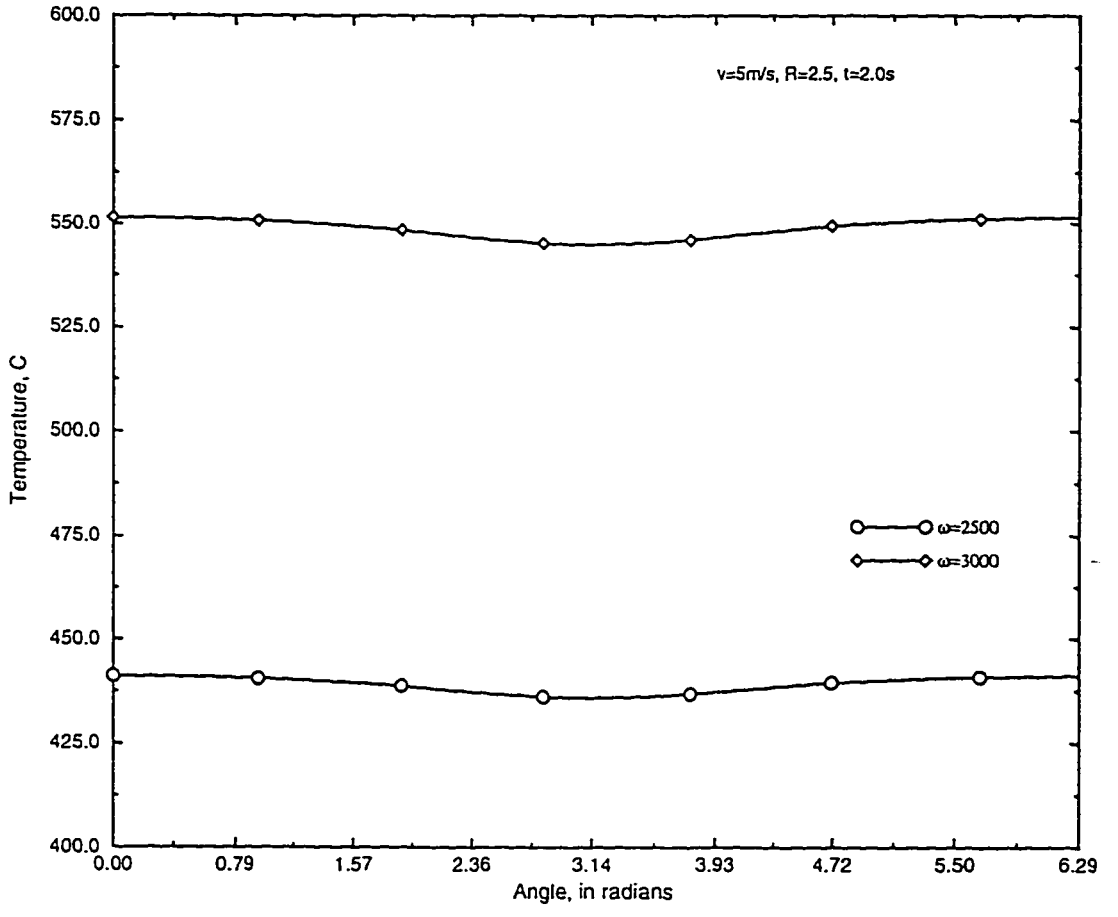

Figure 4.111: Comparison of circumferential temperature profiles at mid-radius of a steel-aluminum friction weld at time t=2.0 s with a jet velocity of v=5 m/s for different angular speeds.

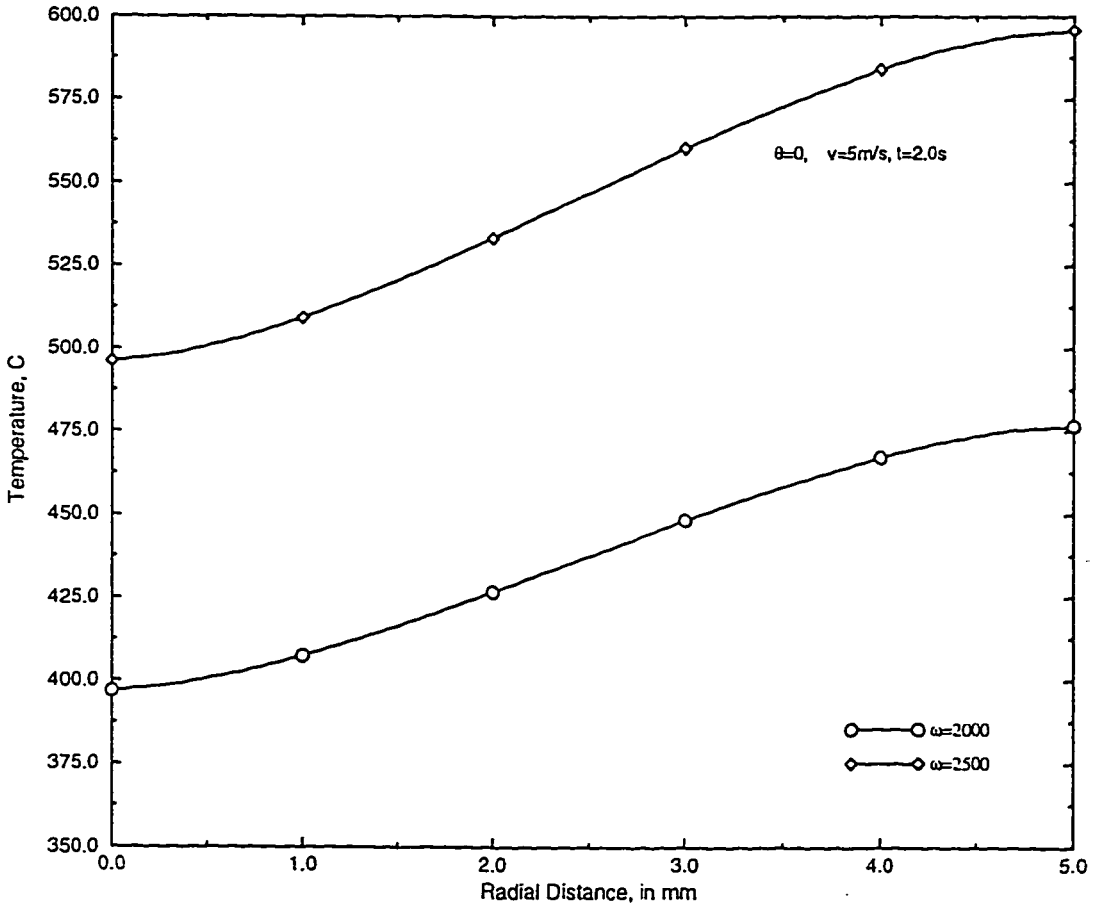

Figure 4.112: Comparison of radial temperature profiles at back stagnation point of a steel-aluminum friction weld at time t=2.0 s with a jet velocity of v=5 m/s for different angular speeds.

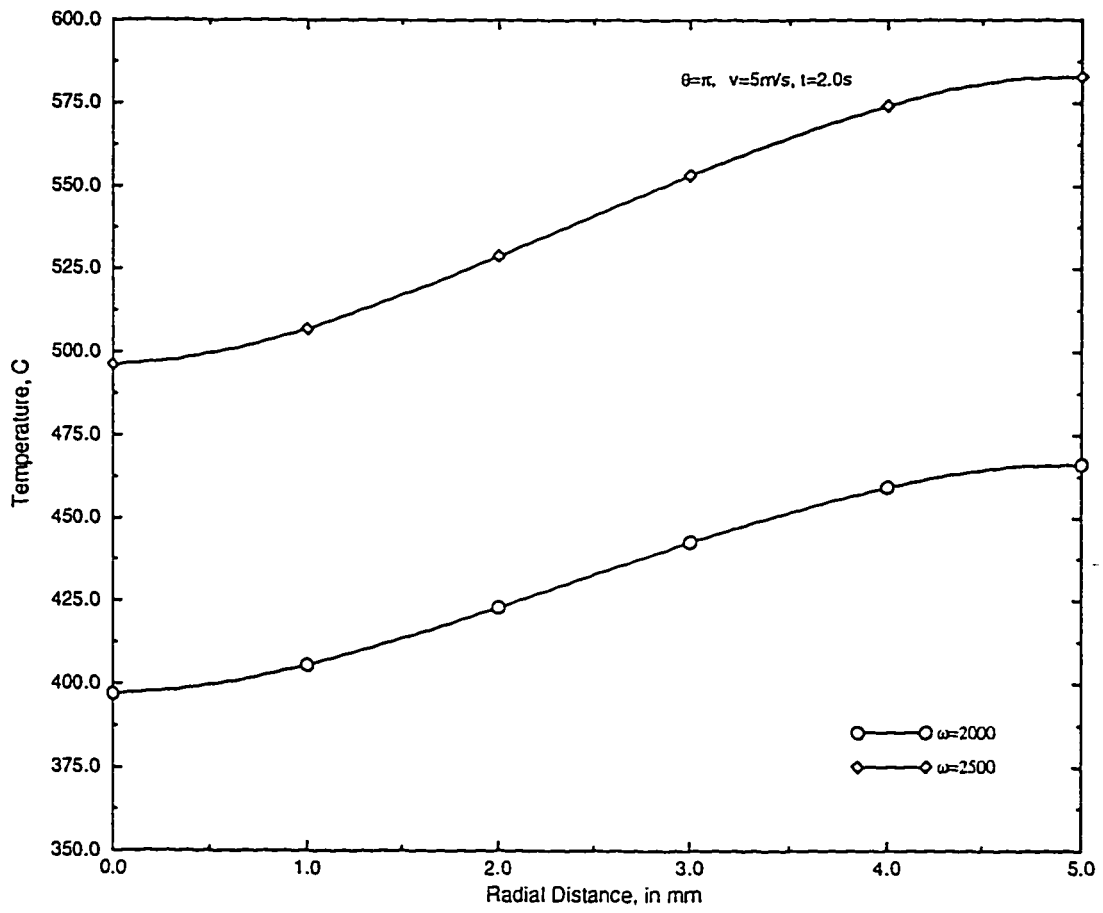

Figure 4.113: Comparison of radial temperature profiles at front stagnation point of a steel-aluminum friction weld at time t=2.0 s with a jet velocity of v=5 m/s for different angular speeds.

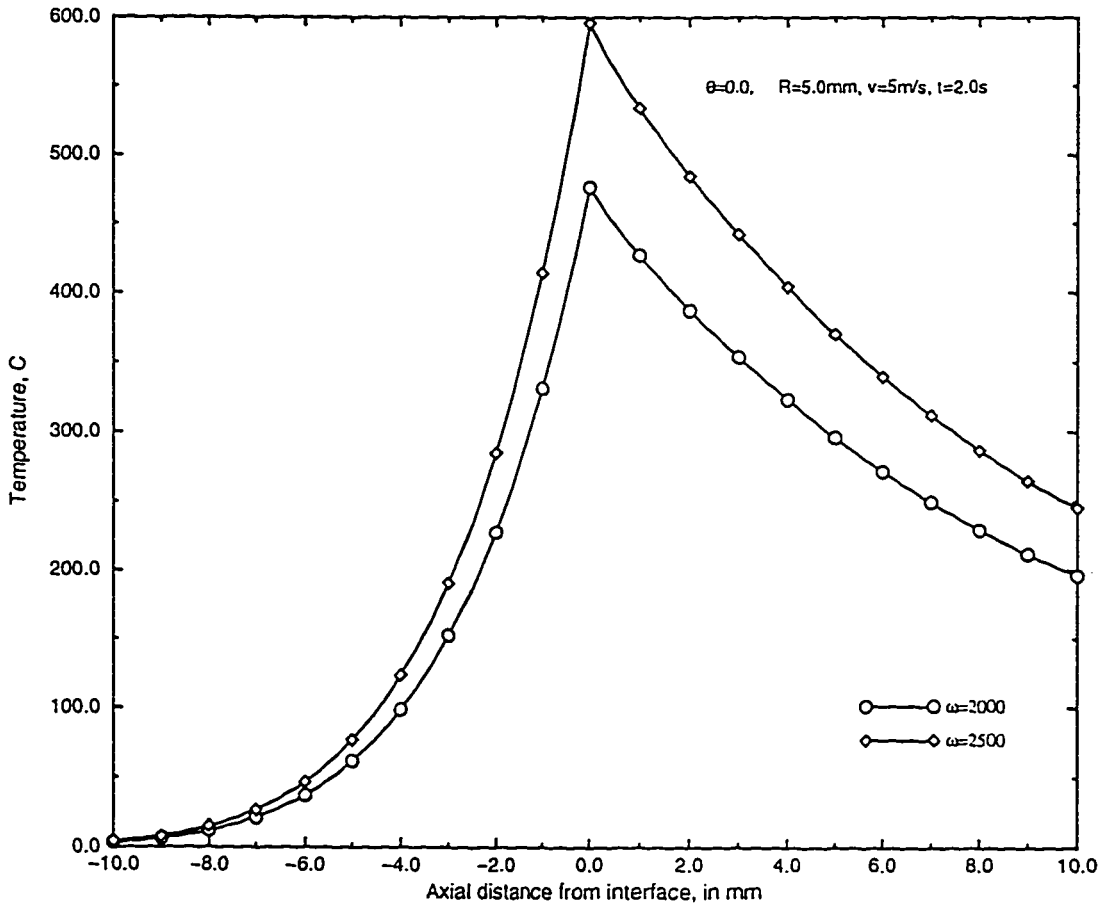

Figure 4.114: Comparison of axial temperature profiles at back stagnation point of a steel-aluminum friction weld at time t=2.0 s with a jet velocity of v=5 m/s for different angular speeds.

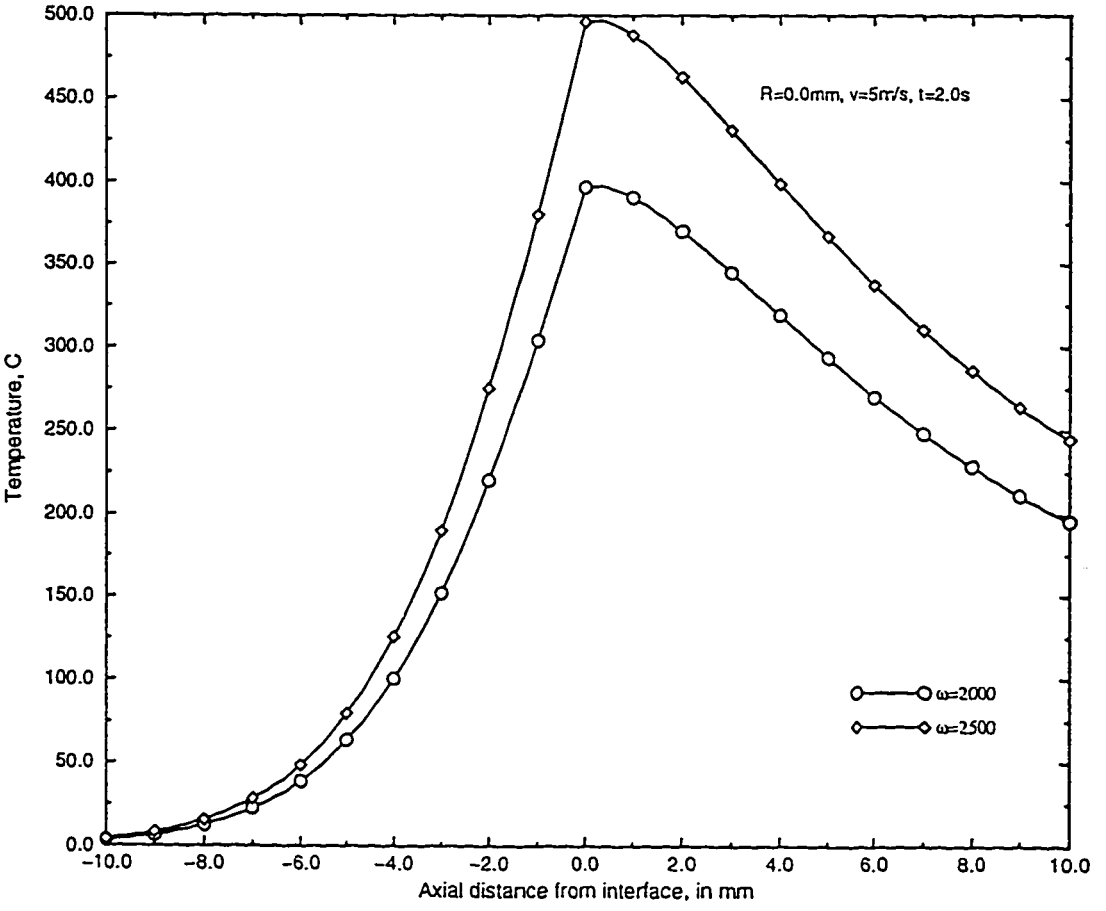

Figure 4.115: Comparison of centerline temperature profiles of a steel-aluminum friction weld at time t=8s with a jet velocity of v=5 m/s for different angular speeds.

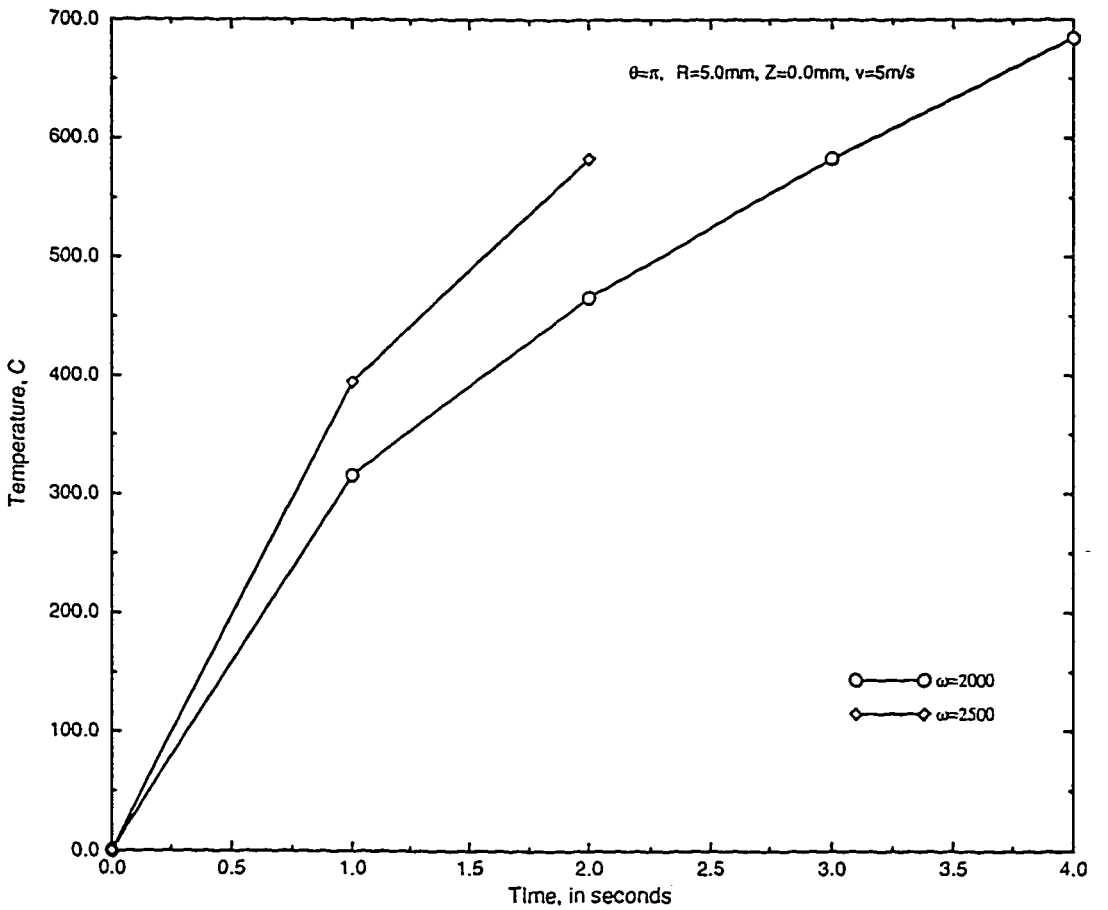

Figure 4.116: Comparison of temperature raise at front stagnation point of a steel-aluminum friction weld with a jet velocity of v=5 m/s for different angular speeds.

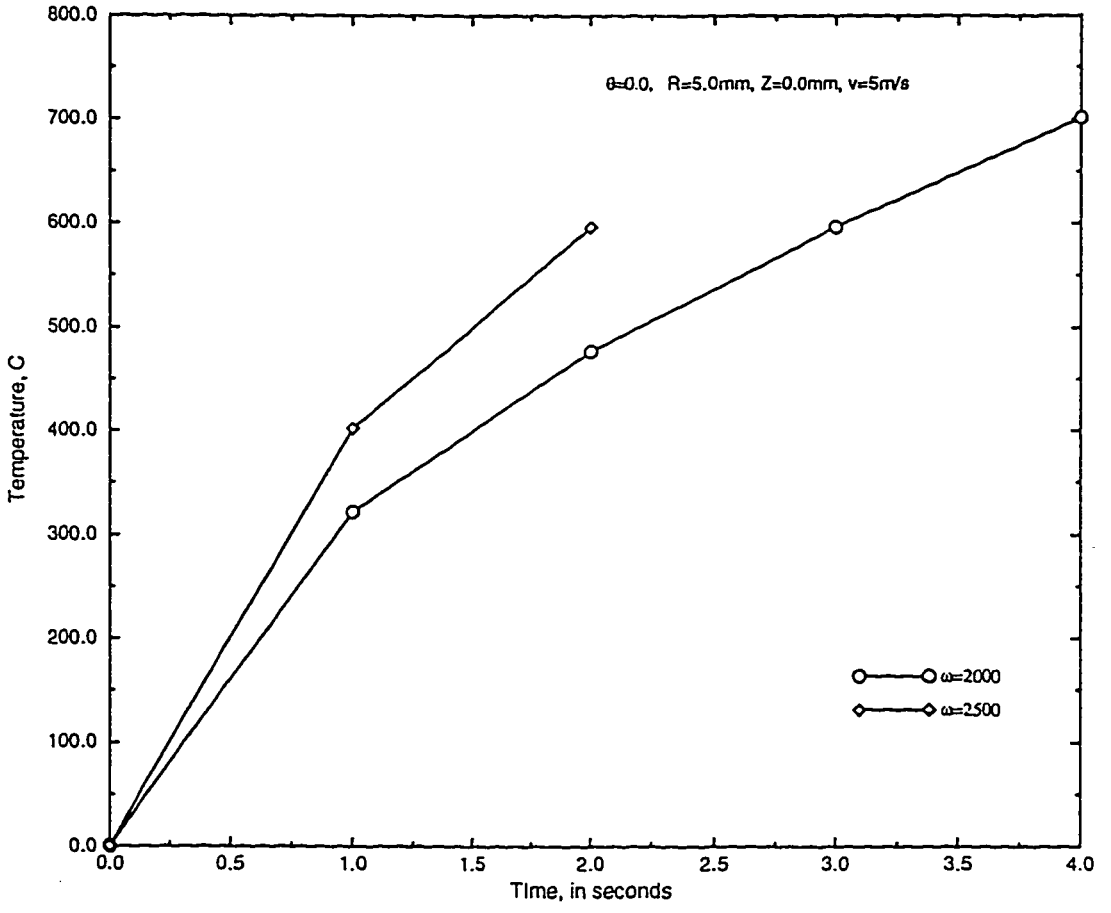

Figure 4.117: Comparison of temperature raise at back stagnation point of a steel-aluminum friction weld with a jet velocity of v=5 m/s for different angular speeds.

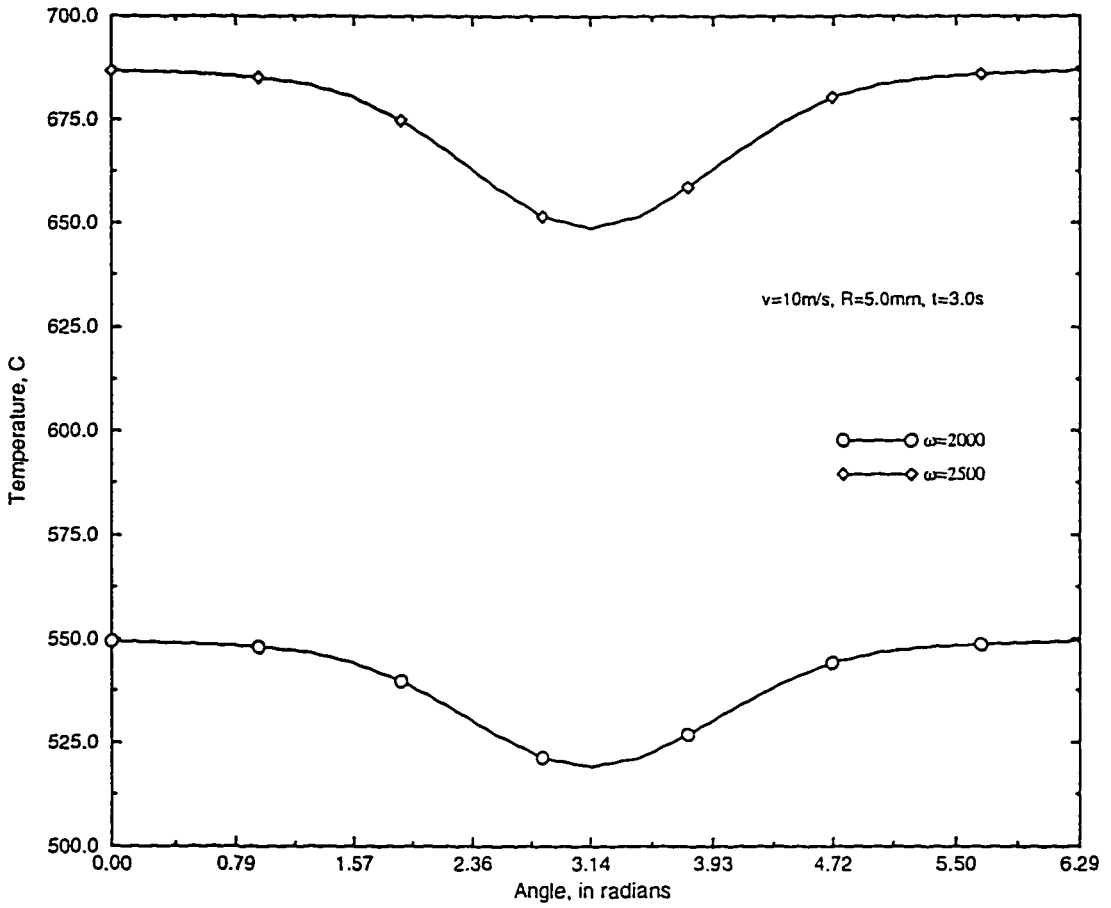

Figure 4.118: Comparison of circumferential temperature profiles on the surface of a steel-aluminum friction weld at time t=3.0 s with a jet velocity of v=10 m/s for different angular speeds.

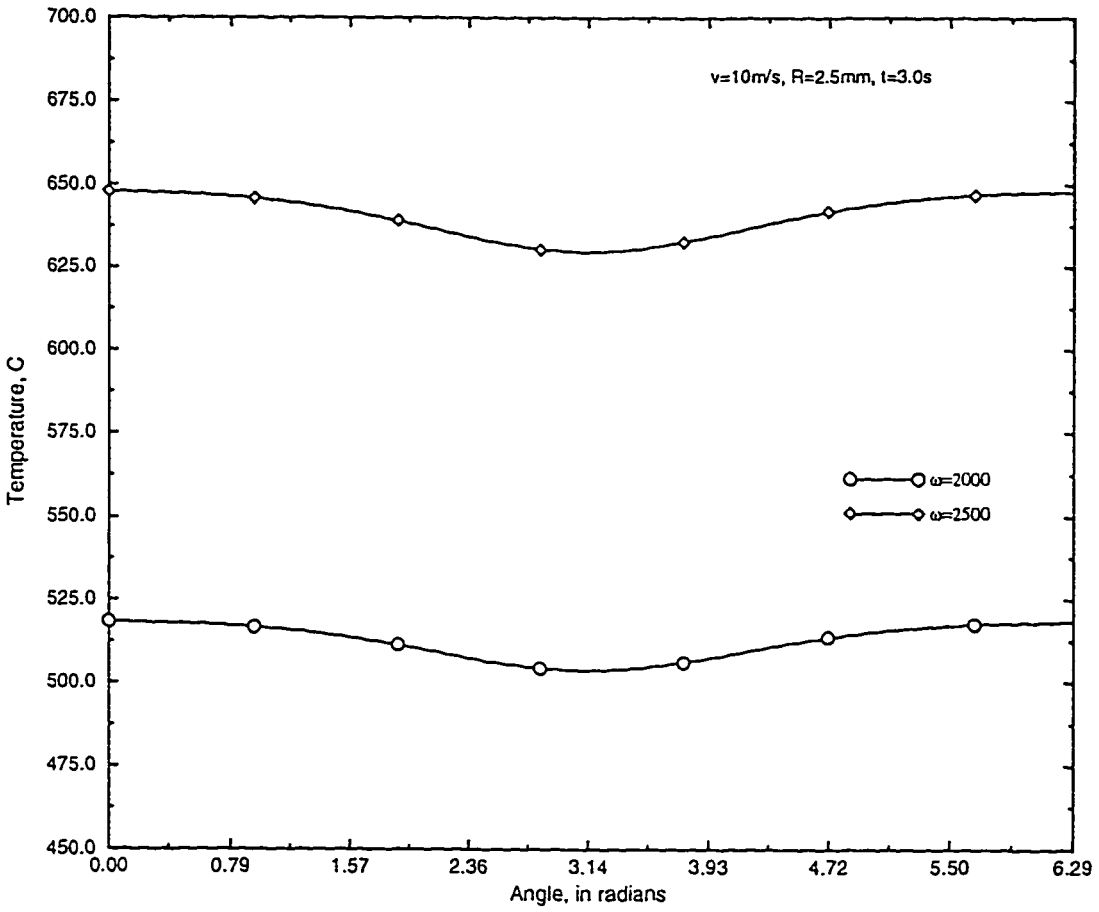

Figure 4.119: Comparison of circumferential temperature profiles at mid-radius of a steel-aluminum friction weld at time t=3.0 s with a jet velocity of v=10 m/s for different angular speeds.

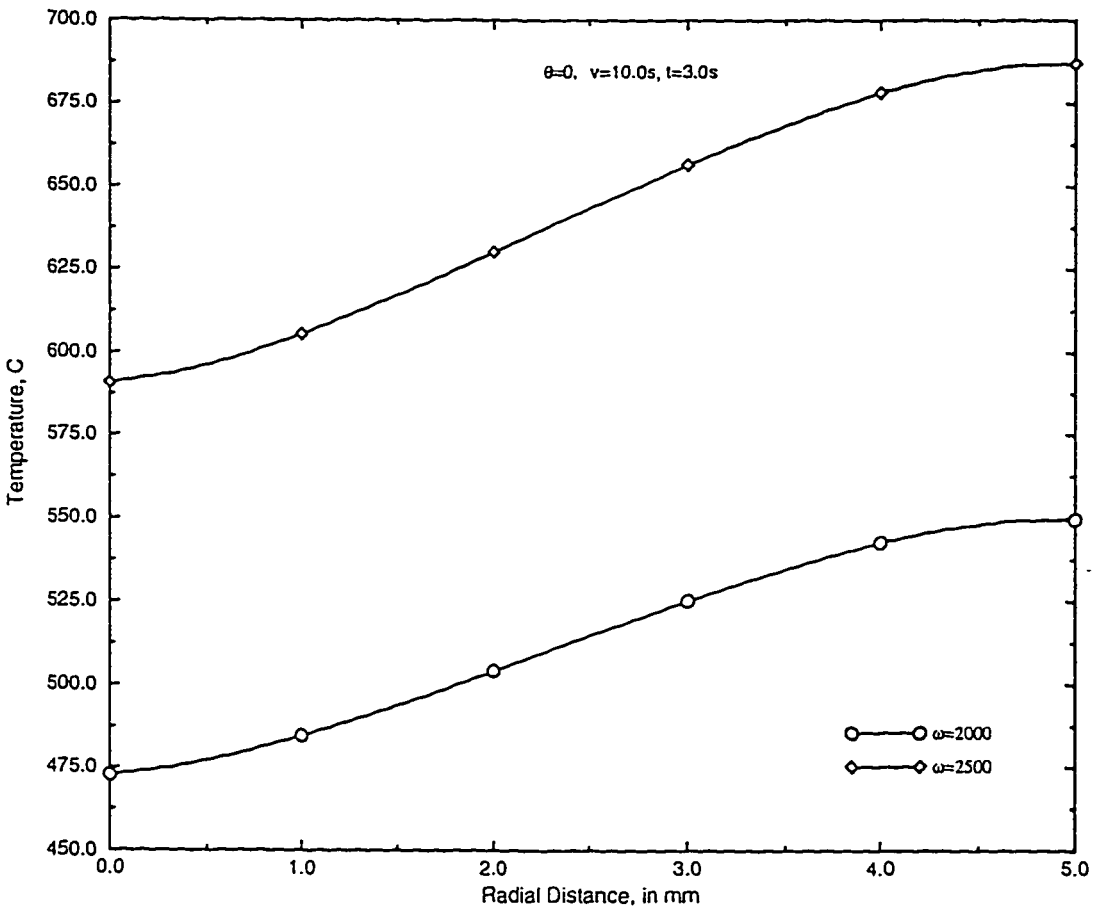

Figure 4.120: Comparison of radial temperature profiles at back stagnation point of a steel-aluminum friction weld at time t=3.0 s with a jet velocity of v=10 m/s for different angular speeds.

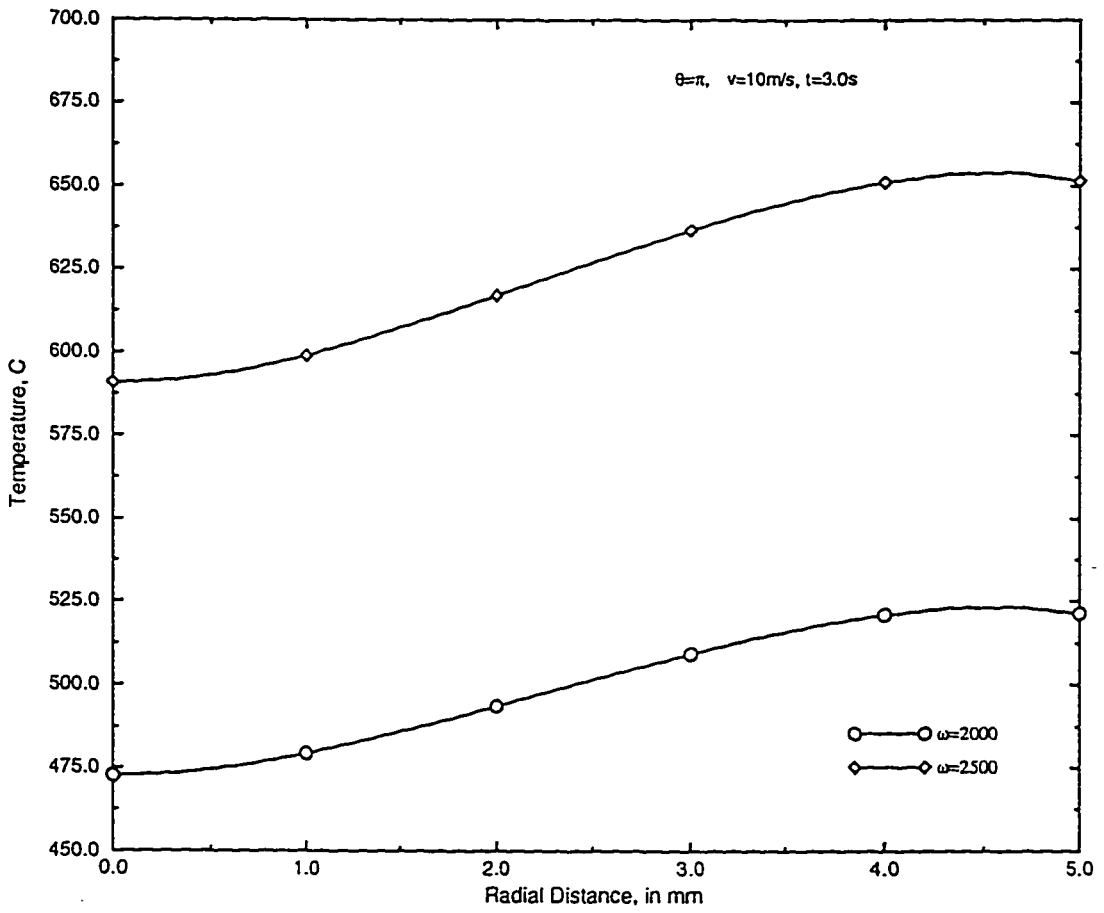

Figure 4.121: Comparison of radial temperature profiles at front stagnation point of a steel-aluminum friction weld at time t=3.0 s with a jet velocity of v=10 m/s for different angular speeds.

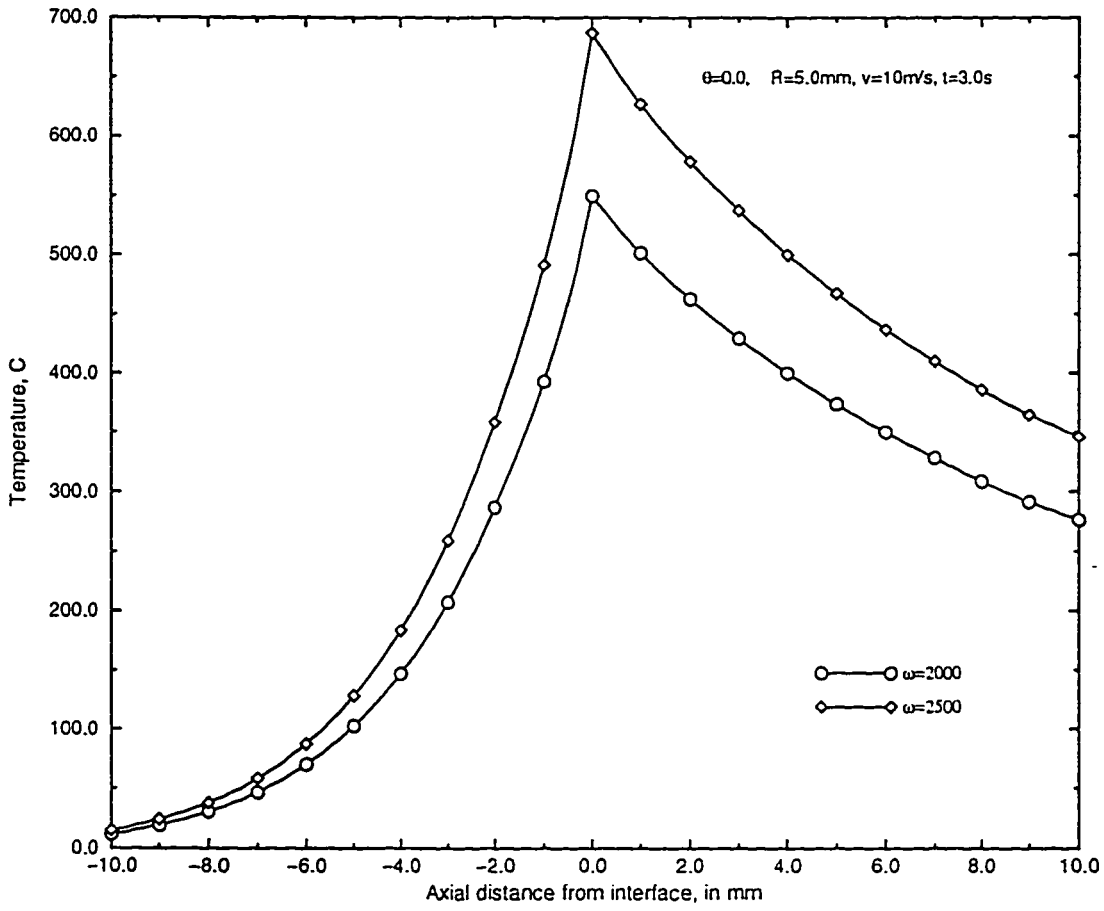

Figure 4.122: Comparison of axial temperature profiles at back stagnation point of a steel-aluminum friction weld at time t=3.0 s with a jet velocity of v=10 m/s for different angular speeds.

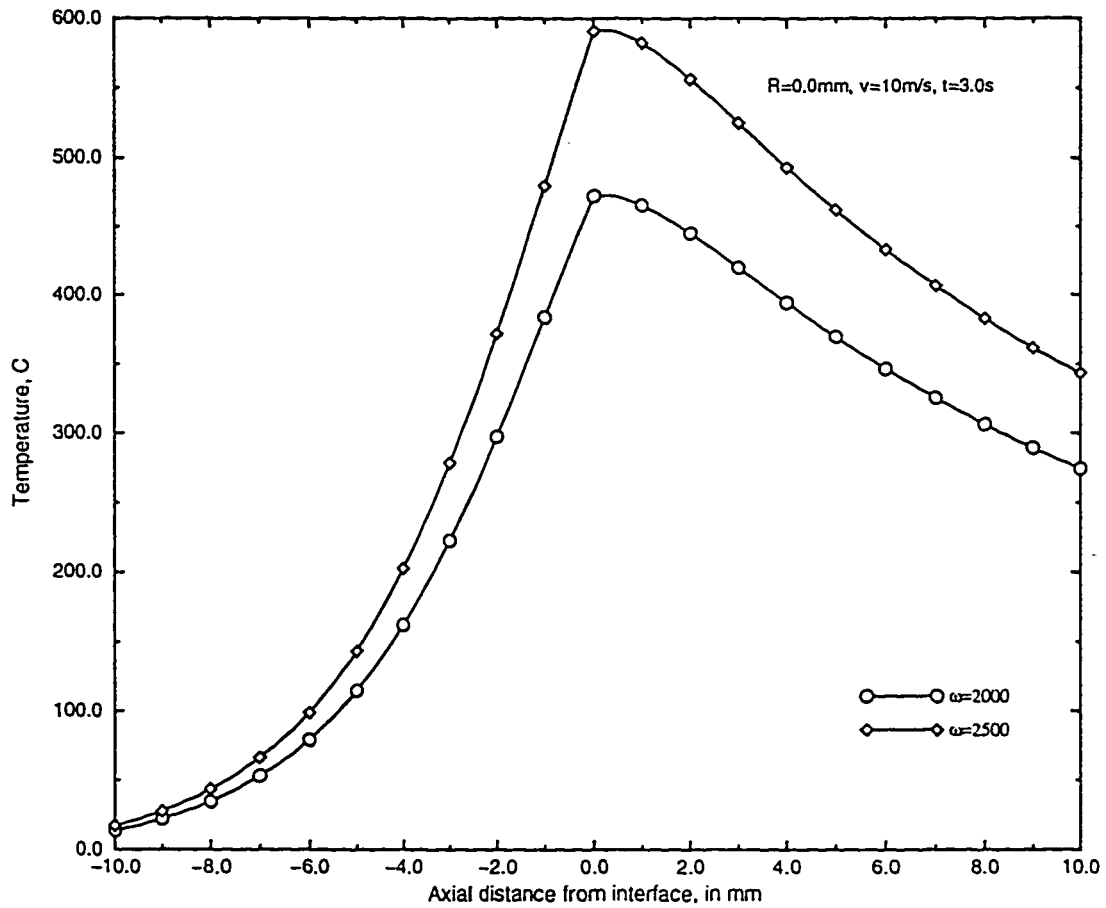

Figure 4.123: Comparison of centerline temperature profiles of a steel-aluminum friction weld at time t=3.0 s with a jet velocity of v=10 m/s for different angular speeds.

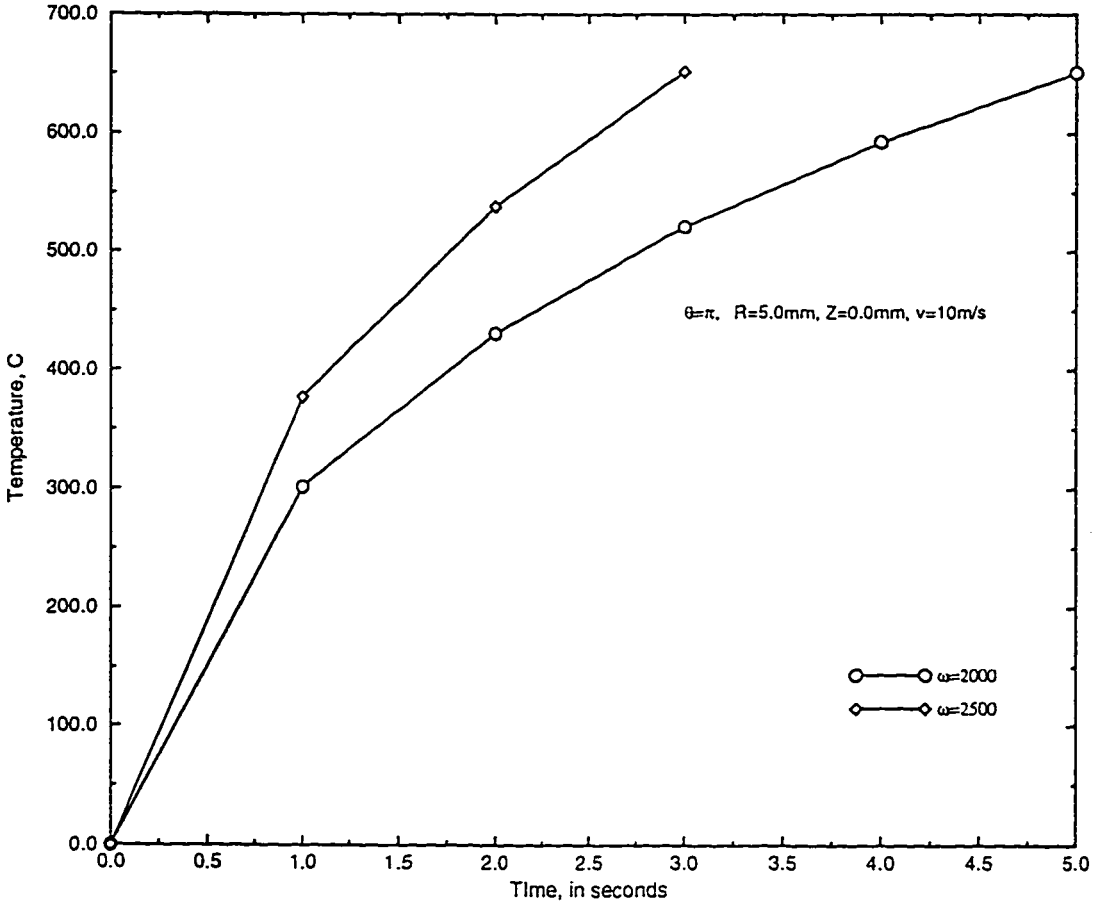

Figure 4.124: Comparison of temperature raise at front stagnation point of a steel-aluminum friction weld with a jet velocity of v=10 m/s for different angular speeds.

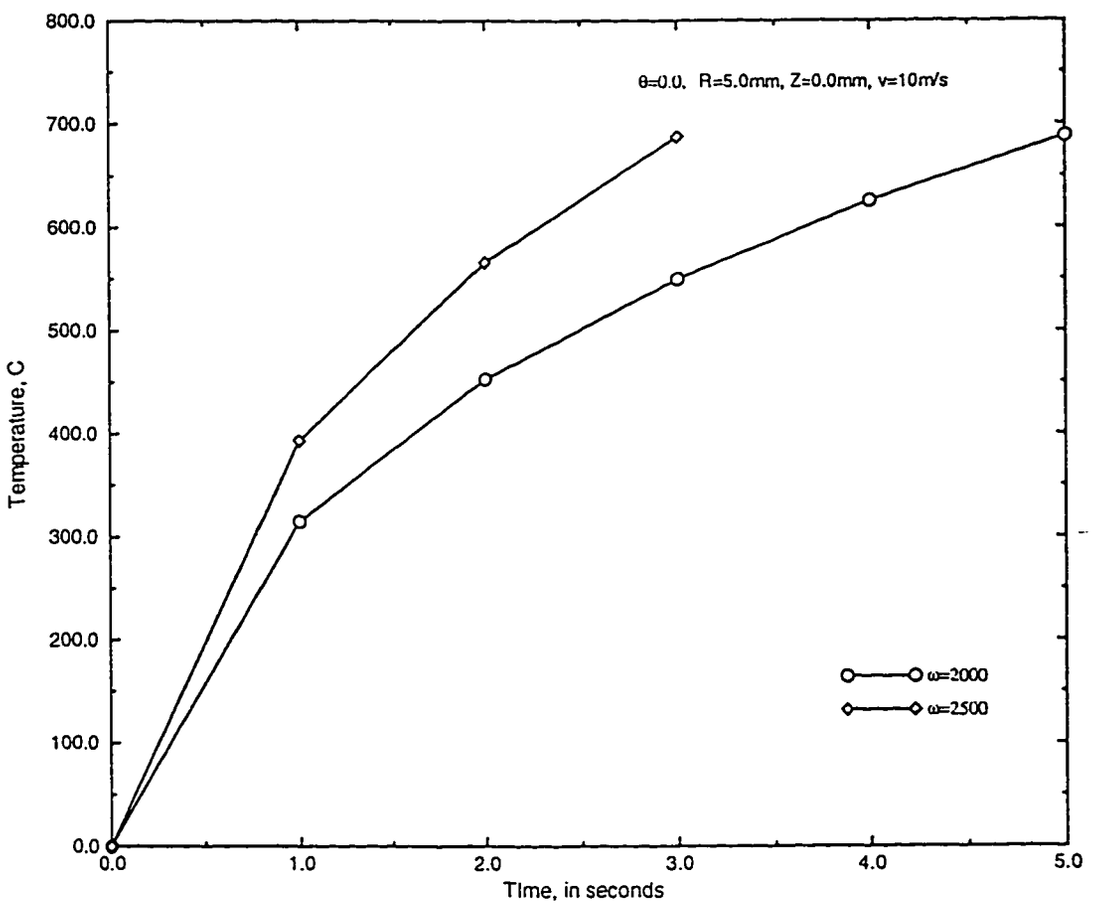

Figure 4.125: Comparison of temperature raise at back stagnation point of a steel-aluminum friction weld with a jet velocity of v=10 m/s for different angular speeds.

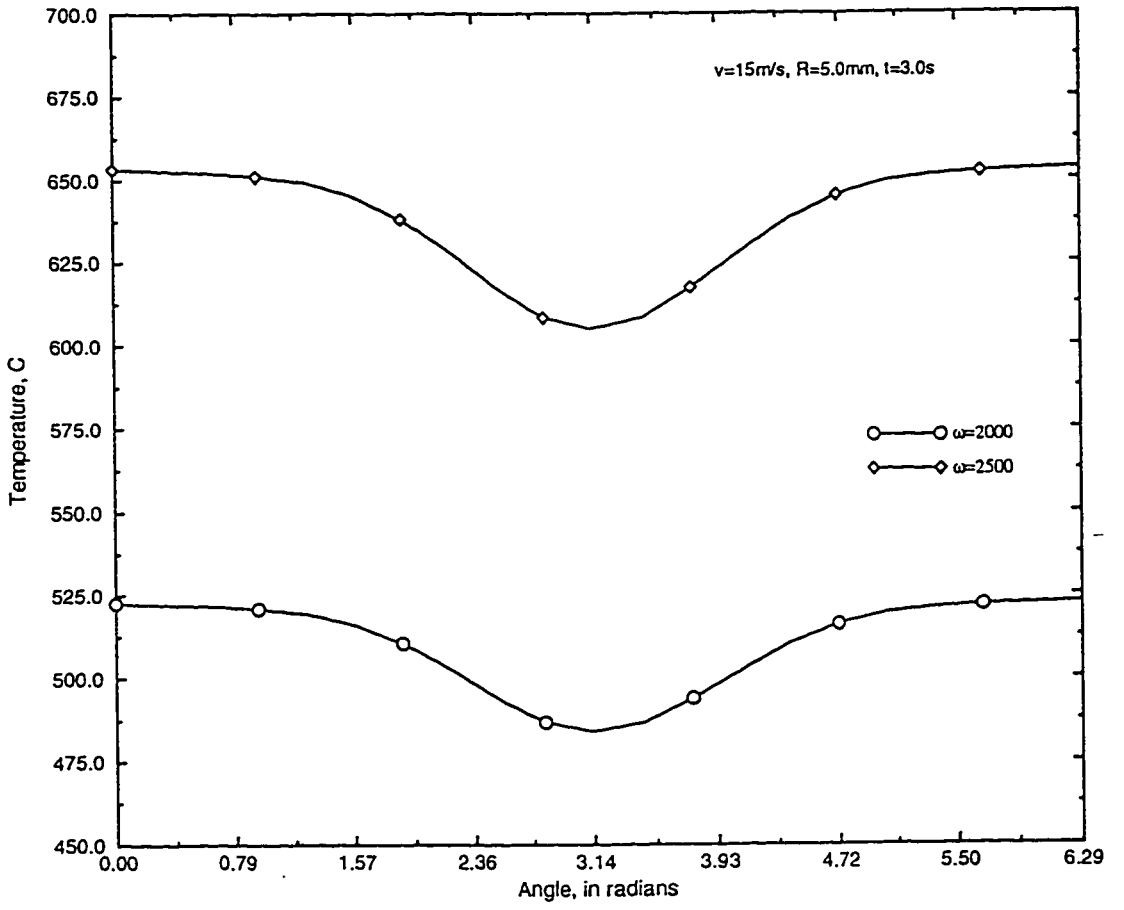

Figure 4.126: Comparison of circumferential temperature profiles on the surface of a steel-aluminum friction weld at time t=3.0 s with a jet velocity of v=15 m/s for different angular speeds.

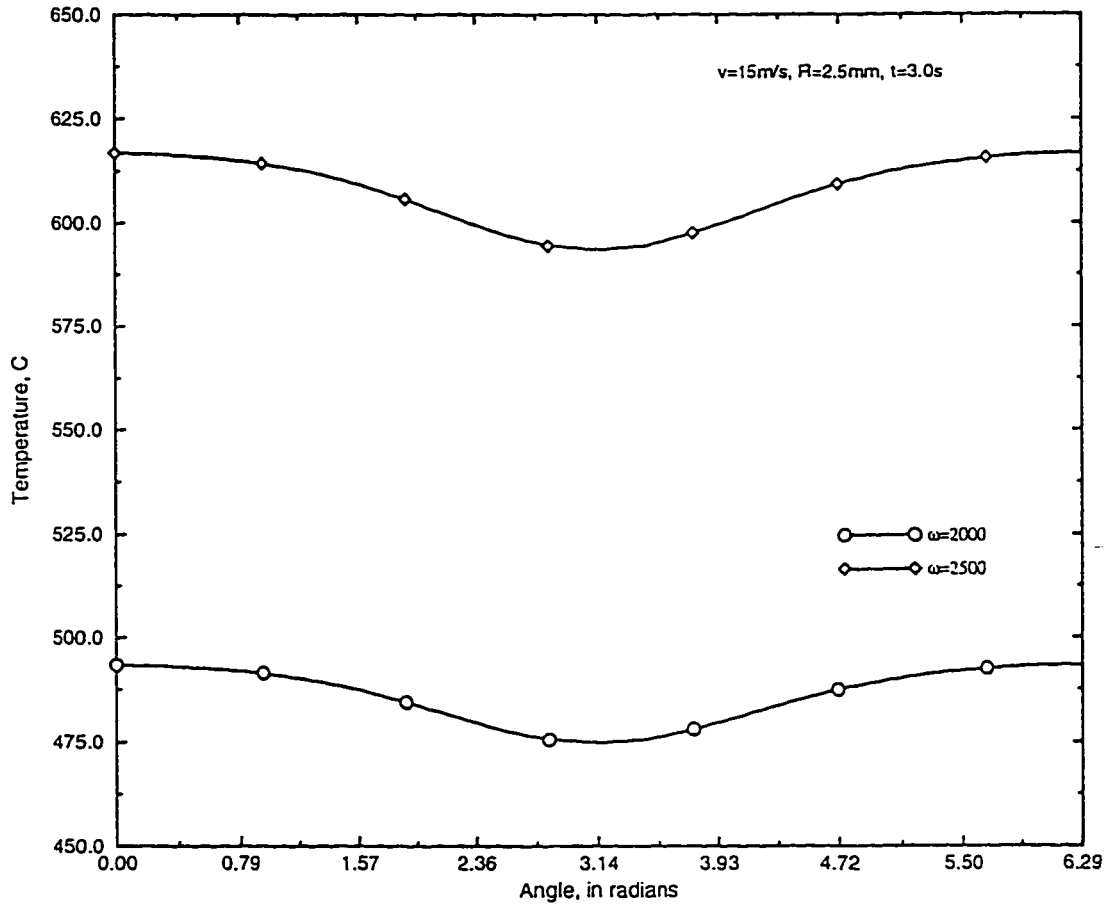

Figure 4.127: Comparison of circumferential temperature profiles at mid-radius of a steel-aluminum friction weld at time t=3.0 s with a jet velocity of v=15 m/s for different angular speeds.

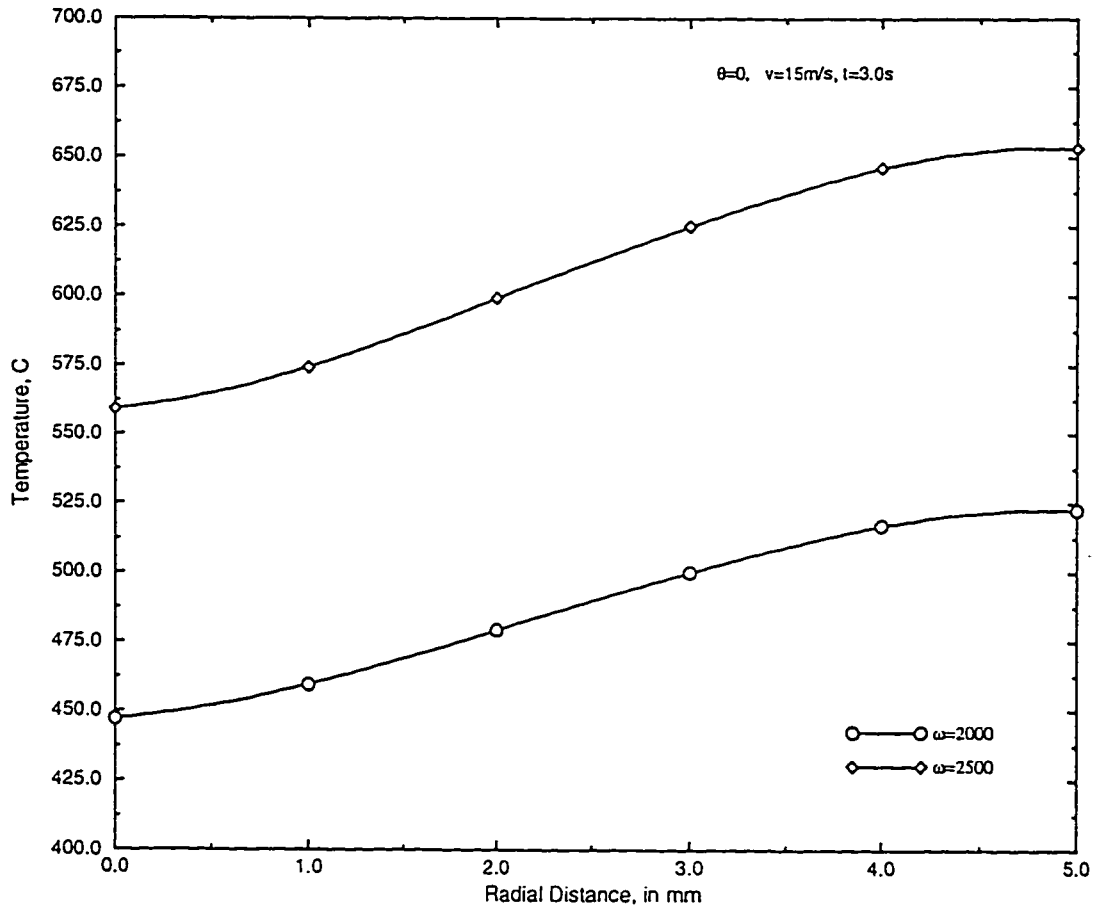

Figure 4.128: Comparison of radial temperature profiles at back stagnation point of a steel-aluminum friction weld at time t=3.0 s with a jet velocity of v=15 m/s for different angular speeds.

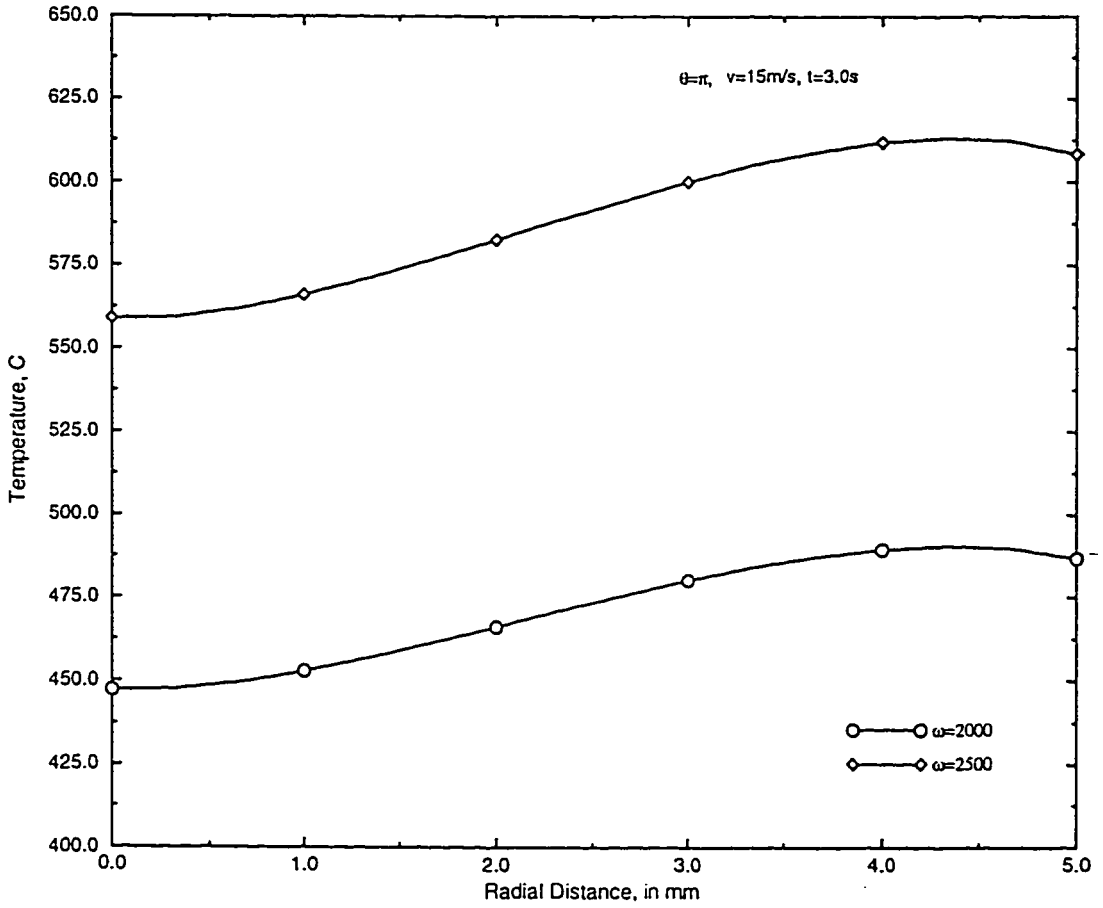

Figure 4.129: Comparison of radial temperature profiles at front stagnation point of a steel-aluminum friction weld at time t=3.0 s with a jet velocity of v=15 m/s for different angular speeds.

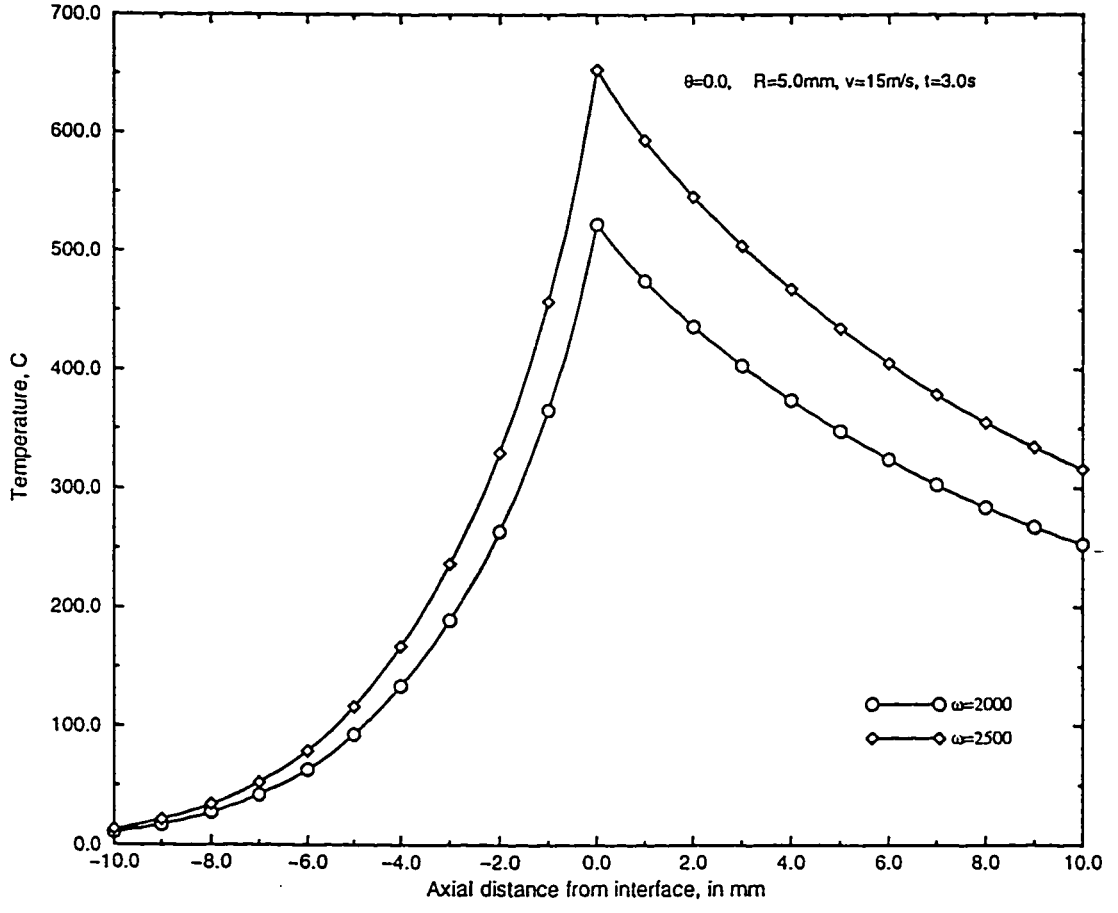

Figure 4.130: Comparison of axial temperature profiles at back stagnation point of a steel-aluminum friction weld at time t=3.0 s with a jet velocity of v=15 m/s for different angular speeds.

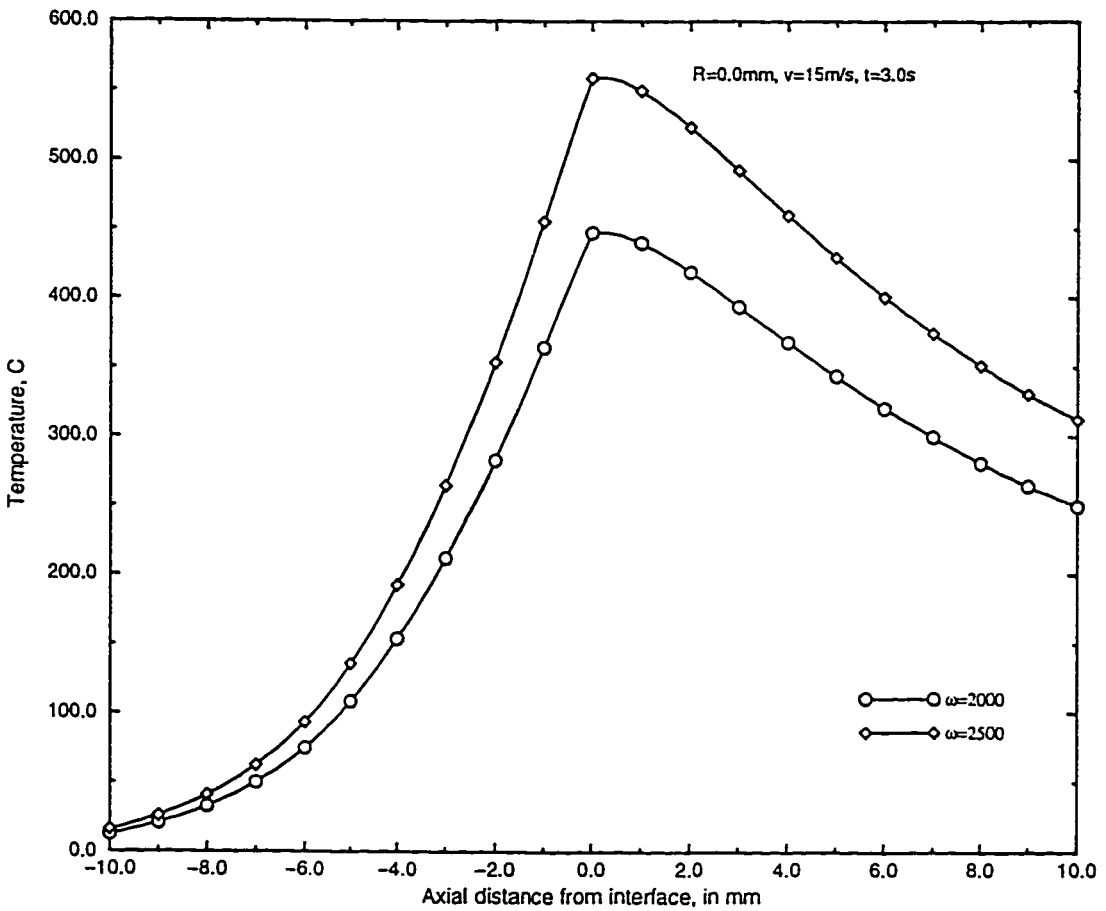

Figure 4.131: Comparison of centerline temperature profiles of a steel-aluminum friction weld at time t=3.0 s with a jet velocity of v=15 m/s for different angular speeds.

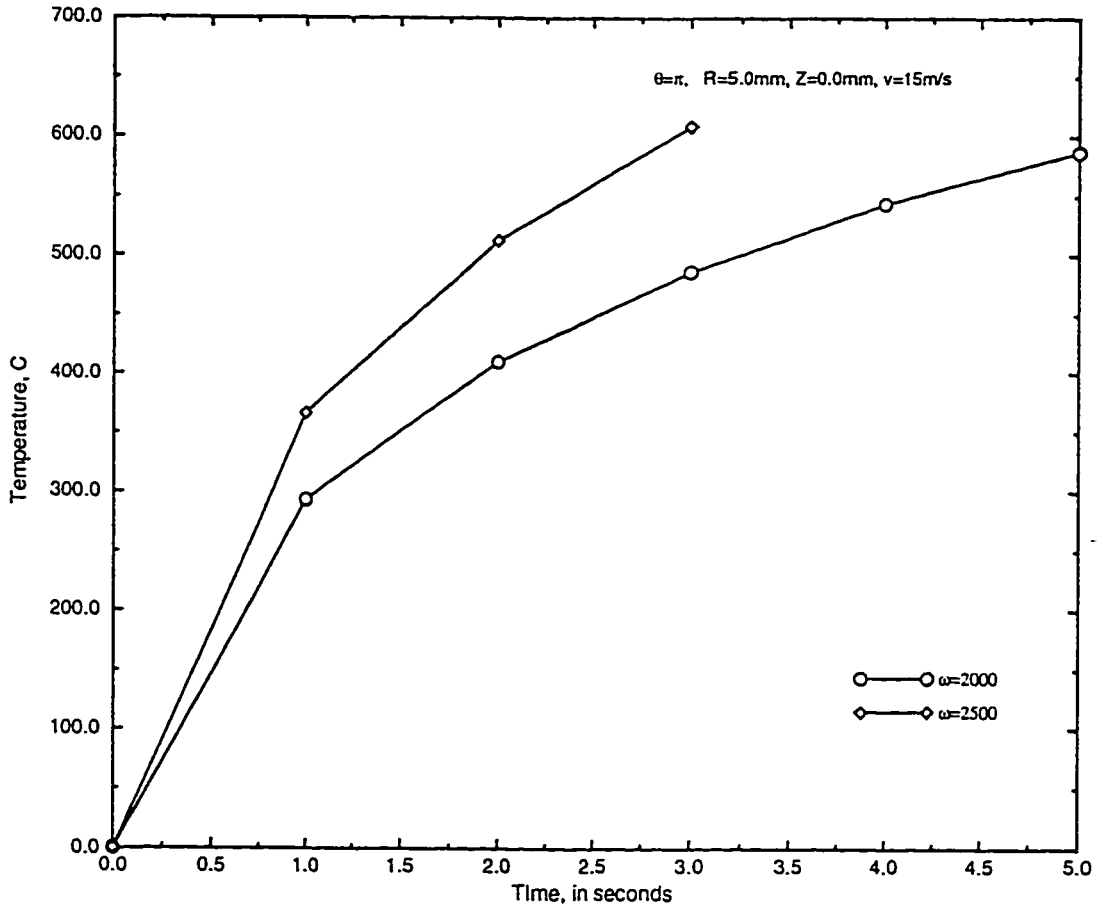

Figure 4.132: Comparison of temperature raise at front stagnation point of a steel-aluminum friction weld with a jet velocity of v=15 m/s for different angular speeds.

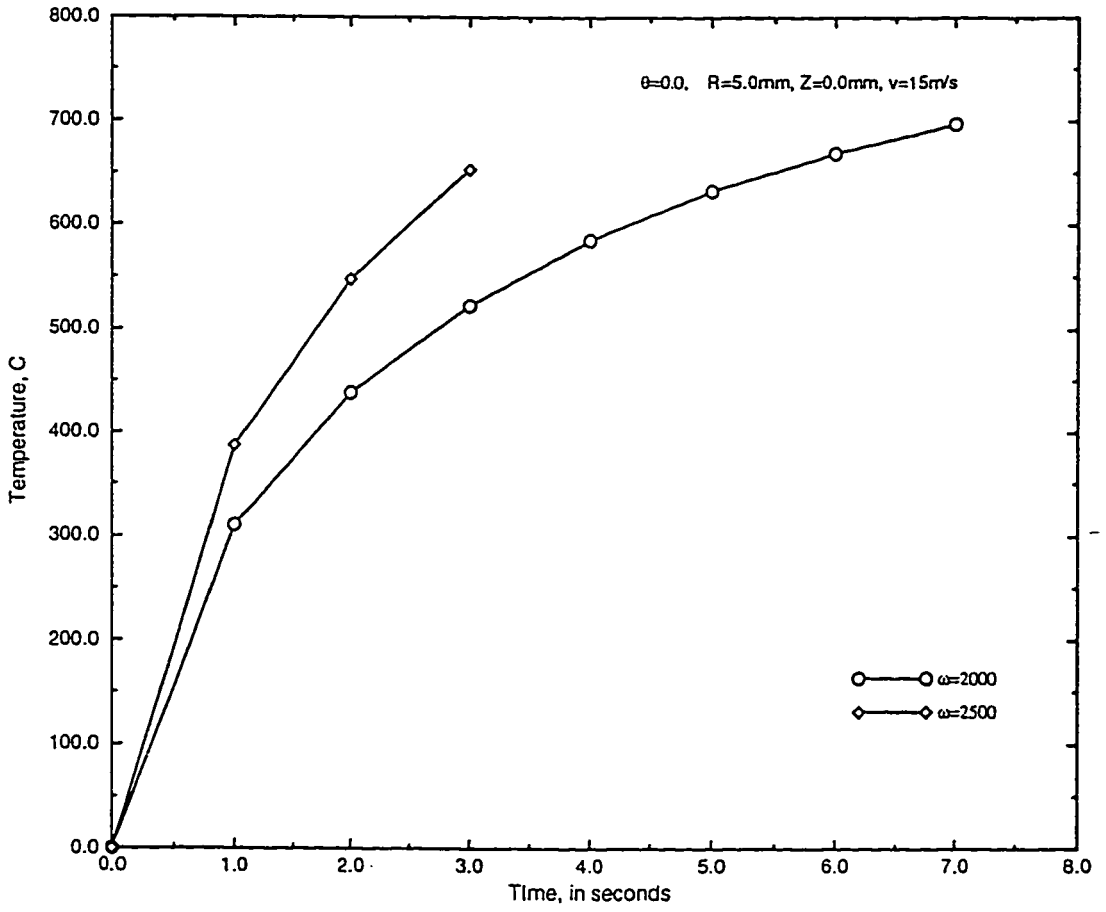

Figure 4.133: Comparison of temperature raise at back stagnation point of a steel-aluminum friction weld with a jet velocity of v=15 m/s for different angular speeds.

To validate of these results, a comparison is made with published results [19]. The discrepancy in the results obtained in this study and the published ones, as shown in Fig. 4.134, is due to the difference in modeling of the heat generation rate at the interface of the two bars. Another reason is the friction coefficient at the interface of the two materials.

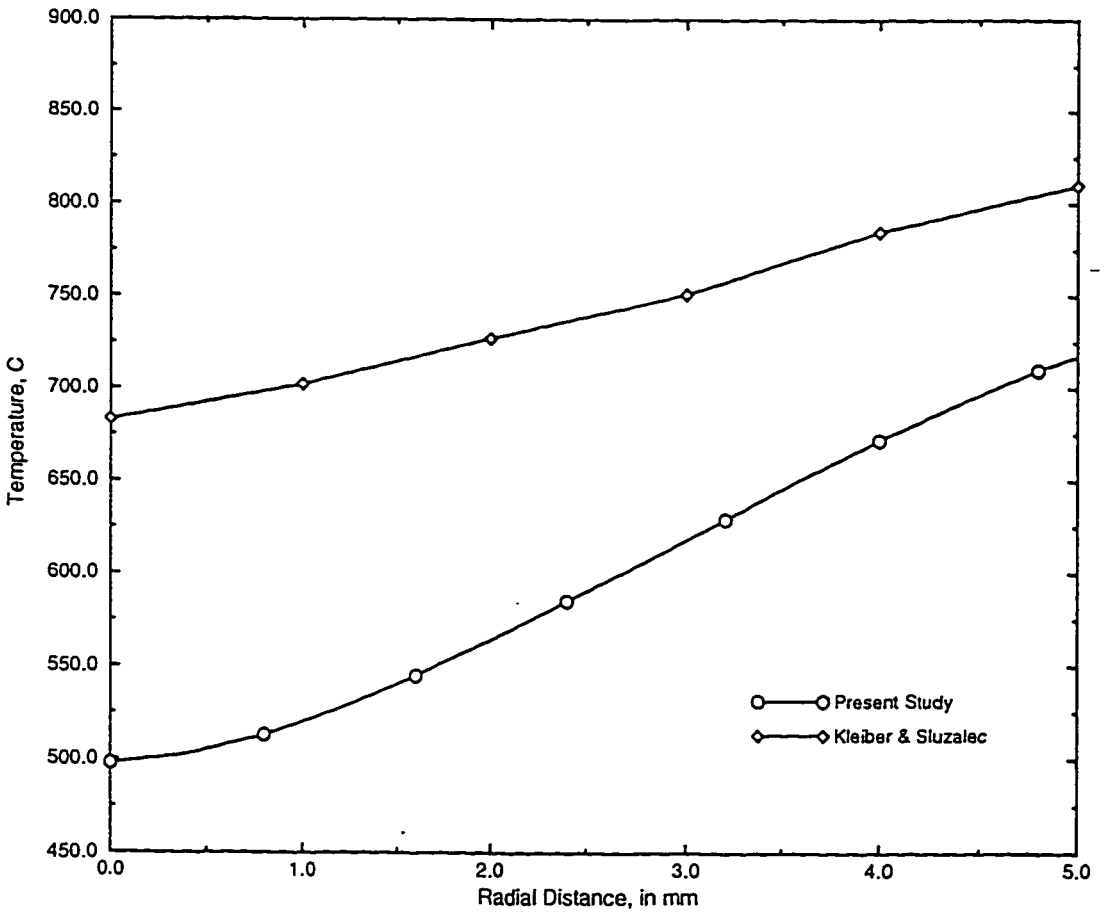

Figure 4.134: Validation

Chapter 5

Conclusions

Governing equations have been written for the three-dimensional, transient temperature analysis during the friction welding of two cylindrical bars. These equations can be used for similar material combinations as well as for dissimilar material combinations. Due to the complexity of the equations to solve analytically, these equations are solved using the finite difference method.

Temperature profiles are drawn in radial, circumferential and axial directions for different jet velocities and different angular speeds for different material combinations. In all the samples, the increase in jet velocity increases the temperature difference between the front and back stagnation points on the surface at the interface. The same phenomenon is observed at mid-radius also but the amount of difference is less than on the surface. This is due to the less heat generation at the mid-radius which is directly proportional to the radius and more cooling effect on the surface due to the jet.

In the radial direction, higher temperatures obtained at back stagnation point

($\theta = 0.0$), where the heat transfer coefficient is minimum, than at front stagnation point ($\theta = \pi$). The maximum temperature point occurs on the surface at back stagnation point. With the increase in jet velocity, due to the increase in cooling effect, this point occurs inside the material and the distance of this point from the surface increases with the increase in jet velocity.

In the axial direction, approximately symmetric temperature profiles were obtained for steel-steel case because of the similar thermal conductivity of the two bars being welded. Due to the high thermal conductivity, in the case of dissimilar material combinations, heat diffuses within the bar which has the higher conductivity of the two bars, increasing the temperature and hence widening the heat affected zone.

The increase in angular speed decreases the welding cycle duration by increasing the heat generation rate. The increase in angular speed decreases the temperature difference among the profiles for different jet velocities. The temperature rises sharply during the beginning of the welding cycle due to the rapid heat generation at the interface of the two materials and diffusion of heat. As the time increases, this diffusion decreases due to the onset of cooling effect caused by the jet and hence the temperature does not rise so sharply in the later part of the welding cycle.

5.1 Future Work

- The present study can be evaluated by an experimental studies.
- In the present study, it is assumed that the thermal properties are independent of temperature. By considering temperature dependent properties, the present study can be extended for variable thermal properties.

Bibliography

[1] D. E. Spindler. What industry needs to know about friction welding. *Welding Journal*, pages pp. 37–42, 1994.

[2] B. Crossland. Friction welding. *Contemporary Physics*, 12(6):pp 559–574, 1971.

[3] V. I. Vill. Fricition welding of metals. *Translated and published by American Welding Society*, 1962.

[4] V. I. Vill. Friction welding of metals. *Svar. Prozvod* (Welding Production, Russian), 3(9):pp. 19–23, 1957.

[5] J. Oriowski. Welding by friction. *Przegl, Tech* (Polish), 78(17):pp. 668–669, 1957.

[6] W Hofmann and H. Schildwachter. Friction welding of metals. *Schweissen Schneiden* (in German), 11(9):pp. 349–352, 1959.

[7] J. Mandaus and J. Voboril. Friction welding. *Strojirenstvi* (in Czechoslovakian), 9:pp. 681–688, 1957.

[8] V. I. Vill. Energy Distribution in Friction Welding of Steel Bars. *Weld Production*, 10:pp. 31–41, 1959.

[9] A. E. Gel'dman and M. P. Sander. Power and Heating in the Friction Welding of Thick-Walled Steel Pipes. *Weld Production*, 10:pp. 53–62, 1959.

[10] C. J. Cheng. Transient Temperature Distribution During Friction Welding of Two Similar Materials in Tubular Form. *Welding Journal* (Research Supplement), 41(12):pp. 542s–550s, 1962.

[11] C. J. Cheng. Transient Temperature Distribution During Friction Welding of Two Dissimilar Materials in Tubular Form. *Welding Journal* (Research Supplement), 42(5):pp. 233s–240s, 1963.

[12] K. K. Wang and P. Nagappan. Transient Temperature Distribution in Inertial Welding of Steels. *Welding Jounal*, 49(7):pp. 419–426, 1970.

[13] F. D. Duffin and A. S. Bahrani. The Mechanics of Friction Welding. *Metal Construction*, 8:pp. 267–271, 1976.

[14] L. G. Petrucci. Temperature Distribution in Friction Welding. *General Engineer*, 89:pp. 179–185, 1978.

[15] A. Francis. *Mathematical Models for Friction Welding.* PhD thesis, University of Southampton, Southampton, England, 1983.

[16] I. L. H. Hansson and Kristensen J. K. Temperature Distribution and Thermal Cycle in Friction Welding. In *Joining of Metals* (JOM-2). Proceedings, International Conference, Helsingor, Denmark, pages 161–167. Helsingor, 1984.

[17] S. J. Na, J. Ruge and K. Thomas. Temperature Determination During the Friction Welding of Dissimilar Materials in Cylindrical Form-Measurement and Calculation. *Schweissen und Schneiden*, 36(3):pp. E43–E45, 1984.

[18] A. Sluzalec. Thermal Effects in Friction Welding. *International Journal of Mechanical Sciences*, 32(6):pp. 467–478, 1990.

[19] M. Kleiber and A. Sluzalec. Finite Element Analysis of Heat Flow in Friction Welding. *Rozprawy Inzynierskie* (Engineering Transactions), 32(1):pp. 107–113, 1984.

[20] Sluzalec Adolf and Sluzalec Andrzej. Solutions of Thermal Problems in Friction Welding-Comparative Study. *International Journal of Heat and Mass Transfer*, 36(6):pp. 1583–1587. 1993.

[21] W. M. Kays and I. S. Bjorklund. Heat Transfer from a Rotating Cylinder With and Without Crossflow. *Transactions of ASME*, 80:pp. 70–78, 1958.

[22] R. M. Fand. Heat Transfer by Forced Convection from a Cylinder to Water in Crossflow. *International Journal of Heat and Mass Transfer*, 8:pp. 995–1010, 1965.

[23] Ryochachi S. et al. Heat Transfer From a Rotating Cylinder With and Without Crossflow. *Heat Transfer-Japanese Research*, pages pp. 109–122, 1992.

[24] C. C. Chiou and S. L. Lee. Forced Convection on a Rotating Cylinder with an Incident Air Jet. *International Journal of Heat and Mass Transfer*, 36(15):pp. 3841–3850, 1993.

[25] Vedat S. Arpaci. "*Conduction Heat Transfer* ". Addison-Wesley Publishing Company, Reading. Massachusetts, 1966.

[26] Frank P. Incropera and David P. De Witt. "*Introduction to Heat Transfer* ". John Wiley & Sons. 1973.

Vita

- **Shaik Ilias Ahamad**
- Born in Hyderabad, India
- Received Bachelor's degree in Mechanical Engineering from the Osmania University, Hyderabad, India in July, 1991.
- Completed Master's degree requirements at King Fahd University of Petroleum and Minerals, Dhahran, Saudi Arabia in April, 1996.